Schulze, Lydia

Development of an Application-Oriented Approach for Two-Phase Modelling in Hydraulic Engineering

Dresdner Wasserbauliche Mitteilungen

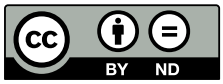

TECHNISCHE UNIVERSITÄT DRESDEN

Fakultät Bauingenieurwesen Institut für Wasserbau und Technische Hydromechanik

Dresdner Wasserbauliche Mitteilungen
Heft 61

Lydia Schulze

Development of an Application-Oriented Approach for Two-Phase Modelling in Hydraulic Engineering

(Entwicklung eines anwendungsorientierten Ansatzes für die Modellierung von Zweiphasenströmungen im Wasserbau)

Der Titel und der Inhalt des Heftes entsprechen der zur Erlangung des akademischen Grades Doktor-Ingenieur (Dr.-Ing.) an der Fakultät Bauingenieurwesen der Technischen Universität Dresden im Juni 2017 eingereichten und genehmigten Dissertation von Lydia Schulze, M.Eng.

Verteidigung: 8.1.2018

Vorsitzender der Promotionskommission:
Prof. Dr.-Ing. Jürgen Stamm, Technische Universität Dresden

Gutachter:
Prof. Dr.-Ing. Jann Strybny, Hochschule Emden/Leer
Prof. Dr. sc. tech. Peter Rutschmann, Technische Universität München

Dresden, August 2018

Bibliografische Informationen

Die Deutsche Bibliothek verzeichnet diese Publikation in der Deutschen Nationalbibliographie. Die bibliografischen Daten sind im Internet über http://dnb.ddb.de abrufbar.

Development of an Application-Oriented Approach for Two-Phase Modelling in Hydraulic Engineering

(Entwicklung eines anwendungsorientierten Ansatzes für die Modellierung von Zweiphasenströmungen im Wasserbau)

Technische Universität Dresden, Fakultät Bauingenieurwesen,
Institut für Wasserbau und Technische Hydromechanik.
Dresden: Institut für Wasserbau und Technische Hydromechanik, 2018
(Dresdner Wasserbauliche Mitteilungen; Heft 61)
Zugl.: Dresden, Techn. Univ., 2018
ISBN 978-3-86780-571-1

Herausgegeben im Auftrag des Rektors der Technischen Universität Dresden von:

Univ.-Prof. Dr.-Ing. J. Stamm, Univ.-Prof. Dr.-Ing. habil. K.-U. Graw

Technische Universität Dresden
Fakultät Bauingenieurwesen
Institut für Wasserbau und Technische Hydromechanik
01062 Dresden

Tel.: +49 351 463 34397
Fax: +49 351 463 37120
E-Mail: mail@iwd.tu-dresden.de
WWW: http://iwd.tu-dresden.de

Redaktion: Lydia Schulze

Redaktionsschluss: 30. August 2018

Verlag: Selbstverlag der Technischen Universität Dresden

ISSN 0949-5061
ISBN 978-3-86780-571-1

Development of an Application-Oriented Approach for Two-Phase Modelling in Hydraulic Engineering

Entwicklung eines anwendungs-orientierten Ansatzes für die Modellierung von Zweiphasenströmungen im Wasserbau

Dissertation

zur Erlangung des akademischen Grades
Doktor-Ingenieurs (Dr.-Ing.)

an der Fakultät Bauingenieurwesen
der Technischen Universität Dresden

eingereicht von
Lydia Schulze M.Eng.
geboren am 16.08.1987 in Nürnberg

Gutachter:	Prof. Dr.-Ing. Jürgen Stamm Technische Universität Dresden
	Prof. Dr.-Ing Jann Strybny Hochschule Emden/Leer
	Prof. Dr.sc.techn. Peter Rutschmann Technische Universität München
Tag der Einreichung:	6. Juni 2017
Tag der Verteidigung:	8. Januar 2018

Preface

The research leading to this thesis was carried out at the Federal Waterways and Engineering Institute of Germany (BAW) in cooperation with the Institute of Hydraulic Engineering and Technical Hydromechanics (IWD) at the Technische Universität Dresden.

I would like to express my deep gratitude to Prof. Dr.-Ing. Jürgen Stamm, chair of the Hydraulic Engineering and director of IWD at the Technische Universität Dresden, for his support and the supervision of this work. Very special thanks are also due to Dr.-Ing. Carsten Thorenz, head of section hydraulics at structures at the BAW, for his valuable and constructive suggestions, his continuous support and the guidance during the development of this research work. Additionally, I am particularly grateful for the supervision of Prof. Dr.-Ing. Jann Strybny, chair of Maritime Technology and Fluid Dynamics at the University of Applied Sciences Emden Leer, who was the first to give me an insight into the interesting field of hydraulic engineering and awoke my pleasure for Computational Fluid Dynamics.

Furthermore, I would like to thank all colleagues, who provided a positive working environment, lots of motivating words and supported me on technical and personal level. Particular thanks to Udo Pfrommer and the laboratory staff for finally enabling the collection of data from the physical model and to Franz Simons for his assistance with the photo technology.

This work would not have been the same without the C++ library of OpenFOAM which provided the framework for the implementations. Therefore, I would like to extend my gratitude to all who helped to develop and improve the framework and those who provide valuable support through forums. The NUMAP-Summer school organized by the OpenFOAM specialists Prof. Hrvoje Jasak and Dr. Henrik Rusche, which I attended in September 2013, gave me valuable inspiration and knowledge for my project. I am particularly grateful for the support of the organizers.

Finally, I wish to sincerely thank my family, my partner and my friends for their encouragements and unconditional support throughout the way. Your contribution to this work was of inestimable value for me. Thank you!

Lydia Schulze

Abstract

In this thesis a numerical approach for the modelling of air transport and degassing processes within turbulent free-surface flows is developed, implemented and tested.

Aiming to find an approach to enable the investigation of the near-field flows at hydraulic structures including air-water intermixing processes, the applicability of existent mathematical approaches was analysed and evaluated. A suitable approach has to be able to capture multiple two-phase phenomena, which occur during simultaneous physical processes. Here the capturing of processes at various interface scales provides a challenge. The model has to reproduce the large stretched free surface with sufficient precision, the interaction between the entrained air bubbles and the surrounding water body as well as the detrainment process at the free surface. The flow under consideration is strongly influenced by turbulence. Therefore, a suitable turbulence model to be coupled with the two-phase approach has to be found. As the above mentioned requirements cannot be met by any of the existent two-phase models, a new model was developed.

This new approach extends a mixture model with a new method of physically modelling the bubble rising process. Three different variants for the calculation of the bubble rising velocity were implemented into the developed model. This allows the model to capture the effect of rising bubbles, even if they are not directly captured by the grid. Since the model is formulated for incompressible flow, the compression of the air bubbles below the water surface cannot directly be accounted for. In order to consider the influence of the bubble size to the bubble rising velocity an extension for “pseudo-compressibility” was included. With this additional feature the bubble diameter, which is used to calculate the bubble rising velocity, is adapted according to the surrounding water pressure.

At large-scale free surfaces the model operates as a volume of fluid approach. To allow a sharp representation of the interface between the phases,

which is modelled by a scalar transport equation, higher order discretisation schemes can be applied. In this study various Total-Variation-Diminishing schemes were tested regarding stability and accuracy with reference to hydraulic structure flow simulations. In addition, a flux-corrected transport algorithm was introduced to ensure the boundedness of the solution. With this method, the necessity for complex geometrical reconstruction methods or methods with artificial compression at the interface can be avoided.

The formulation of the model is based on the finite volume method formulated for arbitrary structured meshes. The C++ library OpenFOAM was used as framework for the implementation of the model. Relying on the available structure of the framework the parallelization of the solver is inherent. Furthermore, the available sets of discretisation schemes and matrix solvers are directly applicable with the implemented model. The framework also enables the coupling with a variety of turbulence models. As the common Reynolds-Averaged-Navier-Stokes (RANS) turbulence models are not specifically adapted for two-phase flows, the interaction between the bubbles and the velocity fluctuations of the flow field cannot be captured. As a consequence the transport capacity of the flow is reduced and the bubbles of the mixture model with RANS turbulence model rise too fast. To counteract this, the developed mixture model is extended with an additional term in the transport equation for the gaseous phase. The term produces additional diffusion in the bubbly zone dependent on the local turbulent viscosity of the flow. As a consequence bubble rising in turbulent flow is decelerated.

Simple test cases show that the developed solver meets the defined demands concerning multiscale two-phase flow. Comparisons of analytical and experimental results demonstrate the functionality and the accuracy of the implemented model. Particularly the influence of grid resolution, discretisation schemes and bubble diameter is tested. Furthermore, the influence of the pseudo-compressibility dependent on the water depth is presented.

With two application-oriented test cases, the utilisation of the new model to real-world engineering applications is presented. On the one hand, the efficiency and the performance of the solver are proven to be suitable for large parallel computations. On the other hand, examples of applying the theory in

applications are shown. A comparison with measurement results from a physical model reviews the comparability with reference to the bubble transport with the flow. Moreover results from various turbulence models are compared and evaluated. This comparison illustrates the necessity for the extension of the transport equation for the gaseous phase with the additional diffusion term when RANS turbulence models are applied.

With the means of the solver, a vast amount of information of the effect of entrained air in the nearfield flow of hydraulic structures can be gained. The output could be used for future structure design and operation optimization. Particularly in the field of lock design and optimisation the new approach enables new insights: with the model, the influence of defined air content on the forces on the ship during the filling process can be tested for a head-filling lock system.

The test cases also reveal limitations of the model applicability: the air entrainment process due to a falling water jet cannot be represented by the model. As this process is relevant for many different questions in hydraulic engineering, more research is required in this field. Additionally, the modelling of turbulences is of large importance for many applications. Thus, validation test cases should test the applicability of the current implementation.

Kurzfassung

In dieser Arbeit wurde ein numerischer Ansatz für die Modellierung von Lufteintrags- und Transportprozessen für turbulente Strömungen mit freier Wasseroberfläche entwickelt, implementiert und getestet.

Mit dem Ziel das Nahfeld von Wasserbauwerken mit freien Wasseroberflächen sowie mit Luft-Wasser-Durchmischungsprozessen untersuchen zu können, wurde die Anwendbarkeit bestehender Ansätze analysiert und bewertet. Ein geeigneter Ansatz muss mehrere Zweiphasen-Prozesse abbilden können, die bei den gleichzeitig auftretenden, verschiedenen physikalischen Prozessen entstehen. Eine Herausforderung stellen dabei vor allem die unterschiedlichen Größenskalen der Grenzflächen dar. Das Modell muss sowohl die großflächige freie Wasseroberfläche mit ausreichender Genauigkeit reproduzieren, als auch die Interaktion der in Form von Blasen eingetragenen Luft mit dem umgebenden Wasser, sowie das Entgasen der Luft an der freien Wasseroberfläche berücksichtigen. Die betrachteten Strömungen werden außerdem stark von der auftretenden Turbulenz beeinflusst. Daher muss ein geeignetes Turbulenzmodell für die Kopplung mit dem Zweiphasen-Ansatz gefunden werden. Da die genannten Anforderungen von bestehenden Modellen nicht erfüllt werden, wurde ein neuer Ansatz entwickelt.

Der neue Ansatz erweitert ein Mixture-Modell mit einem neuen Ansatz für die physikalische Blasenaufstiegsmodellierung. Im hier entwickelten Ansatz wurden drei verschiedene Varianten für die Berechnung der Blasenaufstiegsgeschwindigkeit implementiert. Das entwickelte Modell ist in der Lage auch den Effekt von aufsteigenden Luftblasen auf die Strömung zu berücksichtigen, die nicht durch das Gitter direkt abgebildet werden können. Da das Modell für inkompressible Phasen formuliert ist, kann die Kompression der Luftblasen unterhalb der Wasseroberfläche nicht direkt berücksichtigt werden. Um dennoch den Einfluss der Blasengröße auf die Aufstiegsgeschwindigkeit untersuchen zu können, wurde das Blasenaufstiegsmodell mit einer „Pseudo-Kompression“ erweitert. Mit Hilfe dieser Zusatzfunktion wird der Blasen-

durchmesser, der für die Berechnung der Aufstiegsgeschwindigkeit der Blase verwendet wird, an den umgebenden Wasserdruck angepasst.

Im Bereich großflächiger freier Wasseroberflächen funktioniert das Modell wie ein Volume-of-Fluid Ansatz. Damit die freie Wasseroberfläche mit Hilfe der skalaren Volume-Fraction-Transportgleichung mit möglichst klarer Grenzfläche zwischen den zwei Phasen abgebildet wird, können Diskretisierungsschemata höherer Ordnung eingesetzt werden. Im Rahmen dieser Arbeit wurden verschiedene Total-Variation-Diminishing Schemata auf ihre Stabilität und Genauigkeit in Bezug auf die Anwendung bei wasserbaulichen Fragestellungen getestet und evaluiert. Zusätzlich wurde für die Lösung der skalaren Transportgleichung ein Flux-Corrected-Transport-Algorithmus eingesetzt, der eine Lösung ermöglicht, die definierte Grenzwerte nicht unter- oder überschreitet. Dadurch kann die Notwendigkeit von komplexen geometrischen Rekonstruktionsmethoden oder Methoden mit künstlicher Kompression für die Schärfung der Oberflächen vermieden werden.

Die Formulierung des Modells basiert auf der Finiten-Volumen-Methode für unstrukturierte Gitter. Die C++ Bibliothek OpenFOAM diente als Framework für die Implementierung des Lösers. Dadurch konnten die inhärente Parallelisierung sowie die vorhandenen Disketisierungsschemata und Gleichungslöser für die Anwendungen genutzt werden. Auch die Kopplung mit einer Vielzahl an Turbulenzmodellen wird durch das Framework ermöglicht. Da die gängigen Reynolds-Averaged-Navier-Stokes-Turbulenzmodelle (RANS-Turbulenzmodelle) nicht speziell für die Modellierung von Zweiphasen-strömungen angepasst sind, kann die Interaktion zwischen den Blasen und den Geschwindigkeitsschwankungen der Strömung nicht abgebildet werden. Dadurch verringert sich die Transportkapazität der turbulenten Strömung und die Blasen im Mixture-Modell mit RANS-Turbulenzmodell entweichen zu schnell. Um dem entgegen zu wirken, wird das Mixture-Modell mit einem zusätzlichen Term in der Transportgleichung für die Gasphase erweitert. Dieser sorgt in Abhängigkeit von der lokal berechneten turbulenten Viskosität für Eintrag von Diffusion und verhindert damit den zu schnellen Aufstieg von Blasen in turbulenter Strömung.

Zwei einfache Testfälle zeigen, dass die definierten Anforderungen an den Zweiphasenlöser erfüllt werden können. Vergleiche mit analytischen und experimentellen Daten dienen der Überprüfung der Funktionalität sowie der Genauigkeit des implementierten Modells. Insbesondere wird der Einfluss von Gitterauflösung, Diskretisierungsschemata und Blasendurchmesser getestet. Außerdem wird der Einfluss der Pseudo-Kompressibilität in Abhängigkeit von der Wassertiefe dargestellt.

Die Anwendbarkeit des Lösers für Untersuchungen im Nahbereich von Bauwerken wird anhand von zwei anwendungsorientierten Fallstudien untersucht. Zum einen wird die Effizienz und Leistungsstärke des Lösers bei großen parallelen Rechnungen analysiert, zum anderen zeigen die Fallstudien mögliche Einsatzbereiche des Lösers für die Beantwortung von aktuellen Fragestellungen. Der Vergleich mit Messwerten aus einem gegenständlichen Modell überprüft die Übereinstimmung für den Transport des Luftgehaltes mit der Strömung. Außerdem werden die Ergebnisse von verschiedenen Turbulenzmodellen verglichen und evaluiert. Dieser Vergleich verdeutlicht die Notwendigkeit der Erweiterung der Transportgleichung für die Gasphase mit dem Diffusionsterm beim Einsatz von RANS-Turbulenzmodellen.

Mit Hilfe des neuen Lösers kann eine Vielzahl von Informationen über den Einfluss von eingemischter Luft auf die Strömung im Nahbereich von Wasserbauwerken gewonnen werden. Diese können für die Optimierung von bestehenden und zukünftigen Bauwerken genutzt werden. Insbesondere im Bereich der Schleusenplanung und -optimierung ermöglicht der entwickelte Ansatz neue Erkenntnisse: so kann mit Hilfe des neuen Ansatzes beispielsweise getestet werden, welchen Einfluss ein definierter Luftgehalt in einem Vor-Kopf-Füllsystem auf die Schiffskräfte während der Schleusung hat. Anhand der Fallstudien zeigen sich auch die Grenzen des Modells: der Lufteinmischungsprozess durch einen fallenden Wasserstrahl kann mit der entwickelten Methodik nicht abgebildet werden. Da dieser für die vollständige Modellierung von vielen Fragestellungen notwendig ist, besteht hier weiterer Forschungsbedarf. Außerdem ist in vielen Anwendungsfällen die Turbulenzmodellierung von großer Bedeutung. Daher sollte mit Hilfe von Validierungsfällen überprüft werden, ob die Implementierung für die Anwendung geeignet ist.

Content

List of Figures

List of Tables

Nomenclature

Symbol	Description	SI Units
$\{\mathbf{A}\}$	square coefficient matrix	[-]
A	area	[m²]
b	turbulence diffusion influence factor	[-]
$\mathbf{b}$	vector describing the difference between the velocity of the centre of mass and the velocity of the centre of volume	[m/s]
ΔB	influence of surface roughness on the wall	[-]
c	speed of sound	[m/s]
c_2	mass fraction of the dispersed phase	[-]
C_d	drag coefficient	[-]
C_μ	dimensionless constant for the wall stress calculation	[-]
Co	Courant number	[-]
C_S	roughness coefficient	[-]
d_B	bubble diameter	[m]
$\mathbf{d}_{PN}$	vector between two cell centres	[m]
D_t	turbulent diffusivity	[m²/s]
E	empirical constant	[-]
E_b	bulk modulus of elasticity	[Pa]
Eo	Eötvös number	[-]
F_{ext}	external forces	[N]
f_{drag}	drag force function	[-]
Fr	Froude number	[-]

Symbol	Description	SI Units
Fr_i	Froude number at the crest of an overflow structure	[-]
F_{st}	surface tension force	[N]
g	gravity	[m/s²]
g	gravitational acceleration vector	[m/s²]
h	water level	[m]
h_0	initial water level	[m]
Δh	water level difference	[m]
$\mathscr{H}$[U]	matrix of the neighbour coefficients multiplied by the vector U and the source term contributions	[-]
H	second auxiliary function for approach by Zheng and Yapa (2000)	[-]
I	turbulent intensity	[m/s]
I	identity tensor	[-]
IC	crest conditions	[-]
j	velocity of the centre of volume of the mixture/volumetric flux	[m/s]
J	first auxiliary function for approach by Zheng and Yapa (2000)	[-]
K	non-dimensional fit coefficient	[-]
$\boldsymbol{k}$	non-orthogonal part of the face normal vector	[m]
k_P	turbulent kinetic energy at the cell centre	[m²/s²]
K_S	effective roughness height	[m]
K_S^+	non-dimensional roughness height	[-]

Symbol	Description	SI Units
L	length	[m]
Ma	Mach number	[-]
M_{drag}	momentum due to drag force	[kg·m/s]
M_{hist}	momentum due to history force	[kg·m/s]
M_{lift}	momentum due to lift Force	[kg·m/s]
Mo	Morton number	[-]
M_{vm}	momentum due to virtual mass force	[kg·m/s]
p	pressure	[N/m²]
p_{abs}	absolute pressure	[N/m²]
p_p	local pressure	[N/m²]
Q	discharge	[m³/s]
Q_{Water}	water inflow rate	[m³/s]
Q_{Water}	total inflow rate	[m³/s]
r	ratio of successive gradients	[-]
$\boldsymbol{r}$	source term contributions in the momentum matrix	[-]
Re	Reynolds number	[-]
Re_p	particle Reynolds number	[-]
s	shrinking factor	[-]
Sc_t	turbulent Schmidt number	[-]
S_f	face area vector	[m²]
t	time	[s]
TV	total variation	[-]
$\mathbf{U}$	velocity vector	[m/s]
$\mathbf{U}_1$	velocity of phase 1	[m/s]
$\mathbf{U}_2$	velocity of phase 2	[m/s]

Symbol	Description	SI Units
$\mathbf{U}_c$	artificial compression velocity	[m/s]
$\mathbf{U}_f$	velocity interpolated to the cell face	[m/s]
$\mathbf{U}_{j,2}$	drift velocity of phase 2	[m/s]
$\mathbf{U}_m$	velocity of the centre of mass of the mixture	[m/s]
$\mathbf{U}_{m,1}$	diffusion velocity of phase 1	[m/s]
$\mathbf{U}_{m,2}$	diffusion velocity of phase 2	[m/s]
$\mathbf{U}_r$	relative velocity between phase 1 and phase 2	[m/s]
U_t	terminal velocity	[m/s]
V	volume	[m³]
υ	velocity	[m/s]
υ_i	velocity at the crest of an overflow structure	[m/s]
υ_r	relative velocity between continuous and dispersed phase	[m/s]
We	Weber number	[-]
[**x**]	solution vector	[m]
y^+	dimensionless distance	[-]
α	volume fraction	[-]
α_p	volume fraction of the dispersed phase	[-]
α_{pm}	concentration for maximum packing	[-]
γ	switching criterion by Damian (2013)	[-]
ε	average dissipation rate	[m²/s³]
η	smallest length scale in turbulent flow	[m]
θ	weighting factor	[-]
κ	surface curvature of the interface	[1/m]
κ_υ	Kármán's constant	[-]

Symbol	Description	SI Units
μ_c	dynamic viscosity of continuous phase	[kg/(m·s)]
μ_g	dynamic viscosity of gaseous phase	[kg/(m·s)]
μ_l	dynamic viscosity of liquid phase	[kg/(m·s)]
μ_m	dynamic viscosity of the mixture	[kg/(m·s)]
μ^*	local viscosity	[kg/(m·s)]
ν	kinematic viscosity	[m²/s]
ν_t	turbulent diffusion	[m²/s]
ρ	density	[kg/m³]
ρ_c	density of continuous phase	[kg/m³]
ρ_g	density of the gaseous phase	[kg/m³]
ρ_l	density of the liquid phase	[kg/m³]
σ	surface tension	[N/m]
τ	kinematic viscosity	[m²/s]
τ_{Tk}	averaged turbulent stress tensor	[Pa]
τ_w	wall shear stress	[Pa]
ϕ	general tensorial quantity	[-]
$\psi(r)$	limiter function for total variation diminishing schemes	[-]
ω	turbulent eddy frequency	[1/s]
Γ	interface	[-]
Γ_k	mass generation of phase k	[kg]
Δ	orthogonal part of the face normal vector	[m]

1 Introduction

1.1 Background and Motivation

Air entrainment, transport and detrainment processes occur where intermixing of air and water takes place. Considering the field of hydraulic engineering these phenomena can be observed at a large variety of natural and artificial structures. Man-made dams, drop structures or natural barrages at rivers, lakes or canals cause water to surmount barriers and subsequently free falling water jets evolve. When the turbulence at the free surface is large enough to overcome gravitational and surface tension forces, air is entrained into the falling water body. At the lower end of the barrier the jet plunges into the water reservoir on the downstream side and thereby air pockets and bubbles can be entrapped. Air entrainment also occurs due to surface and velocity discontinuities at the toe of hydraulic jumps and the breaking of waves. Dependent on the velocity and the turbulence of the flow the entrained air is either directly detrained or transported with the flow.

The intermixing of the two phases can significantly influence the characteristics of the flow. Due to buoyancy the entrained air bubbles introduce vertical momentum to the flow. Moreover, the bulk properties of the mixture like density and compressibility are changed through the intermixing. As a consequence, the water depth in free-surface flow can be increased. Local detrainment of many air bubbles may cause waves or bulging of the water surface.

Generally, aeration of the flow can be beneficial at structures, where the entrainment of air causes counteracts reductions of the pressure and thereby preventing cavitation damages. This positive effect is used at structures like valves or spillways. Furthermore, the enrichment of the water flow with more oxygen can be favourable for environmental reasons at natural rivers, lakes or at sewage treatment structures. In other cases, the uncontrolled intermixing of air and water is undesirable. This is the case for closed hydraulic systems, where unintended air entrainment and subsequent accumulations of the air inside closed systems can lead to uncontrolled release of the air. The resulting blow-backs or blow-outs can cause severe damages and risks. Unregulated entrainment of air can also bias the flow characteristic inside complex hydraulic structures like navigation locks, where the exact knowledge of the flow behaviour is essential for an optimal operation. Inflow and outflow processes are precisely regulated, to minimize the resulting forces acting on the ship hull inside the lock. At the same time, the filling and emptying times as well as building and maintenance costs should be minimized when designing lock systems. Although the intermixing of air into those systems can significantly affect their functionality, the entrainment of air is inevitable for many designs. As the consequences of air-water intermixing processes inside the structures are not yet fully understood, a high need for appropriate investigation methods arises.

Tools like Computational Fluid Dynamics (CFD) in combination with high-tech measurement techniques on physical scale models provide an opportunity of investigating details of existing systems and approving new ideas. Yet, current multiphase models are designed for a specific flow pattern and a certain scale. Therefore, the simultaneous modelling of bubble transport and detrainment processes is unfeasible, when a large stretched water surface has to be captured simultaneously. Therefore, new methods for the investigation have to be developed, approved and applied.

It is the aim of this work to provide a contribution to improve the understanding of two-phase flows and their effect on the flow in the nearfield of hydraulic structures. Focus is put on the simultaneous capture of a large variety

of flow patterns with various levels of scales. The patterns considered include large stretched water surfaces as well as small air bubbles which are transported with the flow. Aiming for an application-oriented approach the method should be robust in handling large complex geometries. Parallelisation as well as the careful choice of stable but accurate discretisation schemes is essential for the applicability of a new approach.

Currently, the ability to model of bubble transport, detrainment and free-surface flow simultaneously is of special interest in the field of lock design. Here, a deeper insight into the effects of entrained air might allow improving existent systems and optimizing designs for new structures. The application-oriented test cases in this study therefore concentrate on the applicability of the new approach to navigation lock modelling.

The next section gives an overview to the state-of-the-art of the available analysing methods and evaluates their applicability for the investigation of air entrainment, transport and detrainment processes.

1.2 Review and Evaluation of Available Analysing Methods

For analysing the hydraulic properties of a structure the following principle methods are available:

- field measurements,
- physical scale models and
- numerical models.

All methods have their advantages and drawbacks, which precludes their exclusive use. Therefore, the question “Which methods are worth considering?” must be answered individually for every case. This section reviews and evaluates the methods generally available for the investigation of flow in the nearfield of hydraulic structures.

1.2.1 Field Measurements

With **field measurements**, existent structures are used to gain information about the properties of interest. For this purpose physical measurement tools are temporally or permanently installed close to or inside the structure in order to

record defined parameters of the flow. Subsequently the recorded data can be analysed and evaluated. Field measurements are very valuable when existing structures are to be investigated. The in-situ data enables a genuine and straight insight into the present flow situation, whereby influences of unknown construction features resulting e.g. from an ageing structure and/or natural vegetation are directly reproduced in the data. However, due to the complexity of the data mining, the measurement data is often restricted to a very limited number of measuring points and series. Additionally external conditions, like the weather or water level situation or the course of the measuring ship etc. affect the quality and the reproducibility of the results.

In **existent locks** problems with air entrainment mostly occur inside the culverts (as described in e. g. Roux and Wong, 2012), where low pressure in proximity to valves promotes air entrainment and thereby avoids cavitation erosion. Cavitation occurs in low pressure regions, where water changes from liquid phase to gaseous phase at ambient temperature. The resulting vapour bubbles implode downstream when they are exposed to higher pressures. The implosions form micro water jets, which impinge on the structure surface. In unaerated flows resulting jet impact pressures are not dampened. In contrast, aerated flow enables the dampening of the implosion pressures due to the compressibility of the mixture flow. These phenomena can be investigated by analysing solely the pressure conditions causing the situation. In the lock, the air entrainment is not caused by pressure changes, therefore no analogy concerning field or physical measurement techniques can be drawn. However, similar air entrainment processes can be regarded at some existent lock systems: in locks with “through-the-gate” filling systems the water enters through the upstream gate and directly drops down several metres and a free plunging jet develops and entrains air into the lock chamber. As this system is only used for lift heights up to 10 metres, the amount of air entrainment is not directly comparable with the system under investigation, but still very similar phenomena can be observed. Measurements from existing locks could be used for validating results of CFD simulations. To the knowledge of the author, no prototype measurements analysing air entrainment in ship locks are existent and own measurements

campaigns in the field are out of the scope of this work but could be considered as future objective. Evaluating studies about the air entrainment properties of **weir overflows** could also provide a good insight into the air entrainment processes of a plunging jet. Most studies in the named field aim to quantify and enhance the aeration capacities of weirs. Aeration at weir structures is often intended to increase the oxygen content of the water for ecological reasons or to avoid mechanical vibrations at the structures caused e.g. by pressure fluctuations (see e.g. Chanson, 1995, Gebhardt, 2010). Although the quantification of air entrainment features of different weir shapes and heights is of interest for many studies, only very little research has been done on prototype scale. The reason for this lack of data is the complexity of the measurement installation and the mortal danger in proximity to the weir structure. Many more studies can be found which were conducted with small scale models. Another hydraulic structure where air entrainment is of relevance for the hydraulic system is a **spillway**. In particular, spillways are designed with the goal to enable the controlled release of high waters. In these constructions, the air entrainment provides protects the structure against cavitation erosion.

Due to the high complexity of the measuring setup, large uncertainties through natural influences like wind, temperature and due to human influences like inaccurate steering of measuring boats, very few field measurement studies have been performed, which investigate air entrainment processes inside or in the near field of hydraulic structures. A much larger variety of investigations can be found in the field of physical scale model measurements.

1.2.2 Physical Scale Models

Physical scale models use similarity laws for reconstructing hydraulic engineering structures at a chosen scale, inferring that geometric, kinematic and dynamic similitude between prototype and scale model is achieved. Geometric similitude is reached, when all corresponding geometrical dimensions have the same ratio in prototype and scale model. When all ratios of corresponding velocities and accelerations are the same and the flow field has the same shape in prototype and scale model, kinematic similitude is achieved. Dynamic

similitude is reached, when the ratios of all forces in the prototype to all corresponding forces in the scale model are constant.

With upscaled or downscaled models, physical phenomena can be reproduced and investigated in detail, en passant producing visual evidence of the complete flow situation within the model. Compared to field measurement, uncertainty influences like wind or large temperature variations between the measuring series can be prevented, therefore the reproducibility of the measurements is better. Furthermore, data mining can be easier handled than with field measurements, whereby the extent and the accuracy of the obtained data depend on the measuring techniques and devices used. Since modifications of the boundary conditions like inflow, water level or simple shape optimizations at the structure can be easily applied, scale models are profitable, when a large series of modifications or boundary conditions are to be tested. Disadvantageous are the high construction effort and possible scale effects. The latter arise due to force ratios that are not identical in the model and the real-world structure and result in discrepancies in the physical behaviour.

In the field of lock design and optimization, physical scale models are a classical, widely used tool for investigating the hydraulic behaviour of the structure. From the early days of Germany's waterway engineering history till nowadays, scaled models of the planned structures provide valuable data for the design optimisation of ship locks. Whereas in former days the physical models served as a database for the prototype design, nowadays scale model data is also used for validation of numerical models (see e.g. Thorenz and Kemnitz 2006, Thorenz 2010 and Gobbetti 2013).

For the scale model investigation of a **falling water jet** plunging into a water filled pool and thereby **entraining air scaling effects** are inevitable to affect the results of any small-scaled model of the prototype (Bollaert, 2010). This results from the fact, that gravity and viscous forces dominate the system simultaneously, whereas the scale model can only model one of the forces in the correct ratio. Therefore, scale models can only be deployed for the calibration and validation of a numerical model. Quantitative results of the air entrainment are likely to suffer from scale effects.

1.2.3 Numerical Models

Numerical models are based on the solution of partial differential equations that describe the physics of the chosen problem. With sufficient computer resources, suitable model equations and solution methods, detailed information about the physical behaviour of the flow in the near-field of hydraulic engineering structures can be attained. The computed data can produce results for an almost unlimited number of probing points. Numerical simulations can be advantageous when e.g. the hydraulic properties of a structure are to be investigated in large detail, or when the influence of small modifications at structures is to be determined. Even very large models at full scale can be handled with the methods of numerical modelling. However, setup errors as well as the wrong choice of model equations quickly lead to physically wrong results. Numerical background knowledge and user experience is the prerequisite for the successful performance of a simulation.

With a combination of numerical one-, two- and three-dimensional simulations, the most (relevant) hydraulic processes inside a ship lock can be modelled. In particular, three-dimensional one phase models of single hydraulic components are used for optimizing their shape and determining head losses. The head losses are then used in the one-dimensional model to calculate the filling- and emptying times for various scenarios. Then, a two- or three-dimensional model of the complete structure can be used to analyse the water surface slopes of the chamber which are the basis for the calculation of the hawser forces (Thorenz, 2009, 2010). For the three-dimensional simulation a special two-phase model is applied. The model is designed to give accurate information about the evolution of the water surface in the lock chamber. Yet, this approach is only suitable for capturing the long-stretched water surface, but bubbles smaller than the used numerical grid cannot be modelled appropriately. For investigating the effect of entrainment air on the flow behaviour the aforementioned chain of numerical methods cannot be applied, since the models are not able to capture the effects of the phase interaction. Especially in the step, where the hawser forces are calculated from the water level slopes in the lock chamber, the influence of air bubbles within the system has to be considered.

Therefore, alternative numerical methods are necessary to enable the modelling of the air entrainment, the bubble transport and the free surface simultaneously.

1.3 Previous Related Work in Numerical Multiphase Modelling

Multiphase flows consist of multiple phases connected by a movable interface. Each phase is marked with a continuous density, viscosity etc. and can occur in solid, liquid or gaseous state. Between two immiscible phases an interface is formed, which allows mass and momentum to be exchanged. At the boundary of the interface all fluid properties are discontinuous. Furthermore, the scale of the interface varies strongly, dependent on the flow regime. An appropriate representation of the discontinuity of the fluid properties within the interface as well as the mass and momentum exchange are the most challenging tasks when designing numerical multiphase models.

The Navier-Stokes equations allow the mathematical description of the complete spectrum of turbulent two-phase flows. Theoretically, these can be solved without any further manipulation with the means of a direct numerical simulation (DNS) where all time and length scales of the flow are directly resolved by the temporal and spatial discretization. As the computational effort increases with growing resolution, DNS is restricted to small, laminar test cases and not applicable for most engineering applications. To enable numerical multiphase simulation without the necessity of resolving all scales, multiple modelling approaches were developed. For two-phase flow with large, stretched interfaces, Hirt and Nichols (1981) developed the volume of fluid (VoF) method. In the VoF approach both phases are treated as a mixture, an additional equation transports the volume fraction with the flow. Mass and momentum exchange between the intermixing phases is completely neglected. Their method is widely used for free-surface flows, where the position and the shape of the interface are most relevant. When multiphase flows with large numbers of dispersed particles (e.g. bubbly flow) are to be modelled, Euler-Euler approaches are applied. With these approaches, transport equations for both phases are solved. Both phases are considered as continuous phases, interfaces between the phases are not resolved. Mass and momentum exchange at the

interfaces is modelled via source terms in the balance equations. The formulation of these source terms is mostly based on physical experiment. Therefore closure relations must be adapted for each application. As simplification of the Euler-Euler approach, the mixture model was introduced. Similar to the VoF approach, it considers the flow as a mixture. To account for the interfacial exchange, an additional equation for the relative velocity between the phases is introduced. In a large review about the mixture model Manninen *et al.* (1996) concluded that the approach can be sometimes even more reliable than the Euler-Euler approach due to the uncertainties in the closure relations.

For the application to complex engineering applications, it is useful to implement the approaches into a performant software framework. The open source C++ library OpenFOAM, initially developed at the Imperial College of London and currently published under the GNU general public licence by *The OpenFOAM Foundation*, provides a good starting point for this: A large variety of linear equation solvers, turbulence models and discretization schemes which can be reused for individual implementations, allows the focus on the formulation of the multiphase model based on partial differential equations. A large number of **previous works in the field of multiphase flow modelling** with OpenFOAM provide valuable contributions for making OpenFOAM a powerful tool in hydraulic engineering and many other engineering disciplines:

- The volume of fluid solver *interFoam* was developed by Henry Weller (who published the code, but no citable documentation). The numerical foundation of the solver was documented and further improved by Ubbink (1997) and Rusche (2002). More recently Deshpande *et al.* (2012) and Damian (2013) described and evaluated more details of the interFoam implementation. In the current release of The OpenFOAM Foundation Ltd further modifications were included into the interFoam code, which are not yet further specified in any publication. The current solver is able to capture incompressible homogeneous two-phase flow of with interfaces larger than the grid size. Mass and momentum exchanges between the phases are neglected.

- The formulation for the Euler-Euler dispersed flow solver *bubbleFoam* was developed and documented by Rusche (2002) and Marschall (2011). The current version of the solver is renamed to *twoPhaseEulerFoam* and contains further improvements. It is able to capture incompressible, isothermal two-phase flow, where the one phase is mono-dispersed within the second continuous phase. Phases can exchange mass, momentum and energy. Multiple drag model formulations allow the adaption to a large range of dispersed flows.
- An extended Euler-Euler solver was developed and documented by Wardle and Weller (2013). Their *multiphaseEulerFoam* solver couples the Euler-Euler approach of the *twoPhaseEulerFoam* solver with the VoF approach of the *interFoam* solver to allow a sharp capturing of the interface for selected phase pairs.
- Brennan (2001) developed the *settlingFoam* solver for the OpenFOAM toolbox. The incompressible solver is designed for simulating a settling process of a dispersed phase within a continuous phase. The used mixture model formulation is based on the mixture of volume formulation and uses the drift velocity between the phases. In the current release the solver is renamed to *driftFluxFoam* and extended to additionally capture heat transfer between the phases.
- Bohórquez (2008) and Damian (2013) contributed further research in the field of mixture models in OpenFOAM: Bohórquez designed an incompressible three-phase solver, which allows the modelling of free-surface flow including a settling process within the liquid phase; Damian developed an extended mixture model, which combines the VoF and the mixture model approach. The switching between the models is based on the gradient of the volume fraction. Both developments are documented in detail but the code is currently not available to the public.

The named solvers and the software framework of OpenFOAM build a suitable base for the developments of this work.

1.4 Objectives and Present Contributions

It is the aim of this work to provide a contribution to the necessary tools for analysing air-water flows in the near field of hydraulic structures. Available methods for multiphase flow simulation are to be improved, extended and validated to enable the analysis of flow regimes, where the phases share interfaces with varying length scales. In the current study special focus is put on air-water mixtures in the nearfield of navigation locks. The developments are based on the existing CFD toolbox OpenFOAM. Currently, no solver available is able to simultaneously capture bubble transport and detrainment processes in combination with free surfaces. Therefore, this study strives to improve the modelling capacities of the toolbox OpenFOAM in a way that the considered physical processes can be analysed. In particular, the available solvers are analysed in detail and their applicability is evaluated. A solver based on the mixture model approach is developed and implemented into the OpenFOAM framework. Simple test cases prove the functionality of the solver. An extensive study of the available discretization schemes is performed to find the most suitable combination for engineering applications.

With two detailed simulations of the lock filling processes, the applicability of the solver is tested. The first simulation series of an existent through-the-gate lock filling system, shows how air-water intermixing can severely change the flow characteristics of a system. Looking at the resulting forces on a ship lying in the lock chamber, the simulation results allow first conclusions about critical air entrainment rates and water inflow rates. In second set of simulations a newly proposed filling system for large lift heights is investigated, where air-water intermixing within the system is expected. For a first validation of the new numerical approach, a physical scale model of the first test case ship lock is build and equipped with advanced measurement devices. The comparison reveals the advantages and shortcomings of the model. The following specific contributions have been made in this study:

- Detailed analysis and description of the relevant air-water flow patterns occurring in the nearfield of hydraulic structures.

- Description and evaluation of the literature covering the fields of physics of two phase flows, mathematical two-phase flow models, and air entrainment with respect to the applicability to hydraulic engineering applications.
- Research related to multiscale air-water flows:
  - Analysis and testing of the available VoF model in OpenFOAM for flows with free surface and dispersed flow patterns.
  - Implementation of a mixture model with a physically based relative velocity formulation into the OpenFOAM framework.
  - Analysis of the different discretization schemes to obtain bounded, accurate results.
  - Validation against a simple test case to prove the basic functionality.
  - Validation against experimental data of a physical scale model to prove the applicability to engineering test cases.

1.5 Thesis Outline

Subsequent to the explanation of objectives of the thesis, this section aims to give a short overview about the content development of this thesis. The following content is structured into six further chapters. **Chapter 2** introduces the fundamentals for the physical characterization of fluid flows with focus on two-phase flows. The collected information is used to subdivide the physical processes of the in accordance typical flow patterns occurring in the near-field of hydraulic structures. Available empirical models for the estimation of certain physical correlations are explained, which are partly fed into the developed numerical modelling concept. The phenomenological subdivision of the flow patterns is later used to find models for the mathematical description of the occurring processes. To show the necessity of a new numerical approach for the investigation of hydraulic structures with significant air intermixing, the issues of physical scale models are elucidated with a dimensional analysis of the system and the description of resulting scale effects. In **chapter 3** mathematical model concepts for air-water flows are introduced. Similar to the

phenomenological subdivision mentioned before, the mathematical models are also clustered according to the physical patterns that they are designed to model. Here, the scale of the interface between the two phases defines the subsections. In addition to the two-phase models, turbulence models are described, which are necessary when not all turbulent scales of the flows can be resolved. As close of the chapter a rudimentary outline of the chosen modelling concept with the given demanded capabilities is presented. **Chapter 4** describes the details of the developed model. Initially all components of the mathematical model are shown. Subsequently, the numerical framework used for the implementation is presented. In particular, all features necessary for the understanding of the functionality of the developed solver are described. With the test cases of **chapter 5**, the general functionality and the accuracy of the implemented solver is tested. The simple setups are meant to show that the solver produces the expected results. The real-world applicability of the development is demonstrated with the examples of **chapter 6**. Performance and stability for large cases are shown. The examples further highlight the extensive potential for future design and operation optimization in the field of hydraulic structures. The last **chapter 7** presents a summary and conclusions. With its outlook possible future tasks are proposed and justified.

2 Physics of Air-Water Flow

The physical phenomena air entrainment, bubble transport and detrainment play a significant role when regarding the efficiency of hydraulic structures. Dependent on the function of the structure, air entrainment and the subsequent interaction of the entrained air with the flowing water can have positive or negative influence on the functionality and the performance. To understand the impact of the air-water interaction phenomena on the flow behaviour, the characteristics of the single phenomena and their collective influence have to be analysed. In the following, the physical properties of typical flow phenomena occurring in the near-field of hydraulic structures are described in detail.

2.1 Classification of Air-Water Flow

2.1.1 General Classification Criteria

Most models used in hydraulic engineering regard fluids as a continuum and neglect the molecular structure of matter. This continuum assumption is valid when the molecular mean free path of the particles is small compared to the typical lengths and the mean free time is small compared to the relevant time scales of the system under consideration. Fluids can then be specified according to their **thermodynamic properties** like e.g. density, temperature, compressibility, internal energy, specific entropy and speed of sound. The flow of fluids can further be described with **kinematic properties** like velocity and

acceleration and the variation of these properties over time and space. Friction effects are quantified via the viscosity of a fluid. The interaction and possible intermixing between two fluids is mainly governed by the surface tension and the solubility of the involved fluids.

Considering the temporal and spatial variation of the flow properties, further distinctions can be made. Regarding the spatial variation open channel flow can either be **uniform** or **non-uniform.** Uniform flow implies that the hydraulic parameters of the flow do not vary spatially whereas non-uniform flow indicates spatial variation. Flow with variations over time is labelled as **transient flow** whereas temporally constant flow parameters indicate **steady flow**. In turbulent flows, the turbulent structures constantly introduce temporal varying velocities. Therefore natural flows, like they occur in rivers, canals or hydraulic structures, never reach a real steady state. However, when the hydraulic properties of the flow do not significantly change over time, the flow can be designated as **quasi-steady** flow. Fluid flows involving more than one component or phase are termed multiphase or multi-component flows, whereby a phase refers to solid, liquid or vapour state of matter and a component specifies a chemical species. For specifying e.g. spatial distribution of the phases or components in a multiphase or multicomponent system the **volume fraction** is introduced. In a control volume (CV) the volume fraction α of a component i is the volumetric fraction V of one phase in relation to the total volume in consideration:

$$\frac{V_i}{V} = \alpha_i \qquad (2.1)$$

Summing up all volume fractions of all components over the considered control volume unity is obtained: $\sum_{\mathrm{CV}} V_i = 1$. A value of $\alpha = 1$ indicates that the considered phase completely fills the regarded volume. All values between $0 \leq \alpha \leq 1$ imply the presence of multiple phases in the control volume. However, neither the exact shape nor the exact location of the interface can be predicted by solely regarding the volume fraction. Multiphase flows can be classified according to the **physical state** of the immiscible components or

phases which exist simultaneously in the flow (Ishii, 1975). With that two-phase flow can be categorized as gas-solid, gas-liquid, liquid-solid or in the case of immiscible fluids liquid-liquid flow. Under natural conditions as they occur at hydraulic structures (atmospheric pressure and atmospheric, isothermal boundary conditions) air-water flow can consequently be classified as **two-phase gas-liquid flow**. Whereas the liquid phase water can definitely be regarded as incompressible under natural boundary conditions, this cannot automatically be adopted for the gaseous phase air. A fluid is defined as incompressible, when the density ρ does not change along a trajectory due to pressure change while temperature is constant. Mathematically, **incompressibility** can be expressed as substantial derivative of the fluid density ρ over time t:

$$\frac{D\rho}{Dt} = 0 \qquad (2.2)$$

As solid and liquid phases have a very low compressibility it is decisive if gaseous phases are involved. Compressibility must be considered, if the circumstances make a significant compression of the gaseous phases likely to occur and if the compression is relevant for the evolution of the result. In most hydraulic engineering applications the compressibility of air is negligible when modelling free-surface flow. In cases, where the two-phasic air-water flow is exposed to high pressure variations, the compressibility can get significant and thus has to be taken into account. Further, compressibility of entrained air influences the size of bubbles and consequently the bubble behaviour at different pressure levels. Thus, the relevance of compressibility effects has to be determined dependent on the application. Most fluids relevant in water engineering are **Newtonian fluids**, meaning that the viscous forces are linearly proportional to the local strain rate. Up to a certain percentage, air can be dissolved in water. According to Henry's law the **solubility** is proportional to the temperature and the pressure. Considering hydraulic engineering applications the dissolved air quantity does not significantly influence the density of the water. Hence, the dissolved air is mostly neglected. Therefore, air

and water are regarded as **immiscible fluids**, implying that a sharp interface forms between the fluids, where a sudden jump of the fluid properties is present. On the interface **surface tension force** is active, which results from the cohesive forces between the water molecules. The surface tension force always acts normal to the surface, for small accumulations of molecules this results in spherical droplets or bubbles. For the properties of the flow around structures, surface tension is insignificant. However, for air entrainment, transport and detrainment processes the surface tension force cannot be neglected. The influence of the surface tension force in relation to the inertial forces can be expressed with the dimensionless Weber number. The **Weber number** is calculated with:

$$\mathrm{We} = \frac{\rho v^2 L}{\sigma} \qquad (2.3)$$

where ρ is the fluid density, L is the characteristic length. In dispersed flows typically the bubble or droplet diameter is used as characteristic length. In free-surface flows the characteristic length refers to hydraulic system and can be equal to e.g. the water depth. In tube flows without free surface the tube diameter represents the characteristic length. v is the flow velocity and σ represents the surface tension. The importance of the surface tension forces in relation to the body forces can further be described with the **Eötvös number**:

$$\mathrm{Eo} = \frac{\Delta\rho \mathrm{g} L^2}{\sigma} \qquad (2.4)$$

where $\Delta\rho$ describes the difference between the densities of the involved phases and g is the gravitational acceleration. The larger the Eötvös number gets, the smaller is the influence of surface tension. Multiphase flows can be strongly influenced by the mass, momentum and energy transfer between the phases. Driven through discontinuities in the fluid properties at the interfaces, various flow patterns can evolve (Samstag, 1996). By regarding the distribution of the phases and the topology of the interface the flow can be described as **separated**, **dispersed** or **transitional.** In separated flows, the phases share a geometrically simple, continuous interface. Dispersed flows are characterized through the

existence of dispersed particles surrounded by a continuous fluid (Brennan, 2001). Through acceleration of the flow, friction or other factors, a transition from separated to dispersed flow regime can occur. Flows involving both interface distributions can be classified as transitional or mixed. For air-water flows the topology of the interface is strongly dependent on the flow patterns, the topological classification can therefore only be determined for every single application. Dependent on the water velocity, the flow can further be described as **laminar**, **transitional** or **turbulent**. In laminar flow, the streamlines of the flow are parallel and no intermixing between the different velocity layers inside the liquid takes place. Turbulent flows are characterized through their three dimensional intermixing between the different velocity layers through the turbulent eddies. Estimation about the evolving **flow regime** can be made with the dimensionless Reynolds number, which describes the ratio of inertial to viscous forces.

The **Reynolds number** can be calculated as follows:

$$\mathrm{Re} = \frac{vL}{\nu} \tag{2.5}$$

where v is the flow velocity, L represents the characteristic length and ν is the kinematic viscosity of the regarded fluid. For very low Reynolds numbers () the inertial forces can be neglected and viscous forces dominate the laminar flow behaviour. This so-called Stokes or creeping flow occurs e.g. in the field of micro-biology, where the length scales and velocities are very small compared to the viscosity of the fluid. In the field of hydraulic engineering inertial forces are dominating the flow behaviour, resulting in high Reynolds numbers. As soon as the Reynolds number exceeds a critical value $\mathrm{Re} \geq \mathrm{Re}_{crit}$, smallest disturbances can cause a transition from laminar to turbulent flow. The critical value for the transition cannot exactly be defined, but is commonly assumed that it occurs between $\mathrm{Re} = 1000$ and $\mathrm{Re} = 10\,000$. In hydraulic engineering applications almost all kinds of flows can be assumed to be **highly turbulent**. Therefore, modelling of the occurring phenomena due to the turbulence is essential for reproducing the physical phenomena.

2.1.2 Free-Surface Flow

When water and air share a large scale, sharp interface the flow can be labelled as **open channel** or **free-surface flow**, meaning that the flow is not completely surrounded by a rigid boundary, but has an atmospheric boundary, where the surrounding gas (air) and the liquid (water) share a common interface. At this free-deformable interface usually **no intermixing** between the phases takes place and no normal or parallel shear stresses act on the so-called free surface (Jain, 2001). Considering isothermal conditions, the flow is **driven by gravity** which acts against the inertial forces of the fluid. The ratio of the inertial to the gravitational forces can be quantified with the dimensionless **Froude number**:

$$\mathrm{Fr} = \frac{v}{\sqrt{gL}} \qquad (2.6)$$

where v is the flow velocity, g is the gravity and L is the characteristic length, which is equal to the flow depth in open channel flows. With Froude numbers smaller than unity, the flow is called **subcritical**. In subcritical flows the flow velocity is smaller than the wave celerity; gravitational forces dominate. When the flow velocity equals the wave celerity the Froude number reaches unity and the flow is called **critical flow**. Flows with Froude numbers larger than one are described as **supercritical flows** implying that surface waves only propagate downstream. The highly energetic, shallow, fast flow is then dominated by inertial forces. In the transition region between sub- and supercritical hydraulic jumps are likely to occur. Hydraulic jumps or turbulence can cause surface aeration, meaning that the originally sharp water surface is disturbed and air is entrained. Effects of surface aeration are described in 2.1.4. The evolution of the liquid's surface and consequently the depth of the flow and the discharge can change with time and space. The water's surface is subject to atmospheric pressure and surface tension. As the density difference between water and air is very large (approximate factor: 1000) the pressure at the interface is considered as equal to the atmospheric pressure. The surface tension is resulting from the cohesive forces between the liquid molecules which are stronger than the attraction forces of the liquid molecules to the gas molecules. However, in large,

stretched free-surface flows, the **surface tension** is of little relevance for the flow behaviour. In hydraulic engineering the flow characteristics are mainly dominated through the shape and the surface properties of the channel boundaries.

2.1.3 Free Falling Water Jet

When water drops over a horizontal crest, a free falling jet develops. The jet is driven by gravity and follows a parabolic trajectory (Stamm *et al.*, 2013). The energy dissipation mechanisms aeration and atomization of the jet continuously increase the **turbulence level** of the jet with growing length and finally result in a complete **mixing** of the involved fluids. Figure 2.1 schematically illustrates a falling jet and its breakup.

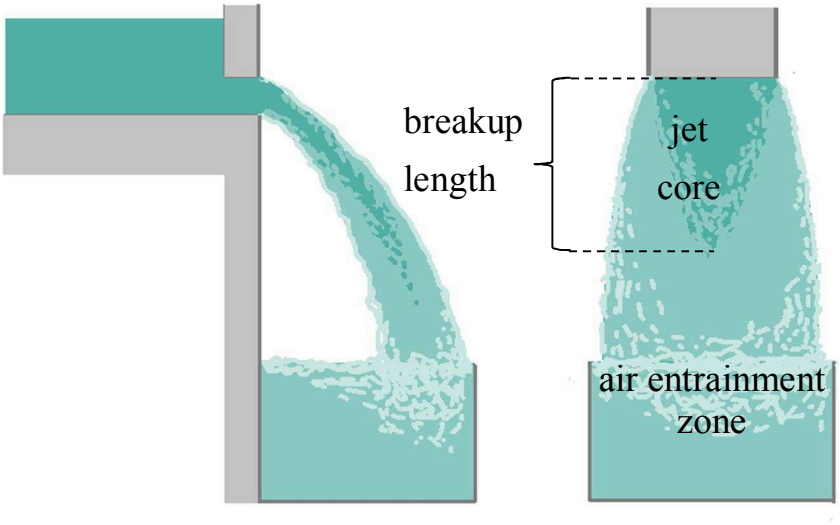

Figure 2.1: Schematic sketch of a falling water jet inspired by Castillo and Luis (2006)

Primarily, the breakup is caused by the internal turbulence of the jet, which is mainly influenced by the flow conditions upstream of the jet (Falvey, 1980). Secondarily, the interaction with the surrounding air contributes to the breakup of the jet: due to friction of the water jet with the surrounding air, the surface gets rough and surface aeration occurs, meaning that small air bubbles are entrained into the jet. The acceleration decreases and the jet gets wider. Additionally, small water drops separate from the initially continuous jet which

starts to disintegrate. The turbulence at the free surface of the jet makes a diffusion zone evolve in which the kinetic energy is partly dissipated (Kraatz, 1989). With growing falling height the disintegration of the jet increases. Concurrently, the size of the discrete water droplets and air bubbles in the jet decrease. After a certain length, the so called **breakup length** of the jet is reached; no continuous jet core exists (Baylar *et al.*, 2009). Castillo and Luis (2006) developed an approach to calculate the breakup length for nappe flow. The approach is based on empirical correlations and was originally developed to characterize nappe flow conditions at dam outlets. Assuming that the same conditions apply for the jet such as those evolving e.g. in lock filling systems, the breakup length for the jet can be calculated. An exemplary calculation of the breakup length for a lock filling system investigated in chapter 0 is shown in appendix A.1.

The results show that the breakup length dependents linearly on the opening width of the rotational gate. At the beginning of the gate opening process, the falling height is larger than the breakup length. With growing opening, the breakup length can be reached. The jet is assumed to get very rough at its surface and could become oscillating and reach the breakup state, which means that the core of the jet is completely aerated. As a consequence high air entrainment must be expected in the plunging pool of the drop shaft.

2.1.4 Air Entrainment

Air entrainment in free-surface flow is defined as the intrusion of air pockets and bubbles below the surface. The process can often be observed at drop structures like weirs, spillways or bottom outlet structures of dams. It is typically recognizable from the white coloration of the water surface. At the point where a water jet plunges into a pool of water at rest air pockets and bubbles may be entrained into the pool (Chanson and Jaw-Fang, 1997). In the near-field of the impinging point momentum transfer between the plunging jet and the pool water evolves and a momentum shear layer develops (Brattberg and Chanson, 1998). When air is entrained an air bubble diffusion layer forms, which may not coincide with the momentum shear layer (Cummings and Chanson, 1997).

Generally, air entrainment of plunging jets is governed by the following local parameters (Kobus, 1985):

- the impact velocity of the plunging jet,
- the length of the intersection line between the plunging jet and the pool surface,
- the density, viscosity and surface tension of the fluid and gravity and
- the character of the plunging pool surface (turbulent velocity fluctuations).

For the entrainment process inertial and gravity forces induced by the jet have to overcome the resisting forces at the pool surface due to viscosity and surface tension (Kobus, 1985). Air entrainment occurs when the jet impact velocity exceeds a characteristic value, which is a function of the fluid properties, jet length and jet core turbulence (Cummings and Chanson, 1999). Cummings and Chanson (1997) concluded the following relevant findings about air entrainment features of plunging jets: Dependent on the impact velocity of the jet, two major air entrainment processes can be identified. With smaller impact velocities, small individual air pockets are formed where the pool surface is not able to follow undulations caused by the impinging jet. With higher jet impact velocities the air entrainment is initiated by a thin air sheet, which enters the pool at the impact point. At the lower end of the air sheet elongated air pockets are formed and then carried downstream and broken up subsequently in the shear flow. The frequency and size of the air pockets depends on the jet turbulence and the jet velocity.

Resolving all relevant scales of a falling jet is hardly possible in most engineering applications. As a consequence, several models have to be designed that account for the effects of the unresolved scales. In the case of air entrainment, the location and the quantity of the entrained air have to be determined phenomenologically. The model results must be included in a global multiphase model used for the fluid flow calculations.

In several publications the research group of Ma *et al.* (2010, 2011a, 2011b) presented a sub-grid approach for modelling air entrainment with a two-

fluid model. Their phenomenological model is capable of predicting quantity and location of air entrainment. It is based on the assumption that turbulence occurring at rough air-water interfaces produces cavities; Air entrainment takes place when the velocity of the entrained air cavities is higher than the downward velocity of the air-water interface. For low jet impact velocities the air entrainment rate can be defined as function of the jet velocity and the surface roughness of the jet. When a certain jet velocity is exceeded, the air entrainment mechanism changes: An air sheet causes the entrainment. The volumetric air entrainment is dependent on the jet velocity and the mean thickness of the plunging air sheet. The research group of Ma et al. tested the proposed sub-grid approach in combination with a RANS-based two-fluid model. The approach is applicable to various flow types including small scale plunging jets, a hydraulic jump and the bubbly flow around ships. Various studies of the research group around Ma proved that the approach shows good agreement with experimental data. When air entrainment cannot directly be resolved, the sub-grid model could help to locate and quantify it. If the prediction is applicable to large nappe flow is unknown.

Souders and Hirt (2004) and Hirt (2003 updated in 2012) published the only available information about the air entrainment model implemented in the commercial CFD software FLOW3D®. Their entrainment model is based on the idea that air is entrained when the intensity of the turbulence is high enough to overcome the forces that stabilize the surface, namely the gravitational and the surface tension forces. To describe the surface disturbances, the definition of the characteristic size of turbulent eddies of the renormalisation group (RNG) k- ε model is used. FLOW3D® includes two variations of their air entrainment model. The first is applicable for low air entrainment rates, simply introducing an additional scalar variable to their VoF model which records the entrained air volume fraction within the liquid phase. For higher volume fractions of entrained air a mixture model formulation is used. The model accounts for bulking and buoyancy effects of the entrained air bubbles. According to Souders and Hirt (2004) the model is suitable for most applications. Within their publications they tested the model for a drop shaft, a hydraulic jump in a

conduit, a spillway and a plunging jet. They evaluate their results as “quite reasonable”. However, no direct comparison to measurement data was shown. All of the described air entrainment models were developed for the integration into a specific multiphase approach. The transferability to other models is questionable.

2.1.5 Bubbly Flow and Air Detrainment

Bubbly flow is characterized by the presence of dispersed gaseous particles within a continuous liquid fluid. By motion of the deformable dispersed particles, the two phases interact with each other. Generally, the presence of air bubbles in water can strongly influence the characteristic of the flow. Bulk properties of the fluid are changed, turbulence structure is affected, and through the buoyancy force on the entrained air vertical momentum is applied upon the flow field. In open channels flow depth is increased and intensive oxygen and nitrogen transfer takes place till saturation is reached. In closed conduits air entrainment can produce changes in the discharge or pressure distribution of the flow (Kobus, 1985). When the surrounding water body is stagnant or has only very small flow velocities, bubbles rise vertically and detrainment takes place at the free surface. In highly turbulent flows the rising motion of the bubbles is disturbed by the turbulent motion of the flow. Thus, the detrainment process is decelerated.

Drag Force on a Bubble

Due to the density difference between air and water, air bubbles in water are subject to a buoyancy force, which counteracts the weight force. For air bubbles in water the weight force is smaller than the buoyancy force, the bubble moves in opposite direction to gravity. A relative velocity between the dispersed particles and the surrounding fluid evolves. Due to the relative velocity the bubble experiences a drag force. The drag depends on the shape of the dispersed particle, the properties of the fluid and the rising speed.

Generally, the drag force for a single bubble can be expressed as:

$$F_{drag} = 0.5\rho_c \mathrm{U}_r^2 C_d A \qquad (2.7)$$

with ρ_c representing the density of the continuous liquid phase, $\mathrm{U}_r = |\mathrm{U}_1 - \mathrm{U}_2|$ being the relative velocity between the phases, C_d defininig the drag coefficient and A being the reference area, which equals the cross section of the dispersed particle.

The surface tension between the phases make the dispersed gaseous particles tend to a spherical shape. Through the gaseous character of the bubble the actual shape can change during the movement and might differ from a sphere. The shape is a function of the acting hydrodynamic, viscous and interfacial forces. For a spherical bubble C_d can be calculated from a stationary balance between the buoyancy and the drag force:

$$C_d = \frac{4}{3}\frac{d_B \mathrm{g}}{\mathrm{U}_r^2} \qquad (2.8)$$

where d_B represents the diameter of the bubble. Since bubbles deform with growing diameter, equation (2.8) is not valid for all bubbles. Therefore, the drag coefficient is determined on basis of empirical correlations. One of the most commonly applied approaches was presented by Schiller and Naumann (1935). Here, the drag coefficient dependent on the particle Reynolds number is defined with the following correlations:

$$C_d = \frac{24}{\mathrm{Re}_p} \quad \text{for } \mathrm{Re}_p < 1 \qquad \text{Stokes' law region}$$

$$C_d = \frac{24}{\mathrm{Re}_p}(1 + 0.15\,\mathrm{Re}_p^{0.687}) \text{ for } 1 < \mathrm{Re}_p < 1000 \qquad \text{Transition region}$$

$$C_d = 0{,}44 \quad \text{for } \mathrm{Re}_p > 1000 \qquad \text{Newton's law region} \qquad (2.9)$$

The drag coefficient depends on the **Reynolds number of the dispersed particle** Re_p:

$$\mathrm{Re}_p = \frac{d_B \rho_c \mathrm{U}_r}{\mu_c} \qquad (2.10)$$

where μ_c represents the dynamic viscosity of the continuous liquid phase. Drag increases when the shape is non-spherical, only when circulation inside the bubble occurs drag might be reduced. As soon as drag, buoyancy and weight forces are in equilibrium, a rising bubble reaches a terminal velocity. Generally, the terminal velocity of a particle can be determined by setting the frictional drag on the particle (as described in equation (2.8)) equal to the slip force. This results in the following general equation for **the terminal velocity**:

$$\mathrm{U}_t = \sqrt{\frac{4}{3}\frac{d_B \mathrm{g}(\rho_l - \rho_g)}{C_d \cdot \rho_l}} \qquad (2.11)$$

In addition to the dependency on the fluid and gas properties in the system the terminal velocity of a bubble is dependent on the diameter and the shape of the bubble. Clift *et al.* (1987) summarized the correlation between the bubble diameter and the terminal velocity with the means of experimental data of Gaudin (1957) in the diagram reproduced in Figure 2.2. Furthermore, the results of the empirical approach of Zheng and Yapa (2000) and of the experimental results of Haberman and Morton (1953) are shown.

From the diagram it becomes visible, that three regimes can be identified for the relation between the bubble diameter and the terminal rising velocity: the spherical regime, the ellipsoidal regime and the spherical-cap regime. In the first regime, the small sized bubbles (typically $d_B \leq 0.001$ m) are of spherical shape and the viscous force dominates the bubble behaviour. Inertial and surface tension effects are negligible.

The terminal velocity for a single spherical bubble can be directly derived from the Stokes' law:

$$U_t = \frac{1}{18}\frac{d_B^2 g(\rho_l - \rho_g)}{\mu_l} \qquad (2.12)$$

where μ_l is the dynamic viscosity of the liquid phase. This is valid in regions where $Re_p < 1$. In the second regime, flow forces on the bubble cannot longer be fully compensated by the surface tension. Therefore, bubbles tend to flatten and deform to an ellipsoidal shape. Here the surface tension dominates the regime, whereas viscous forces are negligible. For bubble diameters ranging between 0.5 mm and 10 mm the terminal velocity values scatter widely.

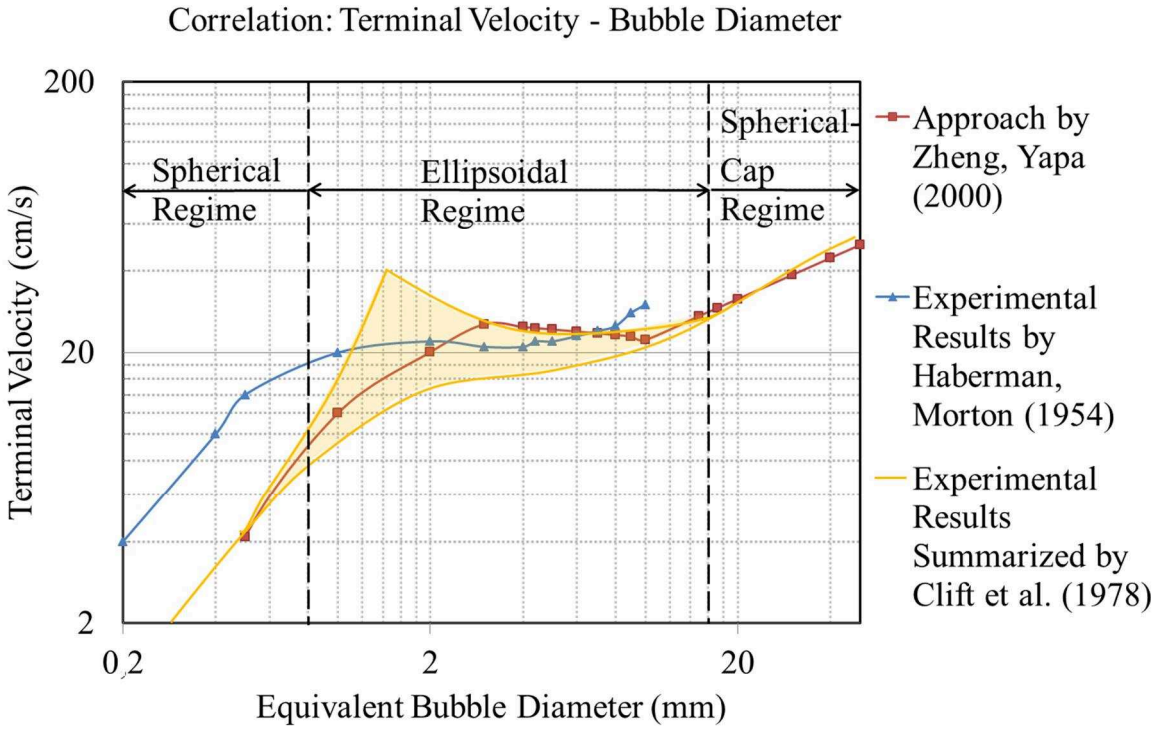

Figure 2.2: Comparison of literature values for the rising velocity for a single air bubble in water

Clift *et al.* (1987) concluded from an experimental data analysis that the variation of the values in the yellow shaded region results from the varying presence of surfactants. In particular, the upper bound of values corresponds to experiments performed without surfactants, whereas the values of lower bound

corresponded to experiments with high surfactant rates. In later studies of Tomiyama (2002) the reason for the scatter is explained with slightly different bubble release conditions.

From the comparison of the three data sources it can be concluded that an exact determination of the terminal rising velocity of a bubble is difficult, as the results can easily be influenced by surfactants, temperature variations or other slightly varying boundary conditions. Yet, the data allows determining the approximate range of the rising velocity. In hydraulic engineering applications typical bubble diameters range between 0.001 m and 0.01 m. As a result, the typical rising velocity of the ellipsoidal bubbles is in the range of 0.2 m/s to 0.3 m/s.

Unsteady Forces on a Bubble

In addition to the drag force, the dispersed particles are influenced unsteady forces: the lateral lift force, the virtual mass force, the Basset force and the turbulent dispersion force. The lateral lift force results from the shear between the particle and the non-uniform incident flow of the surrounding phase. It acts perpendicular to the drag force and causes sideward movements of rising bubbles. The virtual mass force accounts for the additional inertia of a system, which develops when the accelerating dispersed particle has to move a part of the surrounding fluid during the movement. The Basset force accounts for the lagging boundary layer development when the relative velocity of the particle changes. The turbulent dispersion force evolves from the turbulent fluctuations in the continuous phase which tend to scatter a swarm of dispersed particles (Marschall, 2011). In the current study, drag is assumed to strongly dominate the motion of the bubbles. Therefore, unsteady forces are neglected in this work.

Bubble Swarms

When multiple bubbles flow simultaneously within a continuous liquid, the conglomeration of bubbles is called a bubble swarm. Dependent on the outer geometry and interaction between the bubbles, different flow regimes can be classified. According to Kolev (2012) bubble flow patterns have to be

distinguished between pool flow and channel flow. In pool flow, walls of the outer boundary geometry do not influence the flow. In contrary, channel flow patterns are influenced by the walls. Following Serizawa and Kataoka (2010) vertical channel flow can be classified as separated bubble flow, interacting bubble flow, churn turbulent bubble flow or clustered bubble flow. In separate bubble flow the small spherical bubbles do not interact with each other and therefore behave like single bubbles. With larger bubble number density, bubble interactions occur and bubbles start to collide and coalesce to form larger bubbles. A further increase in bubble number density leads to the formation of large cap bubbles. This flow pattern is referred to as turbulent churn flow. When large bubbles occur clustered, the pattern is called clustered bubble flow (Serizawa and Kataoka, 2010). The transition between the different regimes is dependent on the void fraction and the turbulence. For equal sized, spherical particles which do not oscillate while rising, a maximum gaseous volume fraction of approximately $\alpha_g > 0.74$ is possible for separated bubble flows. In turbulent flows, where the particles tend to oscillating movements, maximum volume fractions of $\alpha_g > 0.25$ to 0.3 were observed (Kolev, 2012). With volume fractions higher than the mentioned limits a transition to more turbulent flow patterns with larger interacting bubbles occur. With experiments (Kobus, 1985) found that air bubble swarms induce a substantial velocity in the surrounding fluid. The resulting rising velocities exceed the single bubble rising velocities by a factor of two to three. A horizontal velocity component in the flow, which laterally displaces the bubbles during the rising, influences the bubble induced velocity. To account for the effect of the swarm on the terminal rising velocity Richardson and Zaki (1997) defined the following correlation:

$$U_t = U_{t,\infty}(1 - \alpha_g)^n \qquad (2.13)$$

where $U_{t,\infty}$ is the terminal rising velocity of a single bubble in infinite liquid, α_g is the air volume fraction and n is an adaptable exponent, accounting for the influence of the swarm on the velocity. Through the rising within a swarm, bubbles with nearly spherical shape hinder the rising of each other. Hence, the

drag of the single bubble increases within the swarm. For those kind of swarms regimes, the rising velocity decreases with increasing gas volume fraction. Therefore, the exponent n is larger than unity. For larger, distorted bubbles the wakes in swarms influence each other such that the terminal rising velocity is increased. In these cases, the exponent n is larger than unity (Wörner, 2003).

In addition to the adapted terminal rising velocity of bubbles in swarms, multiple researchers (e.g. Ishii and Zuber, 1979, Rahman and Brebbia, 2012) suggest the following adaption of the mixture viscosity μ_m:

$$\mu_m = \mu_c \left(1 - \frac{\alpha_p}{\alpha_{pm}}\right)^{-2.5\alpha_{pm}\mu^*} \qquad (2.14)$$

where α_p represents the volume fraction of the particles and α_{pm} is the concentration for the maximum packing of the dispersed particles. The local viscosity μ^* is defined dependent on the viscosity of the dispersed phase μ_p and the viscosity of the continuous phase μ_c:

$$\mu^* = \frac{\mu_p + 0.4\mu_c}{\mu_p + \mu_c} \qquad (2.15)$$

This formulation is based on the fact, that a moving particle applies a motion induced deformation on the surrounding fluid. Dispersed particles in proximity to the moving particle are also subject to the motion induced deformation. Due to the Laplace pressure, which describes the pressure difference between the inside and the outside of a curved surface, the dispersed particles show higher resistance to deformation than the surrounding continuous fluid. This leads to a higher local viscosity acting on the moving particle (Rahman and Brebbia, 2012).

Bubble Transport and Detrainment

The bubble transport of a flow is measured with the transport capacity, which defines the distance over which the entrained air is transported with the flow (Kobus, 1985). The general bubble transport capacity of the flow is dependent on the ratio of flow velocity to the bubble rise velocity (Kobus, 1985). In

quiescent water, the transport capacity is zero meaning that rising bubbles are not disturbed. With small flow velocities, which are approximately equal to the rising velocity of the bubbles, the bubbles are displaced while rising. Through the movement of the bubble within the continuous liquid body the flow field is influenced. For flows with velocities much larger than the bubble rising velocity, the transport capacity increases with growing flow velocity and growing turbulence intensity. Turbulent fluctuations in the flow counteract the rising of the bubbles and thereby increase the transport capacity of the flow (Kobus, 1985). When the transport capacity is exceeded, detrainment will evolve.

2.2 Scalability of Air-Water Flows

In many cases entrained air has significant impact on the behaviour and performance of hydraulic structures. To investigate the influence, models are used, which represent the relevant physical features. For both, physical and numerical models it is essential to know, which parameters influence the flow regime. A dimensional analysis can be used to define those parameters. The following section follows the explanations of Chanson (2004).

2.2.1 Dimensional Analysis

A dimensional analysis helps to capture the relationship between the physical quantities that govern the process under investigation. In particular, dimensionless parameters are determined which influence the physical process. It is assumed that all relevant physical laws can be formulated independent from the chosen scale. The parameters influencing a hydraulic system consist of:

- fluid properties of both phases,
- geometrical properties and
- dynamic flow properties.

Considering a general hydraulic engineering application, the following basic parameters govern the processes:

$$F_1(\rho, \mu, \sigma, g, E_b, L, v, \Delta p) = 0 \tag{2.16}$$

The dimensions of the eight parameters can be expressed as functions of the three basis reference units length (L), mass (M) and time (T).

Table 2.2.1: Governing parameters in hydraulic engineering applications

Parameter	Unit	Dimension	Name
ρ	kg/m³	ML^{-3}	density
μ	N s/m²	$ML^{-1}T^{-1}$	dynamic viscosity
σ	N/m	MT^{-2}	surface tension
g	m/s²	LT^{-2}	gravity
E_b	Pa	$ML^{-1}T^{-2}$	bulk modulus of elasticity
L	m	L	characteristic length
v	m/s	LT^{-1}	velocity
Δp	Pa	$ML^{-1}T^{-2}$	pressure differences

Applying the Buckingham theorem five (number of parameters – number of dimensions = number of dimensionless parameters = 8-3=5) dimensionless parameters can be derived:

$$F_2\left(\mathrm{Fr} = \frac{v}{\sqrt{gL}}, \mathrm{Re} = \frac{vL}{\nu}, \mathrm{We} = \frac{v^2 \rho L}{\sigma}, \mathrm{Eu} = \frac{\Delta p}{\rho v^2}, \mathrm{Ma} = \frac{v}{\sqrt{E_b/\rho}}\right) = 0 \tag{2.17}$$

To achieve a proper dynamic similarity all dimensionless parameters have to be equal in model and prototype. For most hydraulic engineering applications the

Mach number (Ma), which defines the ratio of inertial force to the elasticity force, has only very small influence and can be ignored. Only in the case of a large amount of air inside the water body, the compressibility of the fluid mixture can become relevant. The Euler number (Eu), which expresses the ratio of pressure to inertial forces, can be treated as dependent parameter. This is appropriate, when the pressure differences are controlled (Chanson, 2004). Thus, the dynamic similarity in most hydraulic models is subjected to:

$$\frac{\Delta p}{\rho v^2} = F_3\left(\frac{v}{\sqrt{gL}}, \frac{vL}{\nu}, \frac{v^2 \rho L}{\sigma}\right) \tag{2.18}$$

This can also be written in the following form:

$$\mathrm{Eu} = F_3(\mathrm{Fr}, \mathrm{Re}, \mathrm{We}) \tag{2.19}$$

The remaining three dimensionless parameters of the right hand side can be combined in one dimensionless number, called the Morton number (Mo):

$$\mathrm{Mo} = \frac{\mathrm{We}^3}{\mathrm{Fr}^2\,\mathrm{Re}^4} = \frac{g\nu^4\rho^3}{\sigma^3} \tag{2.20}$$

The Morton number is only dependent on physical properties of the fluid. Dependency on the length scales is eliminated. For air-water flows, the Morton number is constant: $\mathrm{Mo} = 3.89 \times 10^{-11}$ for a temperature of 15°C. To ensure dynamic similarity the mentioned dimensionless parameters have to be equal in a scaled model to those in the prototype. A completely similar model can only be achieved, if all mentioned similarities are satisfied simultaneously. In practice, this is not realizable. This can be shown by exemplarily the scaling of the velocity: to meet the requirements of the Froude-similarity, the velocity should be scaled with $\sqrt{\mathrm{L}}$; for the Reynolds-similarity a scaling with $v = 1/\mathrm{L}$ would be appropriate; the Weber-similarity would be fulfilled with $v = 1/\sqrt{\mathrm{L}}$. For most models in hydraulic engineering the same fluids are usually used for the scale model and the prototype and the gravity cannot be adapted. Thus, only one force ratio can be equal between model and prototype.

2.2.2 Scale Effects

In hydraulic engineering most models including a free surface are scaled according to the Froude similarity, regarding the relation between the inertial and the gravitational forces as most relevant. On the contrary, surface tension forces dominate processes like the entrainment of air, bubble coalescence and breakup. Turbulent processes are mainly driven by viscous forces. With Froude similarity, the internal turbulence, represented by the Reynolds number, is underestimated and the surface tension, represented by the Weber number, is overestimated (Heller, 2011). Therefore, small scale Froude models characteristically underestimate air entrainment and transport. In particular, the primary disintegration of the coherent jet surface is similar in model and prototype but the further breakup of the water clusters cannot be properly represented by a scale model. This is due to the fact that the drops in the scale model are too large compared to the occurring drops at the prototype. In the plunging jet region the size of the entrained bubbles in the scale models is overestimated. The larger bubbles reduce are subject to higher buoyancy forces and therefore air detrainment is overestimated.

Using the same fluids in the scale model as in the prototype and applying Froude similarity the given relation in equation (2.1) can be rearranged as:

$$\text{Mo Fr}^{2} = \frac{\text{We}^{3}}{\text{Re}^{4}} \qquad (2.21)$$

meaning that the relation between the Weber number and the Reynolds number should be identical in prototype and scale model to limit scale effects. To achieve a reasonable approximation of the air entrainment the model scale should be limited to a maximum of 10:1 and minimum values of the Weber and the Reynolds number should be respected (Pfister and Chanson, 2014). The necessary minimum depends on the application; for the modelling of air entrainment at hydraulic jumps, aerated stepped spillways and chute aerators the following limitations: $\text{We}^{0.5} > 140$ or $\text{Re} > 2$ to 3×10^{5} were published (as summarized in Pfister and Chanson 2012). For parameters like bubble size and turbulent scales scale effects can hardly be avoided even in relatively large size

(1:3 to 1:2) models (Pfister and Chanson, 2014). Only full-scale tests can provide credible results for these parameters.

3 Mathematical Models for Air-Water Flow

The following chapter aims to give an overview of the available mathematical models for two-phase flows, which could be considered for modelling air-water flows in the near-field of hydraulic structures such as flows inside lock filling systems or at weirs. The general functionality of the individual approaches as well as their applicability to the specific problems is illustrated.

3.1 Modelling of Fluid Flow

For the computational modelling of fluid flow suitable mathematical concepts have to be found, which are able to describe all relevant flow features. The necessary partial differential equations can be derived from defining a balance of the forces acting on the fluid within a pre-defined control volume. Thereby, conservation laws for mass, momentum and energy are applied. Although the gaseous or liquid phases representing the fluid actually consist of a finite number of individual molecules, a continuous fluid is assumed. Since the integration over all individual molecules is not feasible for macroscopic considerations as those used in hydraulic engineering, the **approach of continuum mechanics** is applied. Therewith the fluid is considered as a continuum, where the properties are averaged over a large number of molecules. Within this mathematical description, a fluid particle is defined as an

infinitesimal small region of fluid, which is still large in comparison to the mean spacing between the fluid molecules.

3.1.1 Eulerian and Lagrangian Specification of the Flow Field

The conservation equations for two-phase flows can either be written with Eulerian or with Lagrangian notation. The approaches use different reference frames for the specification of the flow field. The suitability of the notation depends on the desired information. Eulerian approaches generally describe the flow equations referring to a fixed spatial coordinate system. Hence, the flow variables are functions depending on the position x and time t. With an Eulerian frame of reference the velocity of the flow can therefore be described as $\mathbf{U}(x, t)$. By regarding the "Eulerian velocities" for a specific point in time, streamlines can be received by drawing a line that is tangential to all velocity vectors of the flow field. Streamlines can never cross each other, since the flow can only have one specific velocity at a time. In the Lagrangian specification the individual fluid particles are followed through space. Every fluid particle carries its own fluid properties like e.g. density, velocity, pressure etc. which are functions of time. The "Lagrangian velocity" describes the velocity of a single fluid particle P dependent on time t: $\mathbf{U}_P(t)$. By tracking the velocity over time fluid trajectories or pathlines are obtained. Pathlines may cross each other, since different fluid particles can occupy the same space at different times.

When describing multiphase flow, the flow field of continuous phases is usually described in Eulerian notation. Dependent on the occurring flow pattern and the desired information, the second phase can either be described with an Eulerian or a Lagrangian reference framework. When the second phase is dispersed and the motion of the single dispersed particle is of interest, the Lagrangian approach is advantageous. However, tracking every single particle is very expensive regarding computational costs. Therefore, the application of Lagrangian methods is restricted to small dispersed volume fractions. An Eulerian description for the dispersed phase is usually applied when the movement of the single dispersed particle is less relevant and the interest is focused on the effects of the phase interactions.

3.1.2 Local Instantaneous Fluid Flow Equations

Although there is a huge range of different flow regimes encountered in two-phase flows, the same basic set of conservation laws for mass and momentum applies for all of them. Dependent on the available scales, turbulence, phase intermixing and further necessary information, the basic set of equations can be extended with further models. This section describes the basic set of local instantaneous conservation equations for fluid flow which form the basis for all later described models.

The mass conservation equation also referred to as continuity equation states that mass can neither be created nor destroyed within a fixed volume, when sinks or sources are absent. The momentum conservation equation is based on the second law of Newton, stating that the change of momentum over time equals the external forces acting on a body. Applying this to a continuous fluid, the momentum conservation equation is received. The conservation laws for any Newtonian fluid can be described in Eulerian specification as:

Mass conservation equation

$$\frac{\partial \rho}{\partial t} + \nabla \bullet (\rho \mathbf{U}) = 0 \qquad (3.1)$$

Momentum conservation equation

$$\frac{\partial \rho \mathbf{U}}{\partial t} + \nabla \bullet (\rho \mathbf{U}\mathbf{U}) = -\nabla \mathrm{p} + \nabla \bullet \boldsymbol{\tau} + F_{ext} \qquad (3.2)$$

The depicted equations are written in differential form describing how velocity $\mathbf{U}$, pressure p, density ρ, viscous stress tensor $\boldsymbol{\tau}$ and further external forces F_{ext} are related within a moving fluid. The first term in the momentum equation (3.2) describes the temporal variation. The second term accounts for the convective transport. On the right hand side of the momentum equation, the influence of pressure, viscous forces and further external forces are taken into account.

The viscous stress tensor is given by:

$$\boldsymbol{\tau} = \mu\left[\nabla \mathbf{U} + (\nabla \mathbf{U}^{\mathrm{T}})\right] - \frac{2}{3}\mu \mathbf{I}(\nabla \bullet \mathbf{U}) \qquad (3.3)$$

where μ is the dynamic viscosity and **I** refers to the identity tensor. The second term is mostly very small and can therefore be neglected. Assuming incompressibility of the flow, both equations can further be simplified by deploying constant density. Thereby the incompressible set of equations results in:

Incompressible mass conservation equation

$$\nabla \bullet (\mathbf{U}) = 0 \quad \text{with} \quad \frac{D\rho}{Dt} = 0 \qquad (3.4)$$

Incompressible momentum conservation equation

$$\frac{\partial \mathbf{U}}{\partial t} + \nabla \bullet (\mathbf{U}\mathbf{U}) = -\frac{1}{\rho}\nabla \mathrm{p} + \nabla \bullet \left(\nu\left[\nabla \mathbf{U} + (\nabla \mathbf{U}^{\mathrm{T}})\right]\right) + \frac{F_{ext}}{\rho} \qquad (3.5)$$

With the assumption of constant density the velocity field is divergence free. The resulting set of equations is also referred to as incompressible Navier-Stokes equations. It is a coupled system of second order, non-linear partial differential equations. Analytically, the equation system is hardly solvable for practical applications. Therefore, the solution is usually approximated with the means of numerical methods. Suitable methods for hydraulic engineering applications are described in chapter 4.2.

The described Navier-Stokes equations are generally valid for a large variety of fluid flow types, including highly turbulent two-phase flow. Dependent on the characteristic of the flow, the application size and complexity, the standard set of equations has to be adapted and extended. For that turbulence models and multiphase model approaches are available. A selection of relevant modelling approaches for hydraulic engineering applications is exemplified below.

3.1.3 Applicability of the Local Instantaneous Fluid Flow Equations for Two-Phase Flow

Two-phase flow describes the simultaneous flow of two immiscible phases, separated by an explicit interface. At the interface there is a discontinuous jump of fluid properties. Mass, momentum and energy transfer can be exchanged between the phases via the interface. The mathematical description of two-phase flows is very complex, since they occur with various flow regimes. Regimes mainly differ by the topology of their interfaces. Main difficulty of two-phase models is the suitable capturing of the interfaces and the corresponding transfer mechanisms between the phases.

Theoretically, a two-fluid system consists of a finite number of local single phase regions bounded by moving interfaces. For the regions single phase balance equations can be formulated for local instantaneous variables. Considering a spatially fixed volume of arbitrary shape, which contains both fluids, the local instantaneous bulk conservation equations for two-phase flows can be derived. For the closure of these equations local instantaneous jump conditions have to be formulated. A detailed description of the derivation can be found e.g. in Marschall (2011). The resulting generic equations for two phase flows can be applied directly. However, a direct numerical simulation (DNS) on the microscopic level is computationally expensive. Therefore, the application of the instantaneous bulk conservation equations for two-phase flow is not feasible for most engineering investigations. Commonly, details of the local instantaneous formulation are eliminated by using a macroscopic description for two-phase systems (Ishii and Mishima, 1984). For this purpose time-, volume- or ensemble-averaging techniques may be used.

If one component is dominating the nature of the flow and all further components can be neglected, multiphase flows can sometimes be simplified as single phase flows and the conservation equations as shown before can be directly applied. In all other cases, where the multiphasic character significantly influences the fluid dynamics, special modelling approaches for multiphase flows have to be applied. Due to the high complexity of multiphase phenomena no general applicable model exists. It is the task of the engineer to analyse the

relevant physical phenomena and find a suitable model which can capture those. Regarding the models from an engineering perspective, the available approaches are divided according to their main application fields. At first, methods originally designed for free-surface flows with large stretched interfaces are described. Then, approaches developed for dispersed flows are introduced in the following section.

3.2 Free-Surface Flow Models

The following section describes two-phase flow models, which are designed for modelling free-surface flows. Their use is not explicitly restricted to free-surface flow, but it is advantageous when the interface is much larger than the grid size. This also allows e.g. the modelling of bubbles rising in a plume, when the bubbles are resolved with many cells, meaning that the cells intersect only with a small part of the interface of the bubble. With free surface flow models the location of the interface between the two fluids is assumed to be known initially. The evolution of the interface for later points in time is part of the solution. Two boundary conditions can be defined for the free surface: the kinematic boundary condition and the dynamic boundary conditions. The former states that the interface is a sharp boundary between the phases. No flow through the interface is allowed. The latter implies that the forces acting on the interface should be balanced, meaning that momentum is conserved at the free surface (Ferziger and Peric, 1997).

For free-surface models, mass and momentum transfer between the phases at the interface is neglected. The two-phase flow is considered as homogeneous mixture, consisting of two immiscible, incompressible fluids with constant viscosities (Rusche, 2002). The dynamics of the fluid mixture is described by the incompressible Navier-Stokes equations, using spatially averaged densities and viscosities. For determining the distribution of the phases an additional advection equation is introduced which allows the determination of the interface location.

One of the main difficulties is the proper representation of the sharp discontinuous jump of the fluid properties at the interface, when modelling free

surface flows with a large stretched interface between two fluids. For tackling this difficult task two main method classes exist: the interface tracking method and the interface capturing method. The first method directly tracks the interface, the second uses a function which implicitly captures the interface. Generally, the interface tracking method is regarded as being more accurate but not applicable to complex flows with large topological changes at the interface or to complex geometries. With the **interface capturing** methods, the phases are treated as mixture and the actually sharp **interface is not explicitly resolved**. Instead, a colour function or marker particles are introduced, which determine the presence of one phase in the computational cells. With this the interface can be implicitly located. As numerical diffusion occurs at the discontinuity between the phases, the interface is smeared in orthogonal direction. However, due to their simple implementation and their suitability to a wide range of applications, interface capturing methods are most commonly used for free surface flows. The most common methods for free surface modelling are described in the following section.

3.2.1 The Level Set Method

With the level set method introduced by Osher and Sethian (1988) the interface is implicitly represented by the zeroth level set of a smooth and at least Lipschitz continuous scalar function $\varphi(x,t)$, which is defined throughout the whole domain. During the simulation this level set function is advected with the flow field. The advection of the function values of φ, called levels, can be formulated as follows:

$$\frac{\partial \varphi}{\partial t} + \mathbf{U} \bullet \nabla \varphi = 0 \qquad (3.6)$$

with the initial condition

$$\varphi(x = \Gamma, t = 0) = 0 \qquad (3.7)$$

U represents the local velocity field transporting the interface $\Gamma(t)$. The interface encloses a region Ω occupied by one phase. Inside the region Ω the level set function is positive, outside the region, it gets negative values:

$$\varphi(x,t) > 0 \quad \text{for } x \in \Omega$$

$$\varphi(x,t) < 0 \quad \text{for } x \notin \Omega \qquad (3.8)$$

$$\varphi(x,t) = 0 \quad \text{for } x \in \partial\Omega = \Gamma(t)$$

The change of the sign in the level set function implies an instantaneous jump of the fluid properties at the interface. Since this abrupt jump often leads to problems in viscous flow simulations, an interface layer of finite thickness is introduced where a rapid but smooth transition of the properties is artificially enforced (Ferziger and Peric, 1997). The magnitude of the level set function represents the shortest distance of the considered point to the interface. Since the level set equation does not represent any physical conservation law, mass conservation cannot be guaranteed (Salih and Moulic, 2009). For counteracting this major drawback of the level set method, various researchers developed improvements and extensions to the original methodology. With the latest improvements and extensions of the original methodology level set methods are robust, accurate and efficient for modelling complex free surface flows where severe topological changes are to be captured (see e.g. Croce *et al.*, 2004). A successful application of the level set method to three-dimensional hydraulic engineering problems was shown by Strybny *et al.* (2006).

3.2.2 The Volume of Fluid Method

Another important approach for modelling free surface flows was published in 1981 by Hirt and Nichols. Their volume of fluid (VoF) method introduces an additional equation which transports the phase volume fraction, making a statement about the spatial distribution of the phases. Mathematically the VoF method can be described with the following equations:

Transport equation for the volume fraction

$$\frac{\partial \alpha}{\partial t} + \nabla \bullet (\alpha \mathbf{U}) = 0 \qquad (3.9)$$

with the volume fraction function the local density and viscosity can be determined:

$$\rho = \alpha \rho_1 + \rho_2 (1 - \alpha)$$
$$\mu = \alpha \mu_1 + \mu_2 (1 - \alpha) \qquad (3.10)$$

Index 1 refers to the first phase, which is usually the phase with larger density; index 2 refers to the second phase. The first equation describes the advective transport of the volume fraction α of the first phase. α is physically bounded between 0 and 1. When $\alpha = 1$, only the first phase is present in the considered control volume, with $\alpha = 0$, the control volume is completely filled with the second phase. Volume fraction values between 0 and 1 imply that the interface is present. However, the actually sharp discontinuity between the phases is not explicitly tracked but only captured implicitly through the volume fraction function.

Mass conservation equation for the mixture

$$\frac{\partial \rho}{\partial t} + \nabla \bullet (\rho \mathbf{U}) = 0 \qquad (3.11)$$

Momentum conservation equation for the mixture

$$\frac{\partial \rho \mathbf{U}}{\partial t} + \nabla \bullet (\rho \mathbf{U}\mathbf{U}) = -\nabla \mathrm{p} + \nabla \bullet \mu \left(\nabla \mathbf{U} + \nabla \mathbf{U}^{\mathrm{T}} \right) + \rho \mathbf{g} + F_{st} \qquad (3.12)$$

The second equation (3.11) defines the mass conservation. The third equation (3.12) accounts for the momentum conservation for the locally density-averaged phase mixture. Since the phases share a common velocity and pressure field, no mass or momentum transfer between the phases can be considered. The VoF method is mass conservative and can be applied to complex simulations with severe topological changes. For taking into account surface tension between the

two phases, the additional source term F_{st} is added on the right hand side of the momentum equation. In reality surface tension only acts as a normal and tangential force directly on the interface of the fluid. With the continuous surface tension model of Brackbill *et al.* (1992), the interface is assumed to have a finite thickness and the surface tension force is applied as continuous force across the interfacial region. With the VoF method, the interfacial region is located where the volume fraction has values between $0 < \alpha < 1$. In this region the surface tension force can be defined as:

$$F_{st} = \int_V \sigma \kappa \nabla \alpha \, dV \tag{3.13}$$

The surface tension σ is a thermodynamic property of the fluid and can be handled as a constant, when isothermal conditions are assumed. The curvature of the interface κ can be calculated as divergence of the interface normal unit vector. As the vector $\nabla\alpha$ points in the direction of the interface normal, the curvature can be computed as:

$$\kappa = -\nabla \bullet \left(\frac{\nabla \alpha}{|\nabla \alpha|} \right) \tag{3.14}$$

The surface tension force disappears in regions completely filled with one phase since the gradient of α is zero. A huge drawback of the continuous surface force (CSF) model is the occasional occurrence of unphysical parasitic currents which can severely disturb the real flow field. Those non-physical velocities can either result from the inaccurate approximation of the interface curvature or the inconsistent discretization of the curvature and/or the pressure term (Meland *et al.*, 2007). Various remedies are described exemplarily in Jamet *et al.* (2002).

A huge challenge when using the VoF method is the handling of the **numerical diffusion**, which occurs when the advection equation for the volume fraction is solved. At the interface, where the function of the volume fraction has a step profile, numerical diffusion causes a smearing of the originally sharp interface.

In order to counteract this problem various approaches were developed, which can mainly be categorized into three groups:

- geometrical reconstruction methods,
- compression methods and
- higher order differencing schemes.

Geometrical reconstruction methods approximate the only implicitly known interface between the two phases with geometrical methods. Youngs (1982) introduced the Piecewise Linear Interface Calculation (PLIC) method where the interface in a three-dimensional simulation is represented by a plane which is perpendicular to the normal vector. More recent developments are e.g. the methods published by (López *et al.*, 2004) based on a spline reconstruction method or the least square procedure by (Pilliod and Puckett, 2004). The usage of geometrical reconstruction methods increases the accuracy of the flux calculation across the interface. Since the interface is reconstructed with planes, smearing of the interface is completely banned. Due to the reconstruction algorithms the geometrical reconstruction methods are mostly limited to structured grids with simple cell shapes. Additionally, the necessary number of numerical operations for the interface reconstruction requires substantial computational effort.

Independent of the grid structure the smearing of the interface can be counteracted by introducing an **artificial compression** term into the volume fraction equation (as described in Rusche 2002). The added term creates a velocity normal to the interface and thereby compresses it. Mathematically the transport equation for the volume fraction with artificial compression term can be described as follows:

$$\frac{\partial \alpha}{\partial t} + \nabla \bullet (\alpha \mathbf{U}) + \nabla \bullet [\mathbf{U}_c \alpha (1 - \alpha)] = 0 \qquad (3.15)$$

The third term introduces an artificial velocity $\mathbf{U}_c$ acting normal to the surface. Through the multiplication with $\alpha(1-\alpha)$ it is only influencing the interfacial area. With the artificial compression method the smearing of the interface is reduced but not completely avoided. The sharpness of the interface depends on

the definition of the artificial velocity term and the discretization schemes used. Although the resulting interface is never as accurate as the interface reconstructed with a geometrical reconstruction scheme, the artificial compression method is often preferable for engineering applications. This is due to the fact, that the implementation is much simpler and the calculation is much faster in most cases (Gopala and van Wachem, 2008)

Alternatively or additionally to the artificial compression **higher order differencing schemes** like the Compressive Interface Capturing Scheme for Arbitrary Meshes (CICSAM, as described by Ubbink and Issa 1999) or the High Resolution Interface Capturing (HRIC) scheme (as described by Muzaferija *et al.* 1998) can be used for discretizing the VoF equation. The schemes use a blended discretization. By the blending between a stable but diffusive scheme and a more accurate scheme which tends to instability, the numerical diffusion is minimized. A more detailed description of blended schemes is presented in section 4.2.2.

3.2.3 Applicability and Limitations of the Free Surface Flow Models

The application of interface capturing methods is limited to cases where the interface is much larger than the control volume size. Structures being smaller than the containing control volume cannot be modelled. Considering the lock filling system, the interface capturing methods like the VoF method are most suitable for modelling the free surface in the lock chamber. However, neither the air entrainment nor the bubble transport in the drop shaft and the pressure chamber can be modelled in a realistic way, if the single bubble is not resolved via the computational grid. A suitable resolution, which captures the complete spectrum of scales including bubbles in the range of some millimetres in diameter resolved by at least 3^3 cells in a complete lock chamber with a volume of several thousand cubic metres, is not feasible with reasonable temporal and computational expenses. For the air entrainment, bubble transport and air detrainment processes alternative methods have to be found.

3.3 Dispersed Flow Models

Dispersed flow models focus on the representation of the interaction between the dispersed and the continuous phase, whereas the detailed representation of the interface is neglected. In contrast to free surface models, where the phases are assumed to share one velocity field, dispersed flow models account for different velocities between the phases. Additionally, the interfacial mass and momentum transfer can be considered. The main difficulty in the dispersed flow models consists in the definition of closure terms, which account for the interfacial transfer between the phases.

3.3.1 Two-Fluid Method

The two-fluid method assumes the flow system to consist of a continuous and a dispersed phase, which interact and interpenetrate mutually. Mathematically both phases are treated as continua, where the description of both phases refers to the same spatially fixed coordinate system. Due to this Eulerian reference frame for both phases, the method is also referred to as Euler-Euler method. It is generally applicable to all kind of flow regimes, since the topology of the flow is not predefined (Rusche, 2002). However, its application is most suitable where the interface between the dispersed and the continuous phase is much smaller than the chosen grid size (Yan and Che, 2010). The interface between the phases is not explicitly resolved but the interfacial processes are taken into account. For every phase one set of averaged conservation equations is solved. Through the averaging process the phase fraction variable α_k is introduced into the equation system. The phase fraction can be interpreted as the probability, that a certain phase is present at a certain location in time and space (Hill, 1998). For the two-fluid model the following local time-averaged equations have to be solved for the first phase $k = 1$ and the second phase $k = 2$:

Mass conservation equation for phase k

$$\frac{\partial}{\partial t}(\alpha_k \rho_k) + \nabla \bullet (\alpha_k \rho_k \mathbf{U}_k) = \Gamma_k \qquad (3.16)$$

Momentum conservation equation for phase k

$$\frac{\partial}{\partial t}(\alpha_k \rho_k \mathbf{U}_k) + \boldsymbol{\nabla} \bullet (\alpha_k \rho_k \mathbf{U}_k \mathbf{U}_k) = -\alpha_k \boldsymbol{\nabla} \mathrm{p} + \boldsymbol{\nabla} \bullet \left[\alpha_k (\boldsymbol{\tau}_k + \boldsymbol{\tau}_{Tk})\right] + \alpha_k \rho_k \mathbf{g} + M_k \tag{3.17}$$

where ρ_k is the average material density. Γ_k accounts for the mass generation of the phase k at the interface, e.g. for boiling or condensation. $\mathbf{U}_\mathrm{k}$ is the phase velocity field. $\mathrm{p_k}$ is the phase pressure. $\boldsymbol{\tau}_k$ represents the average viscous stress tensor and $\boldsymbol{\tau}_{Tk}$ is the averaged turbulent stress tensor. The source term M_k results from the averaging process and accounts the momentum exchange between the phases. For the interfacial transfer terms Γ_k and M_k balance laws at the interface can be formulated. Using an average of the local jump conditions the following interfacial transfer conditions are obtained:

$$\sum_{k=1}^{n=2} \Gamma_k = 0 \tag{3.18}$$

and

$$\sum_{k=1}^{n=2} M_k = 0 \tag{3.19}$$

Due to averaging, information about the interaction between the two phases is lost. This must be compensated by defining constitutive equations for Γ_k and M_k based on experiments. Referring to the various physical aspects contributing to interfacial momentum transfer, the momentum transfer term M_k can be decomposed into several components (Porombka and Höhne, 2015):

$$M_k = M_{k,drag} + M_{k,lift} + M_{k,vm} + M_{k,hist} + \cdots \tag{3.20}$$

$M_{k,drag}$ describes the momentum transfer resulting from the drag force per unit volume, $M_{k,lift}$ accounts for the lift force acting on a dispersed particle, $M_{k,vm}$ represents the virtual mass which is necessary to accelerate the surrounding fluid

and $M_{k,hist}$ is the history force related to the particle boundary layer development. To find appropriate models for the inter-phase momentum transfer terms is the most challenging part of the two-fluid model, because no generally applicable formulations exist.

3.3.2 Mixture Model

The mixture model is a multiphase model, which treats the phases as a continuous mixture instead of considering each phase separately. However, it still accounts for the interaction between the phases. Hence, it can be regarded as simplification of the two-fluid model. Similarly, it is applicable to two-phase flows with intermixing phases, where the influence of the dispersed phase on the fluid dynamic behaviour cannot completely be ignored (Manninen *et al.*, 1996). Other than the two-fluid model, the mixture model assumes that a local equilibrium between the phase velocities is reached within short length scales, meaning e.g. that bubbles quickly reach their terminal rising velocity. With this assumption the inter-phase momentum transfer terms are eliminated, producing a more robust system which requires less computational resources and less closure assumptions than the two-fluid model (Brennan, 2001). In many practical applications the mixture model provides a sufficiently accurate solution for modelling two-phase flows (Manninen *et al.*, 1996). It can almost be regarded as equally accurate as the two-fluid model, when considering the amount of uncertainties in the closure resulting from empirical correlations. With the mixture model, the set of equations can be significantly reduced to one mass and one momentum conservation equation for the mixture of both phases. One additional equation per dispersed phase accounts for the dispersed phase continuity. For the closure, the dynamic interaction between the phases has to be replaced by constitutive laws. The fluid is assumed to consist of a two-phase liquid-gaseous mixture, where the gaseous phase is dispersed within the liquid phase. “phase 1” is the continuous liquid phase with higher density, “phase 2” represents the dispersed gaseous phase. In the case of bubbly flow, the main source of slip between the phases results from the rising of the dispersed phase. Therefore, some approaches use experimentally determined rising velocities for

the closure. In the following two variants of the mixture model are shown, which use different reference systems for the description of the mixture. The derivations follow Manninen *et al.* (1996), Brennan (2001) and Damian (2013).

Diffusion Model

In the diffusion model the equations for the mixture are formulated with a density-averaged velocity field referring to the centre of mass of the mixture. Starting from the continuity equation for each phase *k*,

$$\frac{\partial}{\partial t}(\alpha_k \rho_k) + \nabla \bullet (\alpha_k \rho_k \mathbf{U}_k) = \Gamma_k \tag{3.21}$$

The continuity equation for the mixture can be derived by summing over *n* phases:

$$\frac{\partial}{\partial t}\sum_{k=1}^{n}(\alpha_k \rho_k) + \nabla \bullet \sum_{k=1}^{n}(\alpha_k \rho_k \mathbf{U}_k) = \sum_{k=1}^{n}\Gamma_k \tag{3.22}$$

As the total mass within the system must be conserved the rate of mass generation Γ_k summed over all phases equals zero. Thus, the right hand side vanishes. The mass conservation equation for the mixture results in:

$$\frac{\partial \rho_m}{\partial t} + \nabla \bullet (\rho_m \mathbf{U}_m) = 0 \tag{3.23}$$

Here, averaged variables for describing the mixture are used. $\boldsymbol{U}_m$ represents the density-averaged velocity of the mixture. It is defined as:

$$\mathbf{U}_m = \frac{1}{\rho_m}\sum_{k=1}^{n}\alpha_k \rho_k \mathbf{U}_k \tag{3.24}$$

ρ_m describes the mixture density, which is defined as:

$$\rho_m = \sum_{k=1}^{n}\alpha_k \rho_k \tag{3.25}$$

The resulting conservation equation for the continuity of the mixture [equation (3.23)] resembles the single-phase continuity equation. However, there is one relevant difference: even if the mixture is assumed to be incompressible, the velocity of the centre of mass is not divergence-free. The momentum equation for the mixture can also be derived by summing the momentum equations of all phases:

$$\begin{aligned}\frac{\partial}{\partial t}\sum_{k=1}^{n}\alpha_k\,\rho_k\mathbf{U}_k+\boldsymbol{\nabla}\bullet\sum_{k=1}^{n}\alpha_k\,\rho_k\mathbf{U}_k\mathbf{U}_k=-\sum_{k=1}^{n}\alpha_k\,\boldsymbol{\nabla}\mathrm{p}_k\\+\boldsymbol{\nabla}\bullet\sum_{k=1}^{n}\alpha_k\left[\mu_k\left(\boldsymbol{\nabla}\mathbf{U}_k+\boldsymbol{\nabla}\mathbf{U}_k^{T}\right)\right]+\sum_{k=1}^{n}\alpha_k\,\rho_k\mathbf{g}+\sum_{k=1}^{n}M_k\end{aligned}\qquad(3.26)$$

Then, the diffusion velocity $\mathbf{U}_{\mathrm{m,k}}$ is introduced:

$$\mathbf{U}_{m,k}=\mathbf{U}_k-\mathbf{U}_m\qquad(3.27)$$

The diffusion velocity describes the velocity of a phase $\mathbf{U}_k$ in reference to the velocity of the centre of mass of the mixture $\mathbf{U}_m$. Using this in addition to the definitions for the averaged variables [equations (3.24) and (3.25)] the second term of the momentum equation (3.26) can be redefined as:

$$\begin{aligned}\boldsymbol{\nabla}\bullet\sum_{k=1}^{n}\alpha_k\,\rho_k\mathbf{U}_k\mathbf{U}_k&=\boldsymbol{\nabla}\bullet\left[\alpha_1\rho_1\mathbf{U}_1\mathbf{U}_1+\alpha_2\rho_2\mathbf{U}_2\mathbf{U}_2\right]\\&=\boldsymbol{\nabla}\bullet\left[\rho_m\mathbf{U}_m\mathbf{U}_m+\sum_{k=1}^{n}\alpha_k\,\rho_k\mathbf{U}_{m,k}\mathbf{U}_{m,k}\right]\end{aligned}\qquad(3.28)$$

The resulting momentum equation for the mixture reads:

$$\begin{aligned}\frac{\partial\rho_m\mathbf{U}_m}{\partial t}+\boldsymbol{\nabla}\bullet(\rho_m\mathbf{U}_m\mathbf{U}_m)=-\boldsymbol{\nabla}\mathrm{p}_m+\boldsymbol{\nabla}\bullet\left[\mu_m\left(\boldsymbol{\nabla}\mathbf{U}_m+\boldsymbol{\nabla}\mathbf{U}_m^{T}\right)\right]\\-\boldsymbol{\nabla}\bullet\sum_{k=1}^{n}\alpha_k\,\rho_k\mathbf{U}_{m,k}\mathbf{U}_{m,k}+\rho_m\mathbf{g}+M_m\end{aligned}\qquad(3.29)$$

The included pressure gradient of the mixture is defined as:

$$\boldsymbol{\nabla}\mathrm{p}_m=\sum_{k=1}^{n}\alpha_k\,\boldsymbol{\nabla}\mathrm{p}_k\qquad(3.30)$$

For most applications, the pressure gradients of the two phases are assumed to be equal. The source term M_m accounts for the surface tension forces on the

mixture. Compared to the single fluid flow equations, the diffusion stress tensor $\sum_{k=1}^{n} \alpha_k \rho_k \mathbf{U}_{m,k} \mathbf{U}_{m,k}$ and the source term M_m resulting from surface tension are added to the momentum equation in the mixture model. The additional terms account for the phase interactions in the two-phase flow.

In addition to the mass and momentum equation for the mixture one mass conservation equation for the dispersed phase is necessary. By using the formulation for the diffusion velocity [Eqn. (3.27)], the following phase continuity equation is received:

$$\frac{\partial}{\partial t}(\alpha_2 \rho_2) + \nabla \bullet (\alpha_2 \rho_2 \mathbf{U}_m) = -\nabla \bullet \left(\alpha_k \rho_k \mathbf{U}_{m,2}\right) \qquad (3.31)$$

Since the term in the mass conservation equation for the dispersed phase appears similar to the diffusion coefficient in a single-phase two-component system, this mixture model formulation is also referred to as diffusion model (Wörner, 2003).

With seven unknowns, namely α_1, α_2, $\mathbf{U}_m$, $\mathbf{U}_{m,1}$, $\mathbf{U}_{m,2}$, p_m, M_m and three equations [(3.23), (3.29), (3.31)] the resulting set of equation is unclosed in the given form. The source term for inter-phase momentum transfer M_m has to be determined empirically. For simplicity, it is assumed to be zero for all further derivations. α_1 can be related to α_2 with the identity $\alpha_1 = 1 - \alpha_2$. With that the number of unknowns reduces to five, but the system remains under-determined. For the closure of the system the diffusion velocities $\mathbf{U}_{m,1}$ and $\mathbf{U}_{m,2}$ have to be determined with the means of a constitutive equation or an algebraic correlation.

The diffusion velocities of the phases $\mathbf{U}_{m,1}$ and $\mathbf{U}_{m,2}$ do not have a direct physical meaning. Additionally, they are difficult to determine empirically or with an algebraic relation, but they can be related to the relative velocity between the phases.

When only two phases are present the relative velocity of the gaseous phase $\mathbf{U}_r$ with respect to the liquid phase is defined as difference between the velocity of the dispersed phase $\mathbf{U}_2$ and the velocity of the continuous phase $\mathbf{U}_1$:

$$\mathbf{U}_r = \mathbf{U}_2 - \mathbf{U}_1 \tag{3.32}$$

Inserting this definition into the definition for the diffusion velocity [equation (3.27)] and using equations (3.23) and (3.24) for the description for the mixture velocity the relation between the relative velocity and the diffusion velocity of the dispersed phase can be described with:

$$\mathbf{U}_{m,2} = \left(1 - \frac{\alpha_2 \rho_2}{\rho_m}\right) \mathbf{U}_r = (1 - c_2)\mathbf{U}_r \tag{3.33}$$

The introduced mass fraction c_2 is defined as:

$$c_2 = \frac{\alpha_2 \rho_2}{\rho_m} \tag{3.34}$$

The derivation of the correlation described in equation (3.33) can be found in the appendix A.2. With this correlation the complete set of equations for the mixture can be re-written in the following form:

$$\frac{\partial \rho_m}{\partial t} + \boldsymbol{\nabla} \bullet (\rho_m \mathbf{U}_m) = 0 \tag{3.35}$$

$$\begin{aligned} \frac{\partial \rho_m \mathbf{U}_m}{\partial t} \; + \; & \boldsymbol{\nabla} \bullet (\rho_m \mathbf{U}_m \mathbf{U}_m) \\ = \; & -\boldsymbol{\nabla} \mathrm{p}_m \; + \rho_m \mathbf{g} + \boldsymbol{\nabla} \bullet \left[\mu_m \left(\boldsymbol{\nabla} \mathbf{U}_m + \mathbf{U}_m^T\right)\right] \\ & - \boldsymbol{\nabla} \bullet \left[\rho_m c_2 (1 - c_2) \mathbf{U}_r \mathbf{U}_r\right] \end{aligned} \tag{3.36}$$

$$\frac{\partial \alpha_2}{\partial t} + \boldsymbol{\nabla} \bullet (\alpha_2 \mathbf{U}_m) = -\boldsymbol{\nabla} \bullet (1 - c_2)\mathbf{U}_r \tag{3.37}$$

Assuming that the relative velocity $\mathbf{U}_\mathrm{r}$ is calculated with an algebraic approach a system of the three partial differential equations with three unknown variables

remains to be solved. The unknowns in the system are: the velocity of the mixture $\mathbf{U}_m$, the pressure p_m and the volume fraction of the dispersed phase α_2. A closer look at the system reveals, that the system is of second order, the equations are coupled and an evolution equation for the pressure is lacking. The lack of the pressure evolution equation can either be compensated by introducing an equation of state, defining a relation between the density and the pressure (see Zeidan and Slaouti 2009 and Zeidan 2011). Or, in analogy with other incompressible systems, fractional step methods can be applied for solving the equation system. Contrary to the VoF Method, the boundedness of the dispersed phase volume fraction is not a direct consequence of the mass conservation equation for the dispersed phase (3.37) but rather of the whole system (Gastaldo *et al.*, 2011). Additionally, the mixture velocity is not divergence free. For receiving a system which is divergence free and where the boundedness of the dispersed phase directly results from the dispersed phase mass continuity equation, the velocity of the centre of volume can be used. As the relative velocity between the phases cannot simply be determined, an algebraic relation has to be found.

Drift-Flux Model

Alternatively to formulating the velocity of the mixture with reference to centre of mass, it can be formulated referring to the centre of volume:

$$\mathbf{j} = \sum_{k=1}^{n} \alpha_k \mathbf{U}_k \qquad (3.38)$$

where **j** represents the velocity of the volume centre of the mixture. With this divergence free velocity, the continuity equation for the mixture can be simplified. The derivation of the drift-flux model has the same starting point as the diffusion model.

It starts with a summation of the mass conservation equation over all phases as presented in equation (3.22) which is recalled in the following equation (3.39):

$$\frac{\partial}{\partial t}\sum_{k=1}^{n}(\alpha_k \rho_k) + \nabla \bullet \sum_{k=1}^{n}(\alpha_k \rho_k \mathbf{U}_k) = \sum_{k=1}^{n} \Gamma_k \qquad (3.39)$$

When the density of the phases are assumed to be constant, equation (3.39) can be rewritten as:

$$\frac{\partial}{\partial t}\sum_{k=1}^{n}(\alpha_k) + \nabla \bullet \sum_{k=1}^{n}(\alpha_k \mathbf{U}_k) = \sum_{k=1}^{n} \frac{\Gamma_k}{\rho_k} \qquad (3.40)$$

Due to mass continuity within the system the total rate of mass generation is zero. The continuity equation for the mixture results in:

$$\nabla \bullet \sum_{k=1}^{n}(\alpha_k \mathbf{U}_k) = 0 \qquad (3.41)$$

Using the definition of the velocity of the centre of volume as presented in equation (3.38), the mass conservation equation for the mixture can be formulated as follows:

$$\nabla \bullet \mathbf{j} = 0 \qquad (3.42)$$

The divergence-free velocity field of the centre of volume **j** is also referred to as volumetric flux. It describes the volumetric flow rate $\dot{V} = \partial V/\partial t$ per cross-sectional area A resulting in a vector field with the dimensions of a velocity field (Nabizadeh, 1977). Calling the relative velocity drift velocity the resulting model is also called drift-flux model.

Following (Damian, 2013) the mixture momentum equation (3.36) can be re-written in terms of the continuous phase fraction α_1 by using the following expression for the diffusion stress tensor:

$$\rho_m c_2(1-c_2)\mathbf{U}_r\mathbf{U}_r = \alpha_1(1-\alpha_1)\frac{\rho_1\rho_2}{\rho_m}\mathbf{U}_{-r}\mathbf{U}_{-r} \tag{3.43}$$

$$\text{with } \mathbf{U}_r = -\mathbf{U}_{-r} \tag{3.44}$$

The derivation of the correlation described in equation (3.43) can be found in the appendix A.2.

Inserting this in the momentum equation for the mixture, we receive the momentum conservation equation for the mixture

$$\begin{aligned}\frac{\partial\rho_m\mathbf{U}_m}{\partial t} \; + \; \boldsymbol{\nabla}\bullet(\rho_m\mathbf{U}_m\mathbf{U}_m) = -\boldsymbol{\nabla}\mathrm{p}_m \; + \boldsymbol{\nabla}\bullet\left[\mu_m\left(\boldsymbol{\nabla}\mathbf{U}_m + \boldsymbol{\nabla}\mathbf{U}_m^T\right)\right] \\ +\rho_m\mathbf{g} + \boldsymbol{\nabla}\bullet\left[\alpha_1(1-\alpha_1)\frac{\rho_1\rho_2}{\rho_m}\mathbf{U}_{-r}\mathbf{U}_{-r}\right]\end{aligned} \tag{3.45}$$

The additional mass conservation equation is also re-written for the continuous phase. For that the following relation between the volumetric flux and the velocity of the continuous phase is used:

$$\mathbf{U}_1 = \mathbf{j} + (1-\alpha_1)\mathbf{U}_r \tag{3.46}$$

Inserting this relation into the known mass conservation equation for the continuous phase, the following equation is received.

$$\frac{\partial\alpha_1}{\partial t} + \boldsymbol{\nabla}\bullet(\alpha_1\mathbf{j}) + \boldsymbol{\nabla}\bullet\left[\alpha_1(1-\alpha_1)\mathbf{U}_r\right] = 0 \tag{3.47}$$

The set of equations consisting of the mass and the momentum conservation equation for the mixture and the mass conservation equation for the continuous phase contains five unknowns, namely the volume fraction of the continuous phase α_1, the velocity of the mixture referring to the centre of volume $\mathbf{U}_m$, the

volumetric flux **j**, the relative velocity between the phases $\mathbf{U}_r$ and the pressure p. One additional relation between two of the remaining four unknowns is necessary to get a solvable system. For that a relation between the volumetric flux and the velocity of the mixture of the centre of volume can be used:

$$\mathbf{U}_m = \mathbf{j} + \alpha_1(1-\alpha_1)\frac{\rho_1 - \rho_2}{\rho_m}\mathbf{U}_{-r} \qquad (3.48)$$

The derivation of the described correlation shown in equation (3.48) can be found in the appendix A.4. The given correlation is not directly used to replace the mixture velocity. Instead, the given relation is used in the solving algorithm.

With the divergence-free formulation of the mass conservation equation the system resembles the VoF model. Similarly, the divergence free velocity of the centre of volume, used in the continuity equation, can be used to formulate the pressure equation. To obtain a segregated pressure-velocity algorithm the given relation in equation (3.48) is used to connect the continuity equation, which uses the velocity of the centre of mass, with the momentum equation, which is formulated in terms of the velocity of the centre of volume. Details of the algorithm are described in section 4.2.5.

3.3.3 Euler-Lagrangian Approach

For multiphase flows with one continuous and one dispersed phase, an Euler-Lagrange approach can be applied. With this approach, which can also be referred to as discrete particle model, the conservation laws of the phases are solved on two different reference systems: the transport of the continuous phase is modelled on a fixed coordinate system (Eulerian specification), whereas the dispersed phase is modelled on a coordinate system, that moves with the particles (Lagrangian specification). The general equation of motion for the particle can be derived from the forces F acting on the particle (Matysiak, 2007). These are: the weight force, the drag force, the buoyancy force, the pressure gradient and the contact forces.

The equation for the particle motion description can be formulated as:

$$\rho_p \frac{d\mathbf{U}_p}{dt} = \sum F \qquad (3.49)$$

where ρ_p represents the dispersed phase density, $\mathbf{U}_p$ is the velocity of the dispersed phase particle. The Euler-Lagrange approach is very accurate for predictions of the bubble dynamics and their transport. However, since each bubble is tracked individually, the calculation effort increases significantly with growing bubble numbers.

The fluid flow equation and the particle motion equation can be coupled in multiple ways. The simplest form of coupling is the one-way coupling. With this approach, solely the hydrodynamic forces resulting from the fluid flow are considered via drag and turbulence for the calculation of the particle motion. Forces from the particles on the fluid are neglected. This is reasonable, when the particle have insignificant influence on the flow e.g. due to small particle size or small volume fraction. With two-way coupling, the exchange of mass, momentum and energy can be taken into account: the influence of the particles on the fluid flow is included via source terms in the fluid flow equations. If the interaction between the particles has to be included, four-way coupling is used. For this purpose additional collision models which model the contact forces resulting from the particle-particle and the particle-wall collisions are used.

3.3.4 Applicability and Limitations of the Dispersed Flow Models

Applicability and Limitations of the Two-Fluid Model

Theoretically, the two-fluid model is applicable to model all types of flow regimes. However in practice, the reliability of the model is dependent on the formulation of the model closures. In particular suitable definitions for the interfacial momentum transfer as well as the turbulence closure have to be found for each flow regime. For a large variety of bubbly flows, appropriate closure formulations already exist. Yet, a possibility to model the transition from a continuous to a dispersed phase state is not available, which is necessary when

air entrainment or detrainment is to be modelled. Several coupled models (as described in section 3.4) allow the combination of the two-fluid approach with free surface models. The evaluation of their applicability is described below.

Applicability and Limitations of the Mixture Model

The mixture model is applicable for flows consisting of interpenetrating, strongly coupled, incompressible phases. It accounts for different velocities of the phases using the concept of slip velocities, which are calculated by an algebraic relation. The mixture can consist of one continuous and multiple dispersed phases. Based on the assumption of short particle relaxation times, the model derivation is based on a local equilibrium between the phases. This means that the dispersed particles are always assumed to travel with their terminal velocity. Acceleration or deceleration of the phases is neglected. Furthermore, interactions between dispersed particles are not modelled. To allow a simplified drag calculation within the given algebraic correlation for the relative velocity, the dispersed phase is assumed to consist of spherical particles only. Non-drag forces on the particles are completely neglected. Moreover, the influence of the dispersed phase on the turbulence field of the continuous phase is not accounted for. With the given simplifications, the mixture model is not capable of handling flows, with large non-spherical bubbles, where the deformations of the bubble, the non-drag forces as well as the bubble induced turbulence influence the flow significantly. It is rather designed to model dispersed flows, where local equilibrium establishes over a short length scale and where the spatial distribution of the dispersed particles is homogeneous. This is not the case, when the dispersed particles form clusters, which leads to a decreasing effective drag coefficient and an increasing relaxation time (Manninen *et al.*, 1996). Otherwise, the mixture model has a large potential in the field of dispersed flow modelling with various bubble size and velocity ranges. Compared to the Euler-Euler approach it is less computationally expensive and yet suitably accurate for many engineering applications. Up to now, it was applied in various one-dimensional studies (see e.g. Hibiki and Ishii, 2003, Lima and Rosa, 2009). Applications to three-dimensional, turbulent flow are rarely published (e.g. Shang *et al.* 2014).

Applicability and Limitations of the Euler-Lagrangian Approach

With the possibility to store properties of the dispersed phase (like e.g. size, shape) separately for each dispersed particle, the distribution of those properties and the cross-correlation between them can be predicted accurately with the Euler-Lagrangian approach (Rusche, 2002).

As the computational effort increases significantly with growing dispersed phase fractions, the method is preferably used for bubbly flow with low phase fractions. Transitions between the continuous and the dispersed phase cannot be appropriately modelled with this method. Consequently, air entrainment by a plunging jet into a pool is not possible with the Euler-Lagrangian approach. If the location and quantity of the entrained air would be known, an Euler-Lagrangian approach could be used for the bubble transport simulation.

3.4 Coupled Multiphase Models

In order to overcome the limited applicability to certain scales of the aforementioned two-phase modelling approaches several researchers implemented coupled multiphase models. In most cases the models aim to enable the simultaneous modelling of resolved and unresolved interface length scales. In the following section the most important developments in the field of coupled multiphase models are presented in chronological order.

3.4.1 Coupling of the Interface Tracking and the Two-Fluid Model

Cerne *et al.* (1999, 2000, 2001) developed an approach for coupling the incompressible two-fluid model with a VoF-based interface tracking method: within two-phasic regions where the grid is fine interface tracking is used, for areas where the flow is too dispersed to be described with the interface tracking method the time and space averaged two-fluid model is applied. Coupling between the model is reached via the volume fraction of one of the fluids, which is a variable used in both models. The switching point between the models is based on the dispersion of the mixture. A dispersion function is defined for this purpose. The function compares the position of the phases with the reconstructed linear interface. When the fluids are clearly separated by the

interface the dispersion is zero $\gamma = 0$. It gets larger than zero, when a part of the fluid is located on "the wrong side" of the interface. For switching between the VoF and the two-fluid model a maximum dispersion value is defined as switching parameter γ_0. Regions with dispersion values below the chosen value ($\gamma_{i,j} < \gamma_0$) are handled with the VoF model. For all regions with values higher than the maximum dispersion value ($\gamma_{i,j} > \gamma_0$) are solved with the two-fluid model. The value for γ_0 has to be determined empirically, e.g. by analysing maximum dispersion in the model. The larger γ_0 is defined, the more the VoF method is used. In their tests, Cerne *et al.* (2000) used values between $\gamma_0 = 0.4$ and $\gamma_0 = 0.6$.

The coupling approach of Cerne *et al.* (2000) seems promising for the simulation of the lock filling process, as it is able to capture the free surface as well as the unresolved bubbles. However, the switching criterion is not physically based and therefore difficult to determine. Wardle and Weller (2013) consider the approach as "self-fulfilling prophecy" as the interface compression is applied when the interface is already sharp.

3.4.2 Interface Sharpening in Simulations with Two-Fluid Model

For modelling multiphase flows with multiple scales Štrubelj and Tiselj (2009) developed an interface sharpening extension for the two-fluid model. Their model uses the two-fluid model to capture the general flow field. For the long scale interfaces a conservative level set method for sharpening the interface is applied. For sharpening a high resolution scheme is used for the solution of the volume fraction equation. Moreover, artificial compression is introduced into the volume fraction equation to counteract the numerical smearing in the interfacial zone. An additional sub-model accounts for the surface tension, which is calculated with the approach of Brackbill *et al.* (1992) and split according to the volume fractions between the two momentum equations. For switching between the dispersed and the stratified areas the criterion by Cerne *et al.* (2001) was used. With that the model entails comparable difficulties with switching as the criterion is arbitrary and not based on any physical context. Unlike Cerne *et al.*

(2001) their model overcomes the difficulty of various numbers of equations within one domain by the two-fluid model to the complete domain.

3.4.3 Interfacial Area Density Model for Stratified Flows

For modelling stratified two-phase flows within horizontal pipes Höhne and Vallée (2010) extended the two-fluid Euler-Euler model with the algebraic interfacial area density (AIAD) model as first proposed by Egorov *et al.* (2004). The AIAD model detects the local flow pattern which is used to define the momentum exchange coefficients for the two-fluid model closure. The model differentiates between bubbly flow, droplet flow and free-surface flow. Dependent on the flow pattern appropriate models for the local drag coefficient, the interfacial area density and the local characteristic length scale are chosen. For the switching volume fraction limits and blending functions are defined.

The model seems to perform acceptable in the field of stratified flows. First results documented in the publication show qualitatively good results, quantitative derivations need further studies. If the model is applicable to more complex flow situations than pipe flows cannot be concluded from the publication.

3.4.4 A Coupled Model for Complex Flow Patterns

Another modelling approach for the simulation of multiscale two-phase flows was developed by Yan and Che (2010). To account for the different scales, the two-fluid model and a VoF model with piecewise linear interface reconstruction (PLIC) are coupled. In contrary to Cerne *et al.* (2000) their approach accounts for the characteristics of the flow and both models are included within a uniform framework. In particular, the model classifies three phases distinguished according to the physical state and the length-scale of the interface: the large-length-scale-interface (LSI) phase, the small-length-scale-interface (SSI) phase and the continuous fluid phase. In the LSI phase the interface is much larger than the grid whereas in the SSI phase the interface is equivalent or smaller than the grid size. When the fluid and the LSI phase occupy a cell, interface tracking is applied. For cells including fluid and SSI phase, the two-fluid model is used.

In the unified framework of the new model, the governing equations are written in the form of the two-fluid model. For tracking the interface, the velocity fields are assumed to be equal for both phases, and so the two-fluid model reduces to the VoF formulation. In cells, where all three phases are present, a special "volume fraction redistribution" method is used for the solution.

Generally, the coupling concept within the uniform solution framework of Yan and Che seems very promising. First results show the good agreement with experimental data. Unfortunately, the approach does not guarantee mass conservation for all phases, which is a significant drawback.

3.4.5 Hybrid Multiphase CFD Solver

Similar to Štrubelj and Tiselj (2009) the *multiphaseEulerFoam* solver implemented in the OpenFOAM framework by Wardle and Weller (2013) combines a multiphase fluid model with an interface capturing approach. For coupling the surface tension is included within the governing two-fluid equations. Also the volume fraction equation is extended with an interfacial compression term, which is a mass conservative form in contrary to the PLIC reconstruction method used by Štrubelj and Tiselj. In analogy to Cerne and Tiselj (1999) the normalized magnitude of the gradient of the volume fraction is used as switching criterion between the models:

$$\gamma = \frac{|\nabla \alpha|}{max(|\nabla \alpha|)} \qquad (3.50)$$

A user-defined maximum value has to be chosen to define which model is used in which region. As the model allows for more than two phases, a switching parameter between all phase pairs can be defined. In the presented three-phase liquid-liquid-air tests, Wardle and Weller fixed the model choice for each phase pair: interface capturing is only turned on for the air-liquid interface but off for the liquid-liquid interface. This makes the capturing of air entrainment impossible. This assumption is acceptable for the presented examples, but disadvantageous for the lock filling system under investigation in this work.

3.4.6 The Extended Mixture Model

Damian (2013) coupled the VoF model with the algebraic slip mixture (ASM) model to account for the unresolved scales in two-phase flows. Formulating the governing equations of both models in a similar form, a unified framework was designed to model multiphase flows with short and long scale interfaces. The so called extended mixture model uses the VoF model, where the interface is larger than the cell and switches to the mixture model where interfaces cannot be resolved by the grid. The switching between the models Damian is controlled with the so-called face gradient criterion.

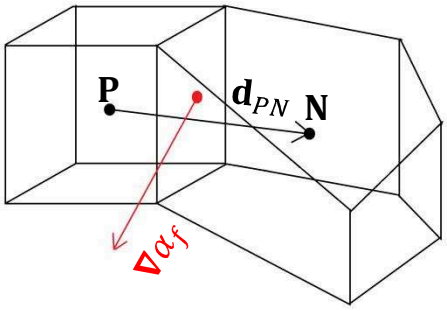

Figure 3.1: Face gradient criterion adapted from Damian (2013)

For this criterion the face gradients are weighted proportional to the mesh size by multiplying the gradient of the volume fraction $\nabla\alpha_f$ with the face's neighbouring centre-to-centre vector $\mathbf{d}_{PN}$:

$$\gamma = \left|\nabla\alpha_f \bullet \mathbf{d}_{PN}\right| \tag{3.51}$$

The face gradient describes the gradient of a variable at a cell face. It is calculated by first calculating the gradients in the cell centres and interpolating the values then to the cell faces. In regions with large face gradients in the volume fraction function the VoF model is chosen, since large gradients are assumed to indicate a large scale interface. For regions with small gradients, the ASM model is applied.

For the switching a limiting threshold value for the switching face gradient γ_0 has to be chosen. Below the threshold value, the mixture model is used. Above the threshold and for cells completely filled with one phase, the VoF model is applied. In his experiments Damian used a threshold value of $\gamma_0 = 0.33$. With the chosen value for the threshold and further assumptions (like e.g. a fixed relative velocity) his test cases show good agreement with experimental data.

Damian's concept of formulating the mixture model in analogy to the VoF model within the OpenFOAM framework is the basis of the developments made in this thesis. However, the switching point between the two models is based on an arbitrary, user-defined value, which is unknown. A connection to a physical correlation is necessary.

3.5 Turbulence Models

In hydraulic engineering all relevant flows are highly turbulent, meaning that instantaneous, non-predictable chaotic changes characterize the flow regime. Turbulent motions increase the mixing within the fluid. Consequently mass, heat and momentum are exchanged throughout the fluid. The evolving three-dimensional transient turbulent structures have a rotational character. Those so-called turbulent eddies significantly influence the characteristics of the flow. Through interaction with the mean flow and the breakup of larger eddies into smaller eddies the kinetic energy is extracted from the mean flow and handed down from the largest to the smallest turbulent structures. This energy passing process through all scales is known as turbulent energy cascade. At the end of the cascade, the inertial forces equal the viscous forces. The kinetic energy in the smallest eddies is converted into internal energy through the viscous shear stress in the fluid. Through the dissipation, energy losses in turbulent flows are higher than in laminar flows (Versteeg and Malalasekera, 2007). The largest eddies contain the most energy. Hence, large eddies are most responsible for the energy transfer and the increased diffusivity in the flow. The maximal size of eddies in water flow is limited by the natural bounds. For example, a turbulent eddy inside the flow of a canal is limited by the canal geometry.

Also the shape and extension of the largest eddies is strongly influenced by the geometry. On the other hand smaller eddies are more homogeneous and have an isotropic character. The minimum vortex scale is limited by the point where viscous forces dominate over inertial forces. Following Kolmogorov's theory of 1941 the smallest turbulent length scale is dependent on the turbulent dissipation and the turbulent viscosity. He defined the smallest length scale in turbulent flow with:

$$\eta = \left(\frac{\nu^3}{\varepsilon}\right) \tag{3.52}$$

where ε is the average dissipation rate of turbulent kinetic energy per unit mass and ν represents the kinematic viscosity of the fluid. With growing Reynolds number the Kolmogorov length decreases.

The incompressible Navier-Stokes equations, as described above, model the complete range of turbulent scales. So, if the temporal and the spatial resolution are high enough and the numerical scheme is excellent, turbulence can be directly reproduced. However, this requires very high computational effort. Therefore, a direct numerical simulation is often not feasible for many engineering applications. Alternatively, the turbulent fluctuations can be modelled partly or completely. With the large eddy approach, only the larger turbulent structures are directly resolved whereas the smaller structures are modelled. Scale separation is done via spatial filtering. Compared to the direct numerical simulation, computational effort is significantly reduced. Even less expensive is the Reynolds-Averaged-Navier-Stokes approach, where the Navier-Stokes equations are time-averaged and the complete turbulence is captured by an additional model.

3.5.1 Direct Numerical Simulation

A proper direct numerical simulation (DNS) is the most precise way of simulating turbulent flow, without applying approximation or averaging to the Navier-Stokes equations. All evolving motions in the flow are directly resolved via the numerical grid. The spatial discretization must capture the largest eddies which are relevant for the system under investigation as well as the smallest

eddies in the range of the Kolmogorov length scale. Stating that the Kolmogorov length underestimates the dissipative scale size Pope (2000) recommends using a maximum spatial resolution of $\Delta x \cong 2.1\eta$ and a minimum domain size of integral length scale. Since the motion of the smallest eddies has to be captured by the temporal resolution, the time-step has to be balanced to the spatial resolution. Those spatial and temporal resolution requirements for DNS make those calculations very costly in terms of computing resources. Therefore, DNS is rarely feasible for real-world engineering applications. Instead, DNS is mostly applied to theoretical research cases.

3.5.2 Large Eddy Simulation

The large eddy approach for modelling turbulence is based on the assumption, that the large eddies, which carry most energy and dominate the turbulent mixing should be directly resolved, whereas the smaller eddies can be modelled. For that, a spatial filter is applied, which separates the different turbulent length scales. Various filtering methods can be used, more detailed information about the filtering can be found e.g. in Pope (2000). In practice, the filter width is often computed from the grid spacing and the filtering is applied to the velocity field. All turbulent structures smaller than the grid spacing are modelled. For the modelling of the unresolved eddies, various different methods are available. Explanations of those can exemplarily be found in Pope (2000). A large eddy simulation (LES) is always grid dependent, meaning that the accuracy can be improved, when the grid is refined. As the cell size reaches the Kolmogorov length, LES transforms into a DNS. With growing computer resources LES got more and more popular in recent years. With feasible computational effort LES achieves a good approximation of the turbulent structures.

3.5.3 Reynolds Averaged Navier-Stokes Models

The Reynolds-Averaged Navier-Stokes (RANS) equations are based on the idea, that every instantaneous flow quantity can be decomposed with a Reynolds decomposition into a time-averaged component and an additional fluctuation component. With that, the Navier-Stokes Equations can be written in terms of

the decomposed quantities. As a consequence of the averaging process, the resulting set of equations contains an additional non-linear term, which is called the Reynolds-Stress-Tensor (RST). The additional term is a symmetric tensor which consists of six normal and three shear stress terms. It accounts for the additional momentum transport introduced by the turbulent fluctuations and can be interpreted as additional viscosity in analogy to the stress term resulting from the molecular viscosity of the fluid. In most turbulent flows the turbulent viscosity is much larger than those resulting from molecular viscosity of the fluid. To find a closure for the underdetermined set of equations, several model approaches have been developed. The RANS models can be divided into Eddy Viscosity models (EVM) and Reynolds-Stress models (RSM). With the RSM all six independent Reynolds stresses are represented with six additional transport equations. Through this, the method is very accurate in predicting complex flows, including rotation, swirl, separation or high strain rates. As the method is relatively expensive concerning computational costs it is only used in very few cases. More common is the application of the EVM. Those models are based on the Boussinesq assumption (1897) stating that the turbulent stresses are directly proportional to the mean flow field. Those models are of first order and can be classified by the number of additional equations, which have to be solved to find the eddy viscosity. For engineering applications two-equation models are state-of-the-art. Those models introduce two additional transport equations, which represent the turbulent properties of the flow. In particular, the k-ε model, the k-ω model and the k-ω-SST model are mostly applied. For the k-ε model (Launder and Sharma, 1974) one transport equation for the turbulent kinetic energy k and a second for the turbulent dissipation ε is solved. The model is relatively simple to implement and converges easily. It is applicable for a large range of flow patterns. However, the model gives unsatisfying results in close proximity to walls. When the near-wall regions are relevant, the k-ω model (Wilcox, 1988) can be used instead. This model replaces the turbulent dissipation with the turbulence eddy frequency ω. To combine the advantages of both aforementioned models Menter (1993) introduced the k-ω shear stress transport (SST) model. The model uses a blending function, which activates the

k- ε approach for the inner flow field and the k-ω model in close proximity to walls. Through this combination, the k- ω-SST model is suitable for a large variety of engineering flows.

3.5.4 Extended Hybrid Models

To find a compromise between the computationally expensive large eddy simulation and the more inaccurate RANS approach, several hybrid models were developed. These try to combine the averages of both models.

The detached eddy simulation (DES) as first published by Spalart *et al.* (1997) is a modified RANS turbulence modelling approach using LES as a sub-grid model. It was designed for modelling the turbulence in high-Reynolds number flows with massive separation: the LES approach is applied in the separated flow regions but for the thin boundary layers less expensive RANS model is used. The switching between RANS and LES is dependent on grid resolution and wall distance. In regions where the grid is larger than the turbulent length scale, LES is used. For the boundary layers and all other areas, where the turbulent length scale is less than the grid spacing, the RANS model is applied. Since the DES model behaves incorrectly in some cases an improved version of the DES model Spalart *et al.* defined the new delayed detached eddy simulation (DDES) model in 2006. The DDES model uses a modified switching approach similar to the SST approach of Menter and Kuntz (2004). In contrary to the DES approach, the DDES assigns the boundary layer to the RANS model even if the wall-parallel spacing would activate the LES model.

An alternative hybrid RANS-LES modelling approach was presented by Piomelli and Balaras (2002). Their wall-modelling in LES (WMLES) approach uses LES in the complete flow domain except for a very thin near wall region, where the wall distance is much smaller than the boundary layer thickness. As shown in various tests the model works reasonable for simple channel flows, but is not applicable for cases with more complex geometries (Shur *et al.*, 2008).

With the improved delayed detached eddy simulation (IDDES) model Travin *et al.* (2006) presented a further hybrid modelling approach which combines the ideas of the DES and the WMLES model. The IDDES model aims

to include the LES wall-modelling within the DDES approach, where the simulation does have turbulent inflow content. The addition of VLES to the DDES model cures the known shortcomings as grid induced separation or the log-layer mismatch (Shur *et al.*, 2008).

3.5.5 Turbulence Modelling for Two-Phase Flows

In dispersed two-phase flows, the turbulence is additionally influenced by the motion of the dispersed particles. In particular, the presence of dispersed particles can affect the production, the transport and the dissipation of turbulence. The influence of the dispersed particles is dependent on the volume fraction (Brennan, 2001): with dispersed volume fractions of $\alpha < 10^{-6}$ the influence of the dispersed particles on the flow of the surrounding continuous phase can be neglected. For dilute suspensions with volume fractions in the range of $10^{-6} < \alpha < 10^{-3}$ the momentum transfer from the dispersed particles to the continuous phase flow field significantly influences the turbulence structure. A decreasing particle relaxation time leads to increasing dissipation rates. For dense suspension with volume fractions $\alpha < 10^{-3}$ the turbulent flow characteristic is not only influenced by the momentum transfer between the phases, but particle-particle interactions additionally affect the turbulent flow field.

To include the alteration of the turbulent flow structure, several researchers developed adapted turbulence models for multiphase flows. Most approaches are based on the Boussinesq hypothesis, modelling the turbulent momentum transfer with an eddy viscosity. Basically three approaches are suggested in literature (Yam, 2012): in the first approach, the common single-phase RANS approach is extended with additional terms in the turbulence transport equations. These account for the influence of the dispersed phase on the turbulence. This so-called mixture turbulence model is applicable, when the phases are well mixed and when the density ratio is close to unity. The second approach uses RANS equations for the turbulence of the continuous phase. The turbulence transport equations are extended with terms for the interphase momentum transfer. An additional algebraic equation accounts for the dispersed phase turbulence. This

approach is suitable for dilute suspensions, where the particle motion influences the primary phase turbulence. The most sophisticated solution consists of the dispersed RANS model, which solves the turbulence transport equations for each phase. This model is applicable to any kind of multiphase flows. However, the additional equations produce additional complexity and computational effort. Therefore, multiphase turbulence models are rarely applied.

3.6 Developed Modelling Concept

Modelling the proposed lock filling system requires a multiphase approach which is able to capture multiphase flow phenomena with strongly varying length scales. On the one hand the large stretched interfaces at the lock chamber water surface have to be reproduced; on the other hand air bubbles entrained by the plunging jet in the drop shaft have to be accounted for. With a direct numerical simulation a free-surface method like e.g. the VoF method would be able to capture the physics of the given system. However, the direct numerical simulation is not feasible with reasonable computational effort due to the very small turbulent and interface structures. When applying the VoF method without resolving all scales, the fluid behaviour in the bubbly regions becomes unphysical: unresolved air bubbles within the continuous water phase result into fluid chunks, which have the properties of the mixture. Rising of the chunks solely results from the gradient in the volume fraction. Bubble specific forces as for example the drag are completely neglected for all unresolved bubbles. Therefore, the physical process of bubble transport and detrainment cannot properly be modelled since the necessary physics are not included.

For modelling the described system a new modelling concept was developed. The solver is based on the VoF method and the mixture model as described by Damian (2013). Multiple extensions, which are described below, adapt the solver for hydraulic engineering purposes.

Instead of resolving all scales, several parts of the physical phenomena have to be modelled. In particular, the turbulent and the interfacial structures which are smaller than the grid used for the spatial discretization of the domain, are not directly captured. Only their effect on the flow is introduced through

models. To overcome the lack of the VoF method in the unresolved regions, the model is extended to the mixture model, which additionally accounts for the dispersed flow behaviour. Similar to the VoF model with artificial compression, the relative velocity term in the mixture model acts only in regions, where both phases are present. However, the separation of the phases (e.g. the degassing of unresolved bubbles) is based on the physical description of rising bubbles. In particular, the model approach formulated with the volumetric flux (cf. 3.3.2) is applied. The formulation presented by Damian (2013) is extended with an new approach for the calculation of relative velocity. With the means of an algebraic relation based on physical correlations between bubble size and bubble rising velocity the relative velocity between the phases is calculated. Furthermore, the bubble diameter is predicated on the local pressure, to account for their compressibility (which is neglected in the incompressible mixture model formulation). To ensure the best possible description of the free surface in the lock chamber region, high resolution schemes are used for the discretization of the convection terms. With that, numerical diffusion is reduced. Additionally, a special algorithm to guarantee the boundedness of the solution of the volume fraction equation is applied. Moreover a turbulence model is coupled with the mixture model, which accounts for the unresolved turbulent scales in the flow. The interface for the turbulence model is universally applicable with a large variety of available models from the OpenFOAM library. With the turbulence models, the turbulent fluctuations are partly or completely removed from the flow field and replaced by a turbulent diffusion. Thus, the effect of the turbulent flow field on the rising of the bubbles cannot be considered. To account for the interaction of the turbulent fluctuations of the surrounding flow field with the transported bubbles, an additional diffusion term was added to the phase fraction equation. The added term is proportional to the turbulent diffusion. A user-defined factor which is multiplied with the diffusion term controls the size of its influence. With this addition, it is assumed that increasing turbulence in the flow field leads to additional diffusion of the bubbles. As a consequence, bubble detrainment lengths increase with growing turbulence.

4 The Application-Oriented Multiscale Two-Phase Model

The following chapter gives a detailed description of the application-oriented approach, assorted for the simulation of flows in the near field of hydraulic engineering structures that contain air-water intermixing zones. An overview of the mathematical formulation of all necessary components is presented. For the comprehension of the implementation, the software framework and its numerical capabilities are explained. Additionally, important implementation details for the new model are emphasized.

4.1 Mathematical Model

4.1.1 Field Equations

The application-oriented multiscale multiphase (AOMM) model is based on the partial differential equations of the mixture model using the volumetric flux formulation as presented in section 3.3.2 and recalled in the following. The formulation is adapted with a modified pressure formulation, which is taken from the current formulation of the VoF solver interFoam of the OpenFOAM library.

The modified pressure p_{rgh} is received by subtracting the hydrostatic pressure from the total pressure p:

$$p_{rgh} = p - \rho_m \mathbf{g} \bullet \mathbf{x} \tag{4.1}$$

where $\mathbf{x}$ represents the spatial position vector. The usage of the modified pressure in the momentum equation has the advantage to counteract decoupling problems in a cell-centred segregated formulation (Jasak, 2006a). In contrary to the total pressure, which varies even for a free surface flow at rest due to the density differences, the modified pressure formulation is constant for a fluid at rest. With the modified formulation the pressure gradient results in:

$$-\nabla p = -\nabla p_{rgh} - \mathbf{g} \bullet \mathbf{x} \nabla \rho_m - \rho_m \mathbf{g} \tag{4.2}$$

The last term on the right hand side cancels out with the gravity term of the standard momentum equation formulation (cf. equation (3.36). The first two terms of the right hand side are used for the new formulation. Thus, the resulting model consists of the following three equations:

Mass conservation equation for the mixture

$$\nabla \bullet \mathbf{j} = 0 \tag{4.3}$$

Momentum conservation equation for the mixture

$$\begin{aligned} \frac{\partial \rho_m \mathbf{U}_m}{\partial t} \; + \; \nabla \bullet (\rho_m \mathbf{U}_m \mathbf{U}_m) &= -\nabla p_{rgh} \; + \nabla \bullet \left[\mu_m \left(\nabla \mathbf{U}_m + \nabla \mathbf{U}_m^T \right) \right] \\ &+ \mathbf{g} \rho_m \bullet \mathbf{x} + \nabla \bullet \left[\alpha_1 (1 - \alpha_1) \frac{\rho_1 \rho_2}{\rho_m} \mathbf{U}_{-r} \mathbf{U}_{-r} \right] \end{aligned} \tag{4.4}$$

Mass conservation equation for the primary phase

$$\frac{\partial \alpha_1}{\partial t} + \nabla \bullet (\alpha_1 \mathbf{j}) + \nabla \bullet \left[\alpha_1 (1 - \alpha_1) \mathbf{U}_{-r} \right] = 0 \tag{4.5}$$

The equation system is of second order, as it contains the second derivative of the mixture velocity $\mathbf{U}_m$. The momentum equation is non-linear due to the non-linearity of the convection term. With the given formulation a dependency between the mass and the momentum conservation equation is not directly visible, although it exists.

The resulting set of equations of the AOMM model resembles the VoF model and can be treated similarly. An additional algebraic equation for the relative velocity $\mathbf{U}_r$ and a correlation between the velocity of the centre of volume $\mathbf{U}_m$ and the velocity of the centre of mass $\mathbf{j}$ reduces the number of unknowns from five to three. To solve for the remaining unknown variables α_1, $\mathbf{U}_m$ and p_{rgh} an equation for the pressure can be derived from the momentum equation. When pursuing a segregated solution strategy for the solution of the system of equations, a segregated pressure-velocity coupling algorithm can be applied. To obtain credible results it is essential to ensure overall mass conservation and a bounded solution for the primary phase fraction. For the applicability to most hydraulic engineering cases the spatial discretization must be flexible to allow the complex geometry to be capturing of. Numerical stability as well as calculation effort should be optimized to enable reasonable computation times.

4.1.2 Algebraic Equation for the Relative Velocity

To get a coupling relation between the equations, the mixture velocity of the centre of volume $\mathbf{j}$ and the mixture velocity of the centre of mass $\mathbf{U}_m$ are related with as follows:

$$\mathbf{j} = \mathbf{U}_m - \alpha_1(1-\alpha_1)\frac{\rho_1 - \rho_2}{\rho_m}\mathbf{U}_{-r} \qquad (4.6)$$

The relative velocity for bubbly flow $\mathbf{U}_{-r}$ can be approximated by the magnitude of the terminal rising velocity U_t of the bubbles multiplied with a unit vector pointing in opposite direction to the gravitation vector:

$$\mathbf{U}_{-r} = U_t \cdot \left[\frac{-\mathbf{g}}{|\mathbf{g}|}\right] \tag{4.7}$$

To determine the rising velocity of the bubbles, various approaches exist. Below the approaches implemented in the mixture model are presented.

Approach with Fixed Relative Velocity

The simplest approach is the assumption of a constant bubble rising velocity resulting in a fixed relative velocity for the mixture model. Especially for bubbles in the ellipsoidal regime (cf. Figure 2.2), where the rising velocity is hardly dependent on the bubble size and the exact value is difficult to determine, this approach can be most efficient.

Approach Based on Particle Relaxation Time

Several commercial CFD codes (e.g. ANSYS Fluent or Phoenics) apply an approach developed by Manninen *et al.* (1996). For this approach the terminal velocity is calculated as product of the particle relaxation time τ, the fluid properties and the secondary acceleration a (Manninen *et al.* 1996):

$$U_t = \tau \frac{(\rho_1 - \rho_m)}{\rho_1} a \tag{4.8}$$

The particle relaxation time for a particle can be generally calculated with:

$$\tau = \frac{4}{3} \frac{\rho_2 (d_B)^2}{\mu_1 C_d \mathrm{Re}_p} \tag{4.9}$$

For the implementation the general formulation for the particle relaxation time is reformulated as:

$$\tau = \frac{\rho_2 (d_B)^2}{18 \mu_1 \, f_{drag}} \tag{4.10}$$

The drag function f_{drag} accounts for the different bubble regimes:

$$f_{drag} = \frac{1}{24} \left(C_d \mathrm{Re}_p \right) = \begin{cases} 1 & for \ \mathrm{Re}_p < 1 \\ \left(1 + 0.15 \ \mathrm{Re}_p^{0.687}\right) & for \ 1 \leq \mathrm{Re}_p \leq 1000 \\ 0.0183 \ \mathrm{Re}_p & for \ \mathrm{Re}_p > 1000 \end{cases} \tag{4.11}$$

In the intermediate and the Newton regime the drag function is dependent on the particle Reynolds number Re_p:

$$\mathrm{Re}_p = \frac{\rho_2 d_2 |\mathrm{U}_r|}{\mu_1} \tag{4.12}$$

and therefore also dependent on the absolute value of the relative velocity $|\mathrm{U}_r|$. The relative velocity is approximated with the Stokes' law:

$$\mathrm{U}_r = \frac{1}{18} \frac{d_B^2 (\rho_l - \rho_g)}{\mu_l} \mathrm{g} \tag{4.13}$$

Manninen's approach seems most suitable for small spherical bubbles, where Stokes' law can be applied. For larger bubbles, which tend to ellipsoidal or spherical cap shape, the calculated terminal velocities diverge in comparison with experimental data. Comparing the results of the given formulae with experimental results (e.g. Clift *et al.*, 1987) large deviations are visible.

Approach Based on Bubble Regimes

Zheng and Yapa (2000) derived a more sophisticated approach for the calculation of the terminal bubble rising velocity.

For the spherical regime they calculate the terminal rising velocity with:

$$\mathrm{U}_t = \frac{\mathrm{Re}_p \mu_l}{\rho_l d_B} \tag{4.14}$$

The terminal velocity in the ellipsoidal regime is received with:

$$\mathrm{U}_t = \frac{\mu_l}{\rho_l d_B} M^{-0.149}(J - 0.857) \tag{4.15}$$

Hereby, the following auxiliary functions are applied:

$$J = 0.94 H^{0.757} \text{ for } 2 < H \leq 59.3 \tag{4.16}$$

$$J = 3.42 H^{0.441} \text{ for } H > 59.3 \tag{4.17}$$

H is defined as:

$$H = \frac{4}{3}\mathrm{EoM}^{-0.149}\left(\frac{\mu_l}{\mu_w}\right)^{-0.14} \tag{4.18}$$

where μ_w is the viscosity of water. The shown correlations are valid for $\mathrm{M} < 10^3$ and $\mathrm{Eo} > 40$. For the spherical-cap regime the following correlation of Davies and Taylor (1950) is used:

$$\mathrm{U}_t = 0.711\sqrt{d_B \mathrm{g}} \tag{4.19}$$

The approach of Zheng and Yapa (2000) shows high accordance with experimental data with various kinds of fluids and gases. Therefore, it is applied in the case studies below.

Influence of Free-stream Turbulence on the Bubble Rising Velocity

In turbulent flow bubbles experience changing drag forces due to the velocity fluctuations. For small bubbles, where the relaxation time is small compared to the velocity oscillation period, the fluid particles follow the flow. Therefore, the

influence of turbulence on the drag of small bubbles can be neglected. For particles with diameters larger than the turbulent fluctuations the drag forces are affected by free-stream turbulence. However, an exact correlation between the free-stream turbulent intensity and the change of the bubble rising velocity is difficult to define. In this study, the influence of the free-stream turbulence on the bubble rising velocity is neglected. This is considered as acceptable simplification, since the uncertainty in the bubble rising velocities are assumed to be higher than the potential turbulent influence.

Influence of Bubble-Bubble Interaction on the Bubble Rising Velocity

As described in section 2.1.5 the rising velocity of a bubble is affected by the presence of further bubbles. Dependent on the bubble size regime, the interaction between the bubbles can increase or decrease the terminal rising velocity. Following Ishii (1977) the velocity of the dispersed phase with respect to the volume centre of the mixture can be calculated with:

$$\mathrm{U}_r = \mathrm{U}_t \cdot (1 - \alpha_g)^{1.75} \tag{4.20}$$

when the condition $\mu_l \gg \mu_g$ is applicable. This correlation is valid for the ellipsoidal regime, where surface tension effects are more relevant than viscous forces. Here, the terminal velocity for the single bubble U_t is calculated with:

$$\mathrm{U}_t = \sqrt{2} \cdot \left[\frac{\mathrm{g}\sigma\Delta\rho}{\rho_c{}^2}\right]^{0.25} \tag{4.21}$$

In this formulation the terminal velocity of a single bubble is independent from the bubble size and can be considered as constant for air bubbles in water. With increasing gas content, the terminal rising velocity of the swarm decreases.

4.1.3 Pseudo-Compressibility of the Bubbles

To account for the compressibility of the bubbles, which cannot be considered with the incompressible mixture model, the approach is adapted. Particularly the bubble diameter is adjusted according to the water depth. For that, the user

defined bubble diameter is multiplied by a shrinking factor modelling the volume decrease due to pressure increase. Assuming that the defined diameter is valid for bubbles close to the surface, the local shrinking factor for the cell s is defined with:

$$s = \frac{p_{abs}}{p_{abs} + p_P} \qquad (4.22)$$

where p_{abs} is the absolute pressure and p_P is the local pressure in the cell under consideration. Looking at the correlation between the bubble volume and the bubble diameter ($V = d^3\pi/6$) it becomes visible that volume scales with the cube of the diameter. To obtain the adapted local diameter of a bubble, the diameter is multiplied with the third root of the shrinking factor s.

In the approach used the factor is used only to shrink the bubble size, not to adjust the volume fraction in a cell. Hence, it only influences the bubble rising velocity, which is directly calculated from the bubble diameter. The influence of the pseudo-compressibility grows with increasing water depths.

4.1.4 Extension of the Primary Phase Fraction Equation for Highly Turbulent Flows

In highly turbulent flows, the bubble transport is significantly influenced by the turbulent fluctuations of the flow. Due to the arbitrary velocity fluctuations of the surrounding water the rising motion of the bubbles is randomly disturbed. As a result, the bubble transport capacity of the flow is increased meaning that bubbles are transported further with the flow. The current two-phase model is coupled with turbulence models which only account for the effect of one-phase turbulence. Velocity fluctuations are partly or completely removed from the flow and replaced by a calculated additional turbulent diffusion. Therefore, the disturbance of the rising process through turbulent motions of the flow cannot be seen when using the current model. To allow the modelling of highly turbulent flows with larger bubble contents, the numerical model has to be extended. In particular, the influence of the turbulence of the phase fraction transport must be

integrated. For that the primary phase fraction equation is extended with a diffusion term:

$$\frac{\partial \alpha}{\partial t} + \nabla \bullet (\alpha \mathbf{j}) + \nabla \bullet \left[\alpha(1-\alpha)\mathbf{U}_{-r}\right] = \nabla \bullet (D_t \nabla \alpha) \qquad (4.23)$$

Inspired by the transport of a passive scalar quantity, it is assumed that the transport process of the primary phase consists of a convective and a diffusive part. The convective terms describe the transport of the quantity α with the flow field and due to the density difference of the phases. The additional diffusion term accounts for the diffusion of αin regions of high turbulence. To create a connection between the diffusion term in the primary phase equation and the turbulence of the flow, the dimensionless turbulent Schmidt number is introduced (Bates *et al.*, 2005):

$$\mathrm{Sc}_t = \frac{\nu_t}{D_t} \qquad (4.24)$$

The turbulent Schmidt number Sc_t defines the ratio of the turbulent diffusion ν_t and the turbulent diffusivity D_t. In analogy to the turbulent Prandtl number which represents the same ratio for heat transfer processes, the turbulent Schmidt number is assumed to be close to unity for resolved substances (Malcherek, 2005). Setting $\mathrm{Sc}_t = 1$ the diffusion coefficient necessary for the solution of the primary phase transport equation equals the turbulent diffusion:

$$D_t = \nu_t \qquad (4.25)$$

For the current model the turbulent diffusion is calculated by the turbulence model and can be used. To allow the scaling of the influence of the turbulent diffusion term, the term is multiplied by a factor *b*:

$$\frac{\partial \alpha}{\partial t} + \nabla \bullet (\alpha \mathbf{j}) + \nabla \bullet \left[\alpha(1-\alpha)\mathbf{U}_{-r}\right] = b\left[\nabla \bullet (D_t \nabla \alpha)\right] \qquad (4.26)$$

The turbulence diffusion influence factor *b* can be defined by the user. By setting it to zero, the influence on the phase fraction transport of the turbulence is

neglected. For $b = 1$ the diffusion coefficient becomes equal to the turbulent diffusion.

4.2 Numerical Approximation

Since the governing partial differential equations (PDEs) are not solvable with analytical methods, the solution for the chosen mathematical model has to be approximated with numerical methods. Three classical methods available for this purpose: the finite difference method, the finite volume method and the finite element method. All methods aim to approximate the values of the continuous mathematical functions on a set of discrete points. To achieve this, the domain is discretized with a grid, whereby the structure of the grid is dependent on the method used. For the **finite difference** method (FDM) the domain is usually discretized with a uniform grid, meaning that grid point has the same amount of neighbours. The method approximates the integral form of the PDEs with the means of finite differences based on the application of local Taylor series expansions. With all methods the truncation of the series determines the accuracy and the complexity of the solution. The FDM is best suitable for modelling regular shaped geometries which can be discretized with regular, structured grids. For those cases the method is simple to implement. In order to enable the handling of more complex geometries very sophisticated techniques have to be included. The **finite element** m**ethod** (FEM) is capable of handling uniform and non-uniform grids consisting of a finite number of elements. The method is based on the assumption, that every continuous quantity can be approximated by piecewise continuous functions. It interpolates the solution over the elements using a method of weighted residuals. The FEM is capable of handling a large variety of different applications including fluid dynamics. However, in most popular fluid dynamic frameworks the **finite volume method** (FVM) is used. In this method the domain can be discretized with uniform or non-uniform grids consisting of an arbitrary number of volumes, bounded by flat non-overlapping faces. The transformation of the integral form of the governing PDEs into a solvable set of algebraic equation is performed through integration over a volume. Within the volumes a piecewise

linear variation of dependent variables is assumed. The variables can be stored in the cell-centres or in the face-midpoints, depending on the approach chosen. For the transformation of every single operator of the integral equation into an algebraic counterpart, various schemes exist. To find the most suitable representation of the partial differential operators is a field where a lot of research still takes place. More details about these discretization schemes will be given in the next section (4.2.1). In this study, the FVM is applied. To allow greatest possible flexibility, the method is formulated for arbitrary polyhedral meshes.

4.2.1 The Finite Volume Method for Polyhedral Meshes

For the solution of fluid dynamic problems with the means of the FVM, the partial differential with the means of algebraic equations referring to discrete variables. The transformation from a PDE to a set of algebraic equations is called discretization and usually consists of:

- the spatial discretization and
- the temporal discretization.

For the spatial discretization the continuous domain, in which the flow is to be modelled, is divided into a finite number of volumes. In the later calculation one value per variable can be determined for each cell. The temporal discretization divides the simulation time into discrete time-steps. The discretization transforms the PDEs into a set of algebraic equations based on the before defined spatial grid and time-steps. The smaller the volume size and time-step is chosen, the better the accuracy in the solution is achieved. However, the computational effort also grows with decreasing cell and time-step size.

Properties of the Polyhedral Mesh

As most hydraulic structures have a complex shape, which cannot be suitably modelled with a structured grid, a method for discretizing the necessary equations with polyhedral meshes is advantageous. In the following, a very widely applicable variation of the finite volume discretization method is

presented, which is implemented in the Open Source toolbox OpenFOAM. The approach claims to be applicable on all kinds of meshes which fulfil the following restrictions:

- the complete domain has to be filled with computational cells, which are bounded by the domains boundaries and do not overlap each other,
- the cell faces should be flat and have a positive area and
- every cell-face must belong to exactly two cells, except if it is a boundary cell-face.

Geometrically a single control volume can be described with the following parameters: cell centre P (located in x_P); vector connecting centroids of neighbour cells $\mathbf{d}_{PN} = \overline{PN} = x_N - x_P$; face area vector $\mathbf{S}_f$ starting at the midpoint of the face pointing perpendicular from the owner to the neighbour cell, the vector size corresponds to the face area. The parameters are visualized in Figure 4.1.

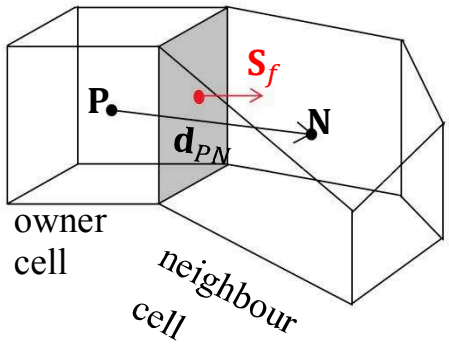

Figure 4.1: Owner – neighbour correlation between two polyhedral cells

In the OpenFOAM approach for polyhedral meshes, the complete discretization concept is based on direct neighbours of the cells. Next neighbours of the cells are not used and therefore also do not have to be explicitly defined. With this concept the complete mesh can be stored with five lists: points, faces, owner, neighbour and boundary.

The **point list** describes the corner vertices of the cell faces with the means of three-dimensional Cartesian coordinates. Additionally all vertices get

consecutive numbers deviated from their line number in the list (which do not have to be stored explicitly). With the help of these reference numbers, the **faces** can be defined in the next list by describing each cell face with the respective vertices that belong to the face. Additionally, the amount of vertices belonging to each face is stored. With the following two lists, each cell face is assigned to an **owner** and a **neighbour** cell, whereby the cell with the lower listing number is always defined as owner. In a correctly defined mesh all faces must have an owner cell. A neighbour cell is only necessary, when internal faces are described. Boundary faces do not have a neighbour cell. For a simpler definition of the boundary faces, the owner list is designed such, that all faces without neighbour entry are listed at the end. The **boundary** list can therefore refer to its associated faces by a starting number, referring to the owner list, and an amount of faces that belong to the boundary. In the boundary list, all boundary faces should be clustered according to their physical properties and their assigned boundary conditions. For easier reference, when defining boundary conditions, the boundary face clusters can be labelled with a name. With the concept explained for the mesh definition, the storage capacity for the grid information is minimized and the calculation with polyhedral cells with an arbitrary number of faces is enabled. All additional geometrical information needed for the calculation can be derived from the information given in the lists.

Equation Discretization

The applied FVM for polyhedral meshes uses a cell-centred approach meaning that all primary variables are principally saved in the centroid of the cells, although they can also be stored on the cell faces. Variables referring to cell faces are indexed with f. The discretization of the equations is performed per operator, meaning that every single operator can be discretized with an independent method.

To illustrate the discretization the following general transport equation for a general quantity ϕ (x, y, z, t) is used:

$$\frac{\partial(\phi)}{\partial t} + \nabla \bullet (\mathbf{U}\phi) - \nabla \bullet \left(\Gamma_\phi \nabla \phi\right) = S_\phi(\phi) \qquad (4.27)$$

The first term in the equation describes the temporal variation of the quantity ϕ. The second term accounts for the convective transport of ϕ and $\mathbf{U}$ being the transporting velocity field. The last term on the left hand side of the equation characterizes the diffusive transport of ϕ, with Γ_ϕ describing the diffusion coefficient. On the right hand side of the equations the source term is depicted. As the diffusion term includes a second derivative of ϕ in space, the equation is of second order. Following Jasak (1996), who performed a very detailed error analysis of the discretization approach described below, the spatial and temporal discretization schemes should at least be of the same order of accuracy as the equation. As the order of accuracy is dependent on the kind of the temporal and spatial variance of variables ϕ around the point P, the variance has to be defined as linear. This is achieved with the following truncated Taylor series expansion.

Spatial discretisation:

$$\phi(\mathbf{x}) \approx \phi_P + (\mathbf{x} - \mathbf{x}_P) \bullet (\nabla \phi)_P \qquad (4.28)$$

where $\mathbf{x} = (x, y, z)$.

Temporal discretisation:

$$\phi(\mathbf{x}^{t+\Delta t}) \approx \phi^t + \Delta t \left(\frac{\partial \phi}{\partial t}\right)^t \qquad (4.29)$$

In this manner the second order discretization is reached for all terms, meaning that the truncation errors in time and space scale with the square of the grid size and the time-step, respectively (Jasak 1996). For the discretization of the general transport equation (4.30) the differential form is first transformed into the integral form.

This is done by integrating all terms over discrete time-steps Δt and control volumes V_P:

$$\int_t^{t+\Delta t} \left[\frac{\partial}{\partial t} \int_{V_P} (\phi)\, dV + \int_{V_P} \nabla \bullet (\mathbf{U}\phi)\, dV - \int_{V_P} \nabla \bullet (\Gamma_\phi \nabla \phi)\, dV \right] dt = \int_t^{t+\Delta t} \left[\int_{V_P} S(\phi)\, dV \right] dt \tag{4.30}$$

In the next step the spatial integrals are discretized, meaning that the volume integrals are interpreted with algebraic expressions, so that a solution for the finite volumes can be calculated. To accomplish this, the volume integrals are transformed into surface integrals using the Gauss theorem, which can generally be written as:

$$\int_{V_p} \nabla \star (\phi)\, dV = \int_S d\boldsymbol{S} \star (\phi)_f \tag{4.31}$$

The star operator $\star$ used stands for any possible tensor product (divergence, gradient or curl). dV is an infinitesimal element of the volume V and $d\boldsymbol{S}$ represents an infinitesimal surface element. The linearization of the convection term results in a sum of the mass flux over the cell faces f:

$$\int_V \nabla \bullet (\mathbf{U}\phi)\, dV = \int_S d\boldsymbol{S} \bullet (\mathbf{U}\phi) = \sum_f \mathbf{S}_f \bullet \mathbf{U}_f \phi_f = \sum_f F \phi_f \tag{4.32}$$

with the mass flux $F = \mathbf{S}_f \bullet \mathbf{U}_f$ being the dot product of the outward pointing face area vector $\mathbf{S}_f$ and the velocity $\mathbf{U}$ interpolated to the cell face f. ϕ_f refers to the face value of the quantity ϕ, which has to be calculated from the cell value. The diffusion term is discretized with:

$$\int_V \nabla \bullet \left(\Gamma_\phi \nabla \phi\right) dV = \int_S d\boldsymbol{S} \bullet (\Gamma_\phi \nabla \phi)_f = \sum_f (\Gamma_\phi)_f (\nabla \phi)_f \bullet \mathbf{S}_f \tag{4.33}$$

where Γ_ϕ is the diffusivity.

For an orthogonal grid the cell-centred gradient interpolated to the cell face can be calculated with:

$$(\nabla\phi)_f \bullet \mathbf{S}_f = |\mathbf{S}_f| \frac{\phi_N - \phi_P}{|\mathbf{d}_{PN}|} \tag{4.34}$$

This formulation is suitable for the owner-neighbour cell concept, as it considers the neighbours of the cell face. To handle non-orthogonal grids, the face gradient discretization has to be extended. As the vector $\mathbf{d}_{PN}$ might not be parallel with the surface normal vector $\mathbf{S}_f$ in non-orthogonal grids, a non-orthogonal correction is introduced.

Therefore, the face normal vector is decomposed into an orthogonal part Δ and a non-orthogonal part $\boldsymbol{k}$:

$$\mathbf{S}_f = \Delta + \boldsymbol{k} \tag{4.35}$$

The following sketch clarifies the correlation:

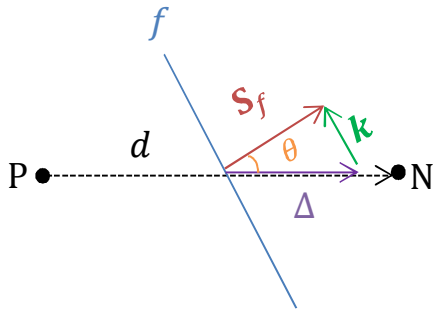

Figure 4.2: Decomposition of the face normal vector into an orthogonal part and a non-orthogonal part

Given this, the cell-centred gradient interpolated to the cell face for non-orthogonal grids can be calculated with:

$$(\nabla\phi)_f \bullet \mathbf{S}_f = \Delta \bullet (\nabla\phi)_f + \boldsymbol{k} \bullet (\nabla\phi)_f \tag{4.36}$$

Applying the over-relaxed approach, meaning that the vector $\boldsymbol{k}$ is orthogonal to the surface normal area vector $\mathbf{S}_f$ (as described by Jasak 2006b, Moukalled *et al.* 2016) the face normal vector components can be described with:

$$\Delta = \frac{\boldsymbol{S}_f \bullet \boldsymbol{S}_f}{\boldsymbol{S}_f \bullet \mathbf{e}} \mathbf{e} \text{ with } \mathbf{e} = \frac{\mathbf{d}_{\mathrm{PN}}}{|\mathbf{d}_{\mathrm{PN}}|}$$

and

$$\mathbf{k} = \left(\mathbf{n} - \frac{1}{cos\theta}\mathbf{e}\right)\left|\mathbf{S}_f\right| \text{ with } \mathbf{n} = \frac{\mathbf{S}_f}{|\mathbf{S}_f|} \tag{4.37}$$

In an orthogonal grid the vectors $\mathbf{n}$ and $\mathbf{e}$ are parallel. With that the non-orthogonal component disappears. For the discretization source terms have to be linearized in the following form:

$$S = S_u + S_p \phi_p \tag{4.38}$$

The integration over the control volume leads to:

$$\int_{v_p} S_\phi(\phi) dV \approx S_u V_p + S_p V_p \phi_p \tag{4.39}$$

After the transfer of the spatial integrals into discrete algebraic expressions the integration of all terms over the time-step Δt is performed to update the solution in time:

$$\int_t^{t+\Delta t} \left[\frac{\partial}{\partial t} \int_{V_p} \phi \, dV + \sum\nolimits_f \mathbf{S}_f \bullet \mathbf{U}_f \phi_f - \sum\nolimits_f (\Gamma_\phi)_f \mathbf{S}_f \bullet (\boldsymbol{\nabla} \phi)_f \right] dt =$$

$$\int_t^{t+\Delta t} \left[S_u V_p + S_p V_p \phi_p \right] dt \tag{4.40}$$

Sorting the transient term to the left hand side and all other terms to the right hand side, the transport equation can be written with:

$$\int_t^{t+\Delta t} \left[\frac{\partial}{\partial t} \int_{V_p} \phi \, dV \right] dt = \int_t^{t+\Delta t} \left[\sum_f \boldsymbol{S}_f \bullet \boldsymbol{U}_f \phi_f - \sum_f (\Gamma_\phi)_f \mathbf{S}_f \bullet (\nabla \phi)_f - S_u V_p + S_p V_p \phi \right] \tag{4.41}$$

The temporal discretization of each of the two sides of the equation is independent. In this thesis, the transient term on the left hand side of equation (4.44) is discretized implicitly. The discretization results in:

$$\int_t^{t+\Delta t} \left[\int_{V_p} \frac{\partial \phi}{\partial t} \, dV \right] dt \approx \frac{\phi^{n+1} - \phi^n}{\Delta t} V_p \tag{4.42}$$

The temporal discretization method for the right hand side of equation (3.38) is case dependent. Generally, the terms can be discretized with the implicit Euler method, the explicit Euler method or the Crank-Nicolson method. For the following explanations of the three methods the terms of the right hand side of equation (4.41) are replaced by $f(t, \phi)$:

$$\int_t^{t+\Delta t} \left[\frac{\partial}{\partial t} \int_{V_p} \phi \, dV \right] dt = \int_t^{t+\Delta t} [f(t, \phi)] \, dt \tag{4.43}$$

The temporal discretization can either be based on the values of the current time-steps or on values of the next time-step. A combination of both is also possible. Thus, the discretized form of the right hand side can be generally expressed with:

$$\int_t^{t+\Delta t} [f(t, \phi)] \, dt = \left[\theta \phi^{n+1} + (1 - \theta) \phi^n \right] \Delta t \tag{4.44}$$

where θ is a weighting factor taking values between 0 and 1. For the **explicit Euler method** the weighting function f is set to zero. Thereby only values from the current time-step are used, which are directly obtained for each node

without solving a system of equations. However, to ensure stability a time-step limitation according to the Courant number limit has to be respected. The Courant number Co (also referred to as Courant-Friedrichs-Lewy number) is defined as:

$$\mathrm{Co} = \frac{|\mathbf{U} \bullet d|}{\Delta t} \tag{4.45}$$

It describes how far the information transported by the velocity within one time-step Δt. In OpenFOAM, the velocity on the faces $\mathbf{U}_f$ is used. By limiting the Courant number to unity, the information is only allowed to be transported through one cell per time-step, described by the distance from owner cell centre to neighbour cell center **d**. The explicit Euler method is of first order accuracy in time. In the **implicit Euler method** all values used for the calculation of the new values stem from the next time-step, meaning that the weighting factor of equation (4.44) is set to $\theta = 1$. As the new time-step values are unknown a system of algebraic equations has to be solved. The implicit Euler method is also first order accurate. A time-step restriction is theoretically unnecessary because the method is unconditionally stable. In coupled systems, as used in the chosen modelling approach, the time-step still needs to be restricted to ensure a proper coupling. Second order accuracy can for example be achieved with the **Crank-Nicolson method**, when the weighting between old and new values is balanced: $\theta = 0.5$. The application of this weighting is often not feasible as it does not guarantee boundedness, and thereby sometimes causes stability problems. As compromise between stability and accuracy weightings of $0 < \theta < 1$ are possible but the accuracy decreases below second order. Comparable with the explicit Euler method a time-step restriction according to the Courant number criterion has to be respected when the Crank-Nicolson method is applied. The new cell values can then be calculated with:

$$\phi_p{}^{n+1} = \phi_p{}^{n} + \frac{\Delta t}{\rho_p V_p}\left[\theta \phi_p{}^{n+1} + (1-\theta)\phi_p{}^{n}\right] \tag{4.46}$$

Basic Boundary Conditions

In addition to the discretization, initial and boundary conditions have to be defined for a complete description of a numerical problem. Generally, all boundary conditions are derived from two basic boundary types: Dirichlet condition and Neumann condition. With a **Dirichlet boundary condition** the value at the boundary patch is fixed to a defined value. The discretization of the convection term at the boundary with a Dirichlet boundary condition reads:

$$\int_V \nabla \bullet (\mathbf{U}\phi)\, dV = \int_S d\boldsymbol{S} \bullet (\mathbf{U}\phi) = \sum_f \mathbf{S}_f \bullet \mathbf{U}_f \phi_f = \sum_{f \neq b} F\phi_f + F_b\phi_b \qquad (4.47)$$

where the index b denotes the values at the boundary. Due to the definition of the boundary values with the boundary condition, the last term can be calculated explicitly. It is therefore added to the source term (Hill, 1998). In the diffusion term the Dirichlet condition affects the calculation of the face gradient. Instead of using owner and neighbour cell values to calculate the gradient, the neighbour value is replaced by the boundary value. For an orthogonal grid the cell-centred gradient at the boundary is calculated with:

$$(\nabla\phi)_f \bullet \mathbf{S}_f = |\mathbf{S}_f| \frac{\phi_b - \phi_P}{|\mathbf{d}_{PN}|} = |\mathbf{S}_f| \frac{\phi_b}{|\mathbf{d}_{PN}|} - |\mathbf{S}_f| \frac{\phi_P}{|\mathbf{d}_{PN}|} \qquad (4.48)$$

Due to the known boundary value the penultimate term can be calculated explicitly. The last term remains implicit (Hill, 1998).

A **Neumann boundary condition** defines a fixed gradient g_b normal to patch face b:

$$(\mathbf{n} \bullet \nabla\phi_f)_b = \left(\frac{\mathbf{S}_f}{|\mathbf{S}_f|} \bullet (\nabla\phi)_f \right)_b = g_b \qquad (4.49)$$

where **n** is the unit normal vector pointing out of the domain.

If a value at the boundary patch is needed, this can be calculated with :

$$\phi_b = \phi_P + \mathbf{d}_n \bullet \nabla\phi_f = \phi_P + |\mathbf{d}_n| g_b \qquad (4.50)$$

$\mathbf{d}_n$ is the boundary normal component of the vector connecting the cell centre and the boundary face centre $\mathbf{d}_{Pb}$. For orthogonal grids, $\mathbf{d}_{Pb}$ coincides with $\mathbf{d}_n$. For non-orthogonal grids, $\mathbf{d}_n$ can be calculated with (Jasak, 1996):

$$\boldsymbol{d}_n = \frac{\mathbf{S}_f}{|\mathbf{S}_f|} \frac{d_{Pb} \bullet \mathbf{S}_f}{|\mathbf{S}_f|} \qquad (4.51)$$

The discretization of a convection term at a boundary with Neumann condition results in:

$$F_b \phi_b = F_b \phi_P + F_b |d_n| g_b \qquad (4.52)$$

The discretization of a diffusion term at a Neumann condition boundary yields to:

$$\mathbf{S}_f \bullet (\nabla\phi)_f = |\mathbf{S}_f| g_b \qquad (4.53)$$

4.2.2 Discretization Schemes

The required interpolation of the cell values to the cell faces can be performed with various differencing schemes. As discretized convection terms tend to unboundedness on the one hand and to inaccurate, “smeared” solutions on the other hand, the scheme must be chosen with great care.

Using the **central differencing** (CD) scheme the determination of the face value is achieved with a linear interpolation of the values in the owner (index P) and the neighbour (index N) cell:

$$(\phi_f)_{CD} = fx(\phi_P - \phi_N) + \phi_N \qquad (4.54)$$

with $fx = \overline{fN}/\overline{PN}$ describing the ratio of the distances from the neighbour cell to the face $\overline{fN}$ to the distance between owner and neighbour midpoint $\overline{PN}$.

Independent from the grid structure, the central differencing scheme is of second order accuracy in space (as shown in Ferziger and Peric 1997) and tends to suffer from severe unboundedness caused by large unphysical over- and undershoots in the solution. This is especially disadvantageous, when the natural value of the transported property is bounded between two values. Alternatively, the **upwind differencing** (UD) scheme can be applied. In this scheme, the face value is adapted according to the direction of the flow:

$$(\phi_f)_{UD} = \begin{cases} \phi_f = \phi_P \; for \; F \geq 0 \\ \phi_f = \phi_N \; for \; F < 0 \end{cases} \qquad (4.55)$$

If the fluid flows from owner to neighbour cell, the face value ϕ_f is adopted from the owner cell. If the flow is directed from neighbour to owner cell, ϕ_f gets the value from the neighbour. The upwind scheme guarantees boundedness, but is only of first order accuracy and strongly smears the solution. Through the process of smearing, caused by artificial numerical diffusion, instantaneous jumps, as they often occur e.g. at the interface between two phases, cannot be accurately depicted. For adapting the advantages and avoiding the drawbacks of both aforementioned schemes, **blended differencing schemes** can be deployed. Generally, the discretization of linearly blended schemes can be expressed with:

$$\text{for } F \geq 0 \;\; \phi_f = (1-\gamma)(\phi_f)_{UD} + \gamma(\phi_f)_{CD} = (1-\gamma)[\phi_P\,] + \gamma\left[fx(\phi_P - \phi_N) + \phi_N\right] \qquad (4.56)$$

$$\text{for } F < 0 \;\; \phi_f = (1-\gamma)(\phi_f)_{UD} + \gamma(\phi_f)_{CD} = (1-\gamma)[\phi_N\,] + \gamma\left[fx(\phi_P - \phi_N) + \phi_N\right] \qquad (4.57)$$

With the linear factor $0 \leq \gamma \leq 1$ the weighting between upwind and central differencing can be regulated. The more the factor tends to unity, the less numerical diffusion is introduced. Simultaneously the tendency to unboundedness increases. Linear blending cannot guarantee boundedness and

high accuracy over the complete domain. Especially in regions of high gradients discontinuities, over- and undershoots are likely to occur.

With non-linear blended schemes boundedness and higher accuracy than with the upwind scheme can be achieved over the entire domain. These schemes can be characterized with the **total variation diminishing** (TVD) method. The method, introduced by Harten (1984), makes the assumption that for bounded schemes the total variation $TV(\phi^n)$ of the solution should not vary between consecutive time-steps. The total variation of a variable ϕ for the time-step n is defined as:

$$TV(\phi^n) = \sum_f \left|\phi_N^n - \phi_P^n\right| \tag{4.58}$$

where N and P are points around the face f.
For schemes, fulfilling the total variation diminishing condition, the following applies:

$$TV\left(\phi^{n+1}\right) \leq TV(\phi^n) \tag{4.59}$$

Sweby (1984) suggested to formulate the non-linear blending as sum of the first order upwind differencing scheme and a higher order correction (index HO), which is limited by a flux limiter $\psi(r)$:

$$\phi_f = (\phi_f)_{UD} + \psi(r)\left[(\phi_f)_{HO} - (\phi_f)_{UD}\right] \tag{4.60}$$

The flux limiter function is dependent on the ratio of successive gradients r. For a structured grid, this ratio is defined as:

$$r = \frac{\phi_P + \phi_U}{\phi_D - \phi_P} \tag{4.61}$$

where ϕ_P is the cell value for which the flux is to be calculated, ϕ_U is the upwind neighbour value and ϕ_D is the downwind neighbour value. For an unstructured grid, which is based on the owner-neighbour relation of each face,

next neighbour cells are not directly accessible. Therefore, an adapted formulation of the limiter function is necessary. Darwish and Moukalled (2003) showed that the limiter function can be re-written into a more general form:

$$r = \left(\frac{2(\boldsymbol{\nabla}\phi)_P \bullet \boldsymbol{d}_{PN}}{\phi_N - \phi_P} \right) - 1 \qquad (4.62)$$

Using only the values of the cell under consideration (ϕ_P), the value of the neighbour cell (ϕ_N) and the distance vector from the midpoint of the owner cell to the neighbour cell ($\mathbf{d}_{PN}$) this approach is appropriate for the owner-neighbour face relation. The total variation diminishing schemes in OpenFOAM are based on this formulation. To guarantee the total variation diminishing constraint, the blending function has to lie in a certain region of the diagram in Figure 4.3.

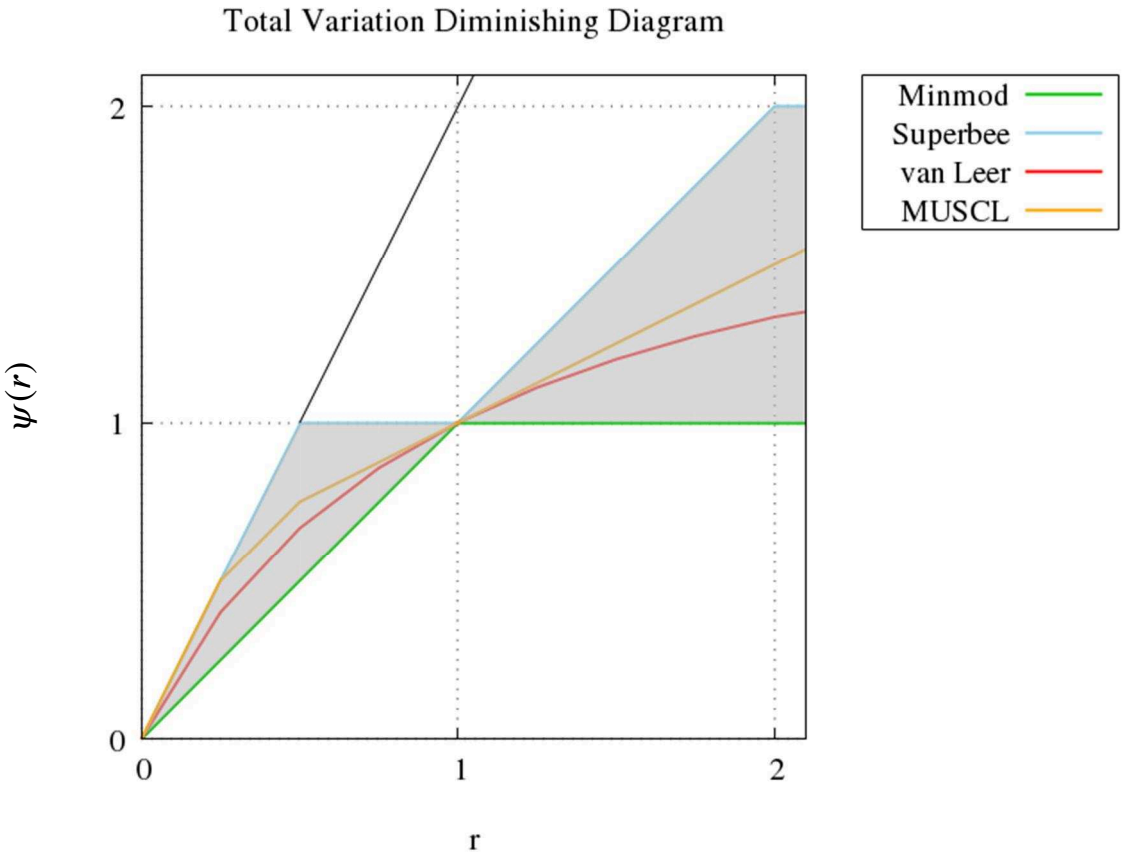

Figure 4.3: Total variation diminishing diagram

The total variation diminishing condition is fulfilled for all functions lying within the grey shaded region. The hatched region describes all second-order schemes.

Mathematically, the TVD constraint can be described as:

$$0 \leq \frac{\psi(r)}{r} \leq 2$$

and

$$0 \leq \psi(r) \leq 2 \tag{4.63}$$

The schemes are second order, if they lie within the grey shaded region in Figure 4.3. The second-order TVD schemes fulfil the following constraint:

$$r \leq \psi(r) \leq 1 \tag{4.64}$$

To guarantee stability, the TVD schemes have to additionally respect the Courant number (CFL) limitation (see section 4.2.1). With increasing CFL numbers the differencing schemes become more and more diffusive, reducing to UD for the limit of CFL=1 (Jasak, 1996).

Personal experience showed that the boundedness and stability of the TVD schemes implemented in OpenFOAM is strongly dependent on the mesh quality and the CFL number. With three-dimensional grids a bounded oscillation-free solution is not inherently guaranteed (see e.g. Denner and van Wachem, 2015). Standard TVD methods cannot be applied to equations with source or sink term, as the total variation diminishing condition is not applicable in these cases. Special adoptions for these cases are available (see e.g. Chalabi, 1997).

4.2.3 Solution Techniques for the Linear Equation Systems

Finally, the discretized partial differential equations result in large sets of linear equations, which can be written in the form of large matrices of the following form:

$$\{\boldsymbol{A}\}[\mathbf{x}] = [b] \tag{4.65}$$

$\{\mathbf{A}\}$ is the coefficient matrix, $[\mathbf{x}]$ is the solution vector and $[b]$ contains explicit terms and the source terms. To allow an effective storage the sparse coefficient

matrix is divided into a three arrays: the diagonal, an upper triangle and a lower triangle. The diagonal array contains all coefficients dependent on the point value of the cell; the neighbour coefficients fill the upper and the lower triangle.

The equation system can either be solved with direct or iterative solution techniques. Direct solution techniques apply a series of algebraic operations for solving the matrix system directly. After a finite number of operations the final solution is reached. In contrast, iterative solution techniques start with a guessed value for the solution and perform then a set of algebraic operations to improve the initial guess. By repeating this procedure several times, the solution should converge, meaning that it tends to the exact solution. The iterative procedure is stopped, when a pre-defined convergence criterion is met. Direct methods have the advantage, that the number of steps to the exact solution is known. Furthermore, they are effective and robust for solving dense matrices. However, the necessary storage is immense. In contrary, iterative methods are advantageous when very large, sparse matrices are to be solved. Here, the iterative methods are far less expensive and much faster than direct methods, where the computational costs scale with the size of the matrix. Dependent on the convergence criteria and the set tolerances, iterative methods can be even more accurate, since direct methods suffer from rounding errors.

The FVM applied to model three-dimensional flow in the nearfield of complex hydraulic structures results in very large, sparse, diagonally dominant matrix systems. Therefore, iterative methods are applied in most cases. The most simple and concurrently oldest methods are point relaxation methods like the Jacobi method, the Gauss-Seidel method or the successive over-relaxation method. These so-called stationary iterative methods are based on relaxing the coordinates. During the iterative process, an initially approximated solution is constantly improved by modifying its components based on the measured error (Saad, 2003). The methods are simple to implement but their convergence rate can be slow for large equation systems (Versteeg and Malalasekera, 2007). Nowadays, the stationary iterative methods are combined or completely replaced by the more sophisticated Kylov subspace methods like e.g. the Generalized Minimal Residual (GMRES), the Conjugate Gradient (CG) method and its

variants like the Biconjugate Gradient (BCG) method, the Bi-Conjugate Gradient Stabilized (BiCGStab) method. The Krylov subspace methods construct a step-wise approximation to the solution which lies within a defined subspace. During the iterative process the residual over the defined subspace decreases. The methods mentioned are known for their robustness and their simple implementation. A further alternative for solving the sparse linear equation system is the application of multigrid methods like the algebraic multigrid solver (AMG) and its variants can be applied. Multigrid solvers use coarse grids with fast solution times to smoothen high frequency errors to find initial solutions for the finer grid (Behrens, 2009). More detailed information about the solvers functionality can be found in e.g. Saad (2003). The choice for each system has to be made dependent on its characteristic. To find the optimal method the symmetry properties and the size of the matrix has to be considered.

Additional speed-up of the convergence of the linear equation systems can be achieved by applying preconditioners. The preconditioner changes the form of the given problem in such a way that it becomes faster to solve for the iterative solver. Under-relaxation can be used to increase diagonal dominance and thereby improve numerical stability.

4.2.4 Bounded Discretizing Procedure for the Mass Conservation Equation of the Continuous Phase

To guarantee a bounded solution of the phase fraction equation, the multi-dimensional limiter for explicit solution (MULES) solver is applied. The MULES procedure is a native method of OpenFOAM, originally designed for the VoF solver *interFoam*. The principle of MULES is based on the method of flux corrected transport for hyperbolic problems as developed by Boris and Book (1973) and Zalesak (1979). The solution procedure combines the advantages of lower and higher order discretization for the flux calculation: where the lower order scheme always produces a bounded but rather inaccurate solution, the higher order scheme discretization results in an accurate but possibly unbounded result for the flux.

To combine the advantages of both, MULES performs the following steps (Damian, 2013):

- compute the flux with a lower order scheme F_f^L, to get a bounded result,
- compute the flux with a higher order scheme F_f^H, to get a more accurate result,
- calculate the anti-diffusive flux A defined as difference between the lower and higher order flux $A = F_f^H - F_f^L$ and finally
- add a portion of the difference to the lower order flux, to obtain corrected flux $F_f^C = F_f^L + \lambda A$.

The definition of the portion λ in the last step is the main challenge in this procedure, because the added portion should be as large as possible but still guarantee boundedness. No new extrema should be created. To achieve this, the local extrema for each cell are calculated:

$$\begin{aligned} \phi_i^{min} &= min(\phi_i^n, \phi_N^n) \\ \phi_i^{max} &= max(\phi_i^n, \phi_N^n) \end{aligned} \tag{4.66}$$

Then, the local extrema are compared with the global extrema ϕ^{minG}, ϕ^{maxG} and clipped if they are larger or smaller than the allowed minimum or maximum:

$$\begin{aligned} \phi_i^{min} &:= max(\phi^{minG}, \phi_i^{min}) \\ \phi_i^{max} &:= min(\phi^{maxG}, \phi_i^{max}) \end{aligned} \tag{4.67}$$

From this the net fluxes

$$\begin{aligned} Q_i^- &= \left(\phi_i^n - \phi_i^b\right) \frac{\Delta t}{V} \\ Q_i^+ &= \left(\phi_i^a - \phi_i^n\right) \frac{\Delta t}{V} \end{aligned} \tag{4.68}$$

are calculated, which would create a local minimum or maximum. With these, the necessary limiter for the bounded fluxes can be calculated. In OpenFOAM

the limiter is determined iteratively. Beginning with $\lambda_f^{\nu=1} = 1$, the limiter values for the faces are determined by iterating over the following equations:

$$\lambda_i^{\pm,\nu+1} = max\left[min\left(\frac{\pm\sum_f \lambda_f^n}{P_i^{\pm}}, 1\right), 0\right] \tag{4.69}$$

$$\lambda_f^{\nu+1} = \begin{cases} min\left\{\lambda_P^{+,\nu+1}, \lambda_N^{-,\nu+1}\right\}, if\ inflows\ \ \geq 0 \\ min\left\{\lambda_P^{-,\nu+1}, \lambda_N^{+,\nu+1}\right\}, if\ outflows < 0 \end{cases} \tag{4.70}$$

For the current code, the number of iterations is set to three. This setting is proven to lead to bounded results in representative engineering applications. The original method by Boris and Book (1973) and Zalesak (1979) directly determines the limiter value by dividing the net fluxes by the summations of inflows P_i^+ and outflows P_i^-

$$\lambda_i^{\pm} = \begin{cases} min\left\{1, Q_i^{\pm}/P_i^{\pm}\right\}\ if\ \ P_i^{\pm} > 0 \\ 0 \qquad\qquad\qquad if\ \ P_i^{\pm} = 0 \end{cases} \tag{4.71}$$

This flux correction limiter allows the calculation of the limited flux within one step, thus produces less computational effort. According to Kuzmin and Gorb (2012) the direct determination of the limiter can sometimes lead to unnecessary corrections, because the formulation for $\lambda_i^{\pm}$ is based on a worst case scenario. The iterative procedure remedies this disadvantage.

The original MULES procedure is explicit, therefore opposes strict Courant number limits to the solution process (Weller, 2015). To overcome this limitation, a semi-implicit variant of the MULES procedure was introduced. This adapted variant first calculates an implicit solution based on purely bounded operators and subsequently performs an explicit correction based on the MULES limiter. With this approach the time-step restriction is not as strict as before. Instead, accuracy considerations govern the time-step restrictions.

4.2.5 Derivation of the Pressure Equation for the Mixture Model

The equation system describing the fluid flow consists of two partial differential equations which are non-linear and coupled. The linear coupling between the

velocity and the pressure has much higher influence than the non-linearity of the convection term, when the computation is performed with low Courant numbers. Therefore, the non-linearity of the momentum in the convection term can be linearized through the discretization.

The continuity and the momentum equation include only two unknowns, namely the pressure p and the velocity $\mathbf{U}$, therefore the problem seems well-posed at first sight. A closer look reveals the difficulty of the problem: the pressure, which is necessary for the solution of the momentum equation, is not included in the continuity equation. The absence of the pressure in the continuity equation makes the derivation of an equation for the pressure necessary. Therefore the continuity criterion of the first equation is imposed on the momentum equation, resulting in a Poisson equation for the pressure. With an iterative solution procedure pressure and velocity can be approximated. The semi-discretized set of equation can be written as:

Mass conservation equation

$$\sum_f \mathbf{j}_f \bullet \mathbf{S}_f = 0 \tag{4.72}$$

Momentum conservation equation

$$a_P(\boldsymbol{U}_m)_P + \sum_N a_N(\mathbf{U}_m)_N = \boldsymbol{r} - \boldsymbol{\nabla}\mathrm{p} + \frac{(\mathbf{U}_m)^0}{\Delta t} \tag{4.73}$$

a_P includes all matrix coefficients of the momentum equation which are directly dependent on the value of the velocity $(\mathbf{U}_m)_P$ in the considered cell P. a_P is the diagonal part of the matrix $\{\mathbf{A}\}$. a_N is the off-diagonal part of the matrix $\{\mathbf{A}\}$, containing all entries of the momentum equation which depend on the neighbour-value of the velocity $(\mathbf{U}_m)_N$. All contributions in the momentum equation, which are not directly dependent on $\mathbf{U}_P$ or $(\mathbf{U}_m)_N$ contribute to the right hand side $\boldsymbol{r}$.

$$\boldsymbol{r} = -\mathbf{g} \bullet x - \boldsymbol{\nabla} \bullet \left[\alpha_1(1-\alpha_1)\frac{\rho_1\rho_2}{\rho_m}\mathbf{U}_{-r}\mathbf{U}_{-r}\right] \tag{4.74}$$

For simplification, the off-diagonal matrix and the entries of the source terms excluding the pressure gradient contribution are combined in the $\mathscr{H}[\mathbf{U}]$ operator:

$$\mathscr{H}[\boldsymbol{U}] = \boldsymbol{r} - \sum_{N} a_N (\mathbf{U}_m)_N + \frac{(\mathbf{U}_m)^0}{\Delta t} \tag{4.75}$$

$\mathscr{H}[\mathbf{U}]$ contains the matrix of the neighbour coefficients multiplied by the corresponding velocity vector $\mathbf{U}$ and the source term contributions $\boldsymbol{r}$. By substituting the $\mathscr{H}[\mathbf{U}]$ expression into the momentum equation, the following is obtained:

$$a_P (\mathbf{U}_m)_P = \mathscr{H}[\mathbf{U}] - \boldsymbol{\nabla} \mathrm{p} \tag{4.76}$$

Resolving for $(\mathbf{U}_m)_P$ gives:

$$(\mathbf{U}_m)_P = {a_P}^{-1} \mathscr{H}[\mathbf{U}] - {a_P}^{-1} \boldsymbol{\nabla} \mathrm{p} \tag{4.77}$$

To obtain velocities at the cell faces, an interpolation to the cell faces is performed:

$$(\mathbf{U}_m)_f = \left[{a_P}^{-1} \mathscr{H}[\mathbf{U}] \right]_f - \left[{a_P}^{-1} \boldsymbol{\nabla} \mathrm{p} \right]_f \tag{4.78}$$

To assemble the fluxes, the correlation between velocity of the centre of volume $\mathbf{j}$ and the mixture velocity of the centre of mass $\mathbf{U}_m$ described in equation (4.6) is used:

$$\mathbf{j}_f \bullet \mathbf{S}_f = (\mathbf{U}_m)_f \bullet \mathbf{S}_f - \left[\alpha_1 (1 - \alpha_1) \frac{\rho_1 - \rho_2}{\rho_m} \right]_f (\mathbf{U}_{-r})_f \bullet \mathbf{S}_f \tag{4.79}$$

The resulting expression can be used to derive a pressure equation.

For that $(\mathbf{U}_m)_f$ in the mass conservation equation (4.72) is substituted by the expression of equation (4.79):

$$\sum_f \mathbf{j}_f \bullet \mathbf{S}_f = \sum_f \left[a_P^{-1} \mathcal{H}[\mathbf{U}] \right]_f \bullet \mathbf{S}_f - \sum_f \left[a_P^{-1} \nabla \mathrm{p} \right] \bullet \mathbf{S}_f$$

$$- \sum_f \left[\left[\alpha_1 (1 - \alpha_1) \frac{\rho_1 - \rho_2}{\rho_m} \right]_f (\mathbf{U}_{-r})_f \right] \bullet \mathbf{S}_f \stackrel{!}{=} 0 \qquad (4.80)$$

Resolving equation (4.80) for the pressure yields to:

$$\sum_f \left[(a_P^{-1})_f (\nabla \mathrm{p})_f \right] \bullet \mathbf{S}_f = \sum_f \left[\left(a_P^{-1} \right)_f (\mathcal{H}[\mathbf{U}])_f \right] \bullet \mathbf{S}_f - \sum_f \left[\left[\alpha_1 (1 - \alpha_1) \frac{\rho_1 - \rho_2}{\rho_m} \right]_f (\mathbf{U}_{-r})_f \right] \bullet \mathbf{S}_f \qquad (4.81)$$

Equation (4.77) is usually referred to as momentum predictor and equation (4.81) as pressure equation.

The Solution Algorithm for the Mixture Model

For the mixture model simulations one mass, one momentum and one volume fraction equation has to be solved in a coupled manner. When designing an algorithm for the coupling of the equation set, the following aspects have to be considered:

- the volume fraction is a bounded property,
- the momentum equation contains a non-linear term and
- the equations are coupled via the velocity.

The solution algorithm chosen is divided into two parts. In the first part of the solution algorithm, the volume fraction equation has to be solved. To obtain an accurate and bounded solution, a higher order, TVD scheme is used for the discretization of the face fluxes. Additionally the standard MULES algorithm

(as described in section 4.2.4) is applied to ensure boundedness. In the second part, a solution for the momentum and the phase continuity equation has to be found. For this purpose, a segregated pressure-velocity coupling algorithm is applied. The approach used resembles the pressure implicit splitting of operators (PISO) technique which was developed by Issa (1986). Instead of using a simple iterative solution procedure, the PISO method splits the operators into an implicit predictor step and multiple explicit corrector steps (Churchfield, 2010). The pressure-velocity algorithm begins with the momentum predictor step. If the momentum predictor is switched on, the predicted velocity is calculated implicitly based on the pressure gradient of the previous time-step.

$$a_P(\mathbf{U}_m)_P = \mathscr{H}[\mathbf{U}] - \boldsymbol{\nabla}\mathrm{p} \tag{4.82}$$

The resulting approximated velocity field $\mathbf{U}_m$ is not divergence free, as stipulated by the continuity equation. Nevertheless, the predicted velocities are used to assemble the fluxes. Intermediate fluxes are denoted with $\tilde{F}$. If the momentum predictor step is neglected, the velocity values from the previous time-step are used instead.

$$\tilde{F}_1 = \sum_f \left[\left({a_P}^{-1} \right)_f (\mathscr{H}[\mathbf{U}])_f \right] \bullet \mathbf{S}_f \tag{4.83}$$

and

$$\tilde{F}_2 = \sum\nolimits_f \left[\left[\alpha_1 (1 - \alpha_1) \frac{\rho_1 - \rho_2}{\rho_m} \right]_f (\mathbf{U}_{-r})_f \right] \bullet \mathbf{S}_f \tag{4.84}$$

Then, the new pressure can be calculated using the explicit fluxes. This step is called pressure solution:

$$\sum_f \left[\left({a_P}^{-1} \right)_f (\boldsymbol{\nabla}\mathrm{p})_f \right] \bullet \mathbf{S}_f = \tilde{F}_1 - \tilde{F}_2 \tag{4.85}$$

With the new pressure the explicit flux field can be corrected to obtain a conservative flux field consistent with the new pressure:

$$F = \tilde{\mathrm{F}}_1 - \left[\left({a_P}^{-1} \right)_f (\nabla \mathrm{p})_f \right] \bullet \mathbf{S}_f \tag{4.86}$$

A corrected velocity field can be calculated explicitly:

$$(\boldsymbol{U}_m)_P = {a_P}^{-1} [\mathscr{H}[\mathbf{U}] - \nabla \mathrm{p}] \tag{4.87}$$

Additionally, the face flux for the velocity of the centre of volume is corrected:

$$F := F - \tilde{F} \tag{4.88}$$

With the explicit velocity correction in equation (4.87), the assumption is made, that the velocity correction solely results from the pressure gradient, neglecting the influence of the neighbouring velocities (Jasak, 1996). To account for the contribution of the $\frac{1}{a_P} \mathscr{H}[\mathbf{U}]$ term, the pressure solution and the explicit velocity correction have to be repeated for a defined number of loops or until a defined tolerance is reached. Due to the assumption that non-linear effects are of minor influence, the $\mathscr{H}[\mathbf{U}]$ operator is not re-assembled within the correction procedure.

4.3 Implementation Details

4.3.1 The OpenFOAM library

The widely known CFD-toolbox “OpenFOAM” (Open Field Operation and Manipulation) is a well-designed C++ library that allows the numerical simulation of various engineering applications. Through its object-orientated structure it is very flexible and can be adjusted to very specific problems. The class based structure divides the software into the smallest possible units, where each is designed for performing one specific task. With its object orientated structure the maintenance of the code and development of extensions are generally simplified. Utilizing this it is possible to add functionality to the outer layers of the code without the necessity to know everything about the inner

layers. Furthermore, code duplication is avoided, since all parts of the library can be used at multiple positions. Since the code is open source, code analysis and manipulation are possible. In general, the library is designed for tackling complex physical problems, which can be described with the means of partial differential equations (PDEs). These PDEs are then discretized on the basis of the above described finite volume method in space and with a finite differences method in time. With its specific data types for describing the PDEs and the usage of operator overloading, OpenFOAM allows formulating the equations in a way that resembles the mathematical formulation (Weller *et al.*, 1998). Thus, operators like **divergence**, **gradient** or **laplacian** can simply be written as `div`, `grad` and `laplacian`. With its ingenious concept for the discretization, which is described above, the software allows the usage of arbitrarily shaped cells in the mesh. A message passing interface based parallelization concept is embedded seamlessly which enables highly effective massive parallel computing. As the code is open source, parallel computing with OpenFOAM is limited by the hardware resources available and not by the number of licenses available. But, as the parallelization is based on a domain decomposition approach, the efficiency of parallelization is given only, if the problem size is large enough (Hinkelmann, 2003). The official version of OpenFOAM is distributed under the GNU license by ESI/OpenCFD (www.openfoam.org). Besides the official release some forks and adaptions are available. One noteworthy release is the community-driven distribution by the "extend-project", which aims to "open the OpenFOAM CFD toolbox to community contributed extensions in the spirit of the Open Source development" (www.extend-project.de). Containing various valuable user-developed extensions, it is widely used by many researchers. With the ongoing developments the differences between the two main release branches are growing, therefore switching between different versions is not recommended. The following description refers to the official version 2.2.2.

4.3.2 Mixture Model Fields and Variables

For the AOMM model variables for each cell are stored in arrays. Dependent on the type of the variable, scalar, vector or tensor fields can be defined. Variable fields, which are stored in the cell centres, are defined as volume fields. Variable fields, which are stored on the cell faces, are defined as surface fields. For the mixture model the following fields are defined:

Table 4.3.1: Model fields in the mixture model

volScalarFields

volScalarField name	Unit	Description
alpha1	-	volume fraction of the primary phase
p	kg/m/s²	pressure
dB	m	bubble diameter
rho1	kg/m³	density of the primary phase
rho2	kg/m³	density of the secondary phase
p_rgh	kg/m/s²	pressure without hydrostatic pressure
g	m/s²	gravity
sigma	N/m	surface tension

volVectorFields

volVectorField name	Unit	Description
U	m/s	velocity of the mixture
Vpq	m/s	relative velocity between the phases

surfaceScalarFields

surfaceScalarFields	Unit	Description
phi	m^3/s	face flux
phiVpq	m^3/s	face flux of the relative velocity

4.3.3 Summarized Solution Algorithm

The solution algorithm applied in the mixture model implementation is a combination of the PISO and the SIMPLE algorithm, called PIMPLE algorithm. It enables under-relaxation to improve the convergence and outer iterations to enforce the coupling between mass and momentum conservation (Venier et al 2014). The solution procedure can be summarized with the following steps:

- Primary phase conservation equation solved with MULES algorithm (alpha sub-cycling)
- Momentum predictor step if switched on by the user
- PIMPLE loop performed n times over the following steps:
  - Assembly of $\mathscr{H}$[**U**] operator
  - Solution of pressure equation
  - Flux correction with pressure effect
  - Explicit velocity correction
- Correct flux with relative velocity effect

The single steps are described in detail in the sections below.

4.3.4 Solution of the Mass Conservation Equation for the Primary Phase

In the first step of the mixture model solution procedure the primary phase conservation equation is solved. A sub-cycling loop is used to divide the time-step into smaller steps. The number of sub-cycles is defined by the user. Each sub-cycle provides a new volume fraction field. First, the explicit phase fraction flux is calculated. The flux consists of the volume fraction flux of the primary phase transported by the mixture velocity (from the previous time-step) added to the volume fraction flux in the interface or bubbly regions transported by the

relative velocity (from the previous time-step). The explicit discretization is performed according to the user defined schemes. To obtain good accuracy, either TVD or NVD schemes should be used. Then the volume fraction flux field is transferred to the MULES solver. Moreover, the volume fraction field, the mixture velocity flux field and the global minimum and maximum value for the volume fraction are provided as arguments. In the MULES algorithm a lower order solution for the primary phase conservation equation is calculated explicitly. By subtracting the higher order flux from the lower order flux, an anti-diffusive flux is calculated. In an iterative procedure a limiter is determined, which is finally multiplied with the higher order flux and added to the lower order solution to receive a bounded volume fraction field. After sub-cycling, the new density values for each cell can be calculated.

4.3.5 Velocity Predictor Equation

To predict a new velocity field, the momentum equation is assembled. Except from the contribution from the relative velocity between the phases, source and pressure terms are neglected. When the momentum predictor is switched on, the assembled momentum matrix is equated with the right hand side terms of the momentum equation including the gravitational term and the pressure gradient. The right hand side is formulated in terms of face values and transformed back to the cell values with a special reconstruction function. This is advantageous when large density gradients are present in the flow field.

4.3.6 Pressure Equation

For the pressure equation the $\mathscr{H}[\mathbf{U}]$ operator is assembled with the predicted velocity field. If the predictor step is not performed, the velocity field from the previous time-step is used for the operator assembly. To obtain $\mathscr{H}[\mathbf{U}]$ the off-diagonal matrix part of the momentum equation matrix is multiplied with the inverse of the diagonal matrix part of the momentum equation matrix. Next, $\mathscr{H}[\mathbf{U}]$ is interpolated to the cell faces and the previously neglected source term contributions added. To add the source term fields, they have to be interpolated to the faces and multiplied by the inverse of the diagonal momentum matrix.

The pressure gradient is still excluded. In the following, the pressure-velocity calculation procedure starts: at first the pressure equation can be constructed based on the predicted velocity field. The solution gives a new pressure. Then, in the velocity correction step the velocity field on the cell faces is corrected with the new pressure and a new velocity field for the cell values is calculated by adding the reconstructed, corrected face velocity flux to the predicted velocity field. Finally, the relative velocity face flux is corrected by subtracting the flux resulting from the relation between the velocity of the mass of the mixture and the velocity of the volume of the mixture.

4.3.7 Time-stepping Procedure

In the mixture model the time-step restriction results from two aspects: the hyperbolic character of the phase continuity equation and the operator splitting in the pressure-velocity coupling algorithm. Due to these aspects, the time-steps of the simulations have to be restricted to fulfil a certain Courant number criterion. For explicit schemes a Courant number smaller than unity is theoretically inevitable to receive stable results. Implicit schemes entail no theoretical restriction. For the mixture model, the time-step should be restricted to receive Courant numbers smaller than 0.5.

OpenFOAM provides two different time-stepping procedures for transient simulations. Either a user-defined, fixed time-step is used for the temporal discretization or adaptive time-stepping is applied. With the adaptive time-stepping procedure, each time-step is adjusted according to a user-defined maximum Courant number. The Courant number restriction for the mixture model is defined as:

$$\mathrm{Co} = 0.5 \bullet max\left(\frac{\sum_f |F_U|}{V} \cdot \Delta t\right) \qquad (4.89)$$

Additionally, a Courant number restriction for cells containing both phases is introduced, which is calculated only in cells, where both phases are present.

The alpha-Courant Co_α number is defined as:

$$\mathrm{Co}_\alpha = 0.5 \bullet max\left(\frac{\sum_f |F_U + F_{U-r}|}{V} \cdot \Delta t\right) \text{ for } 0 < \alpha < 1 \qquad (4.90)$$

This second restriction is introduced, because the first becomes zero in the two-phase regions. In regions where only one phase is present the divergence terms of the phase continuity equation become zero:

$$\text{if } \alpha = 0 \qquad \nabla \bullet (\alpha\, \mathbf{j}) = 0 \text{ and } \nabla \bullet \left[\alpha_1(1-\alpha_1)\mathbf{U}_{-r}\right] = 0 \qquad (4.91)$$

$$\text{if } \alpha = 1 \qquad \nabla \bullet \mathbf{j} = 0 \text{ and } \nabla \bullet \left[\alpha_1(1-\alpha_1)\mathbf{U}_{-r}\right] = 0 \qquad (4.92)$$

Before starting the solution procedure, the current maximum of all Courant number values in the domain is determined with equation (4.89). If the received value is larger than the user defined maxima Co_{max} or $\mathrm{Co}_{\alpha,max}$ the time-step is reduced. Otherwise the time-step is increased to reach the maximum. To avoid large jumps in time-stepping, the maximum change rate of the time-step size and the maximum time-step size is also fixed. During runtime the size for the next time-step is determined by:

$$\begin{aligned} x &= min\left[\left(\frac{\mathrm{Co}_{max}}{\mathrm{Co} + 1 \cdot 10^{-6}}\right), \left(\frac{\mathrm{Co}_{\alpha,max}}{\mathrm{Co}_\alpha + 1 \cdot 10^{-6}}\right)\right] \\ y &= min[min(x, 1.1x), 1.2] \\ \Delta t^{n+1} &= min\left[y \cdot \Delta t^n, \Delta t_{max}\right] \end{aligned} \qquad (4.93)$$

Δt^n is taken from the previous time-step. For the first time-step of a simulation Δt is user defined and may not exceed the global time-step maximum Δt_{max}. The factors 1.1 and 1.2 used in y are used to dampen sudden jumps between subsequent time-steps. With that, the growth of the Courant number is ensured to be smooth.

4.3.8 Integration of the Turbulence Model

To enable the modelling of turbulent flows without resolving all turbulent scales, a turbulence model can be integrated into the mixture model framework. For that additional transport equations are solved, which account for the effects of turbulence which are not directly resolved. A large variety of turbulence models is available in OpenFOAM. The linkage between the mixture model and the turbulence model is achieved via the effective viscosity. The effective viscosity is calculated as sum of the molecular and the turbulent viscosity, where the molecular viscosity is a constant fluid property and the turbulent viscosity is determined with the turbulence model.

4.4 Modelling Settings

4.4.1 Boundary Conditions for Hydraulic Applications

At the boundary patches conditions for all variables are defined. In the mixture model the momentum and the pressure equation form a coupled set of equations. Consequently, the boundary conditions for p and **U** are dependent on each other. A wrong combination of boundary conditions for these fields may lead to an ill-defined system. At boundary patches, where the pressure is defined the gradient of the pressure will determine the flow rate. For boundaries where the velocity is defined, the value of the pressure is part of the solution and cannot be chosen (Jasak, 2006b).

In addition to the basic boundary conditions (as described in section 4.2.1) derived boundary conditions can be used, which combine the basic conditions in a way, that certain real life conditions can be simulated with more convenience. To simplify the setup of hydraulic engineering cases, Thorenz and Strybny (2012) implemented a set of derived boundary conditions into the framework of OpenFOAM. In particular, boundary conditions for free surface flow simulations with a fixed water level and an atmospheric boundary condition were contributed. The following section describes how these boundary conditions work.

Boundary Conditions to Hold a Fixed Water Level

To enable a fixed water level at a boundary patch, certain conditions for the volume fraction function, the pressure and the velocity at the boundary patch have to be combined. An in-house implementation simplifies the usage. For the application of the fixed water level condition the user defines a reference point on the chosen water level surface. The water level is assumed to be normal to gravity on the level of the given point. Below the surface plane the volume fraction function is assumed to be unity, above the volume fraction function is zero.

$$\text{If } x_{patch} > x_{patch} \qquad \alpha = 1 \tag{4.94}$$

$$\text{If } x_{patch} < x_{patch} \qquad \alpha = 0 \tag{4.95}$$

For the velocity a derived boundary condition is applied. It is defined as Neumann boundary when the velocity vector points out of the domain. For an inflow the velocity is obtained from the normal component of the patch face value.

$$\text{If } phi < 0 \qquad \left(\frac{\partial \mathbf{U}}{\partial t}\right)_{patchf} = 0 \tag{4.96}$$

$$\text{If } phi > 0 \qquad \mathbf{U}_{patchf} = \mathbf{U}_n \tag{4.97}$$

The pressure value at the patch faces can be calculated with two different methods. The first method uses the user defined reference point to find out, whether the face in consideration lies above or below the water surface. For the cells above the water surface the density of the second phase air is used to calculate the pressure. For cells below the reference point $x_{refPoint}$ the density of the primary phase water is used.

Method 1 for the boundary pressure calculation

$$\text{If } \left(g \bullet \mathrm{x}_{patchf}\right) - \left(\mathbf{g} \bullet \mathrm{x}_{refPoint}\right) > 0$$
$$\mathrm{p} = refValue + \rho_1 * \left[\left(\mathbf{g} \bullet \mathrm{x}_{patch}\right) - \left(\mathbf{g} \bullet \mathrm{x}_{refPoint}\right)\right] - stabilization \quad (4.98)$$

$$\text{If } \left(g \bullet \mathrm{x}_{patchf}\right) - \left(\mathbf{g} \bullet \mathrm{x}_{refPoint}\right) < 0$$
$$\mathrm{p} = refValue + \rho_2 * \left[\left(\mathbf{g} \bullet \mathrm{x}_{patch}\right) - \left(\mathbf{g} \bullet \mathrm{x}_{refPoint}\right)\right] - stabilization \quad (4.99)$$

In case of inward pointing velocity vectors (positive flux values) the pressure is decreased by substituting the dynamic pressure. The influence can be controlled by a user defined factor c with which the stabilization factor is exponentiated.

$$\text{If } phi > 0 \qquad stabilization = \left(0.5 * \rho_P * \left|\mathbf{U}_f\right|^2\right)^c \quad (4.100)$$

$$\text{If } phi < 0 \qquad stabilization = 0 \quad (4.101)$$

The second method uses the actual density value in the adjacent cell to calculate the pressure value for the boundary value. For inward flow the same stabilization method is used, where the dynamic pressure is subtracted from the hydrostatic pressure.

Method 2 for the boundary pressure calculation

$$\mathrm{p} = refValue + \rho_P * \left[\left(\mathbf{g} \bullet \mathrm{x}_{patch}\right) - \left(\mathbf{g} \bullet \mathrm{x}_{refPoint}\right)\right] - stabilization \quad (4.102)$$

The first method gives a smooth pressure boundary field, which does not completely match the available density and volume fraction field. In contrary, the pressure boundary field calculated with the second method matches the current volume fraction and density but can be very irregular due to variations in the volume fraction function. From practical experience, the first method is advantageous for complex engineering applications. A stabilization factor of $c = 1$ is recommendable.

Boundary Conditions for Patches Open to the Atmosphere

In two-phase flows with free surface, conditions for boundaries which are open to the atmosphere are often necessary. At the boundary air or water should be allowed to flow out and in. Furthermore, the pressure is assumed to be atmospheric. To define such a boundary, the pressure should be fixed to the atmospheric pressure and the gradient of the velocity is assumed to be zero.

In practice, it is useful to apply the fixed water level boundary conditions to atmospheric boundaries that share one or more edges with a fixed water level boundary. This helps to ensure that the boundary conditions match in corner regions, where the pressure and velocity fields of one cell are defined by more than one boundary condition.

Boundary Conditions for Fixed Walls

Impermeable walls allow only a tangential flow velocity which is equal to the wall velocity. For non-moving walls, the tangential velocity is zero. Additionally, the normal velocity component at the wall has to be zero. The pressure values at the boundary are consequently defined through a zero gradient (Neumann) condition.

In turbulent flows a turbulent boundary layer develops where the wall normal velocity profile is logarithmically decreasing towards the wall. The turbulent boundary layer can be divided into three zones: the outer layer, the log-law layer and the viscous sub layer. Far away from the wall, in the so-called outer layer the flow is inertia dominated. In the log-layer closer to the wall, viscous and turbulent effects are both relevant. Below the log-law layer adjacent to the fixed wall, a viscous sublayer exists where the flow is laminar. To capture the correct velocity profile, the complete boundary layer has to be resolved including the very thin viscous sublayer. Alternatively to resolving the boundary layer, **wall functions** can be applied instead. These functions model the effects of the turbulent boundary layer with the means of empirical formula. With the usage of empirical laws, the wall functions enable the definition of the mean velocity outside the viscous sublayer as well as wall conditions for shear stress

and pressure gradient. Wall functions are based on the following assumptions (Hill, 1998):

- the velocity varies only normal to the wall, a one-dimensional description of the flow is feasible,
- the flow is fully developed in the flow direction; gradients are zero except from the pressure gradient,
- within the boundary layer turbulence production and dissipation are perfectly balanced,
- the length scale of the turbulence changes linearly with distance from the wall and
- the shear stress is constant across the boundary layer.

The calculation of the shear stress for the boundary cell is dependent on the location of the cell centre: when the cell centre lies within the **laminar region** the velocity profile is linear. The wall shear stress in the sublayer region τ_w is calculated with

$$\tau_w = \mu \frac{U_{y,P}}{\Delta y_P} \qquad (4.103)$$

where Δy_P is the distance from the cell centre to the wall and $U_{y,P}$ is the wall-parallel velocity component at the point P. For the **log-layer region** the velocity profile follows a logarithmic law. The wall shear stress for the log-law layer is obtained with

$$\tau_w = \frac{U_{y,P}\, C_\mu^{0.25} \sqrt{k_P} \kappa_v}{ln(E\, y^+)} \qquad (4.104)$$

where C_μ is a dimensionless constant, k_P accounts for the turbulent kinetic energy at the cell centre and κ_v represents the von Karman's constant ($\kappa_v = 0.4187$). E is an empirical constant ($E = 9.793$).

y^+ is the dimensionless distance:

$$y^+ = \frac{\Delta y_P \rho}{\mu} \sqrt{\frac{\tau_w}{\rho}} \tag{4.105}$$

The transition between the laminar and the turbulent flow is expected to be at $y^+ = 11$. For smooth walls the viscous sublayer is found in the region where $y^+ < 5$. The logarithmic velocity profile applies for regions where $30 < y^+$ (Pope, 2000).

When applying standard wall functions, the wall treatment implies that the centre of the first cell adjacent to the wall boundary lies within the logarithmic region of the boundary layer. In OpenFOAM the logarithmic layer wall function treatment is applied when $y^* > 10.97$. y^* is calculated with (Tapia, 2009)

$$y^* = y \frac{\rho C_\mu^{0.25} \sqrt{k_P}}{\mu} \tag{4.106}$$

In the cells adjacent to the wall boundary the velocity in the cell centre is calculated with:

$$\mathbf{U}_P = \frac{1}{\kappa_v} ln(E\, y^*) - \Delta B \tag{4.107}$$

where ΔB models the influence of surface roughness on the wall.

To calculate the roughness ΔB a non-dimensional roughness height K_S^+ is introduced:

$$K_S^+ = \frac{\rho K_S C_\mu^{0.25} \sqrt{k_P}}{\mu} \tag{4.108}$$

where K_S is the effective sand grain roughness height. Dependent on the non-dimensional roughness height, the flow regime at the boundary surface can be divided into three types: a smooth surface regime, a transitional regime and a fully rough regime.

Following the approach by Cebeci and Bradshaw (1977) ΔB can be calculated for the smooth surface regime with $K_S^+ < 2.5$

$$\Delta B = 0 \tag{4.109}$$

for the transitional regime with $2.5 < K_S^+ < 2.5$

$$\Delta B = \frac{1}{\kappa_v}\left(\frac{K_S^+ - 2.25}{87.75} + C_S\, K_S^+\right) sin\left[0.4258(ln\, K_S^+ - 0.811)\right] \tag{4.110}$$

for the fully rough regime with $K_S^+ > 90$

$$\Delta B = \frac{1}{\kappa_v} ln\left(1 + C_S\, K_S^+\right) \tag{4.111}$$

where C_S is a roughness coefficient, which identifies the roughness shape. The roughness also affects the calculation of the turbulent viscosity μ_t which is obtained with

$$\mu_t = \mu\left(\frac{y^+ \kappa_v}{ln(\,E y^* / e^{\kappa_v \Delta B})} - 1\right) \tag{4.112}$$

Alternatively to the standard wall functions which are only applicable for certain y^+values hybrid wall functions exist. These adapt the wall treatment according to the position of the first cell centre adjacent to the wall boundary. The available k-ω-SST turbulence model in OpenFOAM can be used with hybrid wall functions.

4.4.2 Discretization Schemes

For the discretization of the equation terms, schemes have to be specified. In OpenFOAM, each term can be discretized with a different scheme. As described in section 4.2.1 the temporal discretization can be performed with the Euler implicit, the Crank-Nicholson or the backward scheme. A blending between the methods is also possible.

The accuracy of the mixture model results is strongly dependent on the discretization of the convection terms. With diffusive, stable schemes like the upwind scheme, the large scale interfaces show significant smearing. High resolution schemes give more accurate solutions.

4.4.3 Linear System Solvers

For the solution of the linear systems, resulting from the discretization procedure, OpenFOAM offers a bundle of iterative equation solvers. Since the solution of the large sparse matrices is very time consuming, the solution method should be chosen carefully. To enhance convergence, pre-conditioners and smoothers can be selected additionally. The smoother ensures the smoothing of numerical spikes, occurring through ill-formed matrices or uneven intermediate solutions (Behrens, 2009).

Depending on the matrix structure, different solvers are advantageous. In the current thesis, the resulting linear equation systems are very large and sparse. These properties are suitable for applying sophisticated iterative methods, trimmed for fast convergence and low storage costs. It is very common to apply the Preconditioned Conjugated Gradient (PCG) method, the BiCGStab method or the generalized algebraic multi-grid method (GAMG) method. To find the optimal composition of solvers for each test case is tedious and not expedient. Hence, in the scope of this thesis the same combination of solvers, pre-conditioners and smoothers was always used.

4.4.4 Parallel Processing

The study of Keough (2004) gives a good insight in the influencing factors for the speed of parallel computations with OpenFOAM cases. His findings are summarized below. The general calculation speed of computations is dependent on various hardware and software factors. On the one hand properties of the hardware architecture like the speed of the RAM, bandwidth, network speed or the processing speed is relevant significantly determine the efficiency of the calculation. On the other hand, software properties and user-controllable software settings play a significant role for the final calculation speed for CFD

simulations. For most CFD applications parallel processing of the simulations is necessary to ensure feasible computation times. OpenFOAM provides generic parallelisation for all solvers developed with the standard methods. The multiphase solver developed can therefore be used in parallel without further effort. The computation in parallel requires the decomposition of the simulation case into several subsections. If the calculations of all subsection were independent from each other, the speed-up of the case would increase linearly with the number of subsections. However, inter-process communication is unavoidable. Therefore, the communication overhead increases with the growing number of subsections and thereby reduces the speed-up. Thus, the speed-up is influenced by the number of subsections and the resulting communication overhead. The efficiency of a calculation can be further increased when the decomposition method is optimized. Automatic mesh decomposition methods like *scotch* or *metis* allow an effective cutting of the domain, so that the load is balanced between the processor cores and the communication cost is minimized. The associated field information is also decomposed with the provided decomposition utility. Every decomposed section is assigned to a processing unit. For the parallel processing message passing interface (MPI) methods are applied.

4.4.5 Scalability of the Solver

To test the scalability of the solver and find a suitable decomposition correlation between the number of cells and number of computing units used for the parallel computing, speed-up tests were performed on the in-house high performance computer. For the tests one case of the latter described lock filling simulation (see chapter 6) was used. The mesh of the case was refined creating a mesh with approximately 19 million cells. To get a stable starting point for the calculation, the result from the coarser mesh was mapped to the new mesh. Then, the simulation was run for another 15 seconds. The result received was used as initial condition for the tests performed. Afterwards, the test case was run with eight different decompositions. The approximate number of cells per core and the number of applied resources are listed in Table 4.4.1.

Table 4.4.1: Decomposition setups for the scalability tests

Case Name	Number of Cells per Core	Number of Cores
Case 1	958 608	64
Case 2	479 304	32
Case 3	239 652	24
Case 4	119 826	16
Case 5	59 913	8
Case 6	39 942	4
Case 7	29 956	2
Case 8	14 978	1

In all cases the nodes containing 20 CPUs were fully allocated. The decomposition was performed with the *scotch* decomposition method. This method is designed to minimize the boundaries between the subsections. Each simulation was run for 500 time-steps. To ensure comparability the time-step size was fixed during the course of the calculation. As a result, the execution times were compared. Figure 4.4 presents the resulting execution times dependent on the number of cells per core.

In the region between 60 000 cells per core and 960 000 cells per core the execution time scales linearly dependent on the number of cells per core. This means that a doubling of the resources halves the execution time. Only when less than 60 000 cells are processed by one computation unit, the execution time can no longer be reduced by applying more resources. To ensure a linear speed-up, it is therefore advisable to use at least 60 000 cells per core for the simulations with the mixture model.

To find an optimal number of cells per core, not only linear speedup but also the total time of all allocated processing units was considered. For the process of evaluation, the efficiency of the case with the smallest product of

execution time and number of cores is defined as unity. The efficiency of all further cases is the ratio of the minimum product of number of cores and the execution time to the product of the case core number and the case execution time. The efficiencies of the eight cases are shown in Figure 4.5.

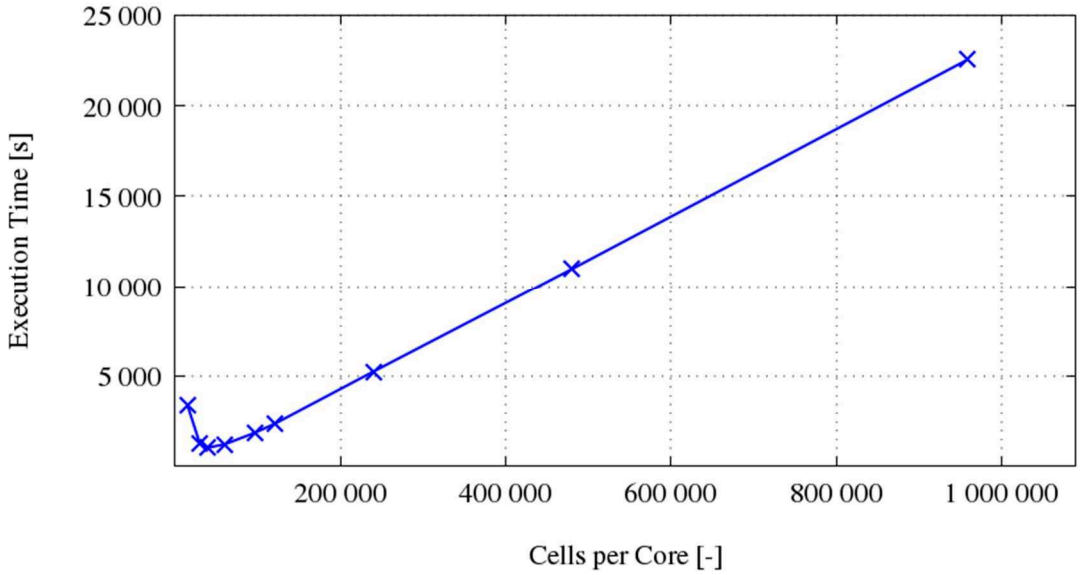

Figure 4.4: Correlation between the number of cells per core and the resulting execution time

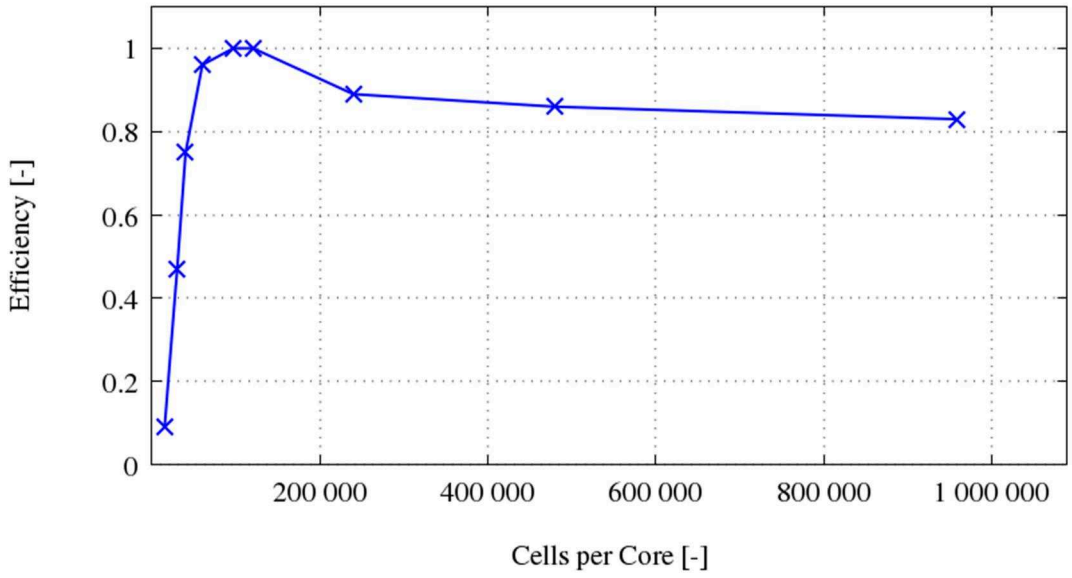

Figure 4.5: Efficiency with various decompositions

With a number of 119 826 cells per core Case 4 was identified to be the most efficient. The efficiency decreases rapidly when the number of cells per core is

smaller than in Case 4. Larger subsections only slightly reduce the efficiency. Thus, it can be concluded that the subsections for the parallel processing on the in-house cluster should contain at least 60 000 cells. With fewer cells a speed-up linear speed-up can still be achieved but the actual costs increase disproportionate. From the results of the tests it can be concluded that the solver is definitely applicable in parallel. An increasing usage of computational resources leads to decreasing execution times. The solver showed similar speed-up as other OpenFOAM solvers which were tested the same way on the same in-house cluster. For all following tests, the decomposition was always adjusted to assign at least 60 000 cells per core, which is the best compromise between speed-up and use of resources.

5 Validation and Verification Examples

The following examples are documented to show, that the solver meets the defined demands concerning multiscale two-phase flow. Comparisons with analytical and experimental results demonstrate the functionality and the accuracy of the implemented model.

5.1 Detrainment of Uniformly Distributed Bubbles in a Tank

The first example proves the ability of the mixture model to model small scale two-phase phenomena like bubble transport. Particularly, it simulates the detrainment of air bubbles, which are uniformly distributed within a water filled tank. The bubbles are not resolved by the grid, meaning that the mesh size is larger than the bubble size. This example shows the advantages of the mixture model compared to the VoF model, which is not able to model this situation correctly.

5.1.1 Model Setup

For the example a rectangular tank was meshed with an orthogonally structured grid, consisting of cube-shaped cells with an edge length of 0.01 m. A two-dimensional section through the grid is shown in Figure 5.1. The tank was 1.5 m high and had a base area of 0.5 m x 0.1 m. It was initially filled up to a height of

1 m with an air-water mixture consisting of 95 % water and 5 % air. The air content in the mixture zone represents the uniformly distributed bubbles. All bubbles were assumed to have a diameter of 0.5 mm. With the bubble diameter being smaller than the edge length of the grid cells, the bubbles were considered as unresolved. Above the air-water mixture the cells were initially filled with air corresponding to a value of $\alpha = 0$. The initial phase distribution in the tank is visualized in Figure 5.1. The tank was surrounded by no-slip walls, meaning that the mixture and the relative velocities were zero. Additionally, the pressure gradient was defined to be zero at the walls. The top boundary was open to the atmosphere and allowed inflow and outflow. At the atmospheric boundary the velocity gradients were defined to be zero and the value of the pressure is set to zero. The initial velocity in the complete tank was set to zero in all directions and the pressure field, which was calculated in the first time-step, represented a hydrostatic pressure distribution corresponding to the fluid mixture distribution.

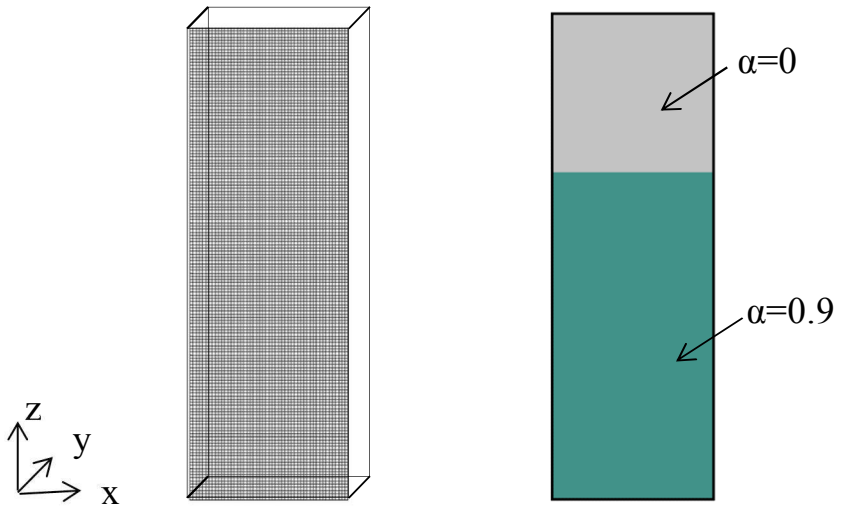

Figure 5.1: Sketch of the mesh and initial water air distribution in the tank

The properties of the primary, liquid phase were defined with a density of $\rho_1 = 1000$ kg/m³ and a viscosity of. $\nu_1 = 1 \bullet 10^{-6}$ m²/s The secondary, gaseous phase had a density of $\rho_2 = 1$ kg/m³ and a viscosity of $\nu_2 = 1.3 \bullet 10^{-5}$ m²/s. The gravitational acceleration was defined as vector parallel to the z-direction of the tank $\mathbf{g} = (0, 0, -9.81)$ m/s². For this test case no turbulence model was applied. The time-step was adaptive, allowing a maximum Courant number of

0.45 and a maximum interface Courant number of 0.5. In the first test the influence of the numerical discretization schemes on the accuracy was studied. For the detrainment height of 1 m the compressibility is considered as negligible. The influence of the compressibility of the bubbles investigated in the last test series, where the tank height was increased step-wise.

5.1.2 Analytical Results

To validate the results of the first test case, the bubble rising velocity is calculated analytically. Furthermore, the expected water level decrease can be determined. For the calculations the influence of the interactions of the bubbles with the wall as well as non-drag forces are assumed to be negligible. The bubble rising velocity is calculated with the approach for the spherical regime developed by Zheng and Yapa (2000) as shown in section 4.1.2. Complete detrainment is reached when bubbles have risen to the water surface and the remaining water region has a volume fraction of $\alpha = 1$. The detrainment is expected to be completed after all bubbles from the lowest point of the tank have reached the water surface.

With the analytically determined rising velocity of $\mathbf{U}_r$ the detrainment time Δt for the mixture can be calculated with:

$$\Delta t = \frac{h_{final}}{\alpha \mathbf{U}_r} \tag{5.1}$$

where the final water level h_{final} is calculated as difference between the initial water level and the water level drop:

$$h_{final} = h_0 - \Delta h \tag{5.2}$$

Due to the detrainment, the water level is expected to drop by:

$$\Delta h = \alpha \cdot h_0 \tag{5.3}$$

For the current example a rising velocity of $\mathbf{U}_r = 0.2413$ m/s is calculated with the implemented model by Zheng and Yapa (2000). Hence, after a detrainment time of $\Delta t = 4.14$ s the final interface height of $h_{final} = h_0 - \Delta h = 0.95$ m = is reached. The initial state and the expected final state are shown in Figure 5.2.

In the initial state all cells below the water level at z = 1.0 m are filled with 95 %

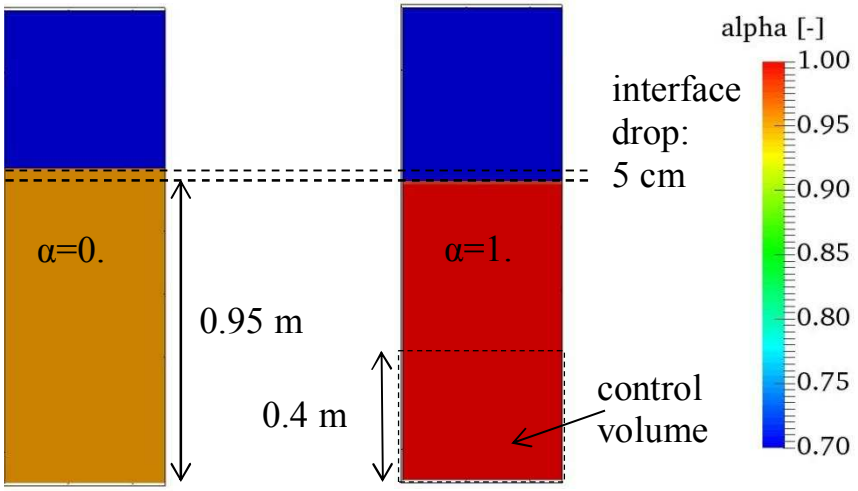

Figure 5.2: Initial water air distribution in the tank (left) and final water air distribution (right)

water and 5 % air. All cells above the water level are solely filled with air. In the final state all cells are either filled with water or air. No more mixture cells are present. After the detrainment of the complete gas content the water level surface dropped by 5 cm which corresponds to the 5 % of the height of the initial mixture filled volume. Analytically, the ratio should increase linearly from the initial value of 0.95 to 1.0 within a time of 4.14 s. For the comparison with the numerical results, an additional control volume is introduced, which includes all cells below z= 0.4 m (see Figure 5.2). During the simulation the air-water ratio within this zone is recorded every ten time-steps. From this the rising velocity of the gas content can be calculated and compared for different scenarios.

5.1.3 Evaluation of the Mixture Model Simulations

When the described case was simulated with the mixture model a smooth and continuous detrainment of the bubbles was observed. Starting from the bottom

of the tank propagating towards the water surface, the volume fraction rose from the initial value to the final value of $\alpha = 1$. Opposed to the direction of the rising bubbles, the water level continuously decreased. Concurrently, the volume fraction in the water region increased. The results of the simulations can be compared with the analytical solution. Particularly, the detrainment time and the water level decrease can be evaluated. In the numerical simulations, detrainment times were measured from the starting time to the time-step until the initial air content within the pre-defined control volume is completely released. Afterwards, the impact of the spatial resolution, the numerical discretization schemes, the bubble size, the gas content and the compressibility were tested and evaluated.

Influence of the Spatial Resolution

To test the influence of the grid resolution on the detrainment behaviour, four different meshes were created. The coarsest grid had an edge length of 0.02 m. For the standard mesh the edge length was halved to 0.01 m. One more halving of the edge length resulted in the fine mesh with an edge length of 0.005 m. The final refinement up to an edge length of 0.0025 m was used for the generation of the very fine grid. With every halving of the edge length the grid size grows with a factor of eight. A summary of the total cell numbers is shown in Table 5.1.1. When the Courant number restriction remains the same, the maximal time-step is halved. Therefore, the calculation effort rises by a factor of 16 with every halving of the edge length. This immense growth of computational effort has to be considered, when the optimal grid resolution is chosen. For real-world engineering application a good compromise between accuracy and calculation effort has to be found.

Table 5.1.1: Variants to test the influence of the spatial resolution in the tank detrainment tests

Name	Edge Length [m]	Total Cell Number [-]
coarse	0.02	9,375
standard	0.01	75,000
fine	0.005	600,000
very fine	0.0025	4,800,000

For the grid resolution test cases, the setup described in section 5.2.1 was used. The discretization of the phase transport terms were performed with the van Leer scheme. The equivalent bubble diameter was set to 0.5 mm. With the application of the approach by Zheng and Yapa (2000) a rising velocity of 0.2413 m/s is expected. All simulations were performed in parallel. For the comparison of the results the air-water ratio within a pre-defined control volume was recorded. The data of the air content within the control volume was probed every ten time-steps with an accuracy of 0.0001.

Due to the constant air-water ratio and the constant bubble rising velocity, the detrainment is expected to be linear up to the point, where the air content is completely detrained. However, the linear detrainment cannot be achieved completely in the numerical simulations, as numerical errors are inevitable. The results with the different mesh resolutions show that a refinement of the mesh improves the detrainment behaviour compared to the analytical solution. During the detrainment the theoretically sharp discontinuity in the volume fraction field between the water and the air-water zone is smeared over several cells. This effect is referred to as numerical diffusion, which results from discretisation errors of the convective and the temporal terms and from errors resulting from the mesh quality (Jasak, 1996). As the same setup is used for all cases, the difference of the numerical diffusion is only dependent on the mesh resolution. The results show that the influence of the numerical diffusion decreases with

increasing mesh refinement. Thus, the lowest error is received with the finest mesh. The results of the simulations are presented in the two diagrams of Figure 5.3: The left diagram shows the air-water ratio within the control volume over time. The right diagram shows the accumulated deviation from the analytical solution during the detrainment progress. In both diagrams only the last part of the complete simulation process is plotted where most deviation is visible.

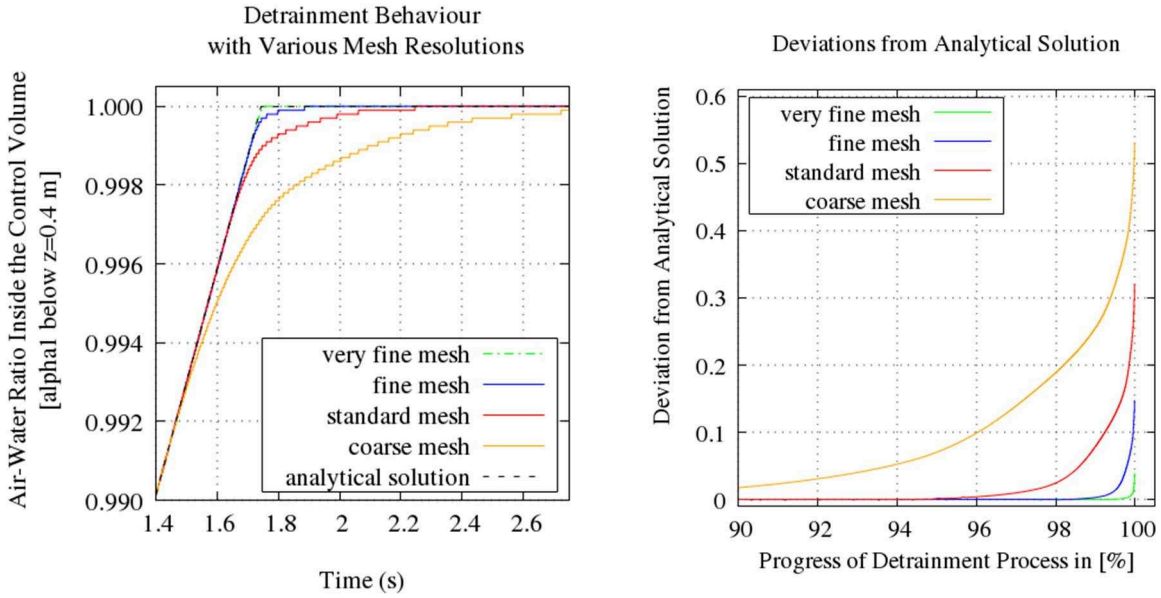

Figure 5.3: Detrainment behaviour with various mesh resolutions

Looking at the first diagram of Figure 5.3 (left), the numerical results of all cases show good agreement with the analytical solution during the first 1.4 seconds of the detrainment process. During this period the exact value of the analytical calculation is met, no difference between the different mesh resolutions is visible. Only towards the end of the detrainment process deviations from the analytical solution become visible. The deviations, which correspond to the smearing of the propagating front, decrease with increasing grid resolution. The recorded data shown in the second diagram of Figure 5.3 indicate that the deviation from the analytical solution increases exponentially towards the end of the detrainment process. For the coarsest mesh it takes approximately 54 % longer until the 99.99 % of the initial air content is released from the control volume. The medium mesh takes 33 % more time than analytically calculated. With the fine mesh, the detrainment process is increased

by approximately 15 %. In the very fine mesh resolution a water content of 99.99 % is reached after a delay of 7 %. As good compromise between computational effort and numerical error the medium mesh was chosen for all further tests.

Influence of the Numerical Discretization Schemes

To test the influence of the numerical discretization schemes on the accuracy of the results, the tank detrainment simulation was performed with six different discretization settings. All bubbles were assumed to have an equivalent diameter of 0.5 mm. In this example, the detrainment time was only dependent on the propagation of the bubbles towards the water surface. Analytically a sharp horizontal front is expected to rise in the mixture, which divides the zone of clear water from the mixture. As all bubbles have the same diameter, a continuous relative velocity equal to the bubble rising velocity is expected to develop in the complete mixture zone. The horizontal front is expected to move with the bubble rising velocity. Due to numerical diffusion, the propagating front does not remain a sharp line. Instead it smears in vertical direction orthogonally to the transport. When using the same mesh and the same time discretisation, the variation of the smearing is dependent on the discretization scheme used for the phase fraction equation. In particular, the discretisation of the divergence term describing the convection of α due to the relative velocity $\mathbf{U}_r$ is responsible for the numerical diffusion. For this test, the following schemes for the discretization of the mentioned divergence term were compared: upwind, Minmod, MUSCL, van Albada, van Leer and Super Bee. A visual analysis of intermediate simulation results after 3.6 s (see Figure 5.4) shows that the upwind discretization causes the most diffusion at the propagating front.

The schemes Minmod, van Albada, van Leer and MUSCL show similar diffusion level at the detrainment front. The sharpest interface was received, when the Super Bee scheme was applied for the discretization of the divergence terms in the volume fraction equation (cf. equation (4.5)).

Due to the perfectly structured grid without complex geometries and the Courant number limitation the simulation ran stable and fast with all tested schemes in the current test case series.

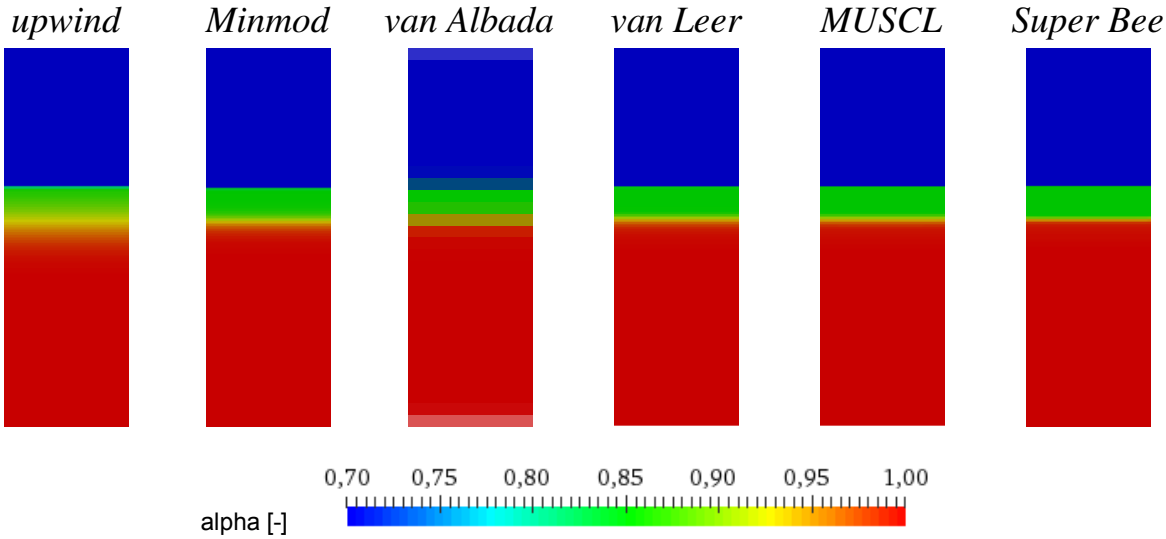

Figure 5.4: Simulation results with different discretization schemes

The influence of the numerical diffusion for the different schemes can be illustrated by measuring the air-water content within a defined volume over time. Figure 5.5 shows the recorded results for the six different discretisation schemes for the phase fraction transport. In analogy to the evaluation of the mesh resolution tests, two diagrams are presented. The first diagram shows the development of the air-water ratio within the control volume over time. The second diagram presents the accumulated derivation between the numerical and the analytical solution.

Both diagrams clearly indicate that the upwind scheme generates results with the largest deviation from the analytical solution. This is reducible to the large numerical diffusion, which widens the propagation front to both sides. Due to the smearing, it takes longer until the complete air content is transported to the surface. All further schemes showed very similar results. Up to an air-water ratio of 0.996 within the control volume no deviation from the analytical solution is apparent.

Looking at the quantitative results the Super Bee scheme shows slightly faster detrainment than all other schemes indicating the lowest numerical

diffusion error. Sorting all further schemes from shortest to longest detrainment times, the following list is achieved: van Leer, van Albada, Minmod, upwind.

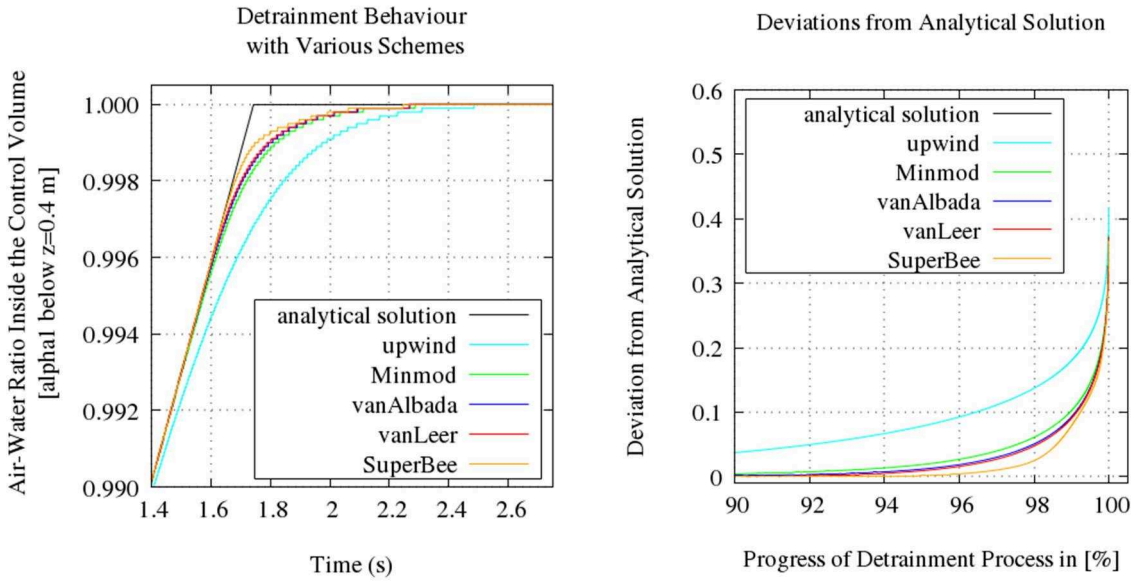

Figure 5.5: Detrainment behaviour with various discretization schemes

As the Super Bee scheme is known for artificially sharpening smooth gradients (Leonard, 1991), the van Leer scheme is chosen for the discretisation of the volume fraction transport in all following tests.

Influence of the Gas Content

To show the influence of the gas content, the tank was filled with four different gas contents. In particular the mixture zone was initialized with α-values of: 0.9, 0.8, 0.7 and 0.6. As in all previous tests an equivalent bubble diameter of 0.5 mm was chosen. All further simulation settings were also preserved. For the evaluation the gas content within a control volume was recorded over time. Analogue to the previous tests, the control volume included all cells of the tank up to a height of 0.4 m. The following diagram (shown in Figure 5.6) compares the results of the cases with different gas contents. To allow a direct comparison of the different cases, the progress of the detrainment process is shown. For that the air-water ratio in the tank was normalized. The results of the simulations indicate that the detrainment times depend on the gas content in the mixture. In

the approach used the relative velocity is calculated as product of the gas content and the single bubble rising velocity. As a consequence the detrainment process is decelerated with growing air content inside the tank. At the same time, the velocity of the surrounding fluid increases with growing air content.

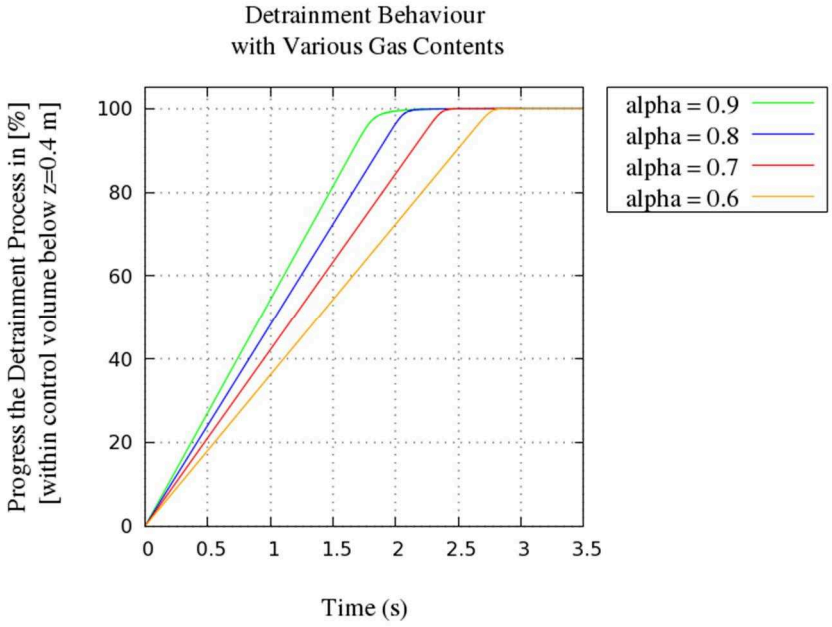

Figure 5.6: Detrainment behaviour with various gas contents

Physically, this can be justified with the increasing interactions between the bubbles when the gas content grows. Simultaneously, the rising air content entails an increased momentum transfer between the two phases. This correlation is commonly referred to as hindrance effect, which occurs in gas-liquid mixtures with gas contents lower than a critical gas content value. With gas contents higher than the critical value, the relative velocity increases with the growing gas content. The increasing rising velocity can be explained with three effects: coalescence, bubble induced turbulence and the rising of bubbles within the wakes of preceding bubbles (Simonnet *et al.*, 2007). For a bubble column, Simonnet *et al.* determined a critical gas content of 15 %. In all further test cases entrained gas contents were lower than 15 %, therefore the implemented correlation between gas content and relative velocity is assumed to be acceptable.

Influence of the Bubble Size

To show the influence of the bubble size on the detrainment times, a set of simulations with eight different bubble sizes was performed. For the tests, the standard case was used. Since the calculation formula for the rising velocity is non-linear and dependent on the bubble size regime, the bubble diameter has non-linear influence on the detrainment times. Figure 5.7 shows the correlation between the bubble diameter and the terminal velocity of a single bubble. The given diagram compares the results from the simulations (red marks in the diagram) with data from literature described in section 2.1.5 .

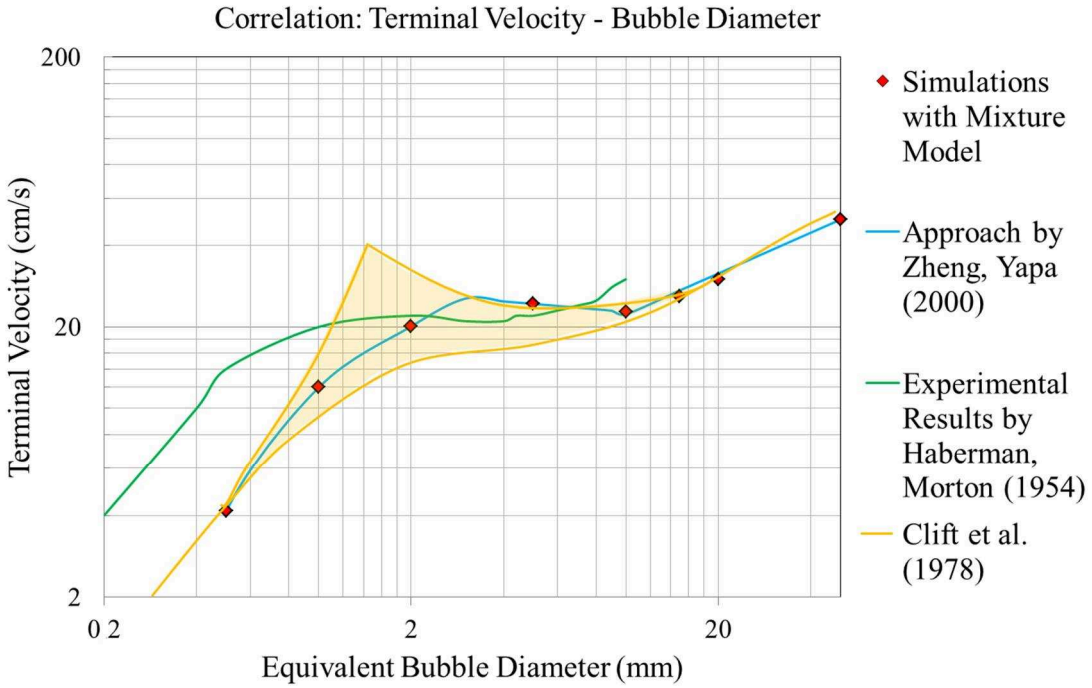

Figure 5.7: Detrainment behaviour with various bubble sizes

This test case serves as verification of the code. The analysis of the results illustrates that the approach by Zheng and Yapa (2000) was implemented correctly and produces the expected results. Up to bubble diameters of 2 mm the terminal velocity of a single bubble grows with growing bubble size. With diameters between 2 mm and 20 mm the terminal velocity remains almost constant at a value of approximately 0.2 m/s. For bubbles larger than 20 mm in diameter the size regains influence on the resulting rising velocity. The approach

chosen also shows good agreement with the experimental values of Haberman and Morton (1953) and Clift *et al.* (1987) for diameters between 0.5 mm and 15 mm. This range of diameters is assumed to be suitable for the investigation of the cases considered within this study.

Influence of the Compressibility of the Bubbles on the Detrainment Process

In the tank used in all previous tests the compressibility of the bubbles is negligible. Due to the small water depth in the tank, the water pressure at the lowest point is not significantly changing the bubble volume. To investigate the influence of the pseudo-compressibility of the bubbles, the height of the tank was increased. The following seven different heights were investigated:

Table 5.1.2: Cases for testing the compressibility influence

Name	Tank Height [m]	Initial Mixture Height [m]
Case 1	1.5	1
Case 2	5.5	5
Case 3	10.5	10
Case 4	20.5	20
Case 5	30.5	30
Case 6	40.5	40
Case 7	50.5	50

In all cases the tank was initialized with an air-water mixture of 95 % up to 0.5 m below the top boundary. Each test case was performed with and without pseudo-compressibility of the bubbles. For comparison the air-water content within a control volume was recorded over time. The control volume included all cells within the expected final water filled region. All simulations were performed with the same settings and their meshes were created with the same edge length. For the evaluation the time until 99 % of the control volume is

filled with water was recorded. Figure 5.8 shows the differences between the detrainment times for the cases simulated with and without the pseudo-compressibility. The results clearly demonstrate the increasing influence of the compressibility with increasing water depth. No relevant difference is visible for water depths of 1 m and 5 m. With a water depth of 10 m the simulation with pseudo-compressibility increases the detrainment time by approximately 17 %. Doubling the height of the detrainment zone, the difference between the two cases grows to approximately 20 %. Further expansion of the height results in significant enlargement of the difference, indicating that the influence of the compressibility gets relevant for larger cases.

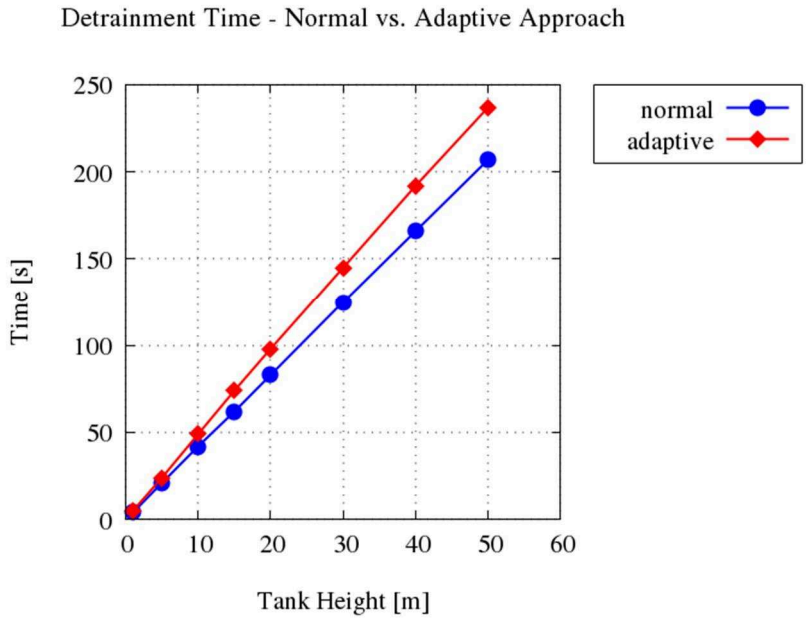

Figure 5.8: Difference between the detrainment times with and without the pseudo-compressibility

5.1.4 Conclusion from the Test Variations

The simulations of this study showed that the implemented mixture model is able to model the detrainment of gas bubbles within a liquid, which are not directly resolved by the computational grid. The presence of the gaseous phase within a cell induces a velocity in the mixture which acts in opposite direction to the gravity. Additionally, momentum is induced. Thus, the main effects of rising

bubbles on the flow can be modelled in a simplified form. As a result the gas content is detrained from the mixture. The magnitude of the velocity field in the mixture-filled cell is dependent on the single bubble rising velocity, the gas content and the prevailing velocity from the existent flow field. The single bubble rising velocity is either defined as a fixed value or calculated dependent on the bubble diameter with an approach by Zheng and Yapa (2000).

The accuracy of the results in the detrainment tests is essentially dependent on the spatial discretization and the chosen discretization schemes. With decreasing cell size the accuracy is increased. As the computational effort rises with a factor of 16 when halving the edge length of the mesh, a compromise between an appropriate edge length and the resulting accuracy has to be found for each case. In addition to choosing an appropriate mesh size the discretisation scheme for the volume fraction transport is most relevant for an accurate modelling of the detrainment process. The tests of this study showed that with higher order TVD schemes the convective transport can be modelled appropriately. Concurrently numerical diffusion is reduced.

5.2 Submerged Free Surface Flow over a Sharp Crested Weir

The second example demonstrates that the implemented mixture model is able to capture large scale multiphase phenomena as they occur in free surface flows. For the demonstration the flow over a sharp crested weir is simulated. Various water level discharge combinations were simulated with the implemented mixture model. To avoid the influence of air-water intermixing processes, only submerged flow situations were considered. The results were compared with measurement results from a physical scale model to evaluate the functionality and the accuracy of the model for the simulation of free surface flow.

5.2.1 Model Setup

The model setup consists of a sharp-crested weir structure installed within a 17 m long flume. The installed weir has a height of 0.301 m a width of 0.02 m and it blocks the flume width of 0.80 m. It is positioned at a distance of 10.13 m to the defined zero position of the local coordinate system.

The weir crest has an angle of 45 degrees. Figure 5.9 shows a sketch of the model setup.

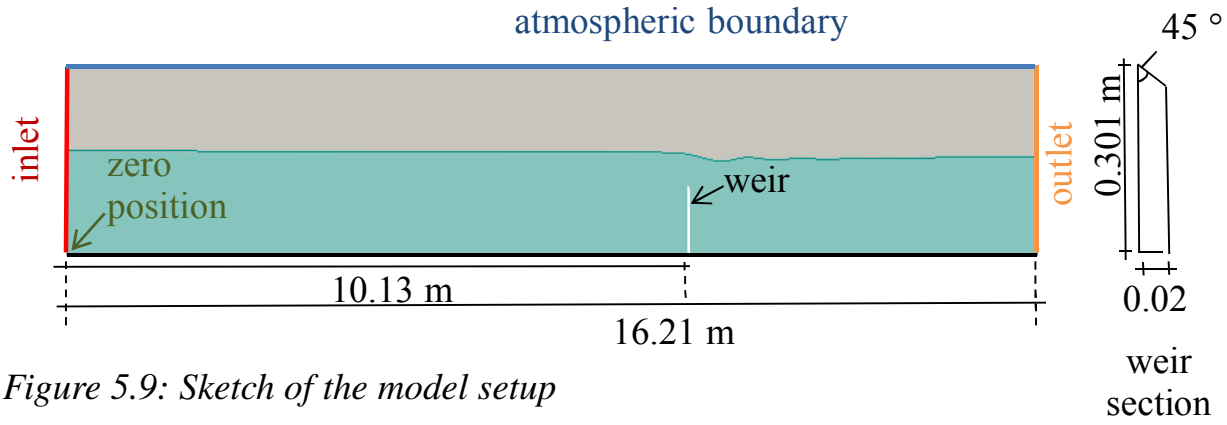

Figure 5.9: Sketch of the model setup

In the physical model the discharge was measured at the upstream inlet before entering the flume. The downstream end of the flume is equipped with a flap to fix the water level. Along the middle axis of the flume bottom measuring pots are connected. With the means of ultrasonic probes the water levels inside the measuring pots can be recorded. For each test case of this study, the water levels were recorded over five minutes. The time-averaged values of water level probes serve as comparison variable for the evaluation of the mixture model simulations. The locations of the probing points are listed in Table 5.2.1.

The numerical model replicates the physical model setup. The model inlet corresponds to the zero position of the flume in the physical model and is located at a distance of 1.36 m to the first water level probing point. The outlet in the numerical model is placed at the position of the last water level probe. A three-dimensional geometry of the weir structure was used to create the hexahedral-dominant mesh. At the inlet the discharge was defined according to the physical model setup. The water level at the inlet boundary can adapt freely. At the outlet boundary the water level was fixed. Pressure and velocity adjust to the given level. The bottom and the structure surface were defined as walls with a roughness height of 0.0001 m. The side walls of the flume were assumed to be frictionless. The top was defined as atmospheric boundary. For the simulation the k-omega SST turbulence model was applied. To achieve a steady result, the simulation was run until no more significant variation of flow field was apparent. Probing points for the determination of the water levels were inserted

at the locations identical to the probing locations of the physical model (cf. Table 5.2.1). At these points, the pressure was measured every ten time-steps.

Table 5.2.1: Probing locations for the water level measurements

Point number	Distance zero position in [m]
1	1.36
2	2.72
3	4.06
4	5.41
5	6.77
6	8.12
7	9.47
8	10.81
9	12.17
10	13.51
11	14.86

5.2.2 Results from the Physical Model

With the physical model, installed within a flume of the BAW, seven water level-discharge combinations were measured. The boundary conditions of the experiments are shown in Table 5.2.2.

Table 5.2.2: Boundary conditions for the physical model cases

Name	Discharge in [m³/s]	Outlet water level in [m]
Case 1	0.04980	0.302
Case 2	0.04989	0.323
Case 3	0.05016	0.344
Case 4	0.05017	0.364
Case 5	0.05008	0.387
Case 6	0.05011	0.407
Case 7	0.05003	0.417

To avoid influence of air-water interactions, only submerged flow situations were considered. From the experiments water levels at ten measuring points in the middle of the flume are received. The resulting water levels at the measuring locations are shown in comparison to the numerical model results (cf. Figure 5.10). The physical model tests build the foundation of the mixture model evaluation.

5.2.3 Evaluation of the Mixture Model Simulations

For the evaluation the water surface curves of the physical model tests are compared with the results of the mixture model simulations. The simulations were run until a quasi-steady flow field was received. Then, the water level at the probing points was recorded and averaged over a period 300 seconds. The measuring locations in the numerical model corresponded to the connection points of the measuring pots in the physical model.

Generally, the simulations of the flume showed satisfactory performance. The parallel calculations run smoothly without showing large numerical instabilities. The received water level curves show satisfactory agreement with the physical model results, proving that the free surface can be modelled

appropriately. Remaining deviations arise from model inaccuracies of both models. Errors or inaccuracies of the measurement methods applied for the physical model results can contribute to the deviations. Furthermore, small discrepancies between the geometrical setup of both models are inevitable and cause differences in the results. In the numerical simulations inaccuracies can result from various sources like convergence or discretisation errors. Due to the iterative nature of the solvers used for solving the linear equation system convergence errors cannot completely be avoided. However, by ensuring that suitable tolerances are met the convergence error is reduced. The discretisation errors can be reduced by improving spatial resolution and finding suitable discretisation schemes. To find a suitable mesh resolution for the simulations of the submerged free surface flow over the sharp-crested weir, the influence of the mesh on the results was tested for one case. Starting with a basis edge length of 0.05 m in the complete model, the mesh was refined step-wise until the change in the solution became negligible. Particularly the regions where strong gradients in the flow field were visible were refined. With decreasing cell sizes, the deviation between the numerical and the physical model water surface curve reduced. However, after the second halving of the basis edge length in the nearfield of the weir, the difference in the water level results gets very small. Thus, the growing calculation effort increases disproportionately compared to the gain in accuracy. As consequence, the final mesh used for all following simulations consists of approximately 5 million cells with a basis edge length of 0.005 m. In the water filled region, the edge length was quartered to 0.00625 m. To get a suitable approximation of the weir structure, the edge length was decreased to 0.003125 m in proximity to the structure surface.

The discretisation of the terms in the equation system was performed with a combination of schemes, which is well-tried and in-house commonly applied for the simulation of free surface flows at the BAW. Of particular significance for the free surface is the choice of the discretisation schemes in the volume fraction equation. In this study the van Leer scheme was applied. After reaching a steady state, the simulation results show good agreement with the measurements from the physical model. A comparison of the results is presented

in Figure 5.10. For better clarity, the results are depicted in two diagrams. Physical model results are represented with black dashed lines, numerical model results are marked with solid, coloured lines. The weir structure is positioned at a model length of 10.13 m.

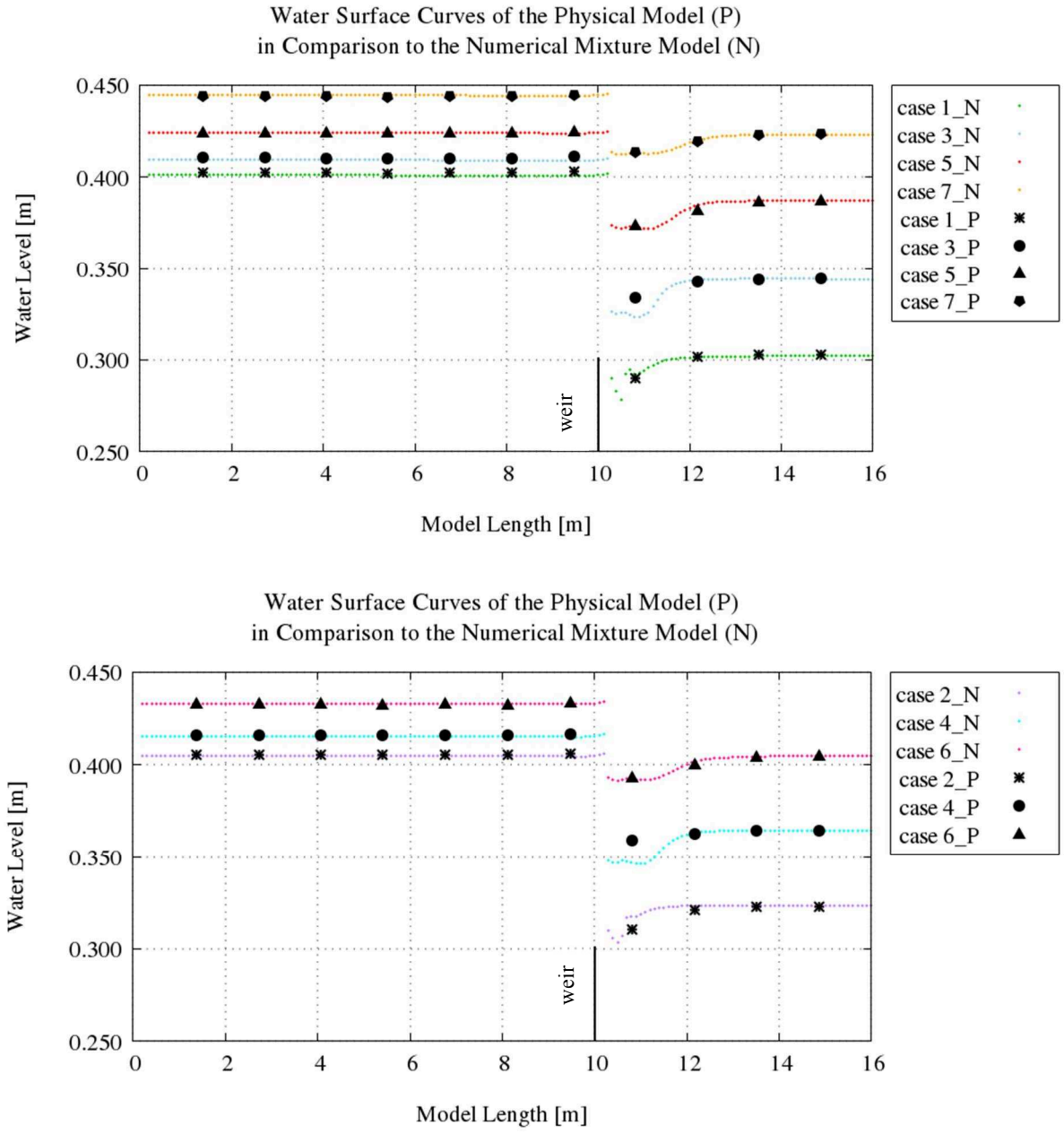

Figure 5.10: Comparison of the physical model tests with the simulation results

Considering the values of the first six upstream water probes, the difference between the time-averaged values of the physical model and the simulation is

less than 0.0017 m for case 1 to case 6. (Only case 7 showed larger deviations of 0.0035 m). In close proximity to the weir structure, higher deviations are observed. Upstream of the weir the physical model values are slightly higher than the numerical model results. The first probe upstream the weir structure shows a maximum difference of 0.0021 m. The first measuring point of the downstream side of the weir shows the largest deviations. In the cases 1, 2, 3 and 4 the water levels at this point are noticeable lower in the numerical model than in the physical models. A maximum difference of 0.0118 m was recorded. In these cases significant waves were observed behind the weir. The height of the waves decreases with increasing downstream water level. The occurring deviation between the models can be assumed to result from the different measuring systems. Whereas the physical model works with communicating vessels, the numerical model directly calculates the water level from the hydrostatic pressure. The measuring system of the physical model is assumed to be more inert than the direct measuring in the numerical model. Hence, fast wavy motions of the flow are differently recorded in the two systems. All other downstream measuring positions correspond well with maximum deviations of 0.0045 m.

In an additional simulation, case 4 was simulated with the standard volume of fluid solver of the OpenFOAM library. The received results from the interFoam solver were compared with the mixture model results. As expected, the results are very similar only showing negligible differences of less than 0.0011 m. This example demonstrates that both models depict the free surface flow with comparable accuracy.

5.2.4 Conclusion from the Test Variations

The modelling of the flow over a sharp-crested weir demonstrated that the mixture model is able to capture free surface flows. The comparison of the water surface curves of the mixture model simulations showed high concordance with measurements from a physical model. Small deviations are expected to result from errors of both models. The numerical model errors were minimized by increasing the mesh resolution and choosing appropriate discretisation schemes.

Inaccuracies in the physical model values can result from the measuring technique, which is not able to capture the exact water level height when the flow is very turbulent and wavy. Despite the small, inevitable differences the received results can be regarded as very satisfactory.

The subsequent comparison of the mixture model to a simulation with the standard VoF solver of the OpenFOAM library also showed convincing results. The received surface curves were almost congruent. The occurring differences were negligible.

6 Application to Navigation Lock Systems

The following test cases show how the developed model can be applied to investigate air transport and detrainment processes within navigation lock systems. The first case presents a case study with relevance for the design and optimization of navigation locks. In the second case, the comparison to physical model tests is paramount.

6.1 Air Transport and Detrainment in a Through-The-Gate Filling System

It is the aim of this test case to show an example application of the developed solver to a real-world engineering structure. In this test case the filling of a typical through-the-gate filling system is modelled, where strong air-water intermixing processes can be observed during the filling. The dimensions of the studied test case were adopted from the existent lock of Bolzum. The prototype structure connects the Mittelland Canal with the side canal of Hildesheim. It was built from 2007 to 2012 and initially operated in 2012. A schematic sketch of the lock filling system is shown in Figure 6.1. The lock has a usable length of 139 m, a width of 12.5 m and a lift height of 8.6 m. The upstream gate is constructed as segment gate. For filling, this segment gate is slightly turned to release the upstream water into the lock chamber. At the gate opening a free falling jet evolves. The falling jet plunges into a stilling zone where most energy

is supposed to be dissipated. A grid structured wall at the end of the stilling basin is expected to homogenize the flow towards the lock chamber. Through the plunging of the jet a lot of air is entrained into the lock chamber water during the filling process. Observations showed that the air degassing takes place in the front part of the lock, within the region where the ships are lying during the lockage. During the air detrainment large surface velocities were noticed in the air detrainment area. Until now it is unknown whether the air detrainment has an effect on the ships lying in the chamber. In the test case the effects of the air transport and detrainment on the flow field during the filling process are investigated. A large variety of simulations are performed with the new solver to show the correlations between air entrainment, the flow field and the forces acting on a ship in the lock. In the test series the water level in the chamber and the inflow discharge are kept constant.

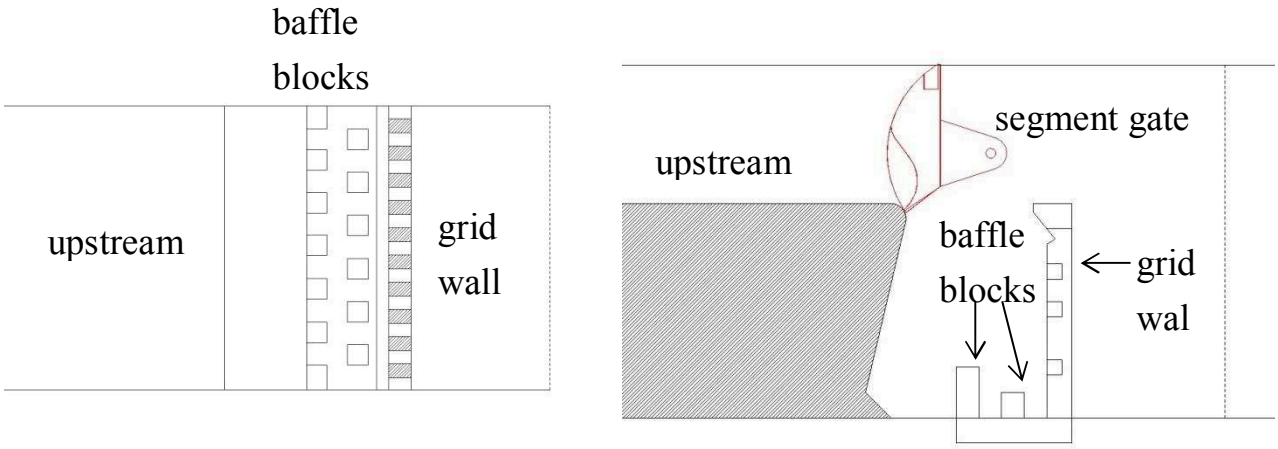

Plan view *Longitudinal section*

Figure 6.1: Sketch of the front part of the lock of Bolzum

With this setup the necessity for moving objects in the simulation is avoided and the effect of the air transport processes is evaluated independent from the complex transient processes resulting from the inflow rate gradients. A rough comparison of the resulting surface velocities in the simulations with video recordings from the Bolzum lock allows initial assessment of the air entrainment range. This leads to first conclusions about the influence of the air transport processes. Finally, the applicability of through-the-gate systems for larger lift

heights is analysed. As before, the focus is put on the evaluation of the influence of the air transport and detrainment processes.

6.1.1 Forces on a Ship in a Through-the-Gate Filling System

When a navigation lock is filled through the upstream gate, the resulting wave and flow phenomena generate longitudinal and transversal forces on the ship which are passed onto the mooring lines (PIANC InCom Working Group 155, 2015). The main hydrostatic forces on the ship result from the sloping water level along the hull in the lock chamber.

At the beginning of the filling process the first rise of the inflow rate provokes a slope pointing towards the downstream chamber wall. Hence, the water level on the upstream side of the chamber is higher than on the downstream side and the ship is forced in downstream direction. The slope can be considered as a shallow water wave, which propagates through the chamber. At the gates and partly at the hull the translatory waves in the chamber are reflected. Through the reflection, the longitudinal forces can change their direction during the filling process. Furthermore, the oscillating surge can be superposed and thereby decreased by the steadily growing inflow from the filling through the gate.

In addition to the hydrostatic forces due to the water level sloping, the ship is exposed to hydrodynamic forces. Those can result e.g. from the dynamic pressure of a jet impinging on the ship. Another effect that influences the ship forces during the filling is the reduction of the flow velocity from the upstream towards the downstream end of the lock chamber (Thorenz *et al.*, 2017). This reduction causes a slope towards the upstream of the lock chamber.

In most through-the-gate filling systems the hydrostatic longitudinal force is the main component of the total forces on the ship (PIANC InCom Working Group 155, 2015). For the dimensioning the direction of the forces is irrelevant; only the largest absolute force values on the ship are decisive. The temporal occurrence of the largest forces in through-the-gate filling systems without air entrainment is dependent on the geometry, the gate size, the gate opening and the resulting inflow gradients.

6.1.2 Forces in the System under Investigation

In this study, the dynamic filling process is not completely reproduced. To avoid movements of the ship during the simulation, a state with constant water level and fixed ship hull is considered. Therefore, forces resulting from the inflow rate gradient at the beginning of the filling process as well as the oscillation of the translatory waves are not considered in this study.

To create a quasi-steady state the water level is kept constant by inserting vertical inflow into the system at the upstream side of the wall and releasing the same amount of water through the bottom. The velocity in the chamber decreases with growing distance to the inlet. As a consequence the water level on the upstream side of the lock chamber is lower than on the downstream side. Neglecting the small velocities produced by the outflowing water, a force on the ship pointing towards the upstream wall is expected to result, when no air is influencing the system.

In the prototype system of Bolzum a significant amount of air is introduced into the lock system during the process of filling through the segment gate. Observations of the filling process lead to the assumption that the characteristic of the flow during the filling is significantly influenced through the air-water intermixing. It is the aim of this study to analyse the effect of the presence of bubbles inside the system. The results of the study are analysed in the following section.

6.1.3 Model Setup

Model Geometry

A three-dimensional geometry of the lock with prototype dimensions was used for the mesh generation. As the geometry is axisymmetric to the longitudinal axis, the model only reproduces one half of the lock. Figure 17 shows the geometry of the lock with the used symmetry axis. The model starts at the upstream lock chamber wall and ends with the downstream mitre gates; the upstream segment gate is not reproduced in the model. To evaluate the effect of

the bubble degassing on the ship forces, an inland vessel of 135 m length and 11 m width is positioned within the lock.

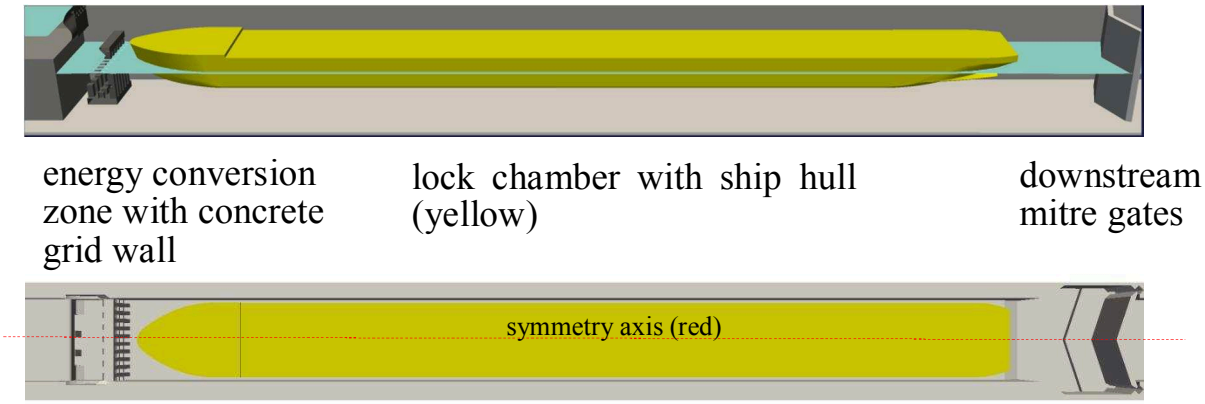

Figure 6.2: Three-dimensional geometry of the Bolzum lock with vessel

The bow of the vessel lies at the foremost position allowed during the lock operation. It is modelled as rigid solid body, which cannot move during the simulation. For the comparison of the water velocities at the surface additional cases without vessel geometry were created.

Mesh

To prove the suitability of the mesh resolution, a pre-study was performed where one case was simulated with four different mesh resolutions. In the mesh comparison study, the edge length in the front part of the lock was varied. The first case (in the following referred to as standard mesh) used the resolution as described below. For the additional three test cases the resolution in the water filled region was once coarsened by doubling the edge length, and refined by halving the edge length once, twice and three times. Comparing the resulting flow patterns in the velocity field, the pressure distribution as well as the air content transportation and degassing, the standard case and the finer mesh cases were very similar. The coarser mesh case showed deviations especially visible in the velocity distribution. The comparison of the resulting ship forces from the mesh-resolution pre-study showed small deviations between the standard and the finest mesh. Comparing the resulting flow patterns in the velocity field, the pressure distribution as well as the air content transportation and degassing, the standard case and the finer mesh cases were very similar. The coarser mesh case

showed deviations especially visible in the velocity distribution. The comparison of the resulting ship forces from the mesh-resolution pre-study showed small deviations between the standard and the finest mesh. Therefore the standard resolution was considered as best compromise between accuracy and consequential time-step size.

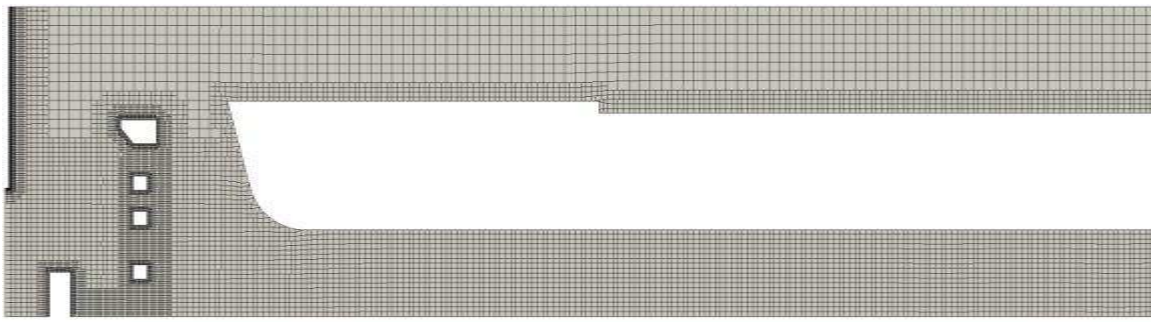

Figure 6.3: Illustration of the mesh resolution in the front part of the lock on a vertical section plane

The standard hexahedral-dominant mesh consists of approximately two million cells with a basis edge length of 0.5 m. The water filled region in the front part of the lock the space was discretized with cubic cells having an edge length of 0.25 m. In proximity to the structure cells are refined three times up to edge lengths of approximately 0.0625 m. Especially in the region around the inlet boundary, very fine discretisation was necessary, to allow an accurate definition of the inlet width. Figure 6.3 illustrates the different discretisation zones in the front part of the mesh. All meshes were created with the OpenFOAM meshing tool `snappyHexMesh`.

Boundary Conditions

The simulations are intended to enable statements about the influence of the entrained air on the ship forces during filling. With the new model, the air transport and degassing processes can be modelled. However, the air entrainment process through the plunging jet cannot be captured suitably. For this purpose a direct numerical simulation of the jet and the entrainment process would be necessary, which is not feasible with reasonable resources. Instead, the jet is omitted and replaced by an inlet boundary condition.

In this study, only steady states are considered, meaning that the water in the chamber is held on one level. Therefore, the bottom patch of the lock is defined as an outlet boundary. The flow rate out of the bottom patch is set equal to the inflow rate at the inlet. The flow rate out of the bottom is small compared to the large release area of the chamber bottom. Therefore, the resulting velocities in the lock chamber towards the bottom can be neglected.

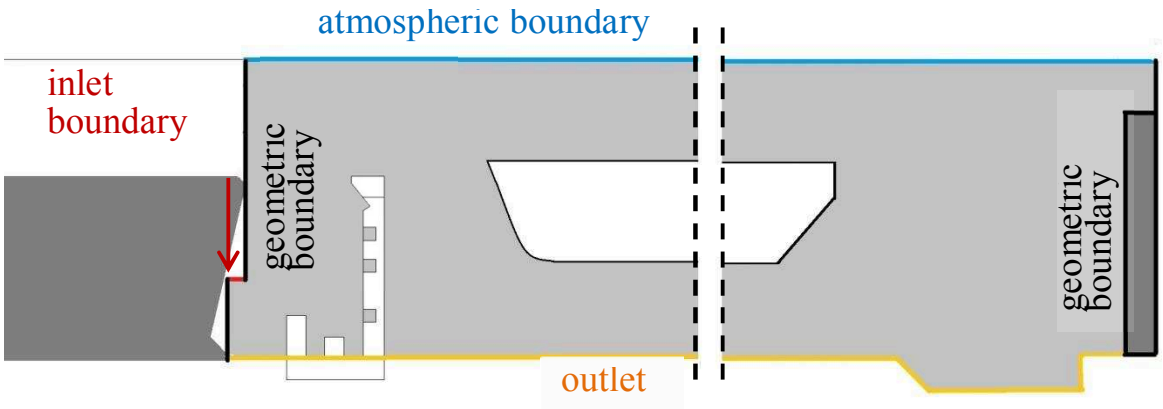

Figure 6.4: Sketch of the boundary conditions for the lock filling simulations

The side wall of the lock and the mitre gate are modelled as wall boundaries. The patch at the longitudinal axis is defined as symmetry plane. The top patch is modelled as open boundary, defining an atmospheric pressure condition. For turbulence modelling, a k-omega SST RANS model is applied.

Model Variants

In this study two water levels in the lock were investigated. The setup conditions of the two cases are summarized in Table 6.1.1. An illustration of the two cases can be found in Figure 6.5. The first water level represents a situation at the beginning of the filling process, when the inflow starts rising steadily and the water cushion below the ship is still very small. In the modelled case, the water level in the lock chamber is 4.5 m. With a draught of 2.80 m the water cushion below the ship bottom has a height of 1.70 m. The second water level represents a situation towards the end of the filling process. At this stage of the filling process the inflow rate should already be very high to allow a fast filling. At the same time a free falling jet in the front part of the lock is still evolving. The

remaining falling height for the jet is 6 m. The water level in the chamber is 6.6 m and the water cushion below the ship has a height of 3.20 m. For the simulations the Bolzum lock geometry (as described above) with a total lift height of 8.6 m was used.

To test the influence of the entrained air content all cases were simulated with four different inlet conditions. The following four variants of the volume fraction at the inlet boundary were defined with: 1.0, 0.9, 0.8 and 0.7. The test matrix was further extended with variants of the discharge to evaluate the influence of the discharge on the ship forces. The test cases were simulated with an inflow of 10 m³/s, 20 m³/s and 30 m³/s. The discharges were applied to the half model.

Table 6.1.1: Case setup conditions

Case name	Remaining lift height [m]	Water level in the chamber [m]	Total lift height [m]
Case 1	8.1	4.5	8.6
Case 2	6	6.6	8.6

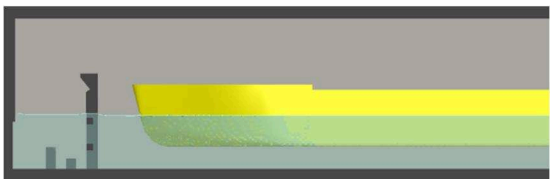

Case 1: At the beginning of the filling process

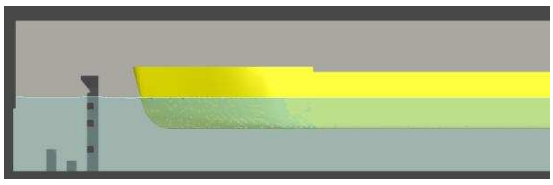

Case 2: Towards the end of the filling process

Figure 6.5: Illustration of the test cases

To test the influence of the entrained air content all cases were simulated with four different inlet conditions. The following four variants of the volume fraction at the inlet boundary were defined with: 1.0, 0.9, 0.8 and 0.7. The test matrix was further extended with variants of the discharge to evaluate the influence of the discharge on the ship forces. The test cases were simulated with an inflow of 10 m³/s, 20 m³/s and 30 m³/s. The discharges were applied to the

half model. From the variations of the flow rate and the inlet air-water distribution 16 simulations result for each setup.

6.1.4 Analysis and Evaluation of the Numerical Model Results

All simulations were performed in parallel on 20 processor cores. After a total simulation time of approximately 800 s changes in the flow field were small so that the results can be considered as quasi-steady. Thus, this state is considered as steady state result for the visual analysis. For the quantitative analysis of the ship forces the simulations were performed for 1500 s and the values were averaged over the last 500 s. The analysis of the results showed that the presence of air within the filling system has major impact on the flow characteristic. As a consequence the ship forces are also affected when air is intermixed into the flow.

Analysis of the Flow Characteristics

The numerical simulations with the new solver allow a detailed insight into the flow characteristic during the filling of the system under investigation. Visualisations of the velocity field and the volume fraction distribution for a water inflow rate of 20 m^3/s are shown in 6 and Figure 6.7. The visualisation of all further results of the simulations can be found in the appendix A.6.

In the model a defined air-water mixture inflow rate is released via the inlet boundary area into the filling system. Due to orientation of the impingement area perpendicular to the water surface the inflow is initially transported towards the lock chamber bottom. The incoming jet is deflected at the bottom and the first row of baffle blocks. Subsequently, a vortex forms in the front part of the stilling area. The vortex formation dissipates a part of the kinetic energy of the flow. The remaining kinetic energy leads the flow through gaps between the remaining baffle block towards the concrete grid wall. Without air entrainment homogenized flow is supposed to be released through the grid wall pointing in downstream direction.

In the simulations of Case 1 (state at the beginning of the filling process) it is visible that without air entrainment at the inlet the water is released through

the gaps in the grid wall at two different heights, forming two jets towards the ship. At the ship bow the upper jet is deflected towards the chamber bottom. With growing inflow rate the velocity of the jets and the velocity of the flow below the ship bottom increase. When the flow contains air, the density difference between air and water applies an upward pointing force component to the flow. As a consequence, the upper jet which is released at the bottom of the grid wall gets stronger; higher velocities are visible over a larger width. The lower jet is deflected towards the water surface. Additionally, the water level on the upstream side rises with growing air volume and the velocity below the ship hull increases. Thus, higher air content leads to growing water level slopes towards the downstream end of the lock chamber. From the visualisations of the velocity field it is visible that the velocity grows with increasing air content even if the inlet velocity and the water inflow rates are constant. The illustrations of the air-water distribution show that larger inflow rates lead to longer transport of the entrained air bubbles with the flow. For the water inflow rate of 10 m^3/s hardly any air reaches the hull. With an inflow rate of 30 m^3/s a large amount of bubbles surrounds the ship bow and accumulate below the hull.

In the simulations of Case 2, where the water level in the chamber is higher, the inflow can spread over a larger area. As a result, the velocities in the vortices and the jets are smaller than for lower water levels. Otherwise, the simulations with the higher water level show the same tendencies: with larger inflow rates the velocities in the system increase. Without air entrainment at the inlet, the flow distributes over the complete height of the water body and the velocities at the ship hull are small. The entrainment of air at the inlet leads to growing velocities in the stilling area and to stronger jets in the upper region behind the grid wall. Also the velocities below the ship hull rise, when more air is present within the water body.

The screenshots in the left column of Figure 6.6 and Figure 6.7 show the water-air distribution. The screenshots on the right in the named figures show the velocity distribution in the front part of the lock projected on a vertical slice parallel to the symmetry axis. The slice was located at a distance of 1.35 m from the middle axis.

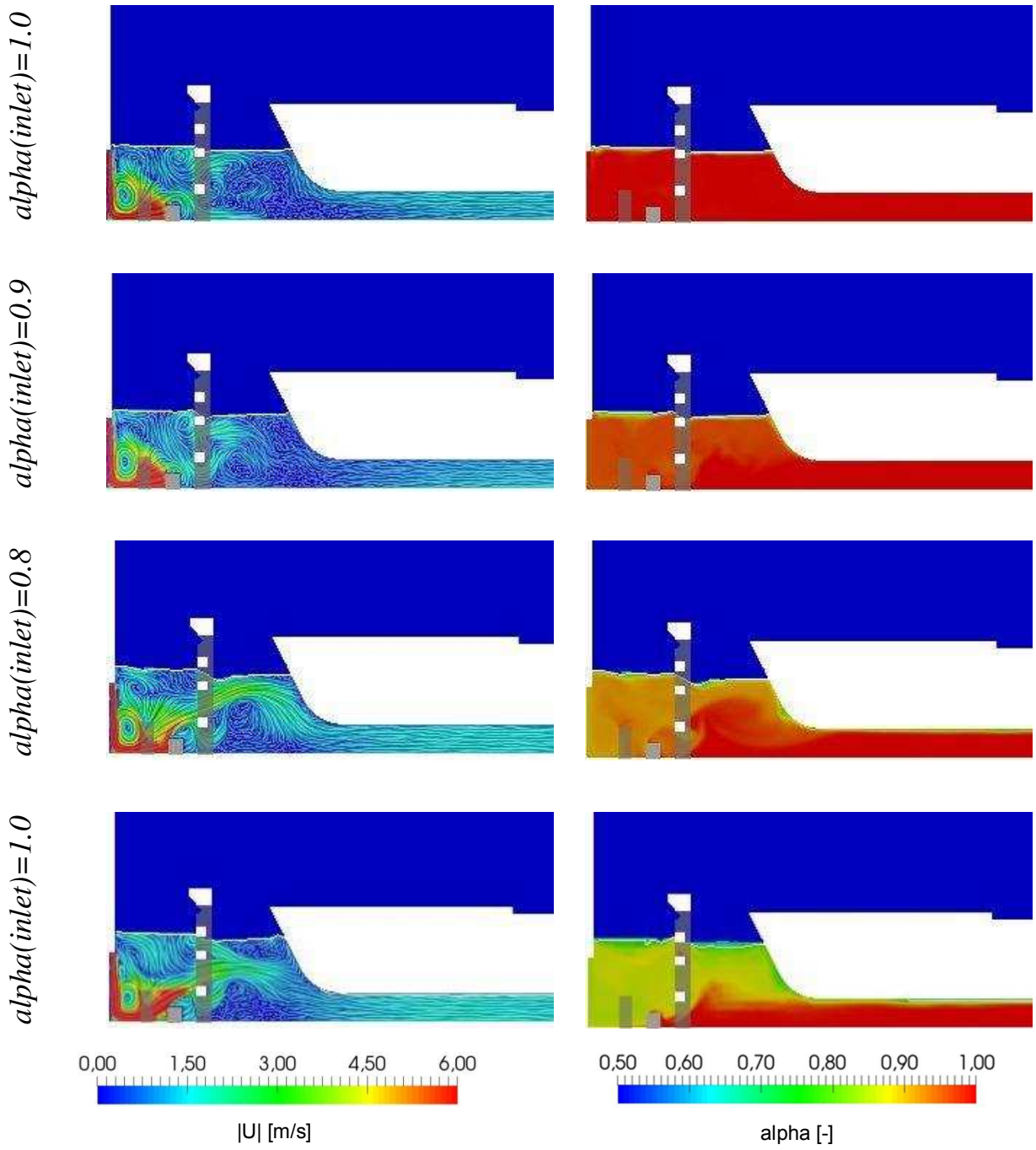

Figure 6.6: Results from the simulations of Case 1 with an inflow discharge of 20 m³/s

Case 2 – Q = 20 m³/s

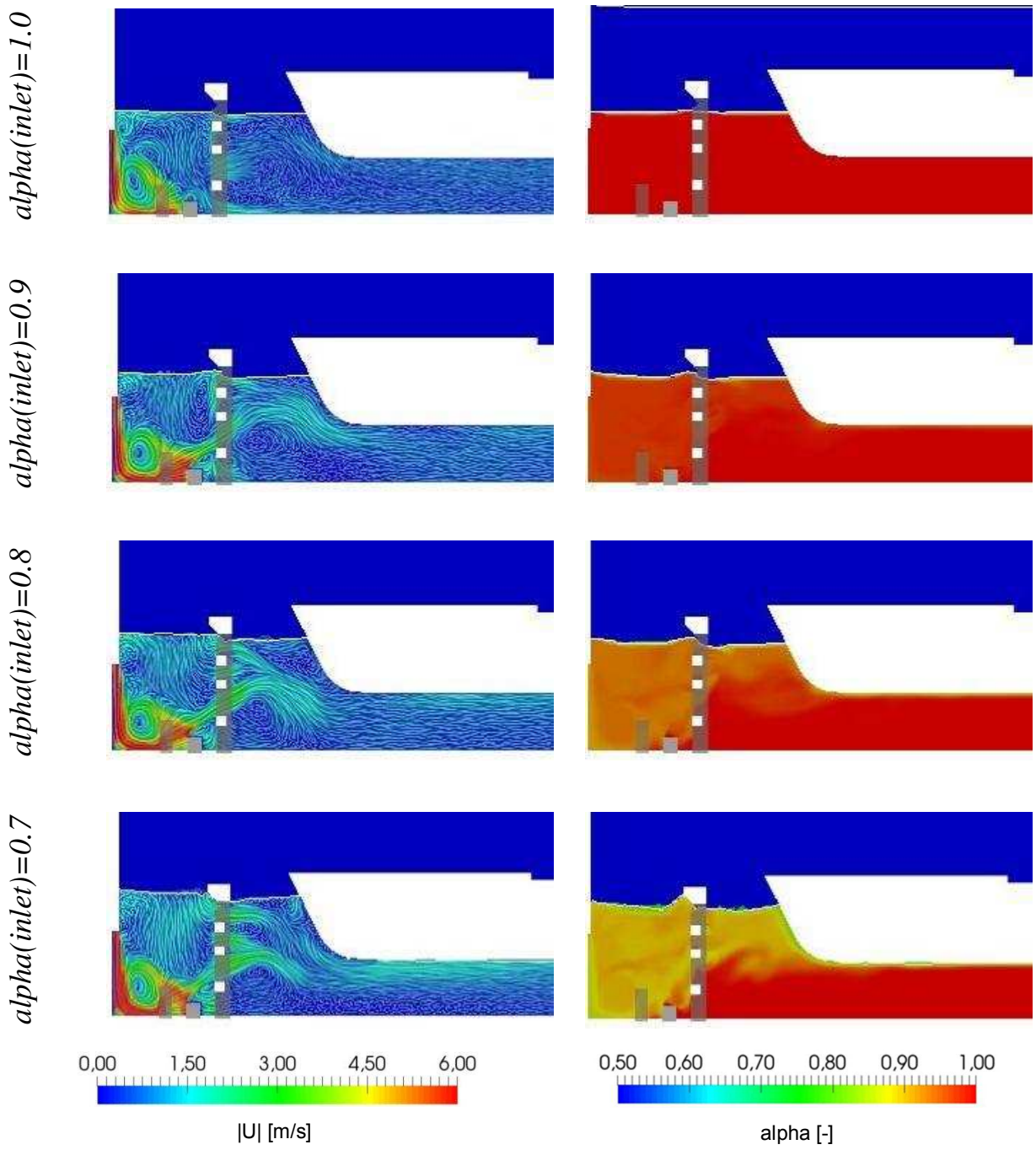

Figure 6.7: Results from the simulations of Case 2 with an inflow discharge of 20 m³/s

Analysis of the Ship Forces

Quantitatively, the influence of the air transport and degassing processes can be captured by measuring the forces on the ship. As the longitudinal forces are much larger than the transversal forces on the ship, only the longitudinal forces were considered in this study. The quantitative results of the ship forces in the numerical simulations are illustrated in a diagram shown in Figure 6.8. The number values can be found in the appendix A.6.

When evaluating the absolute values of the ship forces resulting in the tested scenario, it should be noted that in Germany the forces on the tested ship are usually limited to 23 kN (cf. Partenscky, 1986). The Netherlands allow forces up to 29 kN. When the when the lock is equipped with inset bollards forces up to 39 kN are accepted in the Netherlands (PIANC InCom Working Group 155, 2015). Only when the forces on the ship range in or above the order of the given limits, the influence of the air-water transport and degassing processes can be expected to have relevant influence for the design and the functionality of the ship lock. Considering the given limits it can be concluded, that the air intermixing does not have significant influence on the ship forces in the tested setup, if the inflow rate for the half model is not larger than 10 m^3/s and the maximum air entrainment rate at the inlet is limited to 30 %. Furthermore, the results showed that air contents up to 10 % should be uncritical for the ship forces, when the maximum inlet rate is limited to 30 m^3/s for the half model. Additionally, the results of show that the forces on the ship in the lock system under investigation mainly depend on the following factors:

- air content,
- inflow rate and
- remaining lift height of the inflow jet.

Influence of the Air Content

Looking at the diagrams of Figure 6.8 following tendency can be concluded: growing air contents lead to increasing forces on the ship towards the downstream end of the chamber. The downstream pointing forces result from two effects. On the one hand the forces result from the concentrated velocity jet in the upper water body behind the grid wall, which pushes the bow of the ship towards the downstream end of the lock chamber. The jet gets stronger with growing air content and in all cases where this jet reaches the ship hull, additional rising of the forces can be observed. On the other hand the air entrainment leads to a rising water level in the front part of the lock. As a consequence the water level slope and the resulting ship force towards the downstream end of the lock grow with increasing air content.

Influence of the Inflow Rate

In this study each setup was tested with three inflow rates. The evaluation of the simulation shows that an increasing inflow rate leads to higher forces on the ship. When the flow rate is increased the horizontal velocity component of the flow in front part of the lock gets larger, whereas the vertical velocity component induced by the air is not influenced. In the case where no air is introduced into the system, the higher horizontal velocities in the front part of the lock lead to a larger water level slope towards the upstream end of the chamber. As a result the forces towards the upstream end (marked as negative forces in the current notification) get larger with growing inflow rates when no air intermixing is present. With the introduction of air at the inlet the aerated jet extends further into the lock chamber towards the ship hull when the inflow rate is increased. Thus, higher inflow rates produce higher positive ship forces towards the downstream end of the lock chamber when air is present within the flow.

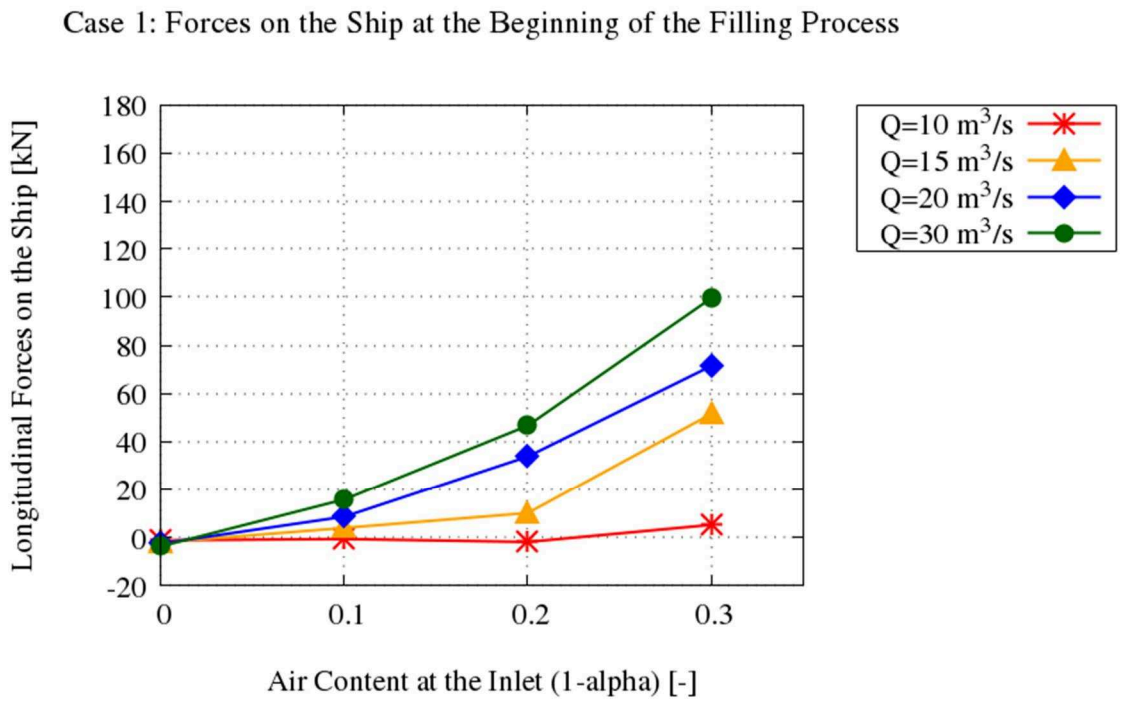

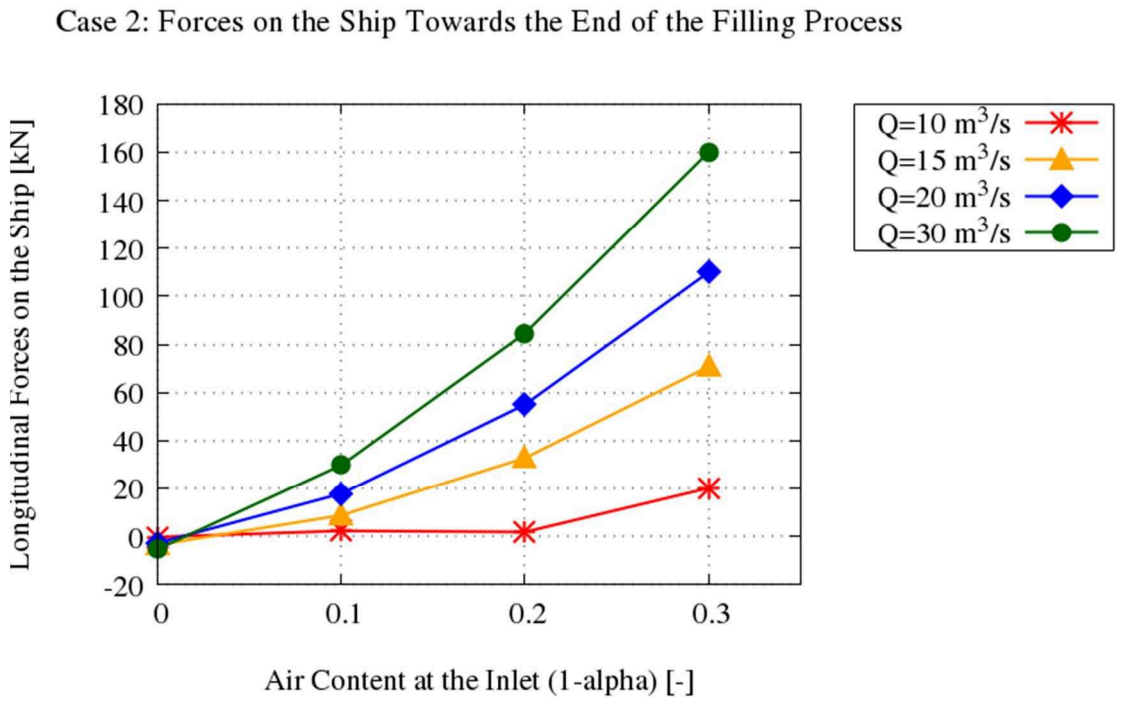

Figure 6.8: Case 1 and Case 2: Forces on the ship dependent on inflow rate and air content

Influence of the Chamber Water Level

When the results of the two cases are compared it can be seen that the forces on the ship resulting from the air transport and detrainment processes are higher in towards the end of the filling process than at the beginning of the filling process. Considering two cases with same inlet conditions (inflow rate and air-water ratio) it can be seen that the absolute water level rise in the front part is larger in Case 2 than in Case 1. Consequently, a larger water level slope results in Case 2 which leads to higher forces on the ship.

6.1.5 Transferability of the Results to the Prototype Structure

To allow conclusions from the results of this study for the prototype structure information about the inflow conditions is inevitable. Especially the knowledge about reasonable inflow rates and realistic air contents is necessary. From the commissioning of the prototype lock in Bolzum three video recordings exist. Additionally, recordings of the water levels during the filling are available, which allow the calculation of the associated inflow rates. In the commissioning test, the lock inflow was phased with three constant inflow rates. In the video recordings the air degassing zone is clearly recognisable from the white crest in the front part of the lock. Three different degassing zone lengths related to the three inflow rates of 7.5 m³/s, 12.5 m³/s and 22.5 m³/s can be clearly distinguished in the videos. From the video recordings of the filling process of the lock in Bolzum the surface velocities in the detrainment zone were estimated for the highest inflow rate.

For a comparison, numerical simulations with the highest inflow rate of 22.5 m³/s (equates to 11.5 m³/s for the half model) and a water level in the chamber of 6.5 m was set up. The simulations without a ship were performed with four different inlet air-water ratios: 1.0, 0.9, 0.8 and 0.7. Comparable to the simulations of the test cases described in section 6.1.4 the simulations were calculated until a quasi-steady state was received. As result the velocities on a plane slightly below the water surface were evaluated. A comparison with the surface velocities resulting in the numerical simulations allows the assumption that the air-water ratio in the intermixing zone ranges between 0.8 and 0.9.

Looking at the results of the test cases in the previous section 6.1.4, it can be assumed, that with an inflow rate maximum of 22.5 m³/s the air transport and detrainment processes only have minor impact on the ship forces in the prototype structure. Inflow rates up to 30 m³/s (corresponding to 15 m³/s for the half model) can probably be realized for the prototype structure of Bolzum without provoking critical ship forces on the vessel used. This first conclusion gives a good starting point for future investigations of air transport and detrainment processes in through-the-gate lock filling systems with construction characteristics and lift heights similar to those of the lock of Bolzum.

For making final statements about absolute values occurring in the lock system of Bolzum, field measurements are indispensable. In the model used the inflow rate and the air content at the inlet have to be defined as boundary conditions. Unlike the inflow rate, which is a controllable quantity in the prototype structure, the value of the air content is an uncontrolled, unknown quantity. To get reliable results, the order of magnitude of the entrained air dependent on the lift height has to be determined with the means of field measurements. Alternatively, an entrainment model for the numerical approximation of the air entrainment through the plunging jet would have to be developed and implemented.

6.1.6 Applicability to Larger Lift Heights

Through-the-gate filling systems are mostly applied to locks with lift heights smaller than 10 m. Due to the relatively small building and maintenance costs in comparison to more complex filling systems it would be desirable to allow the application of through-the-gate systems also to larger lift heights. To investigate the applicability to larger lift heights, the lock system of Bolzum was enlarged to a lift height of 18 m. For that the grid wall and the lock chamber walls where extended in vertical direction. In the lower part of the grid wall the horizontal bars have the same spacing as in the Bolzum lock setup. In the upper part of the extended grid wall the horizontal bars were inserted with regular spacing.

Table 6.1.2: Case setup conditions

Case name	Remaining lift height [m]	Water level in the chamber [m]	Total lift height [m]
Case 3	17.5	4.5	18
Case 4	6	16	18

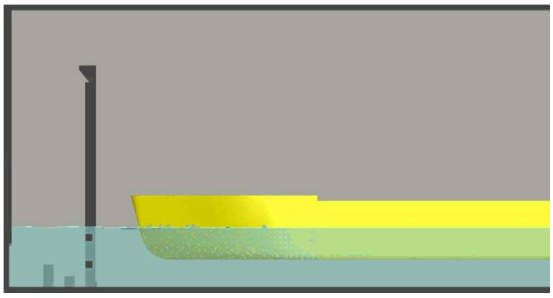

Case 3: At the beginning of the filling process

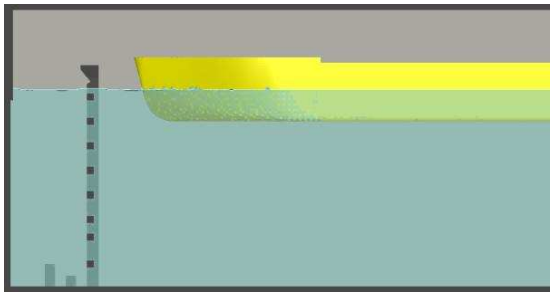

Case 4: Towards the end of the filling process

Figure 6.9: Illustration of the test cases

As in the previous test cases described in section 6.1.4 a constant state is simulated and the focus is put on the analysis of the effect of air entrainment and transport processes. The model setup is similar to Bolzum lock study: to save computational effort a half model is used. The falling jet is replaced by an inlet boundary condition, which inserts a pre-defined inflow rate with a specified air-water ratio into the system. The inlet boundary area is adapted for each simulation, so that a calculated inflow velocity is received. For the calculation of the suitable inflow velocity, it is assumed that the potential energy of the upstream water is converted into kinetic energy by the falling jet.

Model Variants

In this study, the three inflow rates of 10 m³/s, 20 m³/s and 30 m³/s for the half model and four air-water ratios at the inlet boundary of 1, 0.9, 0.8 and 0.7 were tested. All inflow setups are tested with two different filling states. Table 6.1.2

summarizes the setup of the two cases. The first water level of 4.5 m represents a state at the beginning of the filling process. The remaining lift height is 17.5 m. In the second configuration, a state towards the end of the filling process is simulated. The remaining falling height of the jet is 6 m and the chamber is filled up to a height of 16 m above the chamber bottom.

Analysis of the Flow Characteristics

The resulting velocity and volume fraction distributions for a water inflow rate of 20 m^3/s are exemplarily shown in Figure 6.10 and Figure 6.11. The visualisation of all further results can be found in the appendix A.6.

With large total lift heights as those simulated in Case 3 and Case 4 the flow characteristics show significant differences between the beginning and the end of the filling process. At the beginning of the filling process (Case 3), the flow fields are similar to those resulting with the setup of Case 1, where the water level is equal but the total lift height equals 8.6 m. The volume fraction plots show that the entrained air-water mixture distributes throughout the complete dissipation zone. Only behind the second row of baffle blocks pure water is visible. The transport length of the bubbles with the flow is strongly dependent on the inflow rate: the larger the inflow rate, the stronger gets the horizontal velocity component towards the chamber. Thus, with larger inflow rates and constant bubble diameter the bubbles are transported further into the chamber. The illustrations of the velocity distribution show that the larges inflow velocities occur at the inlet, where the inflowing air-water mixture enters vertically. Where inflowing jet reaches the bottom it is first deflected in downstream direction and then again redirected at the first row of baffle blocks towards the surface. As a consequence a vortex forms behind the first baffle block row. A part of the flow which flows between the baffle blocks forms a jet which is slightly deflected in diagonal direction by the second row of baffle blocks. The jet reaches the grid wall and finds its way through the gaps. Most of the flow is released above the first vertical beam of the grid wall, forming a horizontal jet towards the bow of the ship. With growing air entrainment at the inlet or growing water inflow rate, the jet is getting stronger. At the bow the jet

is redirected below and to the sides of the ship. As the ship hull occupies a large volume of the cross section, the velocity below and at the sides of the ship increases. With larger air contents and/or larger inflow rates, this phenomenon intensifies.

Towards the end of the filling process (Case 4), the inflowing velocity correspondent with the smaller remaining falling height is smaller than at the beginning of the filling process. Additionally, the distance from the inlet to the bottom is much larger than in the beginning. Hence, the resulting velocities in the energy dissipation zone are smaller than at the beginning of the filling process. Without air entrainment at the inlet the inflowing water forms a large vortex in the energy dissipation zone, which is deflected at the bottom and at the baffle blocks. The velocities behind the grid wall are small and most flow is released through the bottom part of the grid wall. When an air-water mixture is entrained at the inlet, the forming vortices get shorter as the inflow is redirected before reaching the bottom. Through the introduction of air, a vertical velocity component opposed to the gravitational force is applied to the flow. With growing air content, the upward force rises. As a consequence, the incoming jet is redirected towards the surface before reaching the bottom.

In most cases with air entrainment, the flow is again deflected at the water surface forming a second vortex within the energy conversion zone. Most of the flow is released in the upper part of the grid wall, when air is present in the flow. The resulting jet towards the bow of the ship gets stronger with growing air content and increasing water inflow rate. It can be concluded, that the large water cushion below the ship cannot dampen the impact of the inflow when air is present.

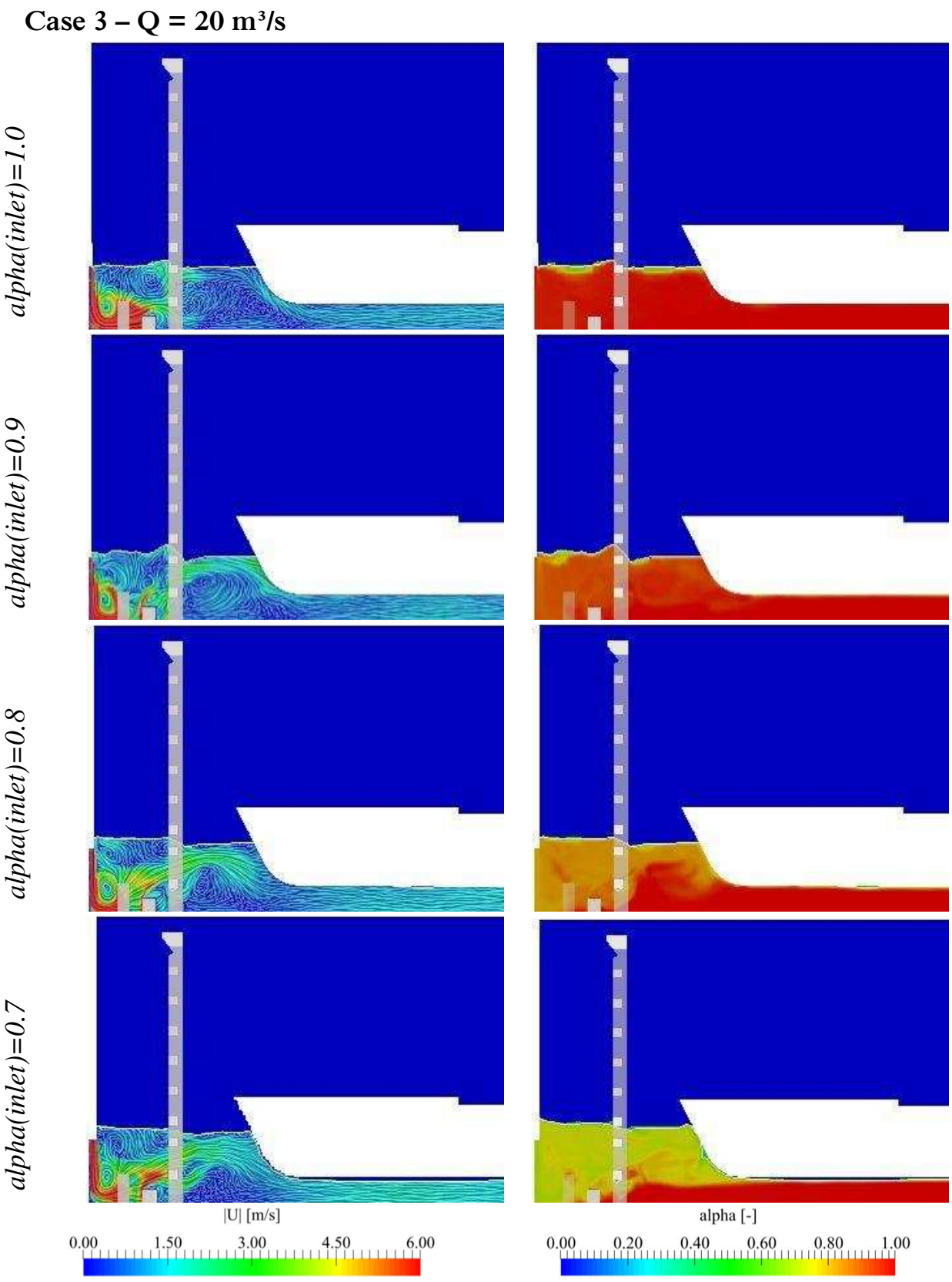

Figure 6.10: Results from the simulations of Case 3 with an inflow discharge of 20 m³/s

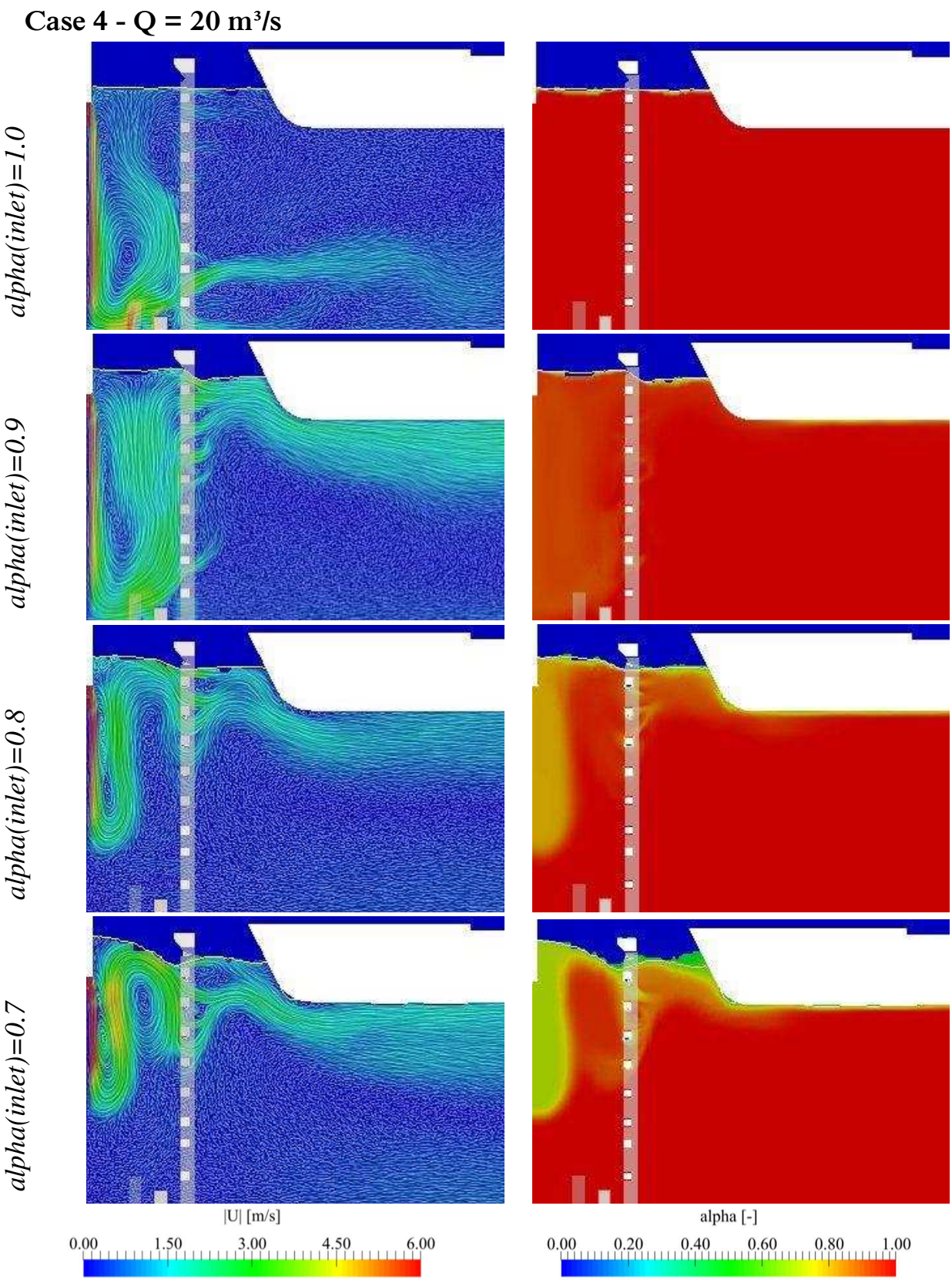

Figure 6.11: Results from the simulations of Case 4 with an inflow discharge of 20 m³/s

Analysis of the Ship Forces

All simulations were run until a quasi-steady state was reached. Then, the ship force measurement was started and averaged over 500 s. The results are presented in the following diagrams shown in Figure 6.12. The associated number values are listed in the appendix A.7.

The evaluation of the ship forces show comparable tendencies as the simulation results from the previous study (cf. section 6.1.2): with growing air content and growing inflow rates, the forces on the ship increase. Without air entrainment the forces on the ship point in the upstream direction. In the shown diagram, these forces are defined as negative forces. Air entrainment leads to rising water levels in the front part of the chamber. The consequent water level slope towards the downstream end of the chamber leads to positive forces on the ship.

In comparison to the smaller lift height studied in the previous section, the larger lift height leads to the following differences: inflow velocities at the beginning of the lock filling process are higher for the larger lift height, corresponding to the larger remaining lift height. The difference between the inflow velocities results in slightly stronger forces on the ship for the larger lift height (Case 3). Towards the end of the filling process, the remaining lift height of the cases is equal in both cases. However, the water cushion is much larger in the cases with larger total lift height. The larger water body below the ship has a dampening effect on the ship forces. Thus, the forces on the ship are smaller for the case with the larger lift height (Case 4).

When comparing the two lift heights it must be noticed that in reality the inflow air-water ratios are likely to vary significantly between the cases with different total lift heights. With growing falling length of the water jet, a higher air entrainment volume is presumable.

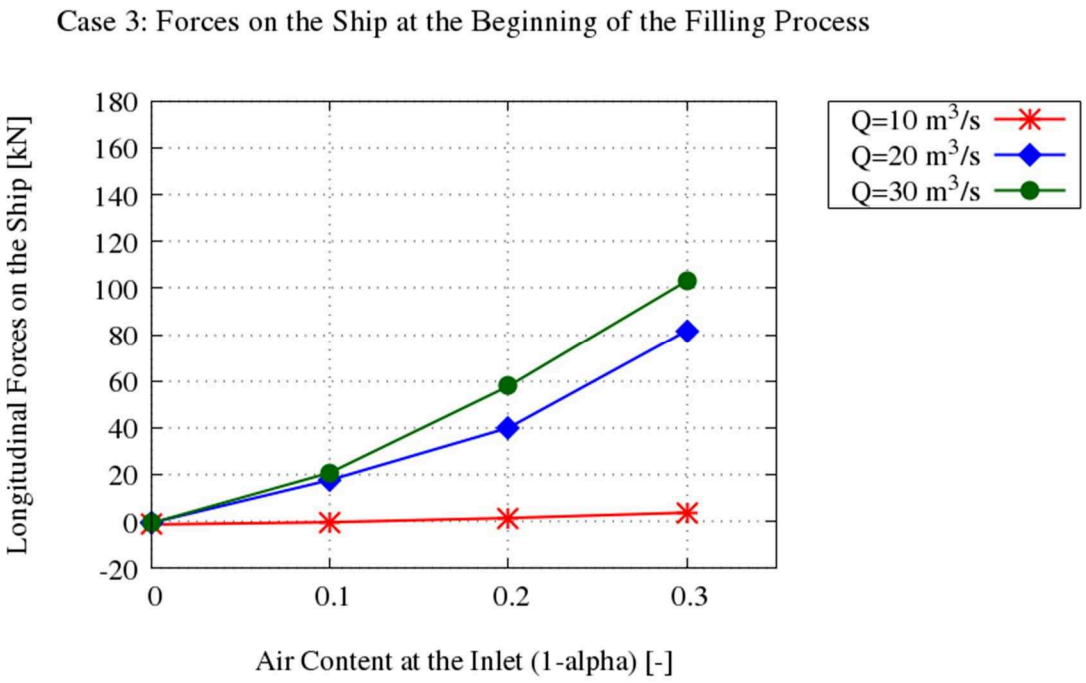

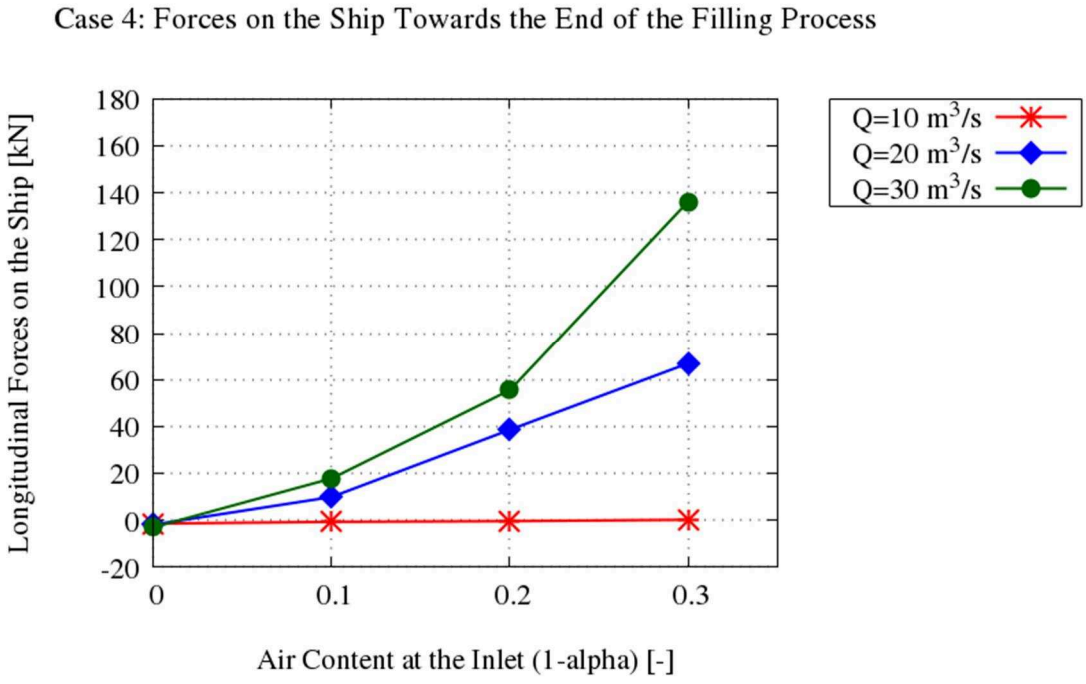

Figure 6.12: Case 3 and Case 4: Forces on the ship dependent on inflow rate and air content

Due to the lack of a correlation between the falling height of a wide large vertical plunging jet and the resulting air entrainment rate, quantitative conclusions for larger lift heights cannot be made. However, the model provides the opportunity of finding an inflow rate for the larger lift height system, where air entrainment is completely irrelevant for the forces on the lock.

Looking at the absolute values of the resulting ship forces it can be concluded that water inflow rates up to 10 m^3/s are uncritical, when the air entrainment is not larger than 30 %. When the air entrainment at the inlet stays below 10 %, the contribution of the air-water intermixing to the ship forces is below the common limits for the given setup.

6.1.7 Uncertainty Factors

The uncertainty of the results in the current study is mainly influenced by the following factors:

- geometrical uncertainty due to the geometry simplification and the spatial mesh configuration,
- boundary data uncertainty due to the estimated inflow conditions,
- numerical uncertainty due to the usage of discretization schemes for the evaluation of the model equations and the RANS turbulence model and
- physical approximation errors due to uncertainty in the formulation and simplifications in the model.

For the benefit of acceptable simulation times a rather coarse mesh resolution was chosen for the current study. Cells were refined such that the main character of the flow was preserved. During the mesh generation particular effort was put into the accurate reproduction of the geometry of the stilling area and of the ship hull, as this is significant for the force calculation. Due to the high pre-processing effort and the high probability of bad mesh quality, boundary layers around the ship for the accurate reproduction of the surface friction were omitted. This is acceptable as form drag is assumed to be dominating the flow situation, whereas surface friction can be neglected. Special focus was further put on the creation of the inlet boundary area, as the size of the boundary area

defines the inlet velocity and thereby represents the falling height of the jet. Due to the mesh creation algorithm it is yet challenging to meet the aspired width. Thus, deviations for the area width up to 10 % were defined as acceptable for this study. Comparing the results of the numerical model with the prototype structure the inlet boundary definition with the specified air content and the inlet velocity is the major factor for uncertainty of the results. The range of reasonable air contents had to be estimated. Field measurements are necessary to improve the knowledge about the real conditions. The feasibility of the results is further influenced by the accuracy of the numerical schemes used for the discretization of the equations. Theoretically, the chosen schemes for the discretization of the divergence terms are of higher order and promise total variation diminishing properties (cf. section 4.2.2). In non-orthogonal three-dimensional meshes this is not guaranteed (Denner and van Wachem, 2015). Nevertheless numerical errors are assumed to be small compared to the resulting total values.

6.1.8 Conclusions

The study described above showed the application of the developed solver to investigate the features of a hydraulic engineering structure significantly influenced by air entrainment, transport and detrainment processes. In the navigation lock under investigation, the filling process is initiated by opening the head segment gate. A free falling jet evolves and plunges into the stilling area in the front part of the lock. Through the plunging jet air is entrained into the lock chamber, which substantially impacts the hydraulic properties of the system. Due to the lack of investigation methods, the consequences of the air intermixing were unclear heretofore.

Influencing Factors for the Structure Design and Operation

From the performed simulations, correlations between various influencing factors valuable for the structure design and operation were found. It was shown, that the air entrainment significantly influences the relevant hydraulic properties in the given navigation lock system during the process of filling. An increasing

air content in the system leads to growing longitudinal forces on the ship. The inflow rate shows a comparable tendency: raising the inflow rate results in larger forces on the ship. The information gained can for example be used to develop optimized structure designs for future projects or even to create more effective operation modes for the existing system.

Performance of the Solver

Regarding the stability during the computation of the simulation results, the solver showed a satisfactory performance comparable to standard solvers of the used C++ library OpenFOAM. No exceptional abortions nor under- or overshoots were observed during the execution of the large case study. Stable calculations were achieved by limiting the Courant number to values below 1. In most cases, Courant numbers of up to 2 were still leading to a stable calculation. The increase of the Courant number limitation was proven to be useful in the beginning of a simulation, to speed up the phase from initialization until a quasi-steady state is achieved.

6.2 Air Transport and Detrainment Processes in a Complex Lock Filling System

6.2.1 Project Background

In the following test case the filling process of a navigation lock system was simulated. The modelled lock system represents a new filling system proposed by Thorenz (2012). A sketch of the system is shown in Figure 6.13. The new system was developed during the planning phase of two structurally identical locks for the Maine-Danube-Canal (MDK) which have to be replaced in the next years. Both locks have a lift height of approximately 18 m, a length of 200 m and a width of 12.50 m. For inland waterway ship locks with lift heights larger than 10 m, it is state-of-the-art not to fill the lock through the gates, but to provide a special filling and emptying system containing several culverts and channels that homogenise the filling flow over the length of the chamber in order to ensure as little water level oscillations as possible.

The proposed system includes a pressure chamber beneath the actual lock chamber. Both chambers are connected through small cylindrical filling nozzles that guide the filling water into the chamber. The three laterally-arranged stepped water saving-basins are connected to the pressure chamber by channels that meet the pressure chamber in the third sections of the length. Approximately 60 % of the water needed for the lock filling from the downstream water level to the upstream water level is provided by the saving basins. The remaining 40 % are taken from the upstream water canal. In the proposed system a drop shaft connects the upstream water level with the pressure chamber.

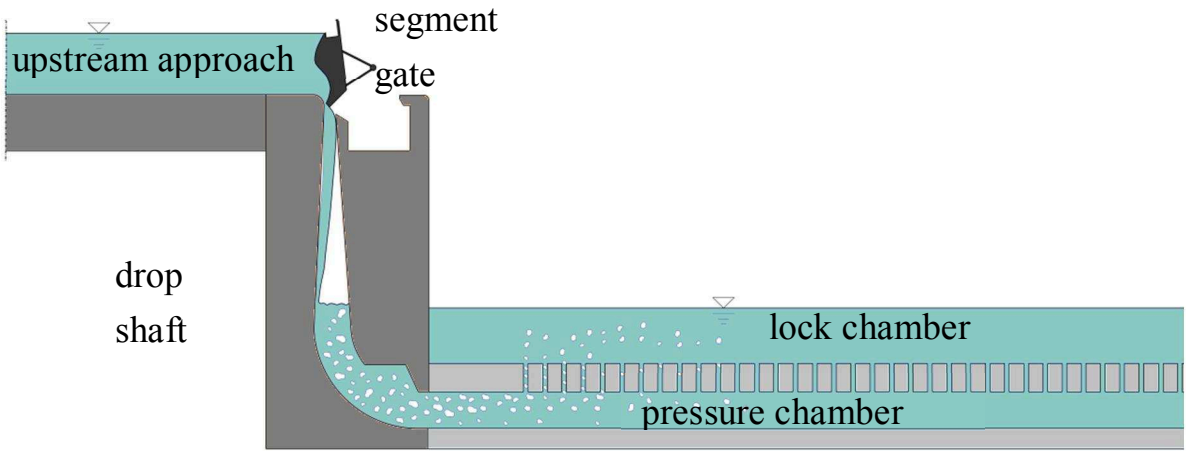

Figure 6.13: Schematic sketch of the lock filling system under investigation

The upstream lock gate, a segment gate, serves as a seal and controller gate for the drop shaft. By turning the gate counter-clockwise, the shaft is gradually unblocked and the water can drop through the shaft into the pressure chamber. After the filling process has been completed, the segment gate can be turned on until it reaches the opening position, so that the ships can vacate the lock chamber.

Before starting the rotation of the gate, the drop shaft is partly filled with air. As soon as a gap from the shaft to the canal is released, the water starts falling into the shaft, reaching the plunging pool at the height of the water level in the lock. Arriving at a relatively high vertical downward velocity, the plunging water jet is likely to entrain a significant amount of air into the system.

Since air entrainment can severely influence the flow properties and consequently the hydrodynamic effects on the structure and the ship, the knowledge about the quantity and the impact on the locking process is crucial for the feasibility of the new system.

6.2.2 Relevant Air-Water Flow Patterns for the Lock Filling System

For the investigation of the lock filling process different flow patterns have to be analysed. The free surface flow from upstream of the lock enters the filling system through the drop shaft. When the water drops into the shaft, a free falling jet evolves. At the bottom of the shaft, the decayed jet plunges into a pool and thereby entrains air into the system. The water air mixture then flows from the pool into the pressure chamber and enters the lock chamber from the bottom through round nozzles. Detrainment of the air takes place all along the flow path and finally reaches the free surface of the lock chamber.

6.2.3 Classification of the Flow in the Lock Filling System under Investigation

In the system under investigation, the filling procedure is a transient process. With Reynolds numbers larger than 10 000 the flow of the system is highly turbulent, meaning that inertial forces dominate the flow behaviour. Within the flow, the two Newtonian immiscible components water and air are involved. Therefore, the flow can be classified as two-component gas-liquid flow. The phases are immiscible; solubility of air in water is neglected. In the system the phases occur in different flow patterns, which are described in the next section. When both components are intermixing, as it is the case in the pressure chamber of the lock, the flow should actually be regarded as compressible. As the examination of compressible fluids is much more complex in many cases, incompressibility is assumed. In reality entrained bubbles are compressible, thus their volume is dependent on the local pressure. In the given system, air entrainment is expected to be most relevant in the beginning of the filling, where the falling height of the jet at maximum. At the same time, the water body where the bubbles are entrained is still very small, meaning that the hydrostatic

pressure acting on the bubbles is still relatively small. Therefore, the error due to the disregard of the compressibility is accepted. Through the interaction of the air bubbles with the surrounding water, mass and momentum transfer takes place, which influences the dynamic of the flow. Surface tension has significant influence of the bubble shape, size and behaviour.

6.2.4 Objectives and Limitations of the Test Case

Air entrainment, transport and detrainment processes are assumed to influence the flow behaviour inside the system significantly. With its ability to model large stretched free surface as well as small-scale bubble transport, the new model is expected to contribute to the understanding of the flow processes involved during the phase of filling.

To avoid the complexity of modelling the turning of the segment gate during the simulation and to allow time-averaged measurements in the physical model, the filling situation was simplified for this test case. Instead of considering the transient filling process, three constant situations were defined. For this, the segment gate is kept at a fixed opening position. Additionally, the water in the chamber is kept on a defined level regulated via the downstream gate of the lock.

With this study, the practical usability of the solver to a hydraulic engineering application is tested. To evaluate the numerical simulation the results are compared with a physical scale model. As discussed in section 2.2.2, some flow phenomena cannot be represented properly with a scale model. Therefore, the data of the scale model are compared with a numerical model of the same size. With its simplified setup and the small scale the tests serve as preliminary study. Final statements about the relevant quantities for evaluating the design concept cannot be made with the results. It is assumed, that once the physical and the numerical model show satisfactory agreement, the numerical model can later be scaled up to gain relevant data for the prototype size. As the filling of the lock is a highly transient process, the complete transient filling process including the segment gate should be considered in future investigations.

6.2.5 Physical Model Setup

Model Structure

The physical scale model was built by the staff in the laboratory facilities of the Federal Waterways Engineering and Research Institute in Karlsruhe. Photos of the physical scale model are shown in Figure 6.1.

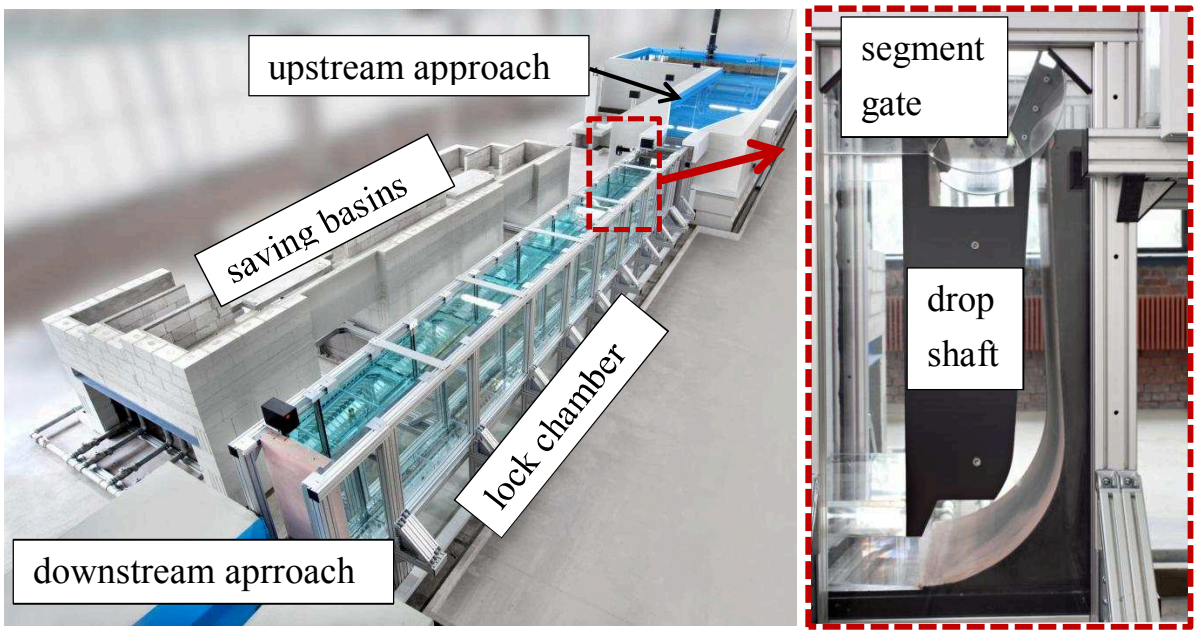

Figure 6.14: Photographs of the physical scale model with the drop shaft construction

The model recreates a navigation lock with a large lift height. The lock structure consists of the upstream lock approach, a cuboid lock chamber with a pressure chamber below, laterally arranged saving basins and the downstream lock approach. Pressure chamber and lock chamber are connected through cylindrical nozzles embedded in the intermediate ceiling. Side channels with included operation valves connect the lateral saving basins with the pressure chamber. A vertical drop shaft connects the upstream water level with the pressure chamber. The upstream lock gate, constructed as segment gate, operates the filling from the upstream canal into the lock filling system and simultaneously separates the water in the upper approach from the lock chamber.

In the physical model (shown in Figure 6.14), the lock and pressure chamber body is constructed from acrylic glass to enable visual observations and recordings of the filling process. The shape of the drop shaft is constructed from polyurethane foam plates, a material which can be milled and is water-repellent. It is designed as interchangeable part, to enable studies of different drop shaft shapes. The segment gate is constructed from polyvinyl chloride (PVC). A motor at the side of the segment gate allows its turning. Through the connected control system, the segment can be turned with pre-defined velocities. The controller allows constant or pre-defined opening curves.

Upstream and downstream approaches are constructed from brickwork walls and concrete, which is sealed with a waterproof coating. At the time of the study the construction of the lateral saving basins was not completed. This is irrelevant as the current study investigates only the process of filling through the drop shaft.

Model Scales

The dimensions of the physical model correspond to the lock of Erlangen at the Main-Danube Canal built with a scale of 1 to 25. For the purpose of scaling Froude similarity was applied. With that, the scaling measures presented in Table 6.2.1 apply.

As described in section 2.2.2 the scale effects are unavoidable in the case of turbulent free-surface flow with air entrainment. With the chosen Froude similarity the air-water intermixing in the plunging pool region cannot be reproduced according to the chosen scale. This must be considered when drawing conclusions for the prototype structure. However, this study focussed on the comparison of the physical model with a numerical model with the same dimensions.

Table 6.2.1: Scaling factors between scale model and prototype structure

Physical Parameter	Unit	Scaling Factor	Conversion Factor
Length, Width, Height	[m]	L	25
Time	[s]	T	5
Velocity	[m/s]	L/T	5
Mass	[kg]	M	25
Discharge	[m^3/s]	L^3/T	3125
Force	[N]	$M*L/T^2$	15625

The complete model has a length of approximately 30 m. At the upstream end of the model a labyrinth weir regulates the water level. Downstream of the lock chamber the water can be released directly into the water circuit of the laboratory hall. Additionally, drain valves on the bottom of the lock chamber allow the regulation and drainage of the model. The lock chamber is jacked up to enable illumination and recordings from below.

Water Level Probes

For analysing the water level in the chamber, the model is equipped with ultrasonic sensors and water level gauges. In the experimental setup of the lock, three ultrasonic water level probes are installed at each approach, for measuring the upstream and the downstream water levels. Within the chamber two water level gauges are installed at the bottom of the chamber. The ultrasonic sensors are installed in laterally connected stilling wells which are connected to the model via communicating pipes. This indirect measuring prevents the measuring system from disturbances resulting from foam or turbulence. By continuously transmitting pulses of ultrasonic waves towards the water surface and measuring the reflection time, the distance between the water surface and the sensor surface

can be calculated. In particular, the sensor consists of a transmitter and a receiver. The ultrasonic transducer transmits sound waves with a defined frequency and constant speed towards the water surface. There, the signal is reflected and returned to the sensor and registered by the receiver. The time between sending and receiving the signal is proportional to the distance. The measured water level is averaged over the projection area.

Radiometric Density Meter

To measure the air entrainment in the drop shaft, a radiometric density meter was installed in front of the pressure chamber (see Figure 6.15). The device records the volume averaged density of the incoming air-water mixture. The sensor setup consists of a transmitter and a detector. The transmitter contains a small portion of an alkaline metal, namely Caesium 137 (intensity 185 MBq), welded into a stainless steel capsule and embedded within a spherical lead covering. The dose rate at the surface of the covering is 1 µSv/h. A 0.01 m wide opening allows the directed emission of radiometric rays. As the rays penetrate the fluid, it is partly absorbed proportionally to the density of the fluid. The detector registers the radiometric rays arriving allowing the average density of the penetrated volume to be calculated. To minimize the necessary ray intensity a vertical setup was chosen. Like this the rays only have to be strong enough to penetrate a height of approximately 0.10 m instead of 0.5 m for the horizontal setup. The measuring volume of the density meter has the shape of a truncated cone which results from the ray beam diameter on the bottom side of the pressure chamber and the beam angle. Before the series of measurements was started, the density meter was calibrated. For this purpose the lock was filled, so that the pressure chamber contained water only. The measured value was set to correspond to the density of water. For defining the value corresponding to air, the chamber was emptied. According to the manufacturer (RGI GmbH) the accuracy of a 1 s measuring interval corresponds to 1 % for a density of 1 kg/m³. Measurements of the density of a constant state (complete chamber empty or full) over a longer time period showed variations of up to 2 %. This inherent

measurement setup inaccuracy has to be taken into account when measuring results are analysed.

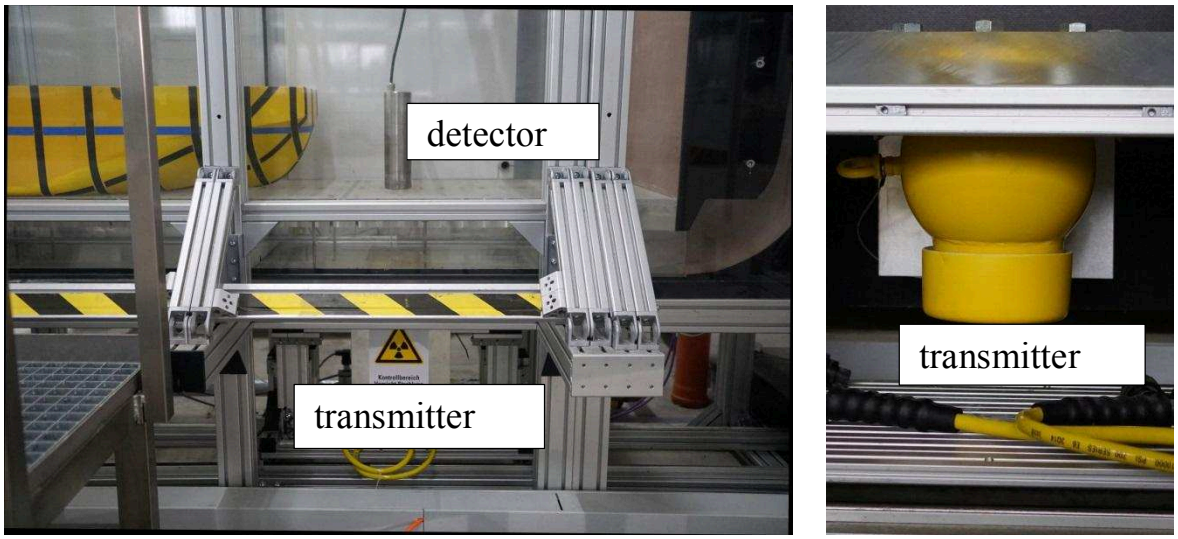

Figure 6.15: Radiometric measurement equipment installation at the physical model

6.2.6 Numerical Model Setup

The numerical model was designed in analogy to the physical scale model. Therefore, the three-dimensional geometry used had the same dimensions. To reduce computational effort, only one longitudinal half of the lock was simulated and the middle patch was defined as symmetry plane. The model was spatially discretised with a hexahedral-dominant, polyhedral mesh, where the cells were refined in proximity to the geometry. In total the mesh consisted of approximately seven million cells. The basic edge length was 0.01 m. Inside the pressure chamber and the drop shaft the mesh was refined to an edge length of 0.0025 m.

As the falling jet and the subsequent air entrainment through the plunging cannot be represented correctly by the numerical model, a suitable inlet boundary condition had to be found. Therefore, a horizontal inlet plane was defined within the drop shaft, allowing the inflow of a defined water-air mixture into the lock filling system. The inlet patch was located slightly below the expected water surface attached on the upstream wall side of the drop shaft encompassing the complete width of the model. The inlet boundary was aimed

to replace the effect of the plunging jet. It was assumed, that the plunging of the jet transfers the potential energy of the upstream water into kinetic energy. For the sake of simplicity, friction losses were discarded. Consequentially, the jet velocity at the height of the inlet could be calculated from the lift height. From the physical model, the inflow rate and a volume averaged air content within the pressure chamber was known. The inflow and the jet velocity were used to calculate the necessary width of the inlet plane. In the simulations an inflow discharge with a prescribed volume fraction directed normal to the inlet were defined, resulting in the calculated velocity. An exemplary calculation of the inflow velocity and the necessary inflow area can be found in the appendix A.5.

To ensure a fixed water level in the lock chamber, the downstream wall was defined as fixed water level boundary. The side wall of the lock chamber was defined as slip wall. For the top atmospheric boundary conditions assuming atmospheric pressure were defined. The geometry surfaces were defined as no-slip walls.

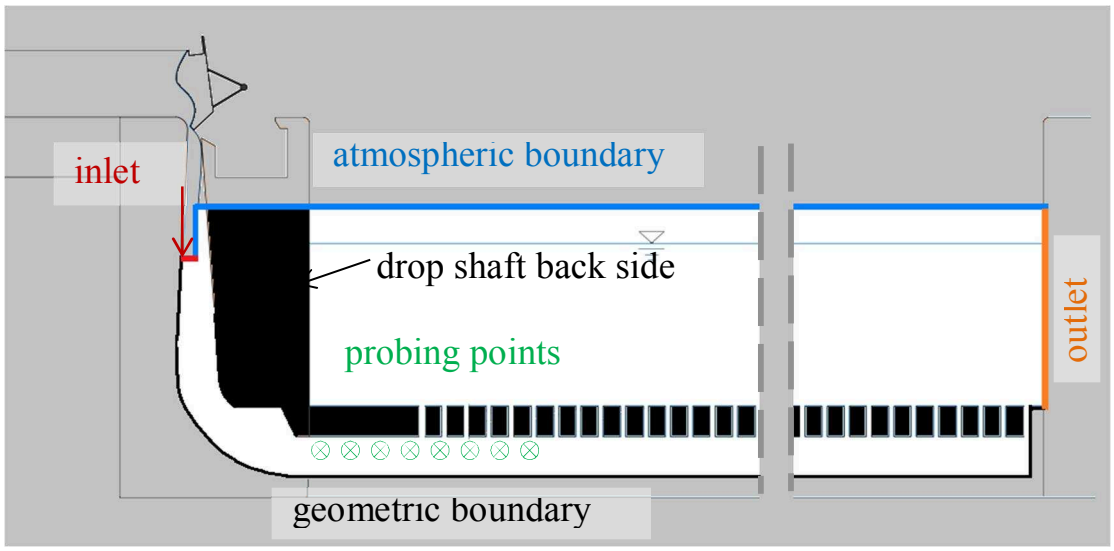

Figure 6.16: Sketch of the numerical model setup for the lock filling simulation

In the first attempt the Spalart-Allmaras DES turbulence model was applied. The first test was used for the analysis of the qualitative flow behaviour. In latter tests the influence of the turbulence modelling was studied by applying various turbulence models. To enable the measuring of the water levels in the numerical model probing points were created, which recorded the calculated pressure and

velocity data at an interval of ten time-steps. For the latter analysis the values were averaged over time.

6.2.7 Model Variants

For the following series of tests the segment opening of the gate is fixed throughout all tests. For each test a different, fixed water level in the chamber is defined. The water levels and corresponding inflow discharges are listed in Table 6.2.2. It is assumed that a quasi-steady state flow situation develops for each opening angle.

In the physical model the measurements were started, when the steady state flow situation could be detected visibly. The resulting measurement values were averaged over time. For the numerical model, the simulation was performed until a quasi-steady flow situation was reached. Afterwards the probing of the relevant variable was started and the simulation was continued. For evaluation, the variables were averaged over time. Within this series of tests three water levels were studied. Table 6.2.2 shows the resulting measurement values from the physical model tests, which were used as boundary conditions of the numerical model.

Table 6.2.2: Boundary conditions for the three tests

Water level inside the lock chamber [m]	Inflow discharge [m³/s]	Volume fraction at the probing location [-]
0.27	0.027	0.847
0.366	0.027	0.856
0.476	0.027	0.856

In all cases the gate was opened by 22° corresponding to a completely opened gate.

6.2.8 Analysis of the Numerical Model Results

The numerical simulations were run in parallel on 100 processor cores. For a simulated time of 115 s the execution time amounted to approximately 140 hours. The simulations run stable; no severe disturbances from numerical instabilities were observed. For the evaluation, additional fields with the time-average values of the volume fraction distribution and the velocity distribution were created. The results of the numerical model were visualized with the post-processing software Paraview. For the quantitative analysis of the flow behaviour two presentation forms were considered: firstly, snapshots of the instantaneous flow field variables were created. Secondly, images of time-averaged variables were made. For the qualitative evaluation, the density distribution inside the pressure chamber was analysed.

Qualitative Analysis of the Instantaneous Flow Behaviour

The following snapshots shown in Figure 6.17 compare the instantaneous velocity and the volume fraction field of the different water levels visualized on vertical section planes of the model, which were created in the middle of the model width. To emphasize the important parts of the simulation, only the cells containing more than 1 % water are coloured according to the velocity or the volume fraction distribution respectively. The air filled region is marked with a uniform blue plane.

Although the water levels and inlet velocities differ visibly in the three cases, no significant difference in the velocity and the air transport characteristic can be identified, when looking at the instantaneous snapshots of the flow fields. Generally, the flow behaviour in the drop shaft and the pressure chamber can be described as highly non-uniform. Thus, the volume fraction, velocity and pressure distributions are very time-dependent. At the inlet the inserted vertical flow forms a thin bundled jet alongside the upstream directed drop shaft wall. The density of the jet increases with growing depth. At the bottom bend towards the pressure chamber, the complete air content is released. Hence, the jet at the bottom end of the shaft has the density of water. The jet follows the shape of the wall and enters the pressure chamber at the bottom. Its velocity decreases with

growing depth. The rest of the drop shaft is filled with an air-water mixture of lower density than the inlet discharge density. At the inner side of the drop shaft bend the flow forms a vortex, reversing the flow direction towards the water surface.

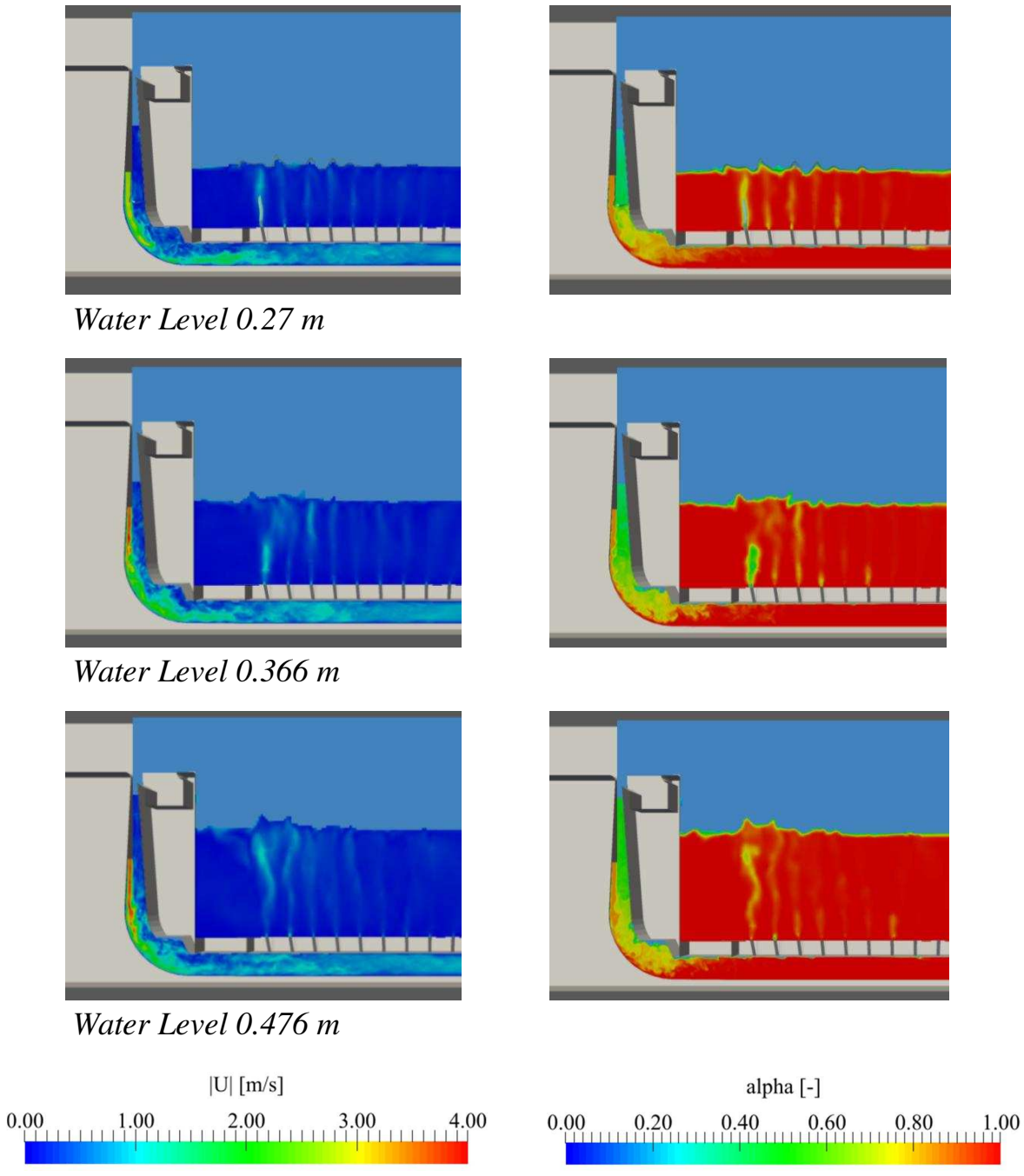

Figure 6.17: Velocity and volume fraction distribution of the three lock filling simulations

The unsteady upward directed velocity in the drop shaft creates a wavy, irregular water surface, which is slightly higher than the water level in the lock chamber. From the bottom towards the water surface a density gradient evolves within the drop shaft. However, not all bubbles contained in the drop shaft are released. Turbulent bubble accumulations surge irregularly through the pressure chamber, releasing bubble jets through the nozzles into the lock chamber. The air-water mixture jets rise vertically and deform the water surface at the penetration point. The intensity of the jets decreases in downstream direction. Corresponding to the bubble transport inside the pressure chamber, the density composition of the jets is very variable.

Air bubbles which do not hit a nozzle when meeting the ceiling are transported further along the ceiling of the pressure chamber until they are released through a nozzle. In all cases, air content is visible only within the first third of the pressure chamber.

Qualitative Analysis of Air Transport within the Pressure Chamber

To gain more detailed information about the air transport behaviour within the pressure chamber, time-averaged values were determined. For the evaluation a section of the pressure chamber was defined in which the received values were visualized to compare the different water level cases (see Figure 6.24). The following Figure 6.18 highlights the section chosen for the evaluation, which captures the pressure chamber over the complete height at a distance of 0.27 m to 0.99 m from the drop shaft back side. The section displays the same location as the long exposure photos taken in the physical model tests. Analysing these time-averaged results helped to understand the mean flow behaviour inside the filling system. In analogy to photographs with longer exposure times, the volume fraction distribution can be averaged over a defined time period. With a volume rendering technique the averaged volume fraction distribution was illustrated. In the images shown, all cells containing an air volume fraction of 0.1 % or more are taken into account for volume rendering. The intensity of the white colour indicates how often air was existent in the cell considered during

the averaging time period. Thus, zones with very dense white colouring were experiencing high air flux.

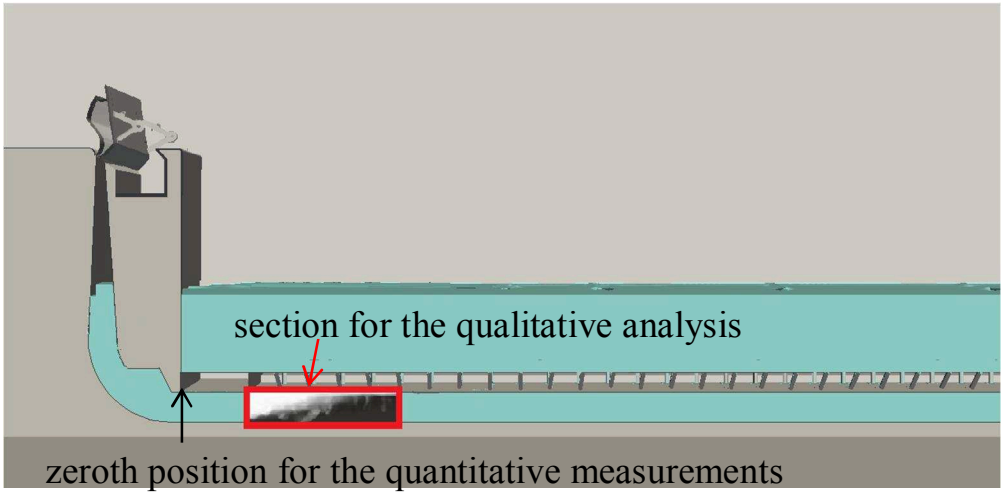

Figure 6.18: Section for the quantitative analysis

Lighter shaded areas were less frequently filled with air. Highest incidence of bubbles becomes visible in a wedge shaped volume in the pressure chamber.

Influence of the Turbulence Model

The flow patterns conceived within the system are strongly dependent on the turbulence model used. For showing the influence the case with the chamber water level at 0.366 m was simulated with different turbulence model setups:

- without applying a turbulence model,
- applying the DES turbulence model,
- applying the k-omega SST RANS turbulence model,
- applying the k-omega SST RANS turbulence model with additional turbulent diffusion of the air bubble distribution.

To allow a comparison between the models the mean detrainment behaviour of the bubbles within the pressure chamber is captured. Figure 6.19 shows the results of the four cases. The comparison of the tested variants shows that the resulting bubble distribution within the pressure chamber significantly depends on the turbulence model. The case with the k-omega SST turbulence model shows the shortest detrainment length, because the flow structure is smoother

than in the other cases. The result with the DES approach shows a longer detrainment length in the pressure chamber. The longest detrainment length was achieved when no turbulence model was applied. This behaviour seems to result from the functionality of the different models.

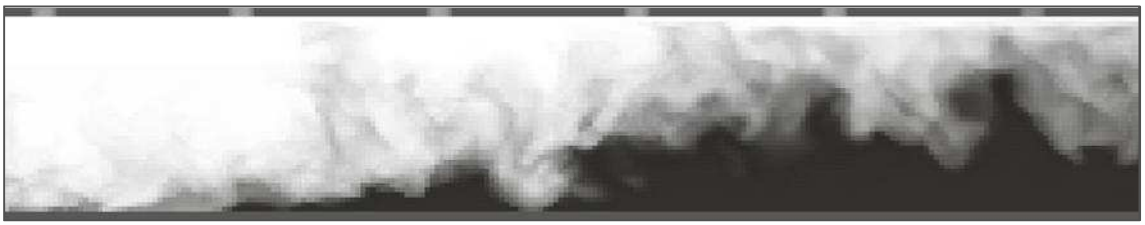

a) without turbulence model

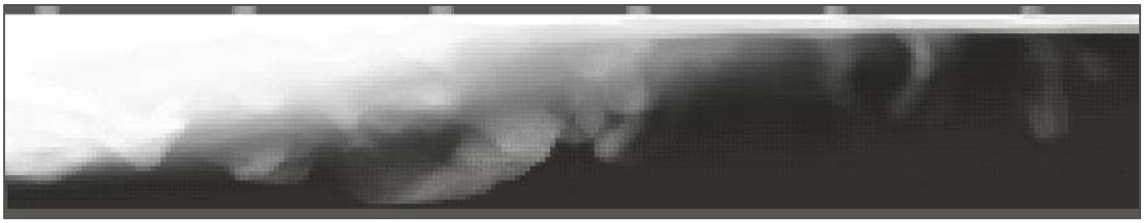

b) DES approach

c) k-omega SST model

d) k-omega SST model and additional turbulent diffusion

Figure 6.19: Volume fraction distribution in the pressure chamber with different turbulence modelling approaches

By applying the RANS k-omega SST model, the complete spectrum of turbulence is eliminated from the velocity field. In the case of the DES model, the near-wall regions are treated with the RANS approach and the regions further away from the wall apply the LES approach. Hence, turbulent structures which are resolved by the grid are directly captured. All smaller vortices are modelled. With the mesh used in this study approximately 77 % of the volume was modelled with the LES approach and 23% applied the RANS approach. The RANS model is applied in all cells that are close to a geometric or symmetry boundary, where the mesh is too coarse to capture the complete turbulent spectrum. In the case without turbulent model only the turbulent eddies which are captured by the grid are captured. The dissipative effect of the unresolved vortices is neglected. It can be assumed that the difference in the detrainment length between the case without turbulence model and the DES case results from the missing diffusive effect of the unresolved turbulent scales. Particularly the bubble transport due to the instantaneous velocity fluctuations is not accounted for in RANS models. With the approach presented in section 4.1.4 this underestimation can be counteracted by extending the primary phase fraction equation with a diffusion term. For this study the diffusion coefficient was set equal to the turbulent diffusion. The effect of the additional turbulent diffusion can clearly be recognized by comparing the results of the normal k-omega SST model application shown in Figure 6.19c with the results from the model with additional turbulent diffusion presented in Figure 6.19d. Due to the extra diffusion in the volume fraction equation bubbles are transported further inside the pressure chamber. The resulting detrainment length is comparable to the DES results. The test of the different turbulence approaches demonstrates that the application of the standard RANS models, which were designed for single phase flows, are not able to capture the highly turbulent two-phase flow in the pressure chamber system. When the mesh is fine enough to resolve the main part of the turbulent scales the DES model presents a suitable alternative. For coarse grid resolution the RANS models should be extended for the two-phase usage. The suggested method of section 4.1.4 presents a simple way for the adaptation. However, a more extensive study is necessary to prove the suitability of this

approach. In the following cases all simulations were performed with the DES approach. Utilizing this approach, different water levels were tested.

Comparison of the Three Water Levels

A comparison of the different water level configurations reveals tendencies similar to the physical model evaluation (see Figure 6.24): an increasing water level implicates a lower falling height and thereby reduces the impact of the plunging jet. Consequently, the bubble transporting velocity declines and the bubble path through the pressure chamber is shortened. Thus, higher water levels lead to shorter degassing length when all other variables like the segment gate opening width and the air entrainment rate are kept constant.

Quantitative Analysis of the Air Content Distribution within the Pressure Chamber

For the quantitative analysis of the simulations, the volumetric air content in the pressure chamber was evaluated for all three water levels. In 0.10 m steps a 0.08 m wide cuboid measuring volume was defined. The measuring volume captures the values over the complete width of the model. Taking the time-averaged values and averaging them over the volume, the mean air content was received. Due to the high computational costs, the time-averaging of the volume fraction in each cell was limited to a period of 20 s. The results obtained are shown in the following Figure 6.20.

The diagram shows the decreasing air content in the pressure chamber with growing distance from the drop shaft. Although different water levels in the chamber with corresponding inflow velocities were chosen for the three simulations, the resulting quantitative distribution of the air content within the pressure chamber is very similar. Within the first 0.7 m most of the entrained air content is released into the pressure chamber. Only approximately 1 % of the air is transported further.

Chamber water level: 0.368 m

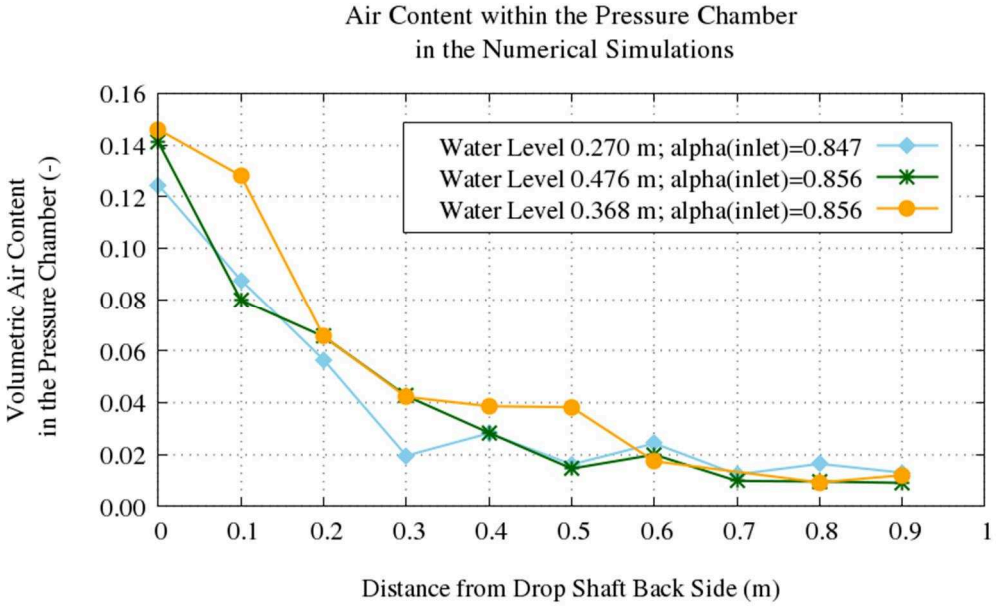

Figure 6.20: Time-averaged air content in the pressure chamber in the numerical model

After the detrainment of the major part of the air content a small air layer remains below the ceiling of the pressure chamber which is further transported with the flow. This corresponds to the above discussed visualisation of the results. However, the difference of the bubble distribution in the three different cases which were visualized in the screenshots of Figure 6.24 is not directly visible in the diagram in Figure 6.20. This is assumed to result from the small air content in this region and the accuracy of the quantitative data. The section of the qualitative evaluation with the screenshot captures the pressure chamber at a distance from the drop shaft back side of 0.34 m to 0.94 m. In this region the quantitative values of the air content range between 0.04 and 0.02.

6.2.9 Analysis of the Physical Model Results

For the analysis of the physical model behaviour, the measurement values were recorded over a time period of 350 s to allow the calculation of time-averaged values. Video recordings were taken to allow the visual analysis of the flow. Two screenshots of the video recordings at two different filling stages are shown in Figure 6.21. Each model test was performed twice.

Qualitative Analysis of the Instantaneous Flow Behaviour

From the visual analysis the flow inside the filling system can be described as follows: comparable to the numerical simulation, the flow behaviour in the physical model is apparently fluctuating. The location of visible bubbles is strongly variable. Along the opened segment gate the water starts falling into the drop shaft. A thin water jet develops along the outer wall of the drop shaft without visibly absorbing a lot of air. Subsequent to the gate opening it attaches to the wall and the width of the jet decreases. After plunging into the pool, the water jet remains visibly attached to the wall.

Figure 6.21: Photographs of the physical model

Above the water level, the remaining volume of the drop shaft next to the water jet is air filled. Below the water level, it is filled with bubble saturated water up to the water surface, which is slightly lower than the water level in the lock chamber. The water surface in the drop shaft is very wavy. A precise observation of the bubbles shows that the bubbles on the side of the inner wall move towards the water surface. The motion seems pulsating. A part of the bubbles is transported into the pressure chamber. With increasing opening angles, the amount of air entrainment grows. As long as the drop shaft is not completely filled with bubbly flow, a part of the bubbles is detrained at the free surface inside the drop shaft, the remaining bubbles degas in the front part of the chamber. Within the first 10 % of the pressure chamber length most bubbles reach the ceiling. Most of the bubbles directly find their way through the nozzles into the lock chamber. There they rise vertically towards the water surface. Inside the pressure chamber, the bubbles are smaller than in the lock chamber. Whilst rising inside the lock chamber, some bubbles accumulate and form larger

bubbles. The transformation of a spherical shape to a cap shape can be observed from time to time. At the free surface in the lock chamber the bubbles create irregular waves. Some of the bubbles inside the pressure chamber which do not directly encounter a nozzle are transported further along the ceiling. Thus, isolated bubbles rising can be recorded throughout the complete length of the chamber. A series of photographs of the same model setup (see Figure 6.22) shows the irregular bubble distribution along the pressure chamber. It can be assumed, that the bubble density decreases along the pressure chamber. After a certain length only very few bubbles are visible inside the pressure chamber. However, a typical degassing length after which the bubbles reach the pressure chamber ceiling is not directly identifiable.

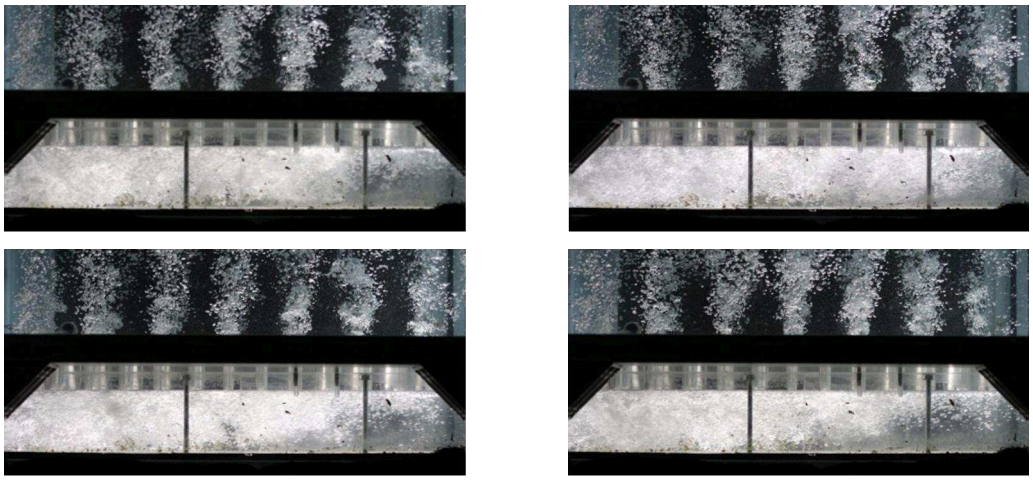

a) Water level 0.27 m

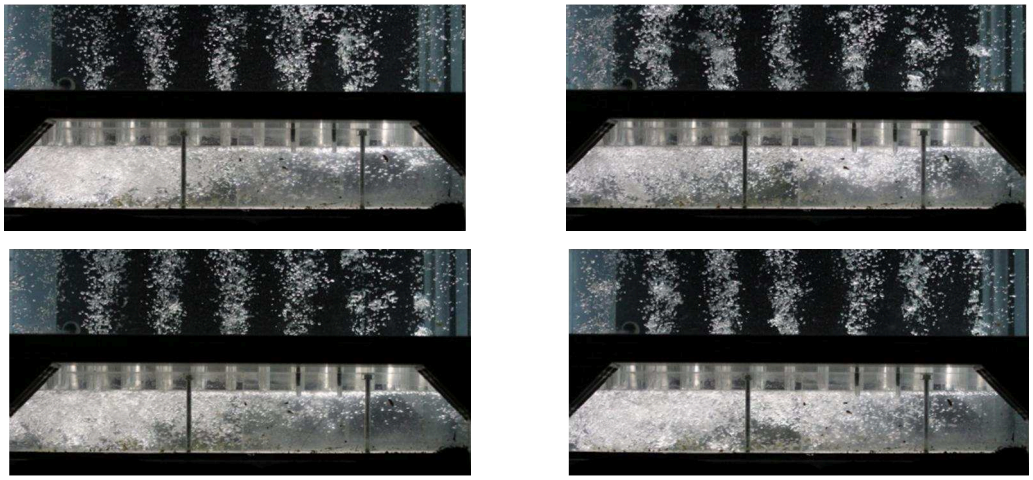

b) Water level 0.366 m

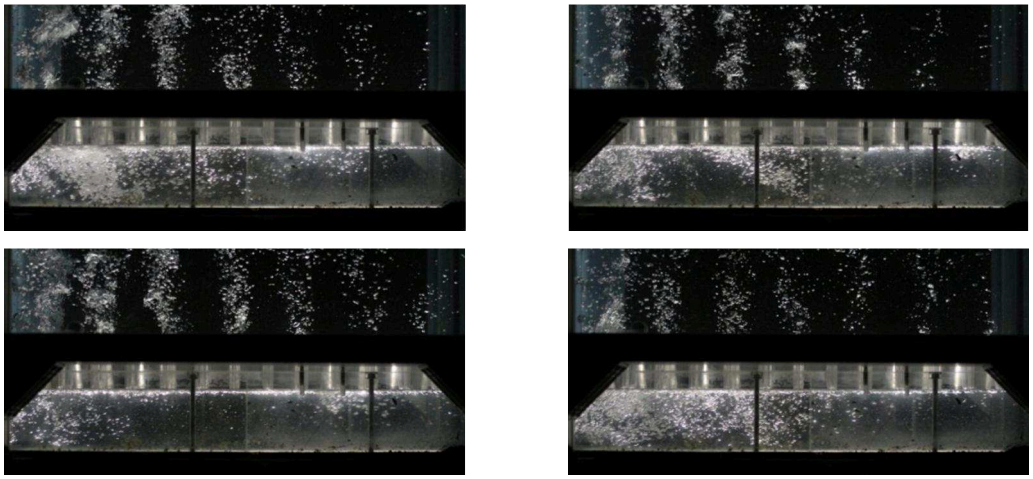

c) Water level 0.475 m

Figure 6.22: Physical model: Photographs of the pressure chamber section for the three water level variations showing the variety of the instantaneous bubble distributions

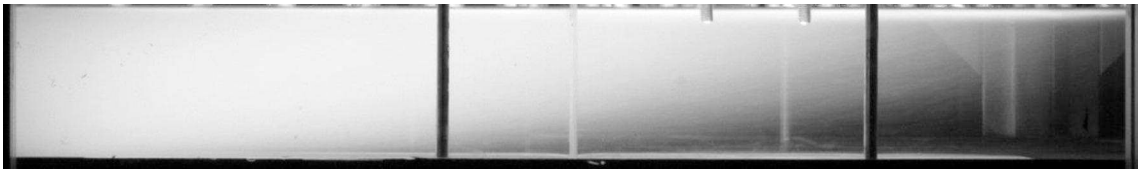

a) Water level 0.27 – 22° opening

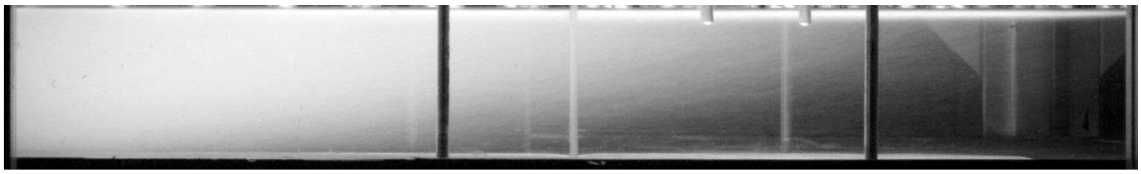

b) Water level 0.368 m – 22° opening

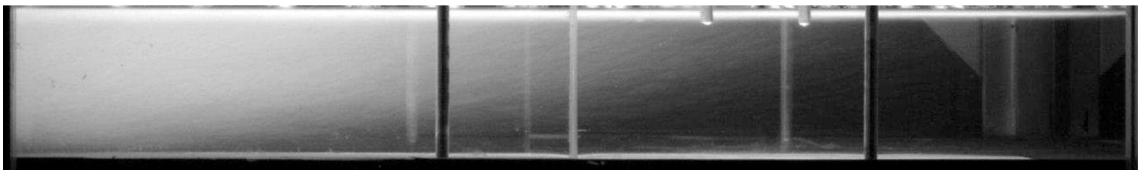

c) Water level 0.475 m – 22° opening

Figure 6.23: Physical model results: Photographs of the pressure chamber section for the three water level variations taken with an exposure time of 15 seconds

a) Water level 0.27 – 22° opening

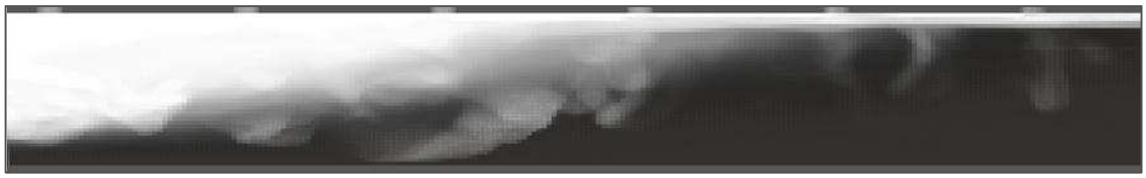

b) Water level 0.368 m – 22° opening

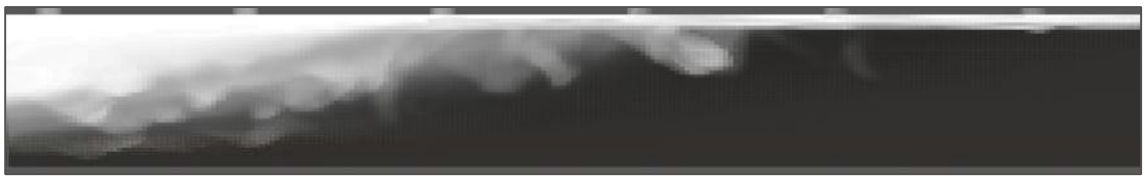

c) Water level 0.475 m – 22° opening

Figure 6.24: Numerical model results: Time-averaged volume fraction distributions in the pressure chamber for the three simulation cases

Qualitative Analysis of Air Transport within the Pressure Chamber

Only the application of longer exposure times improves the identification of the typical bubble flow patterns. For the visualization of the averaged bubble flow behaviour various exposure times were tested. The objective of the exposure was to find out how most bubbles pass through the pressure chamber. It was assumed, that a longer exposure time decreases the visibility of exceptional bubble paths and improves the averaging effect. With an ideal setup, multiple pictures should show the same bubble distribution. Finally, an exposure time of 15 seconds showed the best results. To improve the recognisability of the bubble filled part in the photographs, the contrast of the pictures was increased by post-processing. The resulting images presented in Figure 6.23 show that most bubbles concentrate within a wedge shaped volume during their passage through the pressure chamber. From the resulting wedge angle it can be concluded that the horizontal velocity component on the bubbles is much higher than the vertical rising velocity. The photographed section captures the pressure chamber between the second and the third vertical aluminium strut (shown in *Figure* 6.21) which build the static structure of the physical model.

A quantitative estimation of the degassing length can be made by analysing the bubble filled wedge of the long exposure photographs. Theoretically, the degassing length of the bubbles in the chamber can be roughly estimated with the horizontal flow velocity in the pressure chamber and the vertical bubble rising velocity. For the numerical simulation case with the chamber water level at 0.366 m the horizontal flow velocity is estimated with the pressure chamber section area of 0.01957 m² and the inflow discharge of 0.027 m³/s to approximately 1.4 m/s. With an estimated bubble rising velocity of 0.25 m/s the bubbles should reach the pressure chamber ceiling after 0.56 m, when a distribution of the bubbles across the complete height of 0.1 m is assumed at the beginning of the chamber. Comparing this length with the corresponding results of the numerical and the physical model, the estimated length is too short. In both models, the bubbles travel much further through the chamber. The reason for this is assumed to lie in the turbulent nature of the flow

inside the pressure chamber. Occurring vortices prevent the bubbles from rising. Therefore, most bubbles need longer for reaching the ceiling.

A comparison between the different water levels shows, that with higher water levels less bubbles are captured on the long exposure time photographs. This indicates a decrease of the degassing length with increasing water levels. The data from the radiometric density measuring system shows that the entrained air content is almost constant for all cases considered here in this study. Thus, it can be concluded, that the degassing length depends mainly on the jet induced momentum on the flow in the pressure chamber.

Quantitative Analysis of the Air Content Distribution within the Pressure Chamber

For the quantitative evaluation of the physical model and the comparison with the numerical simulations described below, the volumetric air content in the pressure was measured at ten locations. First, the radiometric density measurement setup was positioned at a defined distance from the drop shaft back side. All nozzles in the measuring area were sealed. Then, a calibration had to be performed for each location. The measurement locations are listed in Table 6.2.3 with distances from drop shaft backside. To receive a reliable average value the recording of the density was performed over a time period of 300 s. Each measurement was performed three times.

The diagram shows that the density strongly decreases within the first meter of the model and finally tends to an air content of 2 %. This corresponds to the visible observations described above. After most of the air is released from the pressure chamber some bubbles accumulate below the ceiling of the pressure chamber. The accumulated bubbles are transported with the flow until the coincidently meet a nozzle. The results of the measurements are shown in Figure 6.25.

Table 6.2.3 Probing locations for the air content measurements in the physical model for a chamber water level of 0.368 m

Point number	Distance from drop shaft backside in [m]
1	0.045
2	0.157
3	0.270
4	0.375
5	0.479
6	0.583
7	0.683
8	0.790
9	0.894
10	0.998

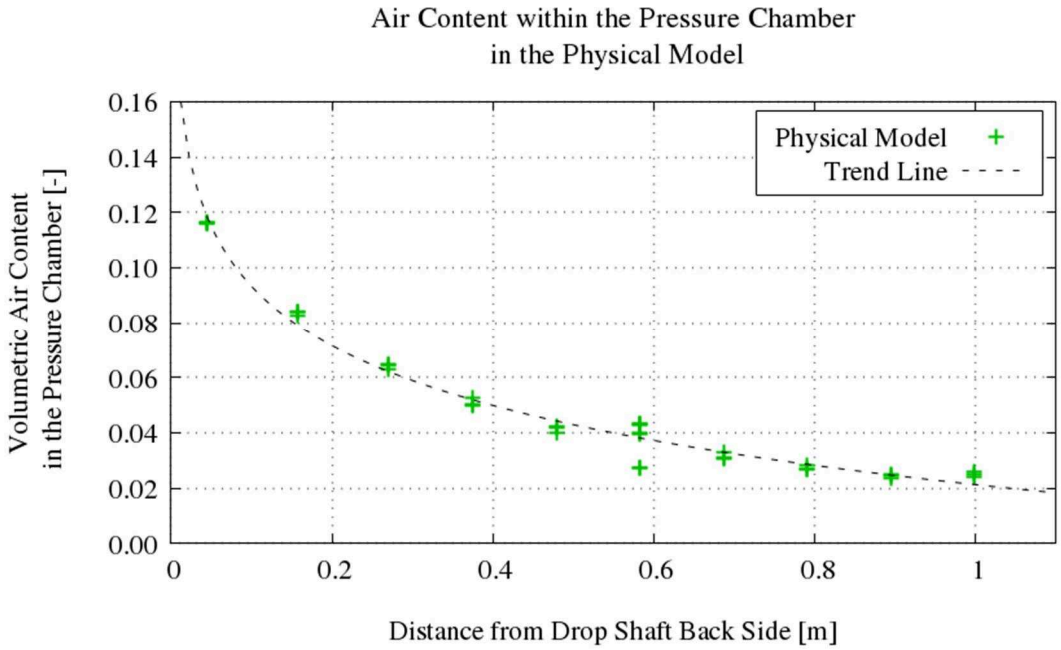

Figure 6.25: Time-averaged air content in the pressure chamber in the physical model

Due to the high expenditure of time only one setup with a fixed water level and a constant segment gate opening was carried out. Further measurements are planned. Except the values at a distance of 0.6 m the three measurements at each location show high agreement. Thus, it can be concluded that evaluated values were reproducible.

6.2.10 Comparison and Evaluation of Both Models

The analysis of the numerical and the physical model showed that the flow under investigation is highly fluctuating although the inflow rate and the outlet water-level were kept on constant levels. The evolving turbulence within the pressure chamber resulted in varying bubble rising behaviour: local turbulent eddies prevented some bubble clusters from their continuous rising, thus several bubbles were transported further into the pressure chamber than expected; others rose much faster. The fluctuating behaviour within the filling system was visible in both the physical and the numerical model. Qualitatively, the numerical models showed similar behaviour to the physical model tests. The averaged results of both models also demonstrated a high qualitative conformity (see Figure 6.23 and Figure 6.24). However, a direct comparison of the photographs from the physical model tests and the screenshots from the numerical simulations is hardly possible, because the representation of the volume fraction distribution is different in the models. Particularly the correlation of the visible bubbles to the corresponding volume fraction is unknown. Whereas in the physical model all bubbles are captured that are visible from the longitudinal view during the exposure time period, the numerical model snapshots show the averaged volume fraction in each cell visible in the chosen longitudinal section. By adapting the colour scale of the numerical model visualization setup, various air contents could be visualized. In the current setup for the averaged images, the limit for the visibility of the air content was set to 0.1%. This corresponds to the assumption that a bubble with a diameter of 0.012 m captured in a water cube of 0.001m³ is still visible on the photographs.

For the quantitative comparison, the volume-averaged air content in the pressure chamber with regard to the distance from the drop shaft was measured

in both models. The following Figure 6.26 presents the results of both models for the water level of 0.368 m (cf. Table 6.2.2). Generally, both models show the same tendency: during the first six measuring points the air content slopes downward tending to a small air content value. Close to the drop shaft, up to a distance of 0.15 m the numerical model produced higher air content than the physical model. In further distance to the drop shaft the numerical model values are slightly lower than the measurements from the physical model. The smallest value measured in the physical model of 2.4 % is slightly higher than the smallest value of 1.2 % measured in the numerical model. The highest deviation between the models occurs in close proximity to the drop shaft. This can be clearly lead back to the different boundary conditions of the models. Especially the inlet conditions of the two models are extremely different. Where the inflow in the physical model is controlled by the upstream water level in the lock approach and the segment gate opening, the inlet boundary of the numerical model replaces the evolving falling jet by a boundary condition imposed on a horizontal plane below the drop shaft water level. Despite this difference in the boundary conditions the received results showed satisfactory agreement.

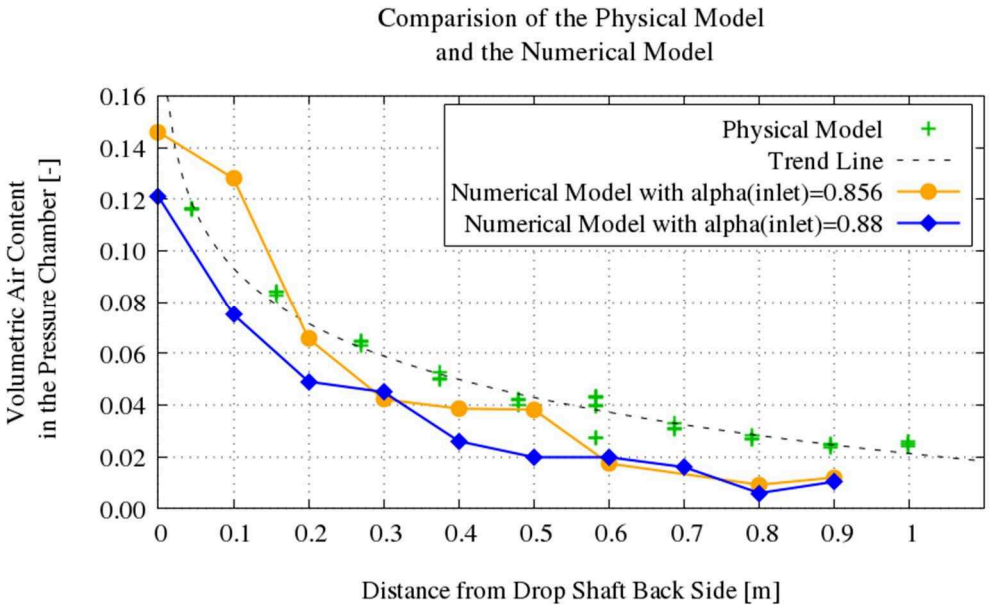

Figure 6.26: Comparison of the physical and the numerical model

A correlation of the air entrainment rate, the inflow discharge and the lift height of the jet is necessary to operate the numerical model of the filling system. Due

to scaling effects, the physical model alone can also not provide quantitative data about the investigated filling system. The wrong representation of the air entrainment, transport and degassing process hinders the extraction of reliable data.

7 Summary, Conclusions and Outlook

7.1 Summary and Conclusion

In this thesis an application-oriented approach for the modelling of multiscale two-phase flows was developed, implemented and tested. The new approach allows the simulation of two-phase flows which include a large free surface and small dispersed bubbles simultaneously. Even when small bubbles are not resolved by the computational grid, their physical behaviour is captured by the implemented model. Dispersed air volumes inside the water body tend to rise in opposite direction of the gravitational acceleration. Due to the rising of the dispersed air momentum is transferred to the surrounding fluid. The rising velocity is calculated dependent on the bubble size and the existent air content in the cell. Three correlations between the bubble diameter and the resulting single bubble rising velocity were implemented in the model. Being derived from the volume of fluid solver the model is based on a single-fluid approach which treats both phases as a mixture. The volumetric distribution of both phases is determined with the volume fraction equation. In addition to this scalar transport equation the set of equations of the solver consists of one mass and one momentum transport equation for the mixture. The deployment of higher order schemes for the discretisation of the volume fraction equation counteracts the typical smearing of the gas-liquid interface. The additional application of the

MULES algorithm for the solution of the scalar transport equation ensures the boundedness of the solution. In contrary to the VoF approach, the approach chosen allows a relative velocity between the phases. As a consequence, detrainment of unresolved bubbles can be modelled. Generally, the compressibility of the gaseous phase is neglected in the approach. This is reasonable, when the water depth is small. With growing water depth the effect of the compressibility increases. This particularly influences the bubble size and subsequently the rising velocity of the bubbles. To account for the changing bubble rising velocity in deep waters, an extension with "pseudo-compressibility" was added to the model. This extension adapts the bubble diameter in accordance with the local pressure, resulting in a pressure-adapted rising velocity for the bubbles. To account for the turbulence in the system, a variety of RANS or LES turbulence approaches can be chosen. The RANS turbulence models, which are most often used in engineering applications, eliminate the complete spectrum of turbulence from the velocity fields and replace them with a model. In the case of free surface flow without dispersed particles, this produces satisfactory results. However, when bubbles are present in the flow, the RANS models cannot model the turbulent flow behaviour properly. Particularly the bubble transport due to the instantaneous velocity fluctuations cannot be reproduced. To overcome this, an extension of the transport equation for the primary phase fraction is proposed. The introduction of a diffusion term introduces additional diffusion into the system, which is proportional to the turbulent diffusion.

Two simple test cases presented in chapter 5 proved the proper implementation of the approach into the software framework of OpenFOAM. With the first test case it was shown that unresolved air bubbles which are located within a water filled tank detrain with the expected velocity. The second test case demonstrated that the approach is able to capture free-surface flows with satisfactory accuracy.

The combination of both two-phase scale phenomena was tested in chapter 6 with two hydraulic engineering applications. Both cases of chapter 6 proved the applicability of the model to hydraulic engineering cases. The first

hydraulic engineering test case exemplified how the approach can be applied for investigating the sensitivity of an existing structure to air entrainment. In the tested lock Bolzum, the effects increasing air entrainment or higher flow rates were investigated. The knowledge gained could be used to optimize the filling schedules of the system.

In the second case the filling of a newly proposed high-head lock system was simulated, including a lot of air entrainment. To prove the feasibility of the new system, the effects of the air-water intermixing on the functionality of the system have to be studied. Here, the developed solver provides valuable insights into the properties of the new system. Particularly the transportation of the entrained air with the highly turbulent flow through the filling system and its detrainment in the lock chamber can be investigated with the solver. Additionally, utilising the solver, an optimisation of the drop shaft shape can be performed. Although the air entrainment rate is unknown, a quantitative analysis can show the effects of shape changes. The comparison to a physical model showed that the numerical model is able to capture the qualitative flow patterns developing inside the filling system. Also the quantitative behaviour of the air transport inside the system is comparable to the measurement data of the physical model.

Due to the implementation within the OpenFOAM framework the parallelisation was inherent. With a scale-up test the optimal decomposition for the solver on the in-house high performance computer was found. When adaptive time-stepping was used the computational speed is dependent on the chosen Courant number. The accuracy of the numerical results is mainly dependent on the grid resolution and the accuracy of the discretisation schemes. The total error in the simulation is further dependent on the accuracy of the geometry approximation. Here, compromises between accuracy, stability and reasonable computation time have to be found for each case.

7.2 Limitations and Outlook

The current model has several limitations which must be considered when applying it and analysing its results. Some of the limitations are intentional, others should still be improved. The following section clarifies the limits and suggests possible improvements.

With the current implementation of the approach bubbles are not directly resolved. Therefore, the resulting drag forces on the bubble are only approximated. Interactions of the bubbles with the wall and unsteady forces on the bubbles are neglected. Furthermore, the interactions occurring between bubbles are not accounted for and the model is only capable to model bubbles of one diameter. These restrictions are acceptable for applications where the total bubble content is small and where the bubble diameters do not vary over a several orders of magnitude. It was assumed that this is true for the hydraulic systems which were investigated in this study. However, bubble size measurements at prototype structures or physical scale model could substantiate the assertion.

The library of OpenFOAM in which the solver was integrated allows coupling the model with a large variety of turbulence models. However, the models commonly used in hydraulic engineering are mostly designed for flows with isotropic turbulence behaviour. Turbulence models which are specifically adapted to two-phase flows modelled with a single-phase approach are not available yet. It is unknown whether the two-phasic nature of the flow significantly influences the turbulence.

To enable an integrated view on the lock systems, the following developments are necessary. For the quantitative analysis of the resulting forces on the ship during the filling process it is essential to know the rate of air which is entrained by the falling jet. In this study the jet was replaced by a boundary condition with a constant water-air inflow rate. The complex physics of the free falling jet cannot yet be captured by the model. Here, further research about the decaying process of the jet, the plunging of the jet, the subsequent entrainment of large air pockets and the influence of the turbulence on the named processes is necessary to find a suitable way of reproducing these processes. On the one

hand, an approach for the numerical approximation of the jet and the air entrainment should be developed. Existent approaches as those discussed in section 2.1.4 could serve as basis. On the other hand, prototype measures are crucial for the validation of the numerical developments. Data of a plunging jet could exemplarily be obtained by prototype measurements at existent structures like the lock of Bolzum. For the measurements, robust devices for the highly turbulent bubbly water zones close to the falling jets have to be developed, which can be setup without danger to life.

In the prototype structure, the falling jet properties are also influenced by the transient process of the segment gate opening. To capture the dynamics, the moving segment gate would have to be integrated into the model. Research towards the numerical simulation of a moving ship in a lock is already ongoing at the BAW (see e.g. Schulze *et al.*, 2015). The direct capturing of the segment gate motion and the falling jet poses demanding requirements to the model. Alternatively, an inlet condition with a variable inflow rate over time could be thought of.

Appendix

A.1. **Breakup Length Calculation for the Falling Jet in the Drop Shaft**

For the calculations the parameters listed in Table A 1.1were used.

Table A 1.1: Values used for breakup length calculation for the jet in the drop shaft

Variable	Value	Dimensional Unit	Variable Description
K	0.85	[-]	non-dimensional fit coefficient
B	f (opening width)	[m]	jet thickness
h	4	[m]	upstream water depth
q	62.5	[m³/s]	discharge (with the assumption of a constant filling rate over 12 minutes filling time)
g	9.81	[m/(kg*s²)]	gravity
Cd	2	[-]	crest discharge coefficient

Applying the approach of Castillo and Luis (2006) to the lock system the following relationship between the opening width and the breakup length is received:

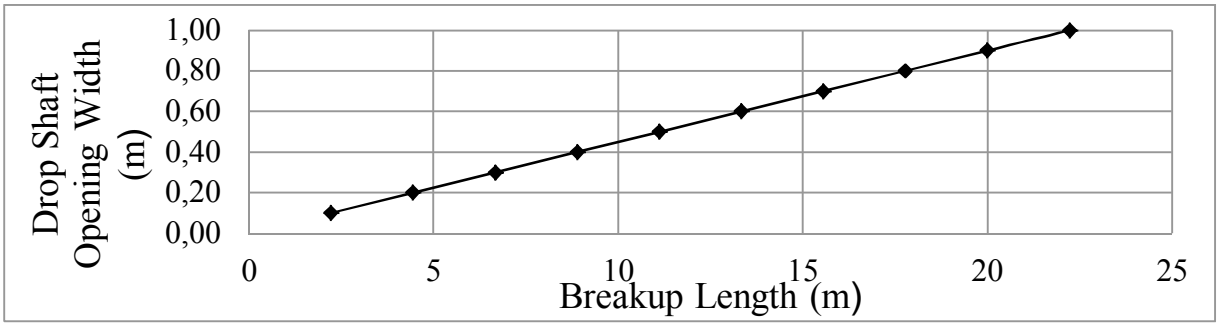

Table A 1.2: Relationship between the drop shaft opening width and the breakup length of the jet

A.2. **Derivation of Equation 3.33**

The following equation is derived:

$$\mathbf{U}_{m,2} = \left(1 - \frac{\alpha_2 \rho_2}{\rho_m}\right) \mathbf{U}_r = (1 - c_2)\mathbf{U}_r \tag{3.33}$$

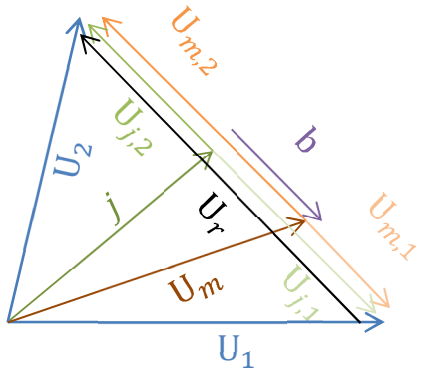

Figure A.2.1: Sketch of the relations between the various velocities

The sketch shown in Figure A.2.1 illustrates the relations between the various velocities used in the formulae. For the derivation equations (3.24), (3.25), (3.27) and (3.32) are used.

$$\mathbf{U}_m = \frac{1}{\rho_m} \sum_{k=1}^{n} \alpha_k \rho_k \mathbf{U}_k \tag{3.24}$$

$$\rho_m = \sum_{k=1}^{n} \alpha_k \rho_k \tag{3.25}$$

$$\mathbf{U}_{m,k} = \mathbf{U}_k - \mathbf{U}_m \tag{3.27}$$

$$\mathbf{U}_r = \mathbf{U}_2 - \mathbf{U}_1 \tag{3.32}$$

Derivation:

$$
\begin{aligned}
\mathbf{U}_{m,2} &= \mathbf{U}_2 - \mathbf{U}_m \\
&= \mathbf{U}_2 - \frac{1}{\rho_m}(\alpha_1\rho_1\mathbf{U}_1 + \alpha_2\rho_2\mathbf{U}_2) \\
&= \left(1 - \frac{1}{\rho_m}\alpha_2\rho_2\right)\mathbf{U}_2 - \frac{1}{\rho_m}\alpha_1\rho_1\mathbf{U}_1 \\
&= \left(1 - \frac{1}{\rho_m}\alpha_2\rho_2\right)\mathbf{U}_r + \left(1 - \frac{1}{\rho_m}\alpha_2\rho_2\right)\mathbf{U}_1 - \frac{1}{\rho_m}(\alpha_1\rho_1\mathbf{U}_1) \\
&= \left(1 - \frac{\alpha_2\rho_2}{\rho_m}\right)\mathbf{U}_r + \left(1 - \frac{\alpha_2\rho_2 - \alpha_1\rho_1}{\rho_m}\right)\mathbf{U}_1 \\
&= \left(1 - \frac{\alpha_2\rho_2}{\rho_m}\right)\mathbf{U}_r - \left(-1 + \frac{\alpha_2\rho_2 + \alpha_1\rho_1}{\rho_m}\right)\mathbf{U}_1 \\
&= \left(1 - \frac{\alpha_2\rho_2}{\rho_m}\right)\mathbf{U}_r - \left(-1 + \frac{\rho_m}{\rho_m}\right)\mathbf{U}_1 \\
&= \left(1 - \frac{\alpha_2\rho_2}{\rho_m}\right)\mathbf{U}_r
\end{aligned}
$$

A.3. **Derivation of Equation 3.43**

The following equation is derived:

$$\rho_m c_2(1 - c_2)\mathbf{U}_r\mathbf{U}_r = \alpha_1(1 - \alpha_1)\frac{\rho_1\rho_2}{\rho_m}\mathbf{U}_{-r}\mathbf{U}_{-r} \tag{3.43}$$

For the derivation, the equations (3.33), (3.34), (3.25) are used:

$$\mathbf{U}_{m,2} = \left(1 - \frac{\alpha_2\rho_2}{\rho_m}\right)\mathbf{U}_r = (1 - c_2)\mathbf{U}_r \tag{A.1}$$

$$c_2 = \frac{\alpha_2\rho_2}{\rho_m} \tag{A.2}$$

$$\rho_m = \sum_{k=1}^{n}\alpha_k\rho_k \tag{3.25}$$

$$\mathbf{U}_r\mathbf{U}_r = \mathbf{U}_{-r}\mathbf{U}_{-r} \tag{3.44}$$

Derivation:

$$\begin{aligned}
\rho_m c_2(1-c_2)\mathbf{U}_r\mathbf{U}_r &= \rho_m \frac{\alpha_2\rho_2}{\rho_m}\left(1-\frac{\alpha_2\rho_2}{\rho_m}\right)\mathbf{U}_r\mathbf{U}_r \\
&= \alpha_2\rho_2\left(\frac{\rho_m}{\rho_m}-\frac{\alpha_2\rho_2}{\rho_m}\right)\mathbf{U}_r\mathbf{U}_r \\
&= \alpha_2\rho_2\left(\frac{\alpha_1\rho_1+\alpha_2\rho_2-\alpha_2\rho_2}{\rho_m}\right)\mathbf{U}_r\mathbf{U}_r \\
&= \left(\frac{\alpha_2\rho_2\alpha_1\rho_1}{\rho_m}\right)\mathbf{U}_r\mathbf{U}_r \\
&= \frac{\alpha_1(1-\alpha_1)\rho_1\rho_2}{\rho_m}\mathbf{U}_r\mathbf{U}_r \\
&= \alpha_1(1-\alpha_1)\frac{\rho_1\rho_2}{\rho_m}\mathbf{U}_{-r}\mathbf{U}_{-r}
\end{aligned}$$

A.4. **Derivation of Equation 3.48**

The following equation is derived:

$$\mathbf{U}_m = \mathbf{j} + \alpha_1(1-\alpha_1)\frac{\rho_1-\rho_2}{\rho_m}\mathbf{U}_{-r} \qquad (3.48)$$

Looking at the sketch shown in Figure A.2.1 the correlation between $\mathbf{U}_m$ and $\mathbf{j}$ can be expressed by using $\mathbf{b}$ as follows:

$$\begin{aligned}
&\mathbf{U}_m = \mathbf{j} + \mathbf{b} \\
&\mathbf{U}_{m,2} = \alpha_2\mathbf{U}_r \\
&\mathbf{U}_{j,2} = \mathbf{U}_2 - \mathbf{j} \\
&\qquad = \mathbf{U}_2 - \alpha_1\mathbf{U}_1 - \alpha_2\mathbf{U}_2 \\
&\qquad = (1-\alpha_2)\mathbf{U}_2 - \alpha_1\mathbf{U}_1 \\
&\qquad = \alpha_1\mathbf{U}_2 - \alpha_1\mathbf{U}_1 \\
&\qquad = \alpha_2(\mathbf{U}_2 - \mathbf{U}_1) \\
&\qquad = \alpha_1\mathbf{U}_r
\end{aligned} \qquad (A.3)$$

b is unknown and must should be replaced with known correlations:

$$
\begin{aligned}
\mathbf{b} &= \mathbf{U}_{j,2} - \mathbf{U}_{m,2} \\
&= \alpha_1 \mathbf{U}_r - \left(1 - \frac{\alpha_2 \rho_2}{\rho_m}\right) \mathbf{U}_r \\
&= \left(\alpha_1 - 1 + \frac{\alpha_2 \rho_2}{\rho_m}\right) \mathbf{U}_r \\
&= -\left(-\alpha_1 + 1 - \frac{\alpha_2 \rho_2}{\rho_m}\right) \mathbf{U}_r \\
&= -\left((1 - \alpha_1) - \frac{\alpha_2 \rho_2}{\rho_m}\right) \mathbf{U}_r \\
&= -\left(\frac{\alpha_2 \rho_m}{\rho_m} - \frac{\alpha_2 \rho_2}{\rho_m}\right) \mathbf{U}_r \\
&= -\left(\frac{\alpha_1 \rho_1 + \alpha_2 \rho_2 - \rho_2}{\rho_m}\right) \alpha_2 \mathbf{U}_r \\
&= -\left(\frac{\alpha_1 \rho_1 + (\alpha_2 - 1)\rho_2}{\rho_m}\right) \alpha_2 \mathbf{U}_r \\
&= -\left(\frac{\alpha_1 \rho_1 - \alpha_1 \rho_2}{\rho_m}\right) \alpha_2 \mathbf{U}_r \\
&= -\left(\frac{\rho_1 - \rho_2}{\rho_m}\right) \alpha_1 \alpha_2 \mathbf{U}_r \\
&= \alpha_1 (\mathbf{1} - \alpha_1) \left(\frac{\rho_1 - \rho_2}{\rho_m}\right) \mathbf{U}_{-r}
\end{aligned}
\tag{A.4}
$$

A.5. **Exemplary Calculation of the Inlet Conditions Replacing the Falling Jet in the Simulations**

As the developed model is not able to model a falling jet, the jet is replaced by an inlet boundary. For the boundary definition it is assumed that the complete potential energy of the upstream water is translated into kinetic energy. To simulate the filling process of a lock with a defined water inflow rate and a fixed

air-water ratio, the necessary inlet area is calculated as described below. The potential energy of the upstream water body is equated with the kinetic energy of the plunging jet:

$$m \cdot g \cdot h = \frac{1}{2} \cdot m \cdot v^2 \tag{A.5}$$

To calculate the impact velocity of the jet, the equation is solved for v:

$$v = \sqrt{2 \cdot g \cdot h} \tag{A.6}$$

Knowing the water inflow rate Q_{Water} and the air-water ratio, the total inflow rate can be calculated:

$$Q_{total} = \frac{Q_{Water}}{\alpha} \tag{A.7}$$

The necessary inlet area A can be calculated with:

$$A = \frac{Q_{total}}{\sqrt{2 \cdot g \cdot h}} \tag{A.8}$$

In the simulations of this study, the width of the model is defined by the lock chamber width. Therefore the inlet area is varied by defining different inlet breadths.

A.6. **Illustrations of the Numerical Results of Chapter 6.1**

In the section below the numerical results of the simulations of chapter 6.2 are visualised. For each simulation two screenshots are presented. The screenshots on the left show the water-air distribution the screenshots on the right show the velocity distribution in the front part of the lock projected on a vertical slice parallel to the symmetry axis. The slice was located at a distance of 1.35 m from the middle axis. The velocity distribution is visualised with a line integral convolution (LIC) vector field visualisation method provided by the visualisation software Paraview. The method brings out the vortices forming in the flow field by producing streaking patterns that follow vector field tangents. The plots of Case 1 and Case 2 with an inflow rate of 20 m³/s, which are also shown in 6 and Figure 6.7, are replicated in the following series of illustrations.

Case 1 - Q = 10 m³/s

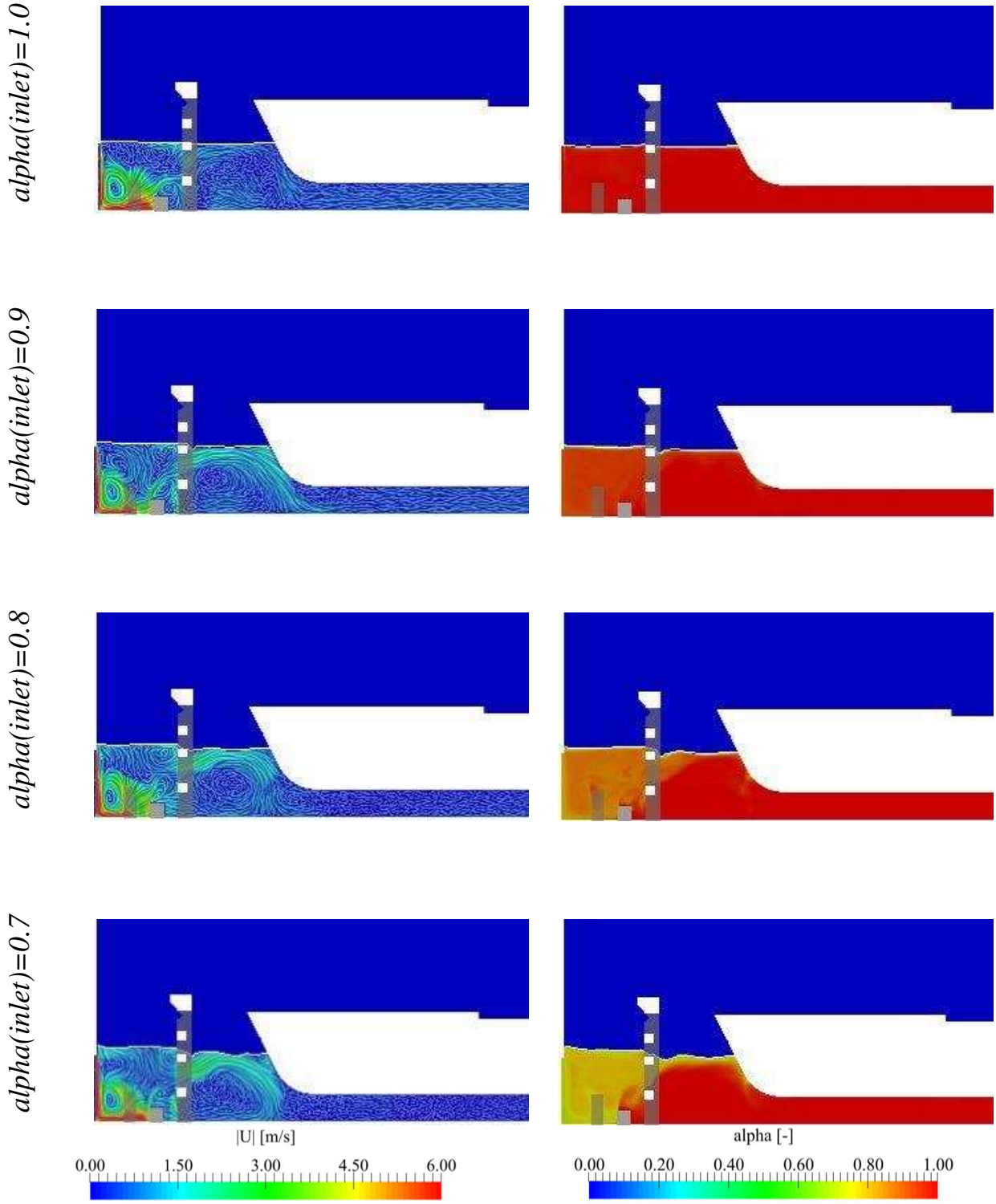

Figure A.4.1: Results from the simulations of Case 1 with an inflow discharge of 10 m³/s

Case 1 - Q = 15 m³/s

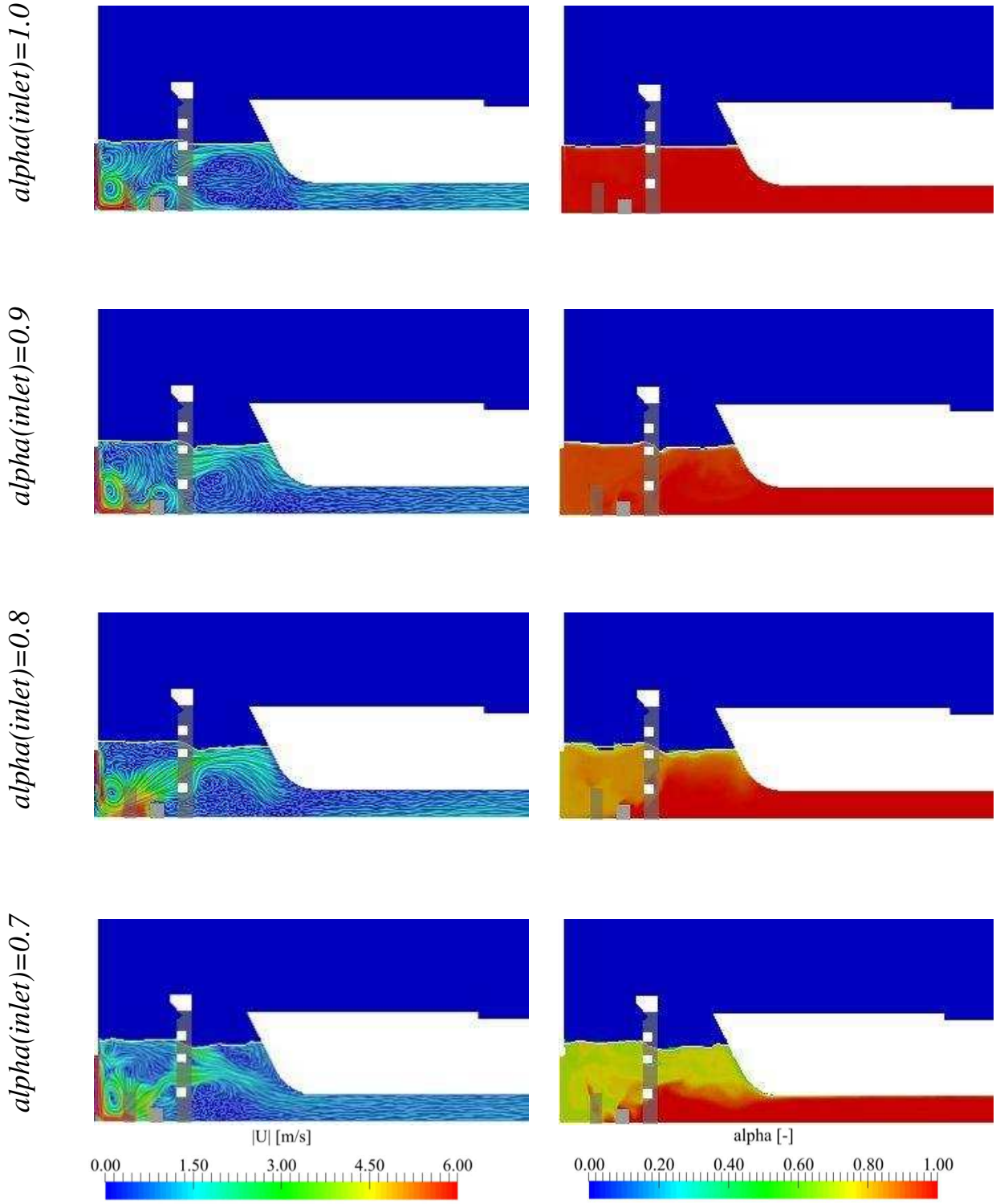

Figure A.4.2: Results from the simulations of Case 1 with an inflow discharge of 15 m³/s

Case 1 - Q = 20 m³/s

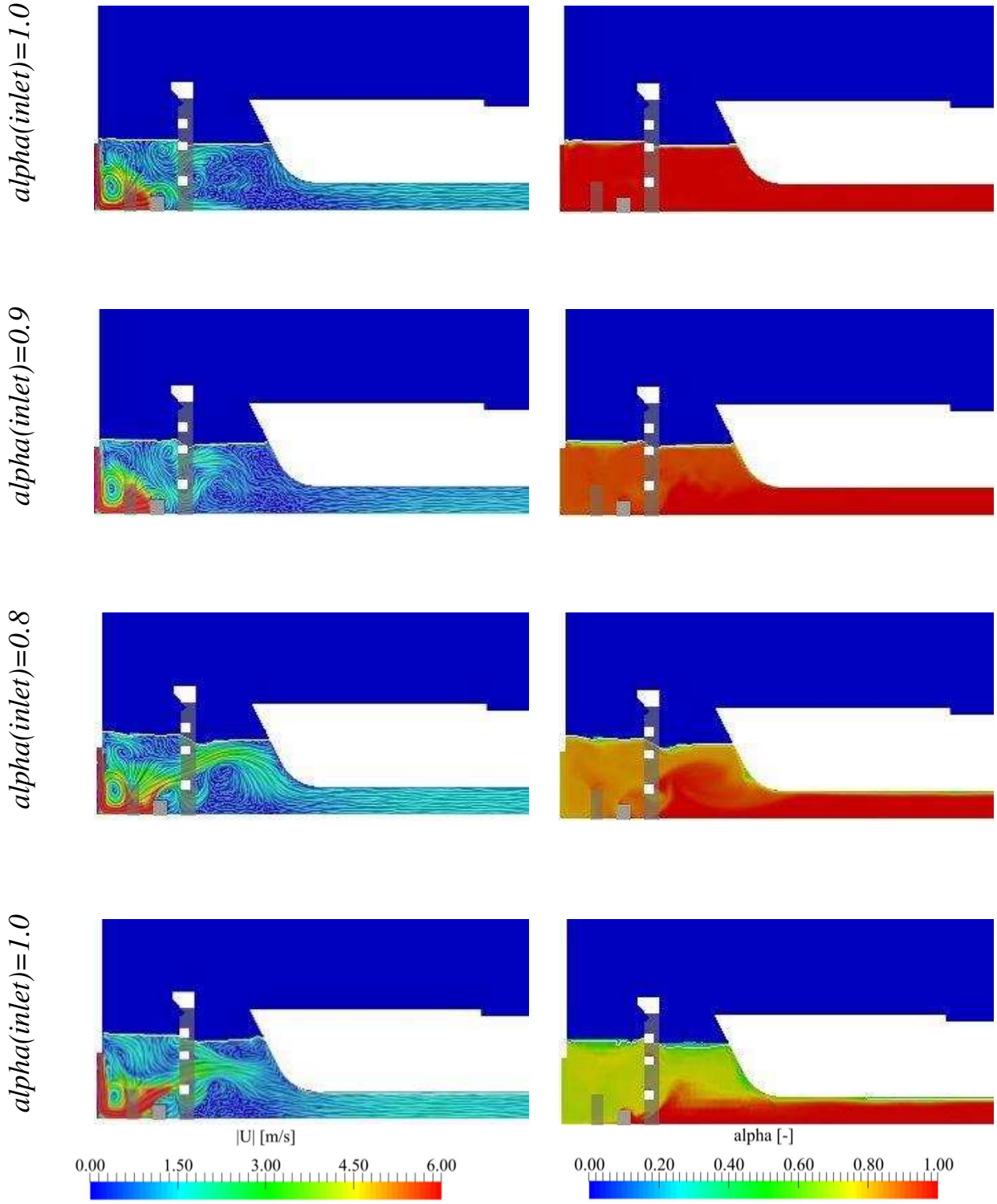

Figure A.4.3: Results from the simulations of Case 1 with an inflow discharge of 20 m³/s

Case 1 - Q = 30 m³/s

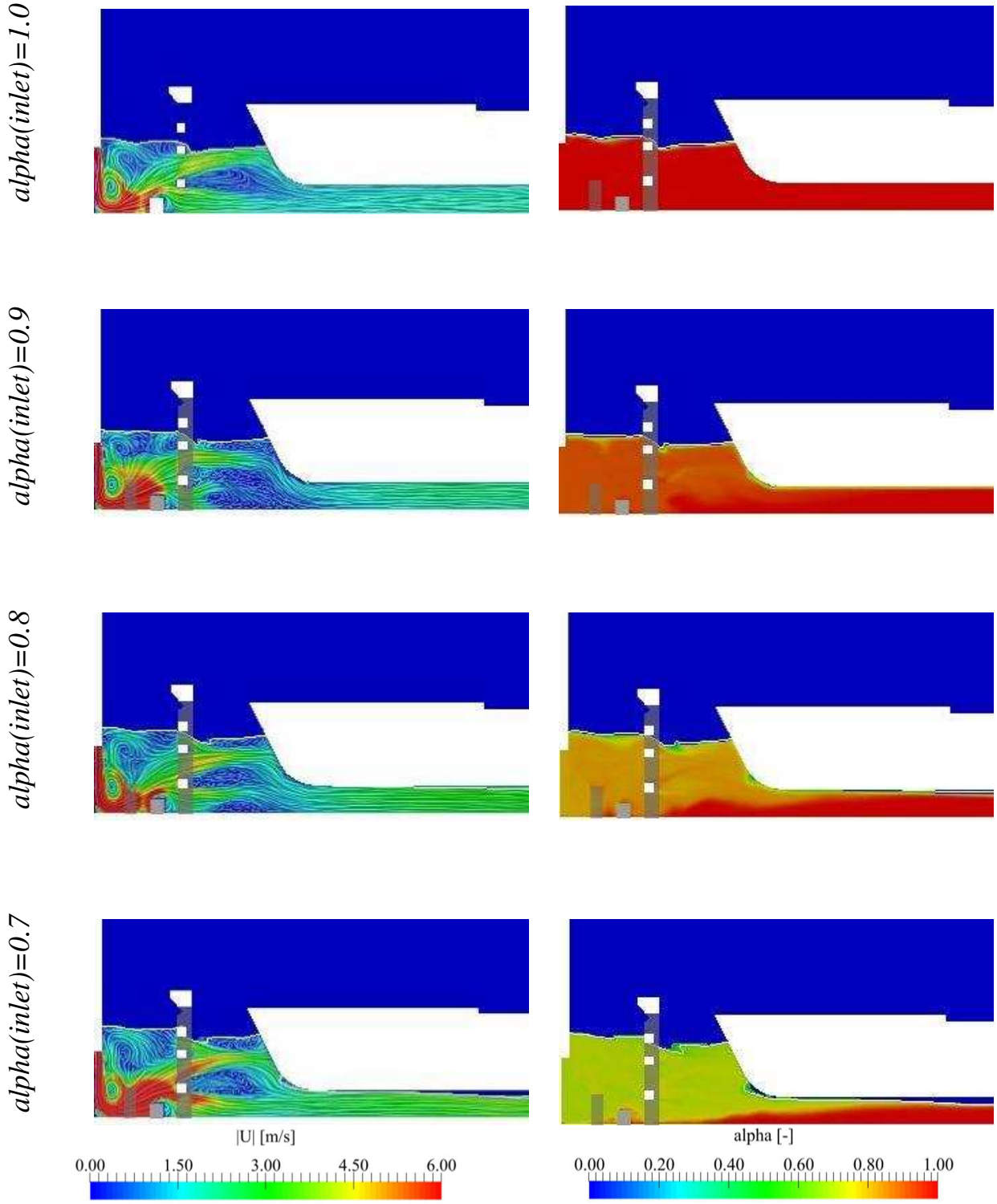

Figure A.4.4: Results from the simulations of Case 1 with an inflow discharge of 30 m³/s

Case 2 - Q = 10 m³/s

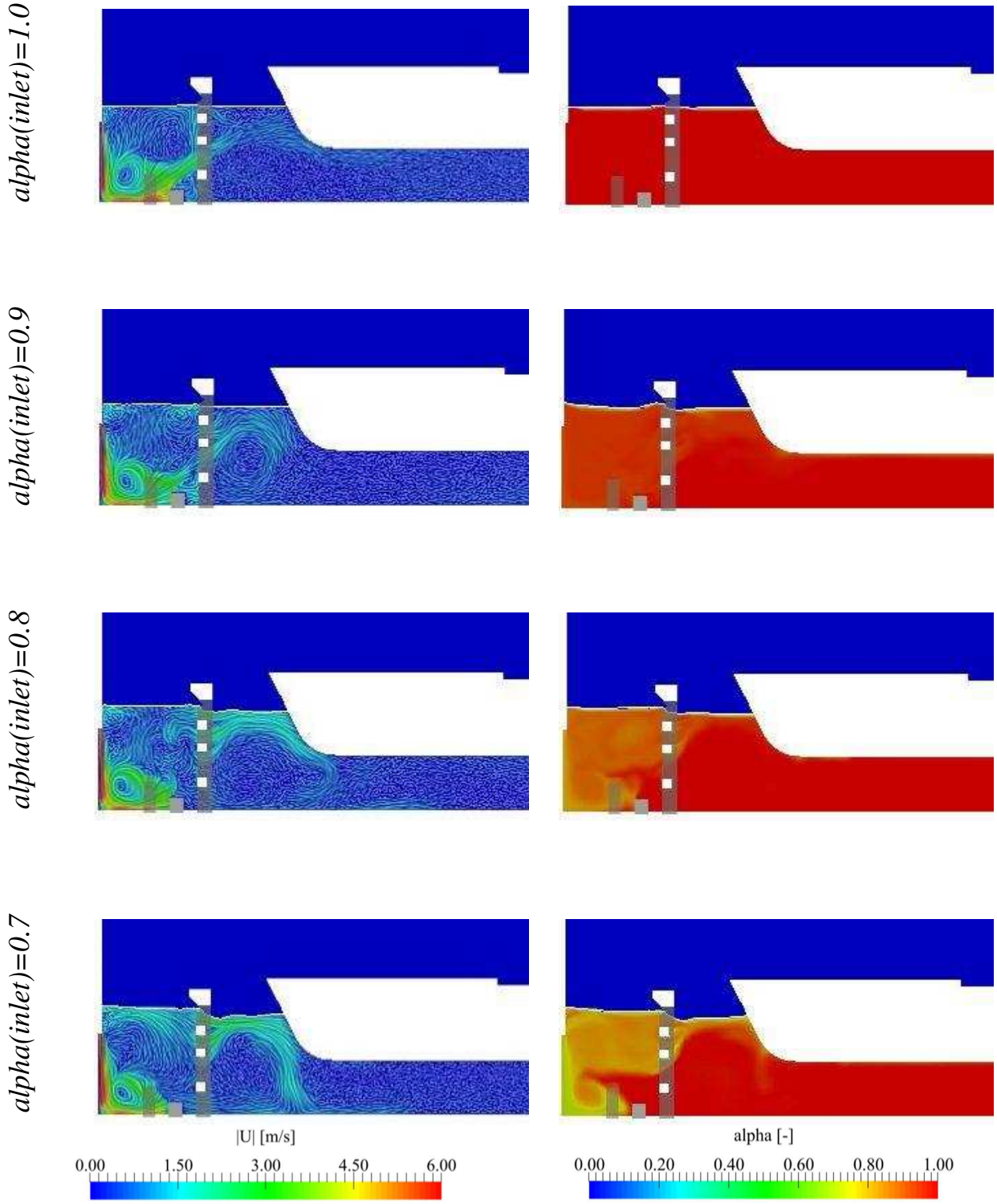

Figure A.4.5: Results from the simulations of Case 2 with an inflow discharge of 10 m³/s

Case 2 - Q = 15 m³/s

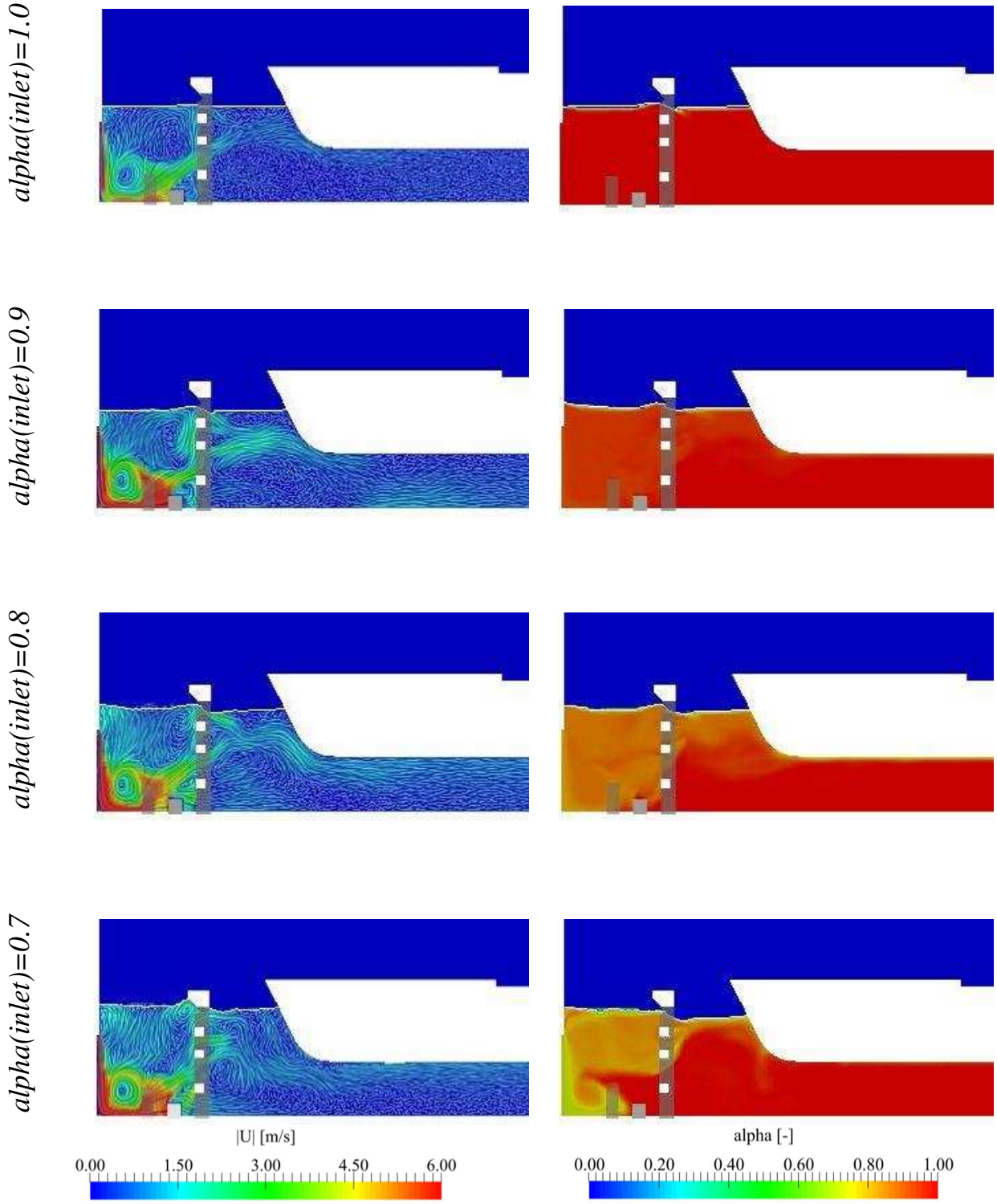

Figure A.4.6: Results from the simulations of Case 2 with an inflow discharge of 15 m³/s

Case 2 - Q = 20 m³/s

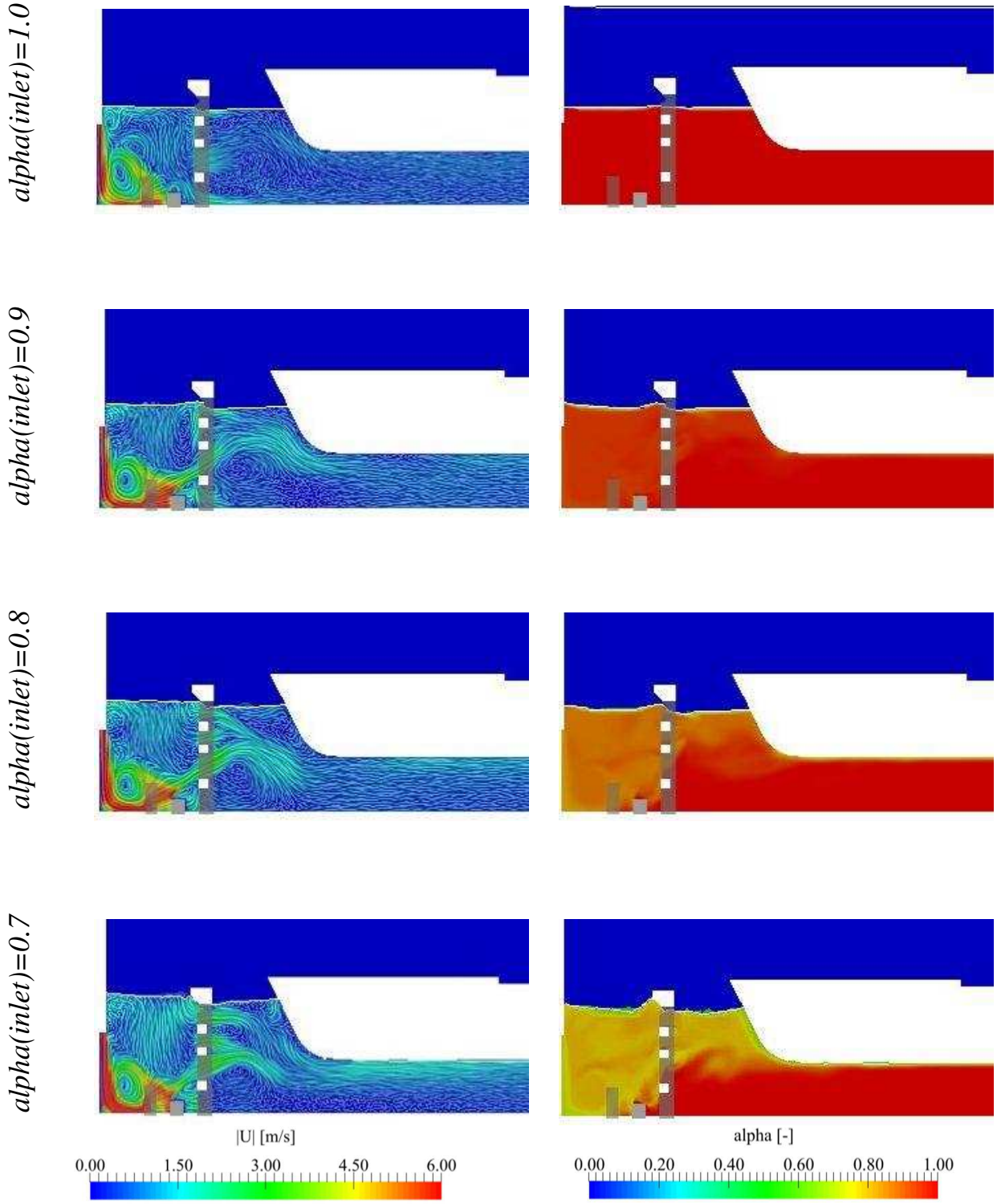

Figure A.4.7: Results from the simulations of Case 2 with an inflow discharge of 20 m³/s

Case 2 - Q = 30 m³/s

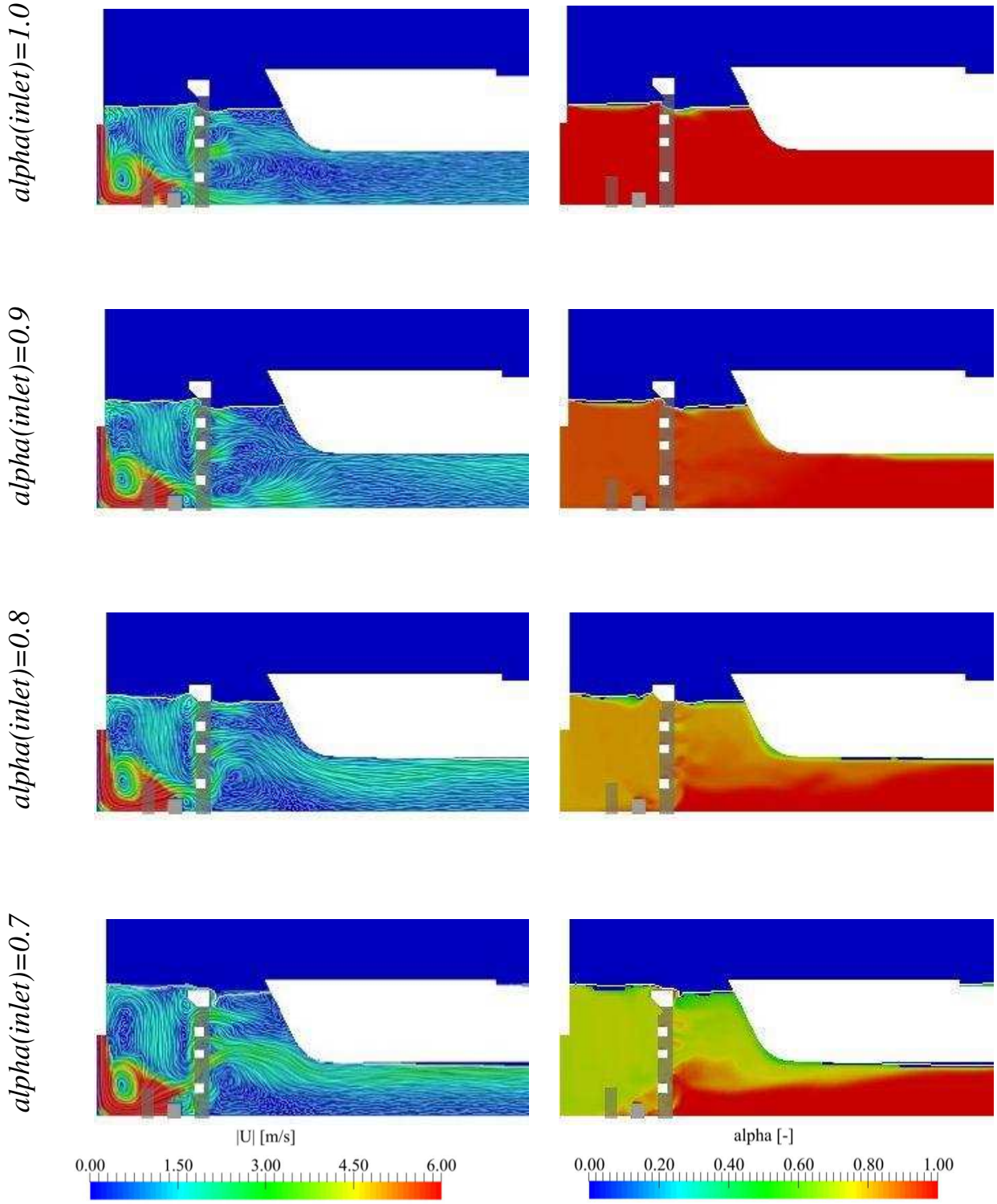

Figure A.4.8: Results from the simulations of Case 2 with an inflow discharge of 30 m³/s

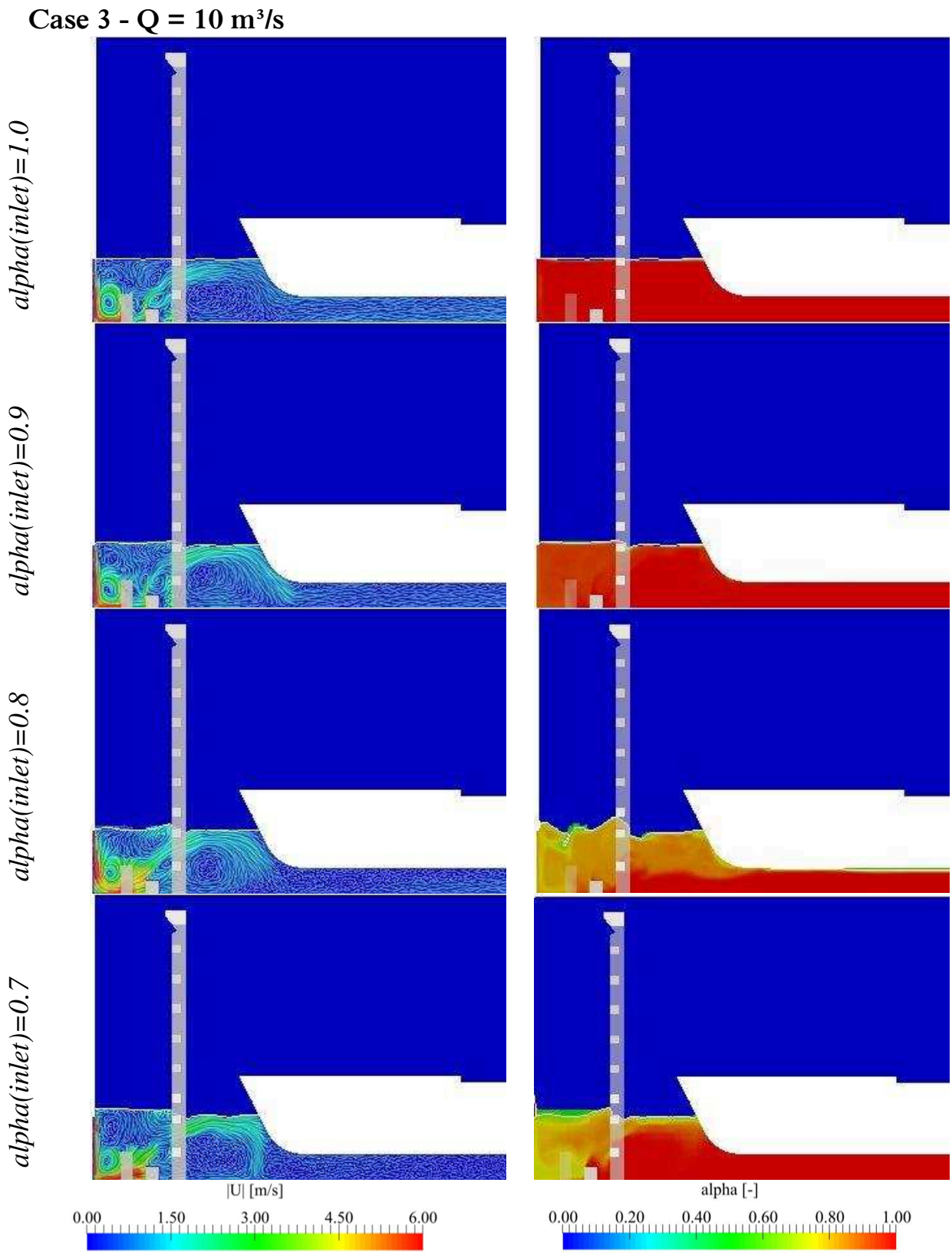

Figure A.4.9: Results from the simulations of Case 3 with an inflow discharge of 10 m³/s

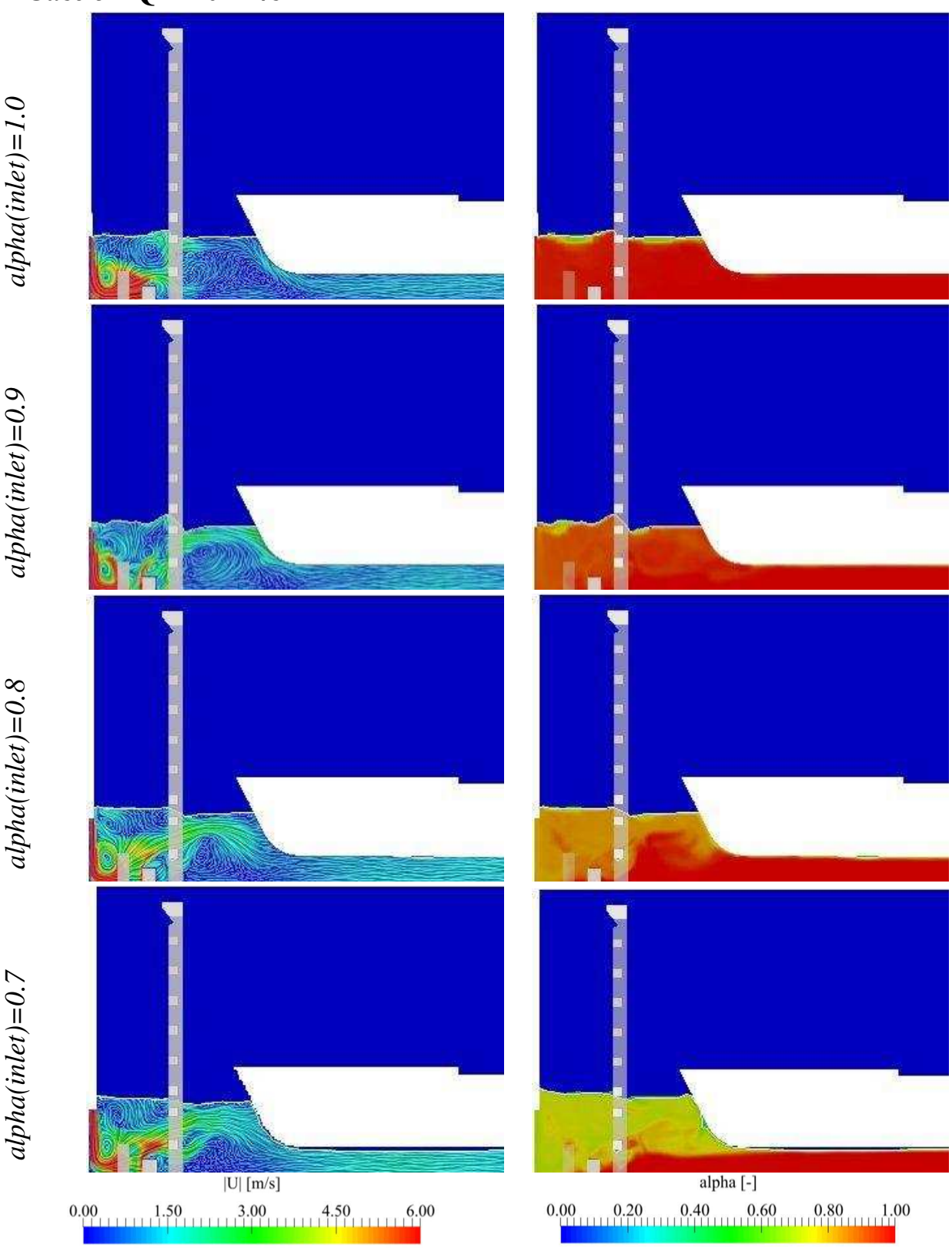

Figure A.4.10: Results from the simulations of Case 3 with an inflow discharge of 20 m³/s

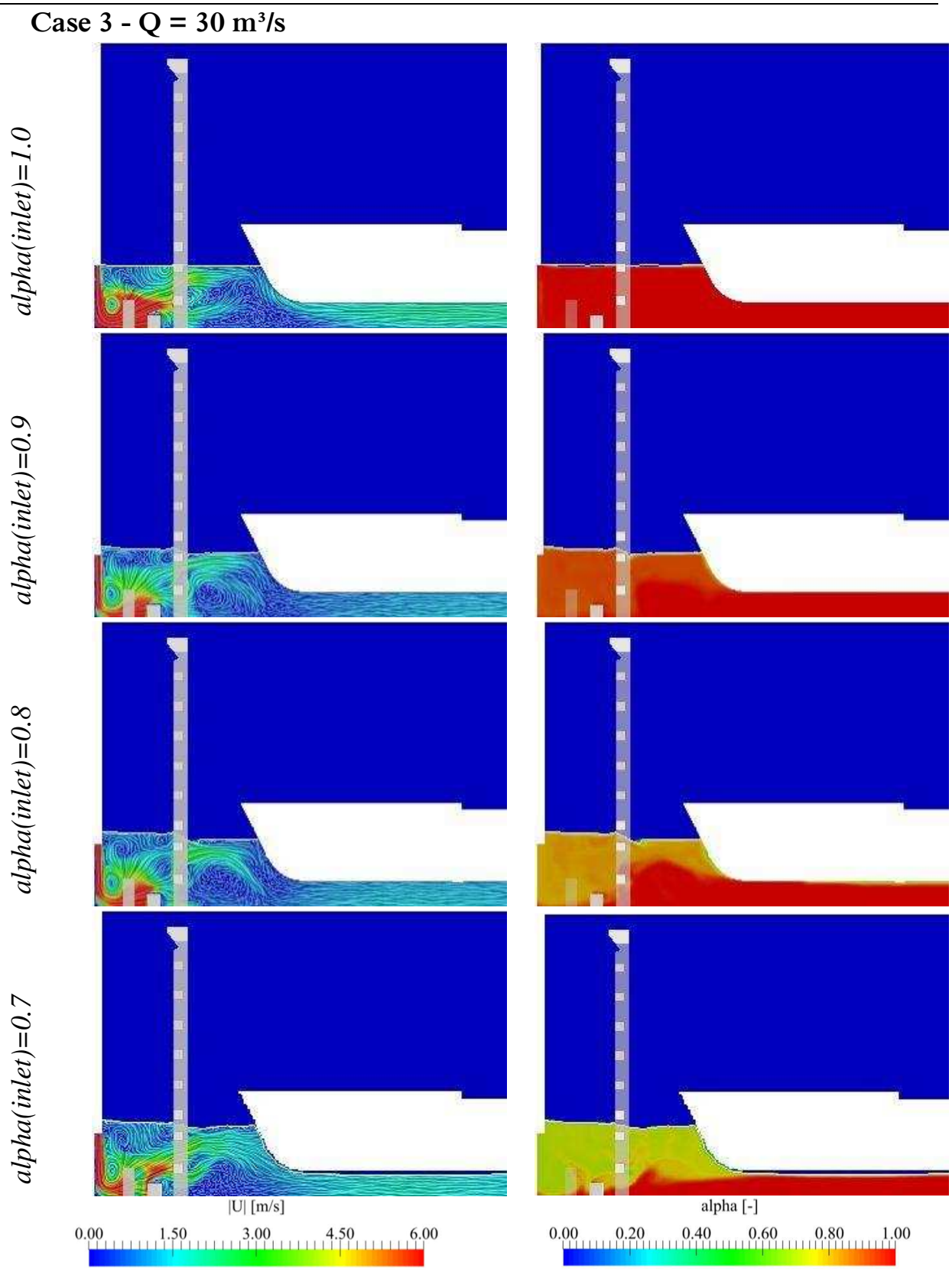

Figure A.4.11: Results from the simulations of Case 3 with an inflow discharge of 30 m³/s

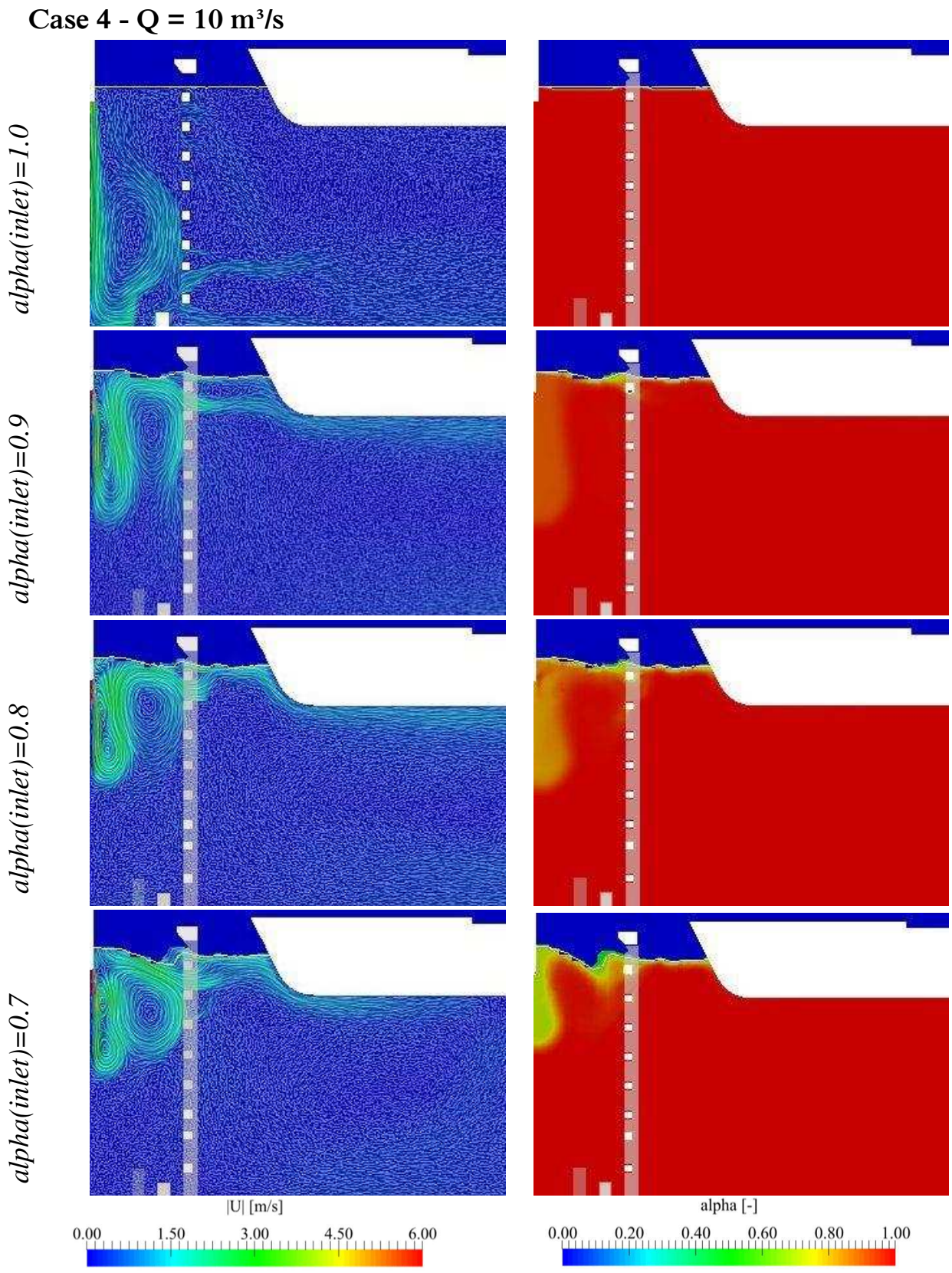

Figure A.4.12: Results from the simulations of Case 4 with an inflow discharge of 10 m³/s

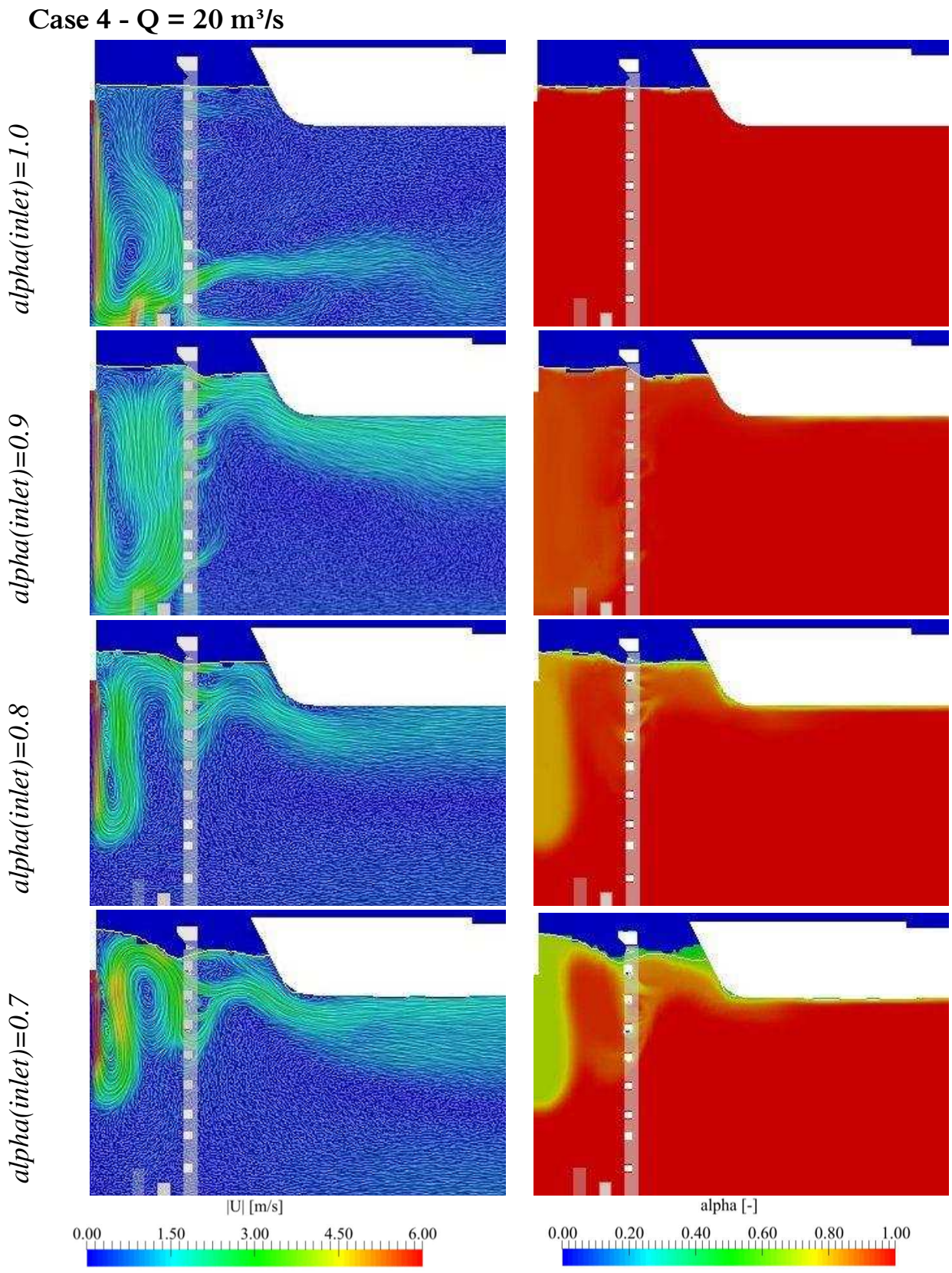

Figure A.4.13: Results from the simulations of Case 4 with an inflow discharge of 20 m³/s

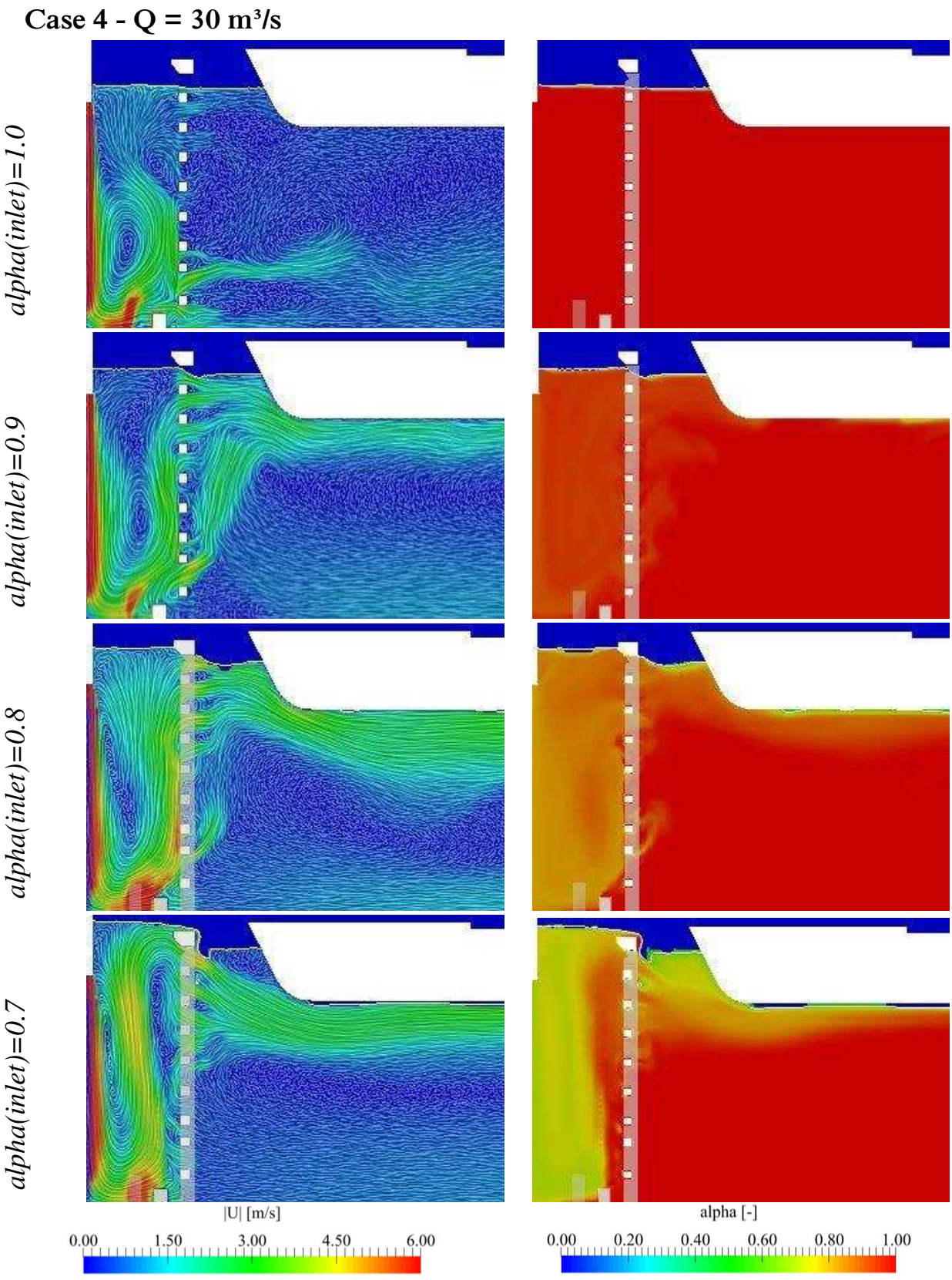

Figure A.4.14: Results from the simulations of Case 4 with an inflow discharge of 30 m³/s

A.7. **Number Values of the Ship Forces of Cases 1-4**

Table A.7.1: Resulting forces on the ship

Q	Air-Water Ratio (alpha)	Case 1 Ship Forces	Case 2 Ship Forces	Case 3 Ship Forces	Case 4 Ship Forces
[m³/s]	[-]	[kN]	[kN]	[kN]	[kN]
10	0	-1.2	-0.3	-1.3	-1.5
10	0.9	-0.6	2.3	-0.3	-0.7
10	0.8	-1.9	1.8	1.5	-0.4
10	0.7	5.2	20.0	3.7	0.3
15	0	-2.1	-3.5	-	-
15	0.9	3.9	8.8	-	-
15	0.8	10.1	32.8	-	-
15	0.7	51.5	70.7	-	-
20	0	-2.5	-2.7	-0.5	-1.9
20	0.9	8.6	17.8	17.7	9.9
20	0.8	33.8	55.0	40.0	38.6
20	0.7	71.4	109.9	81.7	67.0
30	0	-3.7	-5.2	-0.6	-3.0
30	0.9	15.8	29.8	20.8	17.8
30	0.8	46.7	84.6	57.8	55.5
30	0.7	99.5	160.0	103.0	136.2

Remark: A positive force points towards the downstream end of the lock chamber. A negative force points towards the upstream end of the chamber.

References

Bates, P.D., Lane, S.N., Ferguson, R.I. (2005). *Computational fluid dynamics: Applications in environmental hydraulics*. John Wiley & Sons Inc. , Hoboken, NJ, USA.

Baylar, A., Hanbay, D., Batan, M. (2009). Application of least square support vector machines in the prediction of aeration performance of plunging overfall jets from weirs. *Expert Systems with Applications* 36(4), 8368–8374, doi:10.1080/00221680309506897.

Behrens, T. (2009). *OpenFOAM's basic solvers for linear systems of equations*, *Technical Report*, Technical University of Denmark, http://www.tfd.chalmers.se/~hani/kurser/OS_CFD_2008/TimBehrens/tibeh-report-fin.pdf.

Bohórquez, P. (2008). Study and Numerical Simulation of Sediment Transport in Free-Surface Flow. *Dissertation*. University of Malaga, Spain.

Bollaert, E.F.R. (2010). Physics of Rock Scour: The Power of the Bubble. *International Conference on Scour and Erosion (ICSE-5) 2010*, San Francisco, California, United States, November 7-10, S.E. Burns, S.K. Bhatia, C.M.C. Avila, B.E. Hunt, eds., 21–40.

Boris, J.P., Book, D.L. (1973). Flux-corrected transport. I. SHASTA, A fluid transport algorithm that works. *Journal of Computational Physics* 11(1), 38–69.

Boussinesq, J. (1897). *Théorie de l'écoulement tourbillonnant et tumultueux des liquides dans les lits rectilignes a grande section*. Gauthier-Villars et Fils, Paris.

Brackbill, J.U., Kothe, D.B., Zemach, C. (1992). A Continuum Method for Modeling Surface Tension. *Journal of Computational Physics* 100(2), 335–354, doi:10.1016/0021-9991(92)90240-Y.

Brattberg, T., Chanson, H. (1998). Air entrapment and air bubble dispersion at two-dimensional plunging water jets. *Chemical Engineering Science* 53(24), 4113–4127.

Brennan, D. (2001). The numerical simulation of two phase flows in settling tanks. *Dissertation*. London.

Castillo, E., Luis, G. (2006). Aerated jets and pressure fluctuation in plunge pools *The 7th International Conference on Hydroscience and Engineering ICHE-2006. Proceedings of the 7th International Conference on Hydroscience and Engineering*, Philadelphia, USA, 10-13 September, M. Piasecki, S.S.Y. Wang, K.P. Holz, M. Kawahara, A. Gonzalez, B. Beran, eds.

Cebeci, T., Bradshaw, P. (1977). *Momentum transfer in boundary layers*. Hemisphere Publishing Corporation, Washington.

Cerne, G., Petelin, S., Tiselj, I. (2001). Coupling of the Interface Tracking and the Two-Fluid Models for the Simulation of Incompressible Two-Phase Flow. *Journal of Computational Physics* 171(2), 776–804, doi:10.1006/jcph.2001.6810.

Cerne, G., Tiselj, I. (1999). Simulation of the instability in the stratified two-fluid system *International Conference for Nuclear Energy in Central Europe. Proceedings of the International Conference for Nuclear Energy in Central Europe*, Portorov, Slovenia, 6.-9. September, 201–208.

Cerne, G., Tiselj, I., Petelin, S. (2000). Model for the Simulation of the Interface Dispersion *International Conference for Nuclear Energy in Central Europe. Proceedings of the International Conference for Nuclear Energy in Central Europe*, Bled, Slovenia, 11-14 September, 6–9.

Chalabi, A. (1997). On convergence of numerical schemes for hyperbolic conservation laws with stiff source terms. *Mathematics of Computation of the American Mathematical Society* 66(218), 527–545, http://www.ams.org/journals/mcom/1997-66-218/S0025-5718-97-00817-X/S0025-5718-97-00817-X.pdf.

Chanson, H. (1995). Predicting Oxygen Content Downstream of Weirs, Spillways and Waterways. *Proceedings of the Institution of Civil Engineers, Water and Maritime Engineering* 112(1), 20–30. http://espace.library.uq.edu.au/view/UQ:9295/Awgt_12b.doc.pdf.

Chanson, H. (2004). *Hydraulics of Open Channel Flow*. 2. Aufl. Elsevier professional.

Chanson, H., Jaw-Fang, L. (1997). Plunging jet characteristics of plunging breakers. *Coastal Engineering* 31(1), 125–141.

Churchfield, M.J. (2010). *A Description of the OpenFOAM Solver buoyantBoussinesqPisoFoam*. National Renewable Energy Laboratory, National Wind Technology Center, https://docs.google.com/file/d/0B_8DoNQWsRB2OTNmZDk3ZTktYjhjNS00MDdhLWJlZTMtMDMwNDA0OTdhNDM4/edit?ddrp=1&pli=1&hl=en.

Clift, R., Grace, J.R., Weber, M.E. (1987). *Bubbles, drops, and particles*. Academic Press New York.

Croce, R., Griebel, M., Schweitzer, M. (2004). A Parallel Level Set Approach for Two-Phase Flow Problems with Surface Tension in Three Space Dimensions. *Preprint 157*. Sonderforschungsbereich 611, Universität Bonn.

Cummings, P.D., Chanson, H. (1997). Air entrainment in the developing flow region of plunging jets—part 1: theoretical development. *Journal of fluids engineering* 119(3), 597–602.

Cummings, P.D., Chanson, H. (1999). An experimental study of individual air bubble entrainment at a planar plunging jet. *Chemical Engineering Research and Design* 77(2), 159–164.

Damian, S.M. (2013). An Extended Mixture Model for the Simultaneous Treatment of Short and Long Scale Interfaces. *Doctoral Thesis*. Universidad Nacional Del Litoral, Santa Fe, Argentinia.

Darwish, M.S., Moukalled, F. (2003). TVD schemes for unstructured grids. *International Journal of heat and mass transfer* 46(4), 599–611.

Davies, R.M., Taylor, G. (1950). The Mechanics of Large Bubbles Rising through Extended Liquids and through Liquids in Tubes. *Proceedings of the Royal Society A: Mathematical, Physical and Engineering Sciences* 200(1062), 375–390, doi:10.1098/rspa.1950.0023.

Denner, F., van Wachem, B.G.M. (2015). TVD differencing on three-dimensional unstructured meshes with monotonicity-preserving correction of mesh skewness. *Journal of Computational Physics* 298, 466–479.

Deshpande, S.S., Anumolu, L., Trujillo, M.F. (2012). Evaluating the performance of the two-phase flow solver interFoam. *Computational science & discovery* 5(1), 14016.

Egorov, Y., Boucker, M., Martin, A., Pigny, S., Scheuerer, M., Willemsen, S. (2004). Validation of CFD codes with PTS-relevant test cases. *5th Euratom Framework Programme ECORA project*.

Falvey, H.T. (1980). Air-Water Flow in Hydraulic Structures. *Engineering Monograph 41*. United States Department of the Interior - Water and Power Resources Service.

Ferziger, J.H., Peric, M. (1997). *Computational methods for fluid dynamics*. 2. print., corr. Springer, Berlin u.a.

Gastaldo, L., Herbin, R., Latche, J.-C. (2011). A discretization of the phase mass balance in fractional step algorithms for the drift-flux model. *IMA Journal of Numerical Analysis* 31(1), 116–146, doi:10.1093/imanum/drp006.

Gaudin, A.M. (1957): *second edition*. McGraw-Hill Book Co. Inc., New York City.

Gebhardt, M. (2010). On the causes of vibrations and the effects of countermeasures at water-filled inflatable dams *1st European IAHR Congress. Proceedings of the 1st European IAHR Congress Edinburgh*, Edinburgh, 4.-6.5.2010.

Gobbetti, C. (2013). Design of the filling and emptying system of the new Panama Canal locks. *Journal of Applied Water Engineering and Research* 1(1), 28–38, doi:10.1080/23249676.2013.827899.

Gopala, V.R., van Wachem, B.G. (2008). Volume of fluid methods for immiscible-fluid and free-surface flows. *Chemical Engineering Journal* 141(1–3), 204–221, doi:10.1016/j.cej.2007.12.035.

Haberman, W.L., Morton, R.K. (1953). An experimental investigation of the drag and shape of air bubbles rising in various liquids. *Report No. 802*. David Taylor Model Basin.

Harten, A. (1984). On a class of high resolution total-variation-stable finite-difference schemes. *SIAM Journal on Numerical Analysis* 21(1), 1–23.

Heller, V. (2011). Scale effects in physical hydraulic engineering models. *Journal of Hydraulic Research* 49(3), 293–306, doi:10.1080/00221686.2011.578914.

Hibiki, T., Ishii, M. (2003). One-dimensional drift-flux model and constitutive equations for relative motion between phases in various two-phase flow regimes. *International Journal of heat and mass transfer* 46(25), 4935–4948.

Hill, D.P. (1998). The Computer Simulation of Dispersed Two-Phase Flow. *Doctoral Thesis*. Imperial College of Science, Technology & Medicine, London, Great Britain.

Hinkelmann, R.-P. (2003). Efficient Numerical Methods and Information-Processing Techniques in Environment Water. *Habilitation*. University of Stuttgart, Stuttgart.

Hirt, C.W., Nichols, B.D. (1981). Volume of fluid (VOF) method for the dynamics of free boundaries. *Journal of Computational Physics* 39(1), 201–225, doi:10.1016/0021-9991(81)90145-5.

Höhne, T., Vallée, C. (2010). Experiments and numerical simulations of horizontal two-phase flow regimes using an interfacial area density model. *The Journal of Computational Multiphase Flows* 2(3), 131–143.

Ishii, M. (1975). *Thermo-fluid dynamic theory of two-phase flow*. Collection de la Direction des études et recherches d'Électricité de France, 22. second edition. Eyrolles, Paris.

Ishii, M. (1977). One-dimensional drift-flux model and constitutive equations for relative motion between phases in various two-phase flow regimes. *Technical Report*. Argonne National Lab., Ill.(USA).

Ishii, M., Mishima, K. (1984). Two-fluid model and hydrodynamic constitutive relations. *Nuclear Engineering and design* 82(2), 107–126.

Ishii, M., Zuber, N. (1979). Drag coefficient and relative velocity in bubbly, droplet or particulate flows. *AIChE Journal* 25(5), 843–855, doi:10.1002/aic.690250513.

Issa, R.I. (1986). Solution of the implicitly discretised fluid flow equations by operator-splitting. *Journal of Computational Physics* 62(1), 40–65.

Jain, S.C. (2001). *Open-channel flow*. John Wiley & Sons, New York.

Jamet, D., Torres, D., Brackbill, J.U. (2002). On the Theory and Computation of Surface Tension: The Elimination of Parasitic Currents through Energy

Conservation in the Second-Gradient Method. *Journal of Computational Physics* 182(1), 262–276, doi:10.1006/jcph.2002.7165.

Jasak, H. (1996). Error Analysis and Estimation for the Finite Volume Method with Applications to Fluid Flows. *Doctoral Thesis*. Imperial College of Science, Technology & Medicine, London, Great Britain.

Jasak, H. (2006a). *Conversation about the VoF solver interFoam: Posting #4*. www.cfd-online.com, http://www.cfd-online.com/Forums/openfoam-solving/59597-surfacescalarfield-ghf-interfoam-how-does-look-like.html.

Jasak, H. (2006b). *Numerical Solution Algorithms for Compressible Flows*. Course prepared for the Aerospace Engineering Program. Zagreb.

Keough, S. (2004). *Optimising the Parallellisation of OpenFOAM Simulations*. DSTO Defence Science and Technology Organisation Australia.

Kobus, H. (1985). *An introduction to air-water flows in hydraulics*. Mitteilungen, Institut für Wasser- und Umweltsystemmodellierung, Universität Stuttgart. Universität Stuttgart, eng.

Kolev, N.I. (2012). *Multiphase flow dynamics 2: Mechanical interactions*. 4th ed. Springer, Berlin.

Kolmogorov, A.N. (1991). Dissipation of Energy in the Locally Isotropic Turbulence. *Proceedings of the Royal Society A: Mathematical, Physical and Engineering Sciences* 434(1890), 15–17, doi:10.1098/rspa.1991.0076.

Kraatz, W. (1989). Flüssigkeitsstrahlen. In *Technische Hydromechanik: Bd. 2. Spezielle Probleme*. G. Bollrich, ed. Verlag für Bauwesen.

Kuzmin, D., Gorb, Y. (2012). A flux-corrected transport algorithm for handling the close-packing limit in dense suspensions. *Journal of Computational and Applied Mathematics* 236(18), 4944–4951.

Launder, B.E., Sharma, B.I. (1974). *Application of the energy-dissipation model of turbulence to the calculation of flow near a spinning disc*. HTS, 74,23. Imperial College of Science and Technology, Dep. of Mechanical Engineering, London.

Leonard, B.P. (1991). The ULTIMATE conservative difference scheme applied to unsteady one-dimensional advection. *Computer methods in applied mechanics and engineering* 88(1), 17–74.

Lima, L.E.M., Rosa, E.S. (2009). One Dimensional Drift Flux Model Applied to Horizontal Slug Flow *20th International Congress of Mechanical Engineering (COBEM 2010). Proceedings of the 20th International Congress of Mechanical Engineering (COBEM 2010)*, Gramado, RS, Brazil.

López, J., Hernández, J., Gómez, P., Faura, F. (2004). A volume of fluid method based on multidimensional advection and spline interface reconstruction. *Journal of Computational Physics* 195(2), 718–742, doi:10.1016/j.jcp.2003.10.030.

Ma, J., Oberai, A.a., Hyman, M.C., Drew, D.A., Lahey, R.T. (2011). Two-fluid modeling of bubbly flows around surface ships using a phenomenological subgrid air entrainment model. *Computers & Fluids* 52, 50–57, doi:10.1016/j.compfluid.2011.08.015.

Ma, J., Oberai, A.a., Lahey, R.T., Drew, D.A. (2011). Modeling air entrainment and transport in a hydraulic jump using two-fluid RANS and DES turbulence models. *Heat and Mass Transfer* 47(8), 911–919, doi:10.1007/s00231-011-0867-8.

Ma, J., Oberai, A.A., Drew, D.A., Lahey, R.T., Moraga, F.J. (2010). A quantitative sub-grid air entrainment model for bubbly flows–plunging jets. *Computers & Fluids* 39(1), 77–86.

Malcherek, A. (2005). *Hydromechanik der Oberflächengewässer*. Außenstelle Küste, Bundesanstalt für Wasserbau, Hamburg.

Manninen, M., Taivassalo, V., Kallio, S., others. (1996). *On the mixture model for multiphase flow*. Technical Research Centre of Finland Finland.

Marschall, H. (2011). Towards the Numerical Simulation of Multi-Scale Two-Phase Flows. *Dissertation*. Technische Universität München.

Matysiak, A. (2007). Euler-Lagrange-Verfahren zur Simulation tropfenbeladener Strömung in einem Verdichtergitter. *Dissertation*. Helmut-Schmidt-Universität / Universität der Bundeswehr, Hamburg.

Meland, R., Gran, I.R., Olsen, R., Munkejord, S.T. (2007). Reduction of parasitic currents in level-set calculations with a consistent discretization of the surface-tension force for the CSF model. *16th Australasian Fluid Mechanics Conference (AFMC): Gold Coast, Queensland, Australia, 3-7 December, 2007*,

P. Jacobs, ed. School of Engineering, the University of Queensland, Brisbane, 862–865.

Menter, F. (1993). Zonal Two Equation k-w Turbulence Models For Aerodynamic Flows *AIAA 23rd Fluid Dynamics, Plasma Dynamics, and Lasers Conference. Proceedings of the 23rd Fluid Dynamics, Plasmadynamics, and Lasers Conference*, Orlando,FL,USA, 06 July 1993 - 09 July 1993. American Institute of Aeronautics and Astronautics, Reston, Virigina.

Menter, F.R., Kuntz, M. (2004). Adaptation of eddy-viscosity turbulence models to unsteady separated flow behind vehicles. In *The aerodynamics of heavy vehicles: trucks, buses, and trains*. R. McCallen, F. Browand, J. Ross, eds. Springer, 339–352.

Moukalled, F.H., Mangani, L., Darwish, M. (2016). *The finite volume method in computational fluid dynamics: An advanced introduction with OpenFOAM® and Matlab®*. Fluid Mechanics and Its Applications, 113. Springer, Cham.

Muzaferija, S., Perić, M., Seidl, V., Yoo, S.-D. (1998). *Entwicklung und Anwendung eines Finite-Volumen-Verfahrens für die Berechnung viskoser Schiffsumströmungen mit freier Oberfläche*. Bericht / Arbeitsbereiche Schiffbau, Technische Universität Hamburg-Harburg, 594. Techn. Univ. Arbeitsbereiche Schiffbau, Hamburg-Harburg, German.

Nabizadeh, H. (1977). *Modellgesetze und Parameteruntersuchungen für den volumetrischen Dampfgehalt in einer Zweiphasenströmung: EIR-Bericht Nr. 323*. Eidgenössisches Institut für Reaktorforschung Würenlingen Schweiz.

Osher, S., Sethian, J.A. (1988). Fronts Propagating with Curvature Dependent Speed: Algorithms Based on Hamilton-Jacobi Formulations. *Journal of Computational Physics* 79(1), 12–49.

Partenscky, H.-W. (1986). *Binnenverkehrswasserbau: Schleusenanlagen*. Springer Berlin Heidelberg, Berlin, Heidelberg.

Pfister, M., Chanson, H. (2012). Discussion: Scale effects in physical hydraulic engineering models Journal of Hydraulic Research, Vol. 49, No. 3 (2011), pp. 293–306. *Journal of Hydraulic Research* 50(2), 244–246.

Pfister, M., Chanson, H. (2014). Two-phase air-water flows: Scale effects in physical modeling. *Journal of Hydrodynamics, Ser. B* 26(2), 291–298, doi:10.1016/S1001-6058(14)60032-9.

PIANC InCom Working Group 155. (2015). *Ship behaviour in locks and lock approaches*. InCom report 155 - March 2015 issue.

Pilliod, J.E., Puckett, E.G. (2004). Second-order accurate volume-of-fluid algorithms for tracking material interfaces. *Journal of Computational Physics* 199(2), 465–502, doi:10.1016/j.jcp.2003.12.023.

Piomelli, U., Balaras, E. (2002). Wall-layer models for large-eddy simulations. *Annual review of fluid mechanics* 34(1), 349–374.

Pope, S.B. (2000). *Turbulent flows*. Cambridge university press.

Porombka, P., Höhne, T. (2015). Drag and turbulence modelling for free surface flows within the two-fluid Euler–Euler framework. *Chemical Engineering Science* 134, 348–359.

Rahman, M., Brebbia, C.A. (2012). *Advances in Fluid Mechanics IX*. WIT Press.

Richardson, J.F., Zaki, W.N. (1997). Sedimentation and fluidisation: Part I. *Chemical Engineering Research and Design* 75, S82-S100.

Roux, S., Wong, J. (2012). The Panama Canal Third Set of Locks Project *BAW-Kolloquium. Innovation mit Tradition: Hydraulischer Entwurf und Betrieb von Wasserbauwerken*, Karlsruhe, 04-05.07.2012. Bundesanstalt für Wasserbau, Karlsruhe, 39–44.

Rusche, H. (2002). Computational Fluid Dynamics of Dispersed Two-Phase Flows at High Phase Fractions. *Doctoral Thesis*. Imperial College of Science, Technology & Medicine, London, Great Britain.

Saad, Y. (2003). *Iterative methods for sparse linear systems*. 2. ed. SIAM, Philadelphia.

Salih, A., Moulic, S.G. (2009). Some numerical studies of interface advection properties of level set method. *Sadhana* 34(2), 271–298.

Samstag, M. (1996). Experimentelle Untersuchungen von Transportphänomenen in vertikalen turbulenten Luft-Wasser-Blasenströmungen. Univ., Diss.-

Karlsruhe, 1996. *Wissenschaftliche Berichte / Forschungszentrum Karlsruhe, Technik und Umwelt*, FZKA 5662. Als Ms. gedr. FZKA, Karlsruhe, German.

Schiller, L., Naumann, A. (1935). A drag coefficient correlation. *Vdi Zeitung* 77(318), 51.

Schulze, L., Rusche, H., Thorenz, C. (2015). Development of a Simulation Procedure for the 3D Modelling of the Filling Process in a Navigation Lock Including Fluid Structure Interaction. Paper 28. *Proceedings of the 7th International PIANC-SMART Rivers Conference 2015*, Buenos Aires, Argentinia, 7.-11.September 2015.

Serizawa, A., Kataoka, I. (2010). *Bubble Flow*. Thermopedia, A-to-Z Guide to Thermodynamics, Heat & Mass Transfer and Fluids Engineering, 2010, http://www.thermopedia.com/content/8/.

Shang, Z., Lou, J., Li, H. (2014). Numerical Simulation of Water Jet Flow Using Diffusion Flux Mixture Model. *Journal of Fluids* 2014(3), 1–6, doi:10.1155/2014/193215.

Shur, M.L., Spalart, P.R., Strelets, M.K., Travin, A.K. (2008). A hybrid RANS-LES approach with delayed-DES and wall-modelled LES capabilities. *International Journal of Heat and Fluid Flow* 29(6), 1638–1649.

Simonnet, M., Gentric, C., Olmos, E., Midoux, N. (2007). Experimental determination of the drag coefficient in a swarm of bubbles. *Chemical Engineering Science* 62(3), 858–866.

Souders, D.T., Hirt, C.W. (2004). Modeling entrainment of air at turbulent free surfaces. *Proceedings of world water and environmental resources congress*, Salt Lake City, USA, 27. June - 1. July, 1–10.

Spalart, P.R., Deck, S., Shur, M.L., Squires, K.D., Strelets, M.K., Travin, A. (2006). A new version of detached-eddy simulation, resistant to ambiguous grid densities. *Theoretical and computational fluid dynamics* 20(3), 181–195.

Spalart, P.R., Jou, W.H., Strelets, M., Allmaras, SR. (1997). Comments on the feasibility of LES for wings, and on a hybrid RANS/LES approach. *Advances in DNS/LES* 1, 4–8.

Stamm, J., Helbig, U., Gierra, T. (2013). Lufteintrag - Eine Herausforderung bei physikalischen und numerischen Modellierungen. *Wasserwirtschaft* 103(5).

Štrubelj, L., Tiselj, I. (2009). Interface sharpening in simulations with two-fluid model. *International journal for numerical methods in engineering*.

Strybny, J., Thorenz, C., Croce, R., Engel, M. (2006). A Parallel 3D Free Surface Navier-Stokes Solver For High Performance Computing at the German Waterways Administration. *Proceedings of the 7th International Conference on Hydroscience and Engineering (ICHE-2006)*, Philadelphia, USA, 10.-13.09.2006.

Sweby, P.K. (1984). High resolution schemes using flux limiters for hyperbolic conservation laws. *SIAM Journal on Numerical Analysis* 21(5), 995–1011.

Tapia, X.P. (2009). Modelling of wind flow over complex terrain using OpenFoam. *Master's thesis.* University of Gävle.

Thorenz, C. (2009). Computational fluid dynamics in lock design - State of the art. In *WORKSHOP - PIANC Report n°106 on Locks - Innovations In Navigation Lock Design*, Paper 10: 1-4.

Thorenz, C. (2010). Numerical evaluation of filling and emptying systems for the new Panama Canal locks *32nd PIANC Congress, 125th anniversary PIANC - setting the course, PIANC MMX Congress. PIANC MMX Congress Liverpool UK papers*, Liverpool, UK, 11.-14.05.2010.

Thorenz, C. (2012). A novel filling system for high lift locks. In *Staubauwerke: Planen, Bauen, Betreiben ; 35. Dresdner Wasserbaukolloquium 2012, 08 - 09. März 2012*. Wasserbauliche Mitteilungen, 47., ed. Selbstverl. der Techn. Univ, Dresden, 503–512.

Thorenz, C., Belzner, F., Hartung, T., Schulze, L. (2017). Numerische Methoden zur Simulation von Schleusenfüllprozessen. In *BAWMitteilungen Nr. 100: Kompetenz für die Wasserstraßen – Heute und in Zukunft Forschungs- und Entwicklungsprojekte der BAW*. Bundesanstalt für Wasserbau, Karlsruhe, 91–108.

Thorenz, C., Kemnitz, B. (2006). Füll- und Entleersysteme von Schleusen - aktuelle Entwicklungen und numerische Simulation *36. Internationales Wasserbau-Symposium Aachen. Spannungsfeld Fliessgewässer*. Mitteilungen des Instituts für Wasserbau und Wasserwirtschaft der Rheinisch-Westfälischen

Technischen Hochschule Aachen, 146, Aachen, 5.-6. Januar 2006. Shaker, Aachen, M/1-M/18.

Thorenz, C., Strybny, J. (2012). On the numerical modeling of filling-emptying systems for locks. *Proceedings of 10th International Conference on Hydroinformatics - HIC 2012*, Hamburg, 14.-18. July, R.-P. Hinkelman, Y. Liong, D. Savic, K.-F. Daemrich, P. Fröhle, D. Jacob, eds. Tu Tech Innovation, Hamburg.

Tomiyama, A. (2002). Single bubbles in stagnant liquids and in linear shear flows. *Workshop on Measurement Technology (MTWS5)*, Dresden-Rossendorf, 18. -20. September, H.M. Prasser, ed., 3–19.

Travin, A.K., Shur, M.L., Spalart, P.R., Strelets, M.K. (2006). Improvement of delayed detached-eddy simulation for LES with wall modelling. *ECCOMAS CFD 2006: Proceedings of the European Conference on Computational Fluid Dynamics,* Egmond aan Zee, The Netherlands, September 5-8, 2006.

Ubbink, O. (1997). *Numerical prediction of two fluid systems with sharp interfaces*. University of London.

Ubbink, O., Issa, R.I. (1999). A Method for Capturing Sharp Fluid Interfaces on Arbitrary Meshes. *Journal of Computational Physics* 153(1), 26–50, doi:10.1006/jcph.1999.6276.

Versteeg, H.K., Malalasekera, W. (2007). *An introduction to computational fluid dynamics: The finite volume method*. 2. ed.

Wardle, K.E., Weller, H.G. (2013). Hybrid Multiphase CFD Solver for Coupled Dispersed/Segregated Flows in Liquid-Liquid Extraction. *International Journal of Chemical Engineering* 2013, 1–13, doi:10.1155/2013/128936.

Weller, H. (2015). *OpenFOAM: The Open Source CFD Toolbox User Guide*.

Weller, H.G., Jasak, H., Fureby, C. (1998). A tensorial approach to computational continuum mechanics using object-oriented techniques. *Journal of Computational Physics* 12(6), 620–631, http://www.foamcfd.org/Nabla/main/PDFdocs/CompInPhys98.pdf.

Wilcox, D.C. (1988). Reassessment of the scale-determining equation for advanced turbulence models. *AIAA Journal* 26(11), 1299–1310, doi:10.2514/3.10041.

Wörner, M. (2003). *A compact introduction to the numerical modeling of multiphase flows*. Forschungszentrum Karlsruhe.

Yam, K.S. (2012). Physical and computation modelling of turbidity currents: the role of turbulence-particles interactions and interfacial forces. *Doctoral Thesis*. University of Leeds.

Yan, K., Che, D. (2010). A coupled model for simulation of the gas–liquid two-phase flow with complex flow patterns. *International Journal of Multiphase Flow* 36(4), 333–348.

Youngs, D.L. (1982). Time-dependent multi-material flow with large fluid distortion. *Numerical methods for fluid dynamics* 24, 273–285.

Zalesak, S.T. (1979). Fully multidimensional flux-corrected transport algorithms for fluids. *Journal of Computational Physics* 31(3), 335–362.

Zeidan, D. (2011). Numerical resolution for a compressible two-phase flow model based on the theory of thermodynamically compatible systems. *Applied Mathematics and Computation* 217(11), 5023–5040.

Zeidan, D., Slaouti, A. (2009). Validation of hyperbolic model for two-phase flow in conservative form. *International journal of computational fluid dynamics* 23(9), 623–641.

Zheng, L., Yapa, P.D. (2000). Buoyant velocity of spherical and nonspherical bubbles/droplets. *Journal of Hydraulic Engineering* 126(11), 852–854.

List of Publications

Thorenz, C., Belzner, F., Hartung, T., Schulze, L. (2017). Numerische Simulation von Schleusenfüllprozessen *Kapitel 7, BAWMitteilungen Nr. 100, Kompetenz für die Wasserstraßen – Heute und in Zukunft Forschungs- und Entwicklungsprojekte der BAW, März 2017, Karlsruhe.*

Schulze, L., Rusche H., Thorenz, C. (2015). Development of a Simulation Procedure for the 3D Modelling of the Filling Process in a Navigation Lock Including Fluid Structure Interaction Paper 28, *Proceedings, 7th International PIANC-SMART Rivers Conference 2015, 07.-11. September 2015, Buenos Aires, Argentinia.*

Schulze, L., Thorenz, C. (2015). Mehrphasenmodellierung im Wasserbau *BAWKolloquium Tagungsband „Wasserbauwerke – Vom hydraulischen Entwurf bis zum Betrieb, 20.-21. Mai 2015, Karlsruhe.*

Schulze, L., Thorenz, C. (2014). The Multiphase Capabilities of the CFD Toolbox OpenFOAM for Hydraulic Engineering Applications *Proceedings of the 11th International Conference on Hydroscience & Engineering, 28.September -02.Oktober 2014, Hamburg*, Germany.

Schulze, L., Thorenz C., Stamm, J. (2014). Entwicklung eines numerischen Ansatzes für die Modellierung von Lufteintrag und-transport in einem Schleusenfüllsystem *Dresdner Wasserbauliche Mitteilungen „Simulationsverfahren und Modell für Wasserbau und Wasserwirtschaft“, Heft 50, Dresden, 2014. ISBN 978-3-86780-349-6*

Schulze, L., Thorenz, C. (2013). Towards the CFD-modelling of multiscale-multiphase flow phenomena in navigation locks *Proceedings, 6th International PIANC-Smart Rivers Conference 2013, Liège, Belgium, Maastricht, The Netherlands.*

Strybny, J., Thorenz, C., Steinmill, K., Schulze, L., Hess, M. (2012). On the numerical modelling of ship-waterway-interactions in canals *Proceedings, 10th International Conference on Hydroinformatics (HIC), 14.-18. Juli 2012, Hamburg.*

Schulze, L., Thorenz, C. (2012). Physical model tests and simulation approaches for a navigation lock *Book of Abstracts, 7th OpenFOAM Workshop, Center of Smart Interfaces (CSI), TU Darmstadt, 25.- 28. Juni 2012, Darmstadt.*

Förderverein

Im Internet unter http://www.iwd.tu-dresden.de

Zur Unterstützung der wasserbaulichen Forschung und Lehre wurde von Hochschullehrern und Mitarbeitern des Institutes am 24. Mai 1991 ein gemeinnütziger Förderverein, die Gesellschaft der Förderer des Hubert-Engels-Institutes für Wasserbau und Technische Hydromechanik der Technischen Universität Dresden e. V., gegründet. Der Verein unterstützt die Herausgabe der seit 1990 wieder erscheinenden Dresdner Wasserbaulichen Mitteilungen und nimmt aktiv an der Vorbereitung und Durchführung des alljährlich stattfindenden Dresdner Wasserbaukolloquiums sowie der begleitenden Fachausstellung teil. Darüber hinaus werden vom Förderverein u. a. Studentenexkursionen und Forschungsarbeiten finanziell unterstützt.

S A T Z U N G

der

Gesellschaft der Förderer des Hubert-Engels-Institutes

für Wasserbau und Technische Hydromechanik

der Technischen Universität Dresden e. V.

§ 1 Name und Sitz

(1) Der Verein führt den Namen „**Gesellschaft der Förderer des Hubert-Engels-Instituts für Wasserbau und Technische Hydromechanik der Technischen Universität Dresden e. V.**“

Er ist im Vereinsregister unter der Nummer VR 1335 registriert.

(2) Der Sitz des Vereins ist Dresden.

(3) Das Geschäftsjahr ist das Kalenderjahr.

§ 2 Zweck

(1) Der Verein verfolgt ausschließlich und unmittelbar gemeinnützige Zwecke im Sinne des Abschnittes "Steuerbegünstigte Zwecke" der Abgabenordnung. Er dient der Förderung wissenschaftlicher Forschungsarbeiten auf gemeinnütziger Grundlage, der Information seiner Mitglieder und der Öffentlichkeit über die Forschungs- und Versuchsarbeiten des Instituts, der Förderung von Aus- und Weiterbildung sowie der Förderung des Umwelt- und Landschaftsschutzes.

(2) Der Satzungszweck wird insbesondere verwirklicht durch:

1. Durchführung wissenschaftlicher Veranstaltungen und Forschungsvorhaben zu Themen des umweltverträglichen Wasserbaus, der Renaturierung von Gewässern, der Verbesserung der Wasserversorgung und Abwasserbehandlung, des Verkehrswasserbaus (mit dem Ziel umweltfreundlicher Transportdurchführung auf Wasserstraßen), sowie des Hochwasser- und Küstenschutzes
2. Werbung in den interessierten Fachkreisen für den Wasserbau und das hydraulische Versuchswesen
3. Koordinierung der Arbeiten und Zusammenarbeit auf wasserbaulichem und hydraulischem Gebiet mit anderen Instituten

4. Unterstützung von hydraulischen Modellversuchen
5. Unterstützung der Durchführung von Kolloquien und Symposien in den Fachgebieten Wasserbau und Technische Hydromechanik
6. Förderung der Publikation von wissenschaftlichen Arbeiten, Institutsberichten und Informationsmaterial
7. Unterstützung von Reisen zu Fachvorträgen und zur Besichtigung von wasserbaulichen Objekten
8. Durchführung von Informationsveranstaltungen an Schulen und Gymnasien
9. Unterstützung von besonders förderungswürdigen in- und ausländischen Studierenden des Wasserbaus.
10. Würdigung herausragender Leistungen von Absolventen und Studierenden in den Fachgebieten des Wasserbaus und der technischen Hydromechanik.

(3) Der Verein ist selbstlos tätig und verfolgt nicht in erster Linie eigenwirtschaftliche Zwecke.

§ 3 Mitgliedschaft

(1) Ordentliche Mitglieder können natürliche und juristische Personen werden, die den Zweck des Vereins nach §2 unterstützen.

(2) Jungmitglieder können Studenten werden, die an einer Hochschuleinrichtung mit wasserbaulich-wasserwirtschaftlicher Ausbildung immatrikuliert sind.

(3) Korrespondierende Mitglieder können vom Vorstand ernannt werden, wenn sie auf dem Gebiet des Wasser- und Grundbaus, der Wasserwirtschaft und der Hydrologie forschend tätig sind.

(4) Ehrenmitglieder können von der Mitgliederversammlung ernannt werden, wenn sie sich besondere Verdienste bei der Förderung des Vereins erworben haben.

§ 4 Organe des Vereins

(1) Die Organe des Vereins sind

a) die Mitgliederversammlung und

b) der Vorstand.

(2) Die Mitglieder des Vorstands sind ehrenamtlich tätig.

§ 5 Mitgliederversammlung

(1) Eine ordentliche Mitgliederversammlung findet einmal im Jahr (in der Regel in Verbindung mit dem Dresdner Wasserbaukolloquium) statt. Ihre Einberufung erfolgt unter Einhaltung einer Frist von vier Wochen in Textform durch den Geschäftsführer im Auftrag des Vorstandes unter Mitteilung des Termins, des Ortes und der Tagesordnung.

(2) Zusätze zur Tagesordnung können innerhalb einer Frist von 14 Tagen beim Geschäfts-führer beantragt werden.

(3) In der Mitgliederversammlung werden geschäftliche Angelegenheiten in Verbindung mit Vorträgen oder Mitteilungen und deren Beratung behandelt und erledigt.

(4) Die Mitgliederversammlung beinhaltet:

1. den Bericht des Vorsitzenden über das Geschäftsjahr
2. den Bericht der Rechnungsprüfer
3. Genehmigung der Berichte und Entlastung des Vorstandes
4. Beschlüsse über vorliegende Anträge und über Änderungen der Satzung
5. Wahl von zwei Rechnungsprüfern
6. Verschiedenes

(5) Der Vorstand kann jederzeit binnen 14 Tagen eine außerordentliche Mitgliederversammlung einberufen. Er ist dazu verpflichtet, wenn

mindestens ein Zehntel der Mitglieder dies unter Angabe des Zwecks und der Gründe fordert.

(6) Der Vorsitz der Mitgliederversammlung wird vom Vorsitzenden oder vom stellvertretenden Vorsitzenden geführt.

(7) Die Mitgliederversammlung fasst ihre Beschlüsse mit einfacher Mehrheit. Sie ist bei satzungsgemäßer Einladung in jedem Falle beschlussfähig. Bei Stimmengleichheit entscheidet die Stimme des Vorsitzenden.

(8) Satzungsänderungen erfordern eine 3/4-Mehrheit.

(9) Anträge auf Änderung der Satzung, die nicht vom Vorstand ausgehen, können nur dann beraten werden, wenn sie mindestens vier Wochen vor der Mitgliederversammlung unter Angabe der Gründe beim Vorstand eingereicht worden sind.

(10) Jedes Mitglied hat nur eine Stimme. Stimmübertragungen sind durch schriftliche Vollmacht auf ordentliche Mitglieder nur bis zu zwei möglich.

(11) Der Verein kann sich zur Regelung der vereinsinternen Abläufe Vereinsordnungen geben. Die Vereinsordnungen sind nicht Bestandteil der Satzung. Für den Erlass, die Änderung und Aufhebung von Vereinsordnungen ist die Mitgliederversammlung zuständig.

(12) Die Beschlüssen der Mitgliederversammlung sind zu protokollieren. Das Protokoll ist vom Vorsitzenden und dem Protokollführer zu unterzeichnen.

§ 6 Vorstand

(1) Der Vorstand wird von der ordentlichen Mitgliederversammlung für die Dauer von fünf Jahren gewählt und bleibt bis zum Ablauf der ordentlichen Mitgliederversammlung zur Neuwahl im Amt.

(2) Der Vorstand besteht aus vier gewählten ordentlichen Mitgliedern

- dem Vorsitzenden,
- dem stellvertretenden Vorsitzenden,

- dem Geschäftsführer und
- dem Schatzmeister.

Der Vorsitzende vertritt den Verein mit jeweils einem weiteren ordentlichen Mitglied des Vorstands gemeinsam.

(3) Vom Vorstand kann ein Ehrenvorsitzender bestellt werden.

(4) Die Mitgliederversammlung kann durch einfache Mehrheit beschließen, darüber hinaus noch bis zu zwei Mitglieder als Beisitzer zur Vertretung des Vereins in den Vorstand zu bestellen.

(5) Der Vorstand kann einzelnen Personen Vollmachten für Zweige der Geschäftsführung erteilen.

(6) Dem Vorstand obliegt die Vertretung des Vereins nach § 26 BGB. Er ist mit der Führung aller laufenden Geschäfte beauftragt und sorgt für die Durchführung der Beschlüsse der Mitgliederversammlung. Er kann selbständig Maßnahmen treffen, die dem Vereinszweck förderlich sind.

§ 7 Aufnahme oder Beendigung der Mitgliedschaft

(1) Die Aufnahme als ordentliches Mitglied oder als Jungmitglied ist schriftlich beim Vor-stand zu beantragen. Dieser entscheidet über die Aufnahme. Der Aufnahmebeschluss ist dem Antragsteller mitzuteilen. Bei Zurückweisung des Antrages kann der Antragsteller eine Entscheidung durch die Mitgliederversammlung beantragen, deren Zustimmung ei-ne 2/3-Mehrheit voraussetzt.

(2) Die Mitgliedschaft kann beendet werden

a) durch schriftliche Austrittserklärung eines Mitglieds gegenüber dem Vorstand mit einer Frist von drei Monaten zum Ende des laufenden Geschäftsjahres,

b) auf Beschluss des Vorstandes, wenn 3/4 der Mitgliederversammlung dem Ausschluss zustimmen,

c) bei Vereinigungen oder Gesellschaften mit deren Auflösung,

d) bei natürlichen Personen mit dem Tod oder

e) durch Streichung aus der Mitgliederliste, wenn trotz Erinnerung durch den Vorstand in drei Folgejahren kein Mitgliedsbeitrag entrichtet wurde und kein erkennbarer Hinderungsgrund vorliegt.

§ 8 Rechte und Pflichten der Mitglieder

(1) Die Mitglieder des Vereins haben das aktive Wahlrecht, können Anträge an den Verein stellen und an den Veranstaltungen des Vereins teilnehmen. Das passive Wahlrecht haben nur Mitglieder, die natürliche Personen sind.

(2) Juristische Personen müssen eine natürliche Person benennen, welche die Mitgliederrechte wahrnimmt. Ist eine derartige Person nicht benannt, so ruhen die Rechte der juristischen Person als Mitglied des Vereins.

(3) Die Mitglieder des Vereins haben das Recht auf Information über die vom Institut durchgeführten und laufenden Arbeiten sowie zur Besichtigung des Instituts und seiner Versuchseinrichtungen soweit das betrieblich möglich ist und die Interessen der Auftraggeber nicht beeinträchtigt werden.

(4) Die Mitglieder haben Anspruch auf Überlassung von geförderten veröffentlichten Materialien.

(5) Die Mitglieder sind verpflichtet, den Verein entsprechend der Satzung bei der Erfüllung seiner Aufgaben nach besten Kräften zu unterstützen.

(6) Die Mitglieder sind zur Zahlung eines jährlichen Beitrags verpflichtet. Die Höhe des jährlichen Beitrags, die Fälligkeit, die Art und Weise der Zahlung und zusätzliche Gebühren bei Zahlungsverzug oder Verwendung eines anderen als des beschlossenen Zahlungsverfahrens regelt eine Beitragsordnung, die von der Mitgliederversammlung beschlossen wird.

(7) Ehrenmitglieder und korrespondierende Mitglieder sind beitragsfrei.

§ 9 Auflösung des Vereins

(1) Der Verein kann nur auf Beschluss von 2/3 der anwesenden stimmberechtigten Mitglieder einer ordentlichen Mitgliederversammlung aufgelöst werden. Sind in dieser Mitgliederversammlung weniger als 1/3 der stimmberechtigten Mitglieder erschienen, so muss eine neue Mitgliederversammlung einberufen werden, die dann entscheidet.

(2) Im Falle der Auflösung oder Aufhebung des Vereins oder bei Wegfall seiner steuerbegünstigten Zwecke fällt sein Vermögen an das Institut für Wasserbau und Technische Hydromechanik der Technischen Universität Dresden, das es unmittelbar und ausschließlich für die Förderung von wissenschaftlichen Forschungsarbeiten zu verwenden hat.

(3) Die vorstehenden Bestimmungen gelten entsprechend, wenn dem Verein die Rechtsfähigkeit entzogen wird.

§ 10 Gemeinnützigkeit

(1) Mittel des Vereins dürfen nur für die satzungsgemäßen Zwecke verwendet werden. Die Mitglieder erhalten keine Zuwendungen aus Mitteln der Körperschaft.

(2) Die Mitglieder des Vorstandes erhalten keine Vergütung für ihre Tätigkeit. Auslagen im Interesse des Vereins werden auf Antrag ersetzt, wenn sie der Vorstand vorher genehmigt hat und der Verein dazu in der Lage ist.

(3) Der Verein darf keine Personen durch Ausgaben, die dem Zweck des Vereins fremd sind, oder durch unverhältnismäßig hohe Vergütungen begünstigen.

Die Satzung wurde in der Gründungsversammlung am 24. Mai 1991 in Dresden angenommen und am 18. März 2004 sowie am 6. März 2015 geändert.

Bisher erschienene Dresdner Wasserbauliche Mitteilungen

Heft 1 (vergriffen)	1989	**Klaus Römisch** Empfehlung zur Bemessung von Hafeneinfahrten **Eberhard Lattermann** Bemessungsgrundlagen für Dichtungen und Deckwerke im Wasserbau
Heft 2 (vergriffen)	1990	**Frank Krüger** Schubspannungsverteilungen in offenen, geradlinigen Trapez- und Rechteckgerinnen **Helmut Martin, Reinhard Pohl** Überflutungssicherheit von Talsperren
Heft 3 (vergriffen)	1990	**Reinhard Pohl** Die Entwicklung der wasserbaulichen Lehre und Forschung an der Technischen Universität Dresden **Reinhard Pohl** Die Berechnung der auf- und überlaufvermindernden Wirkungen von Wellenumlenkern im Staudammbau
Heft 4 (vergriffen)	1991	**Ellen Haufe** Hydromechanische Untersuchungen von Mischungs-, Flockungs- und Sedimentationsprozessen in der Trinkwasseraufbereitung
Heft 5	1994	**Wasserbaukolloquium 1993** Die Elbe - Wasserstraße und Auen
Heft 6 (vergriffen)	1995	**Wasserbaukolloquium 1994** Wasserkraft und Umwelt ISBN 3-86005-154-7

Heft 7	1995	**Wasserbaukolloquium 1995** Hydromechanische Beiträge zum Betrieb von Kanalnetzen ISBN 3-86005-155-5
Heft 8	1996	**Detlef Aigner** Hydrodynamik in Anlagen zur Wasserbehandlung ISBN 3-86005-164-4
Heft 9 (vergriffen)	1996	**Wasserbaukolloquium 1996** Wellen: Prognosen - Wirkungen - Befestigungen ISBN 3-86005-165-2
Heft 10	1997	**Wasserbaukolloquium 1997** Sanierung und Modernisierung von Wasserbauwerken, aktuelle Beispiele aus Deutschland, Polen, der Slowakei und Tschechien ISBN 3-86005-185-7
Heft 11 (vergriffen)	1997	**Reinhard Pohl** Überflutungssicherheit von Talsperren ISBN 3-86005-186-5
Heft 12 (vergriffen)	1998	**Reinhard Pohl** Die Geschichte des Institutes für Wasserbau an der Technischen Universität Dresden ISBN 3-86005-187-3
Heft 13	1998	**Wasserbaukolloquium 1998** Hydraulische und numerische Modelle im Wasserbau, Entwicklung - Perspektiven ISBN 3-86005-201-2
Heft 14	1998	**Uwe Müller** Deformationsverhalten und Belastungsgrenzen des Asphaltbetons unter den Bedingungen von Staudammkerndichtungen ISBN 3-86005-213-6

Heft 15	1999	**Wasserbaukolloquium 1999** Betrieb, Instandsetzung und Modernisierung von Wasserbauwerken ISBN 3-86005-223-3
Heft 16	1999	**Dirk Carstensen** Beanspruchungsgrößen in Fließgewässern mit geschwungener Linienführung ISBN 3-86005-236-5
Heft 17 (vergriffen)	1999	**Ehrenkolloquium Prof. Martin** anlässlich des 60. Geburtstages von Herrn Univ. Prof. Dr.-Ing. habil. Helmut Martin ISBN 3-86005-237-3
Heft 18	2000	**Wasserbaukolloquium 2000** Belastung, Stabilisierung und Befestigung von Sohlen und Böschungen wasserbaulicher Anlagen ISBN 3-86005-243-8
Heft 19	2001	**Seleshi B. Awulachew** Investigation of Water Resources Aimed at Multi-Objective Development with Respect to Limited Data Situation: The Case of Abaya-Chamo Basin, Ethiopia ISBN 3-86005-277-2
Heft 20	2001	**Stefan Dornack** Überströmbare Dämme Beitrag zur Bemessung von Deckwerken aus Bruchsteinen ISBN 3-86005-283-7
Heft 21	2002	**Wasserbaukolloquium 2002** Innovationen in der Abwasserableitung und Abwassersteuerung ISBN 3-86005-297-7

Heft 22	2002	**Zelalem Hailu G. Chirstos** Optimisation of Small Hydropower Sites for Rural Electrification ISBN 3-86005-304-3
Heft 23	2002	**Ehrenkolloquium Prof. Wagner** Zur Emeritierung von Univ.-Prof. Dr.-Ing. habil. Harold Wagner ISBN 3-86005-307-8
Heft 24	2003	**Wasserbaukolloquium 2003** Gewässer in der Stadt ISBN 3-86005-358-2
Heft 25	2003	**Toufik Tetah** Numerische Simulation des dynamischen Verhaltens von Caisson-Wellenbrecher-Gründungen unter Einwirkung brechender Wellen ISBN 3-86005-363-9
Heft 26	2003	**Ehrenkolloquium Prof. Horlacher** Zum 60. Geburtstag von Herrn Univ.-Prof. Dr.-Ing. habil. Hans-B. Horlacher ISBN 3-86005-376-0
Heft 27 (vergriffen)	2004	**Wasserbaukolloquium 2004** Risiken bei der Bemessung und Bewirtschaftung von Fließgewässern und Stauanlagen ISBN 3-86005-414-7
Heft 28	2004	**Reinhard Pohl** Historische Hochwasser aus dem Erzgebirge ISBN 3-86005-428-7
Heft 29 (vergriffen)	2005	**Wasserbaukolloquium 2005** Stauanlagen am Beginn des 21. Jahrhunderts ISBN 3-86005-461-9

Heft 30	2005	**Nigussie Teklie Girma** Investigation on Sediment Transport Characteristics and Impacts of Human Activities on Morphological Processes of Ehiopian Rivers:Case Study of Kulfo River, Southern Ethiopia ISBN 3-86005-483-X
Heft 31	2006	**Matthias Standfuß** Druckwellenausbreitung in erdverlegten Rohrleitungen aus PE-HD ISBN 3-86005-495-3
Heft 32	2006	**Wasserbaukolloquium 2006** Strömungssimulation im Wasserbau ISBN 3-86005-473-2
Heft 33	2006	**Antje Bornschein** Die Ausbreitung von Schwallwellen auf trockener Sohle unter besonderer Berücksichtigung der Wellenfront ISBN 3-86005-523-2
Heft 34	2007	**Torsten Frank** Hochwassersicherheit in sielbeeinflussten Gewässersystemen am Beispiel des Bongsieler Kanals ISBN 978-3-86780-019-8
Heft 35	2007	**Wasserbaukolloquium 2007** Fünf Jahre nach der Flut ISBN 987-3-86005-571-7
Heft 36	2008	**Aktuelle Forschungen 1993 – 2008** Zum 65. Geburtstag von Herrn Prof. Horlacher ISBN 978-3-86780-083-9

Heft 37	2009	**Dirk Carstensen** Eis im Wasserbau - Theorie, Erscheinungen, Bemessungsgrößen ISBN 978-3-86780-099-0
Heft 38 (vergriffen)	2009	**Reinhard Pohl, Antje Bornschein, Robert Dittmann, Stefano Gilli** Mehrzieloptimierung der Steuerung von Talsperren zur Minimierung von Hochwasserschäden im Unterwasser ISBN 978-3-86780-100-3
Heft 39 (vergriffen)	2009	**Wasserbaukolloquium 2009** Wasserkraftnutzung im Zeichen des Klimawandels, angepasste Strategien - neue Technologien ISBN 978-3-86780-101-0
Heft 40 (vergriffen)	2010	**Wasserbaukolloquium 2010** Wasserbau und Umwelt - Anforderungen, Methoden, Lösungen ISBN 978-3-86780-101-0
Heft 41	2010	**Ralf Tackmann** Erosion 2008 - Ein numerisches Modell zur Prognose des Bodenaustrages von kohäsiven Böden unter Berücksichtigung der Rillenerosion ISBN 978-3-86780-158-4
Heft 42	2010	**Ulf Helbig** Tragverhalten und Berechnung von mehrschichtigen Verbundrohren ISBN 978-3-86780-159-1
Heft 43	2010	**Stefano Gilli** Die Wirkung von Flussaufweitungen auf Hochwasserwellen - Parameterstudie einer Deichrückverlegung im Flussmittellauf ISBN 978-3-86780-160-7

Heft 44	2010	**Negede Abate Kassa** Probabilistic Safety Analysis of Dam - Methods and Applications ISBN 978-3-86780-161-4
Heft 45 (vergriffen)	2011	**Wasserbaukolloquium 2011** Wasserkraft - Mehr Wirkungsgrad + Mehr Ökologie = Mehr Zukunft ISBN 978-3-86780-198-0
Heft 46	2011	**Torsten Heyer** Zuverlässigkeitsbewertung von Flussdeichen nach dem Verfahren der logistischen Regression ISBN 978-3-86780-197-3
Heft 47	2011	**Wasserbaukolloquium 2012** Staubauwerke - Planen, Bauen, Betreiben ISBN 978-3-86780-261-1
Heft 48	2013	**Wasserbaukolloquium 2013** Technischer und organisatorischer Hochwasserschutz - Bauwerke, Anforderungen, Modelle ISBN 978-3-86780-318-2
Heft 49	2013	**Vinzent Sturm** Simulation der Fluid-Struktur-Interaktion mit freier Oberfläche am Beispiel des Schlauchwehres unter Anwendung von Ansys/CFX ISBN 978-3-86780-348-9
Heft 50	2014	**Wasserbaukolloquium 2014** Simulationsverfahren und Modelle für Wasserbau und Wasserwirtschaft ISBN 978-3-86780-349-6

Heft 51	2014	**Holger Haufe** Zwischenauslässe an Talsperren - Beispiele, Bemessung, Konstruktion, Nachrüstung ISBN 978-3-86780-393-9
Heft 52	2014	**Pohl/Bornschein u.a.** Effect of very oblique waves on wave run-up and wave overtopping ISBN 978-3-86780-392-2
Heft 53	2015	**Wasserbaukolloquium 2015** Messen und Überwachen im Wasserbau und am Gewässer ISBN 978-3-86780-420-2
Heft 54	2015	**Mohammed Abdallah** Developing a Multi-purpose Reservoir operating Model with Uncertain Conditions: a Case of Eastern Nile Reservoirs - Sudan ISBN 978-3-86780-431-8
Heft 55	2015	**Paolo Dapoz** Reinigung von Abwasserkanälen mittels Niederdruckspülverfahren ISBN 978-3-86780-432-5
Heft 56	2015	**JuWi-Treffen** 17. JuWi-Treffen: Fachbeiträge zur Tagung vom 26.-28. August 2015 ISBN 978-3-86780-448-6
Heft 57	2016	**Wasserbaukolloquium 2016** Gewässerentwicklung & Hochwasserrisikomanagement ISBN 978-3-86780-475-2

Heft 58	2017	**Wasserbaukolloquium 2017** Bemessung im Wasserbau - Klimaanpassung, Untersuchung, Regeln, Planung, Ausführung ISBN 978-3-86780-509-4
Heft 59	2017	**Roberto Tatis Muvdi** A contribution to the hydro morphological assessment of running waters based on habitat dynamics. ISBN 978-3-86780-512-4
Heft 60	2018	**Wasserbaukolloquium 2018** Wasserbauwerke im Bestand - Sanierung, Umbau, Ersatz-neubau und Rückbau ISBN 978-3-86780-556-8
Heft 61	2018	**Lydia Schulze** Development of an Application-Oriented Approach for Two-Phase Modelling in Hydraulic Engineering 978-3-86780-571-1

Die **Dresdner Wasserbauliche Mitteilungen** können bezogen werden über:

Technische Universität Dresden
Bereich Bau und Umwelt
Institut für Wasserbau und Technische Hydromechanik
01062 Dresden

Telefon: +49 351 463 34397
Fax: +49 351 463 37120
E-Mail: tagungsband@wasserbaukolloquium.de

Ein großer Teil unserer Hefte ist digitalisiert und über das Fachrepository HENRY der Bundesanstalt für Wasserbau einzusehen.

https://henry.baw.de/

Auswahl über „Browsen → Bereiche & Sammlungen“